



HAL
open science

3D Seismic Attributes Enhancement and Detection by Advanced Technology of Image Analysis

Gengxiang Li

► **To cite this version:**

Gengxiang Li. 3D Seismic Attributes Enhancement and Detection by Advanced Technology of Image Analysis. Earth Sciences. Université Michel de Montaigne - Bordeaux III, 2012. English. NNT : 2012BOR30006 . tel-00731886

HAL Id: tel-00731886

<https://theses.hal.science/tel-00731886>

Submitted on 13 Sep 2012

HAL is a multi-disciplinary open access archive for the deposit and dissemination of scientific research documents, whether they are published or not. The documents may come from teaching and research institutions in France or abroad, or from public or private research centers.

L'archive ouverte pluridisciplinaire **HAL**, est destinée au dépôt et à la diffusion de documents scientifiques de niveau recherche, publiés ou non, émanant des établissements d'enseignement et de recherche français ou étrangers, des laboratoires publics ou privés.



UNIVERSITE MICHEL DE MONTAIGNE – BORDEAUX 3

ECOLE DOCTORALE 480

"Montaigne - Humanités"

Doctorat

Discipline : Sciences et technologie

Spécialité : Sciences de l'Image

Gengxiang LI

**REHAUSSEMENT ET DETECTION DES ATTRIBUTS SISMIQUES 3D
PAR TECHNIQUES AVANCEES D'ANALYSE D'IMAGES**

**(3D Seismic Attributes Enhancement and Detection
by Advanced Technology of Image Analysis)**

(Thèse dirigée par : Adrian CEREPi et Mo DAI)

Soutenue le 19 Avril 2012

Jury:

Gilles GRANDJEAN	Directeur de recherche, HDR, BRGM	Rapporteur
Qunhui ZHANG	Professeur, Université de Science et de Technologie de Xi'an	Rapporteur
Adrian CEREPi	Professeur, ENSEGID	Examinateur
Mo DAI	Maître de conférences, Université de Bordeaux 3	Examinateur

Remerciements

Ce mémoire est l'aboutissement d'un travail effectué durant ces quatre dernières années au sein de l'équipe de recherche "Géoressources et Environnement" à l'Ecole Nationale Supérieure en Environnement, Géoressources et Ingénierie du Développement durable (ENSEGID).

Je tiens tout d'abord à exprimer toute ma gratitude à Monsieur Jean-Marie Malézieux, Professeur et Directeur de l'ENSEGID, pour m'avoir accueilli dans son école et pour m'avoir fourni tous les moyens nécessaires au bon déroulement de cette thèse.

Je remercie vivement mon directeur de thèse, Monsieur Adrian CEREP, Professeur à l'ENSEGID, pour avoir accepté de diriger ce travail et aussi pour sa gentillesse et son aide efficace.

J'exprime mes plus vifs remerciements à mon directeur scientifique, Monsieur Mo Dai, Maître de Conférences à l'Université de Bordeaux 3, qui m'a offert la chance inestimable de découvrir le monde passionnant et enrichissant de la recherche dans le domaine de l'analyse d'images et de la reconnaissance des formes et qui m'a beaucoup aidé tout au long de ces 3 ans.

J'adresse également mes sincères remerciements à Monsieur Gilles GRANDJEAN, Directeur de recherche, HDR, BRGM, et à Monsieur Qunhui ZHANG, Professeur à l'Université de Science et de Technologie de Xi'an, qui ont accepté d'être les rapporteurs de mon mémoire.

Je tiens tout particulièrement à remercier les membres de l'ENSEGID pour toutes les conversations et les moments de vie commune que nous avons eue depuis ces quatre dernières années.

Je remercie aussi l'entreprise de «Sharewin Software Co.,Ltd », pour des aides financières.

Enfin, je remercie mes proches, famille et amis qui m'ont beaucoup encouragé et à qui je dédie ce mémoire.

Résumé

L'énergie est l'une des ressources naturelles les plus importantes dans les sociétés modernes. Plus de la moitié des besoins énergétiques dans le monde provient du pétrole et du gaz ([Randen and Sønneland, 2005](#)). Les demandes croissantes en matière de consommation d'énergie dans le monde entier et l'épuisement du pétrole et du gaz de grands réservoirs ont abouti à la nécessité d'explorer les gisements de pétrole plus petit et plus complexe. Il en résulte des exigences élevées pour les ressources en hydrocarbures et rend leur identification et l'extraction plus difficile. Le pétrole et le gaz naturel sont deux des ressources non renouvelables dans le monde, et ils sont les principales sources d'énergie au monde. En raison du niveau élevé de l'énergie stockée dans l'huile, cette source d'énergie est devenu et est actuellement l'un des principaux piliers de nos sociétés industrielles. En raison de leur importance, le pétrole et le gaz naturel ont un impact profond dans les économies du monde et la politique. Aujourd'hui, le pétrole et le gaz naturel fournissent à plus de 90% dans le monde des carburants destinés au transport. Ils sont aussi liés à plusieurs produits que nous utilisons dans notre vie quotidienne et les activités.

Le pétrole est un combustible fossile liquide qui est formé des restes de microorganismes marins déposés dans les fonds marins. Après des millions d'années, les dépôts ont terminés dans les roches et les sédiments où le pétrole est emprisonné dans des petits espaces ([Patel et al., 2008](#)). Il peut être extrait part des plateformes de forage. Le pétrole est le combustible fossile le plus utilisé. Le gaz naturel est également un combustible fossile gazeux qui est polyvalent, abondant et relativement propre en comparaison du charbon et du pétrole. Comme le pétrole, il est formé par les restes de microorganismes marins. Il s'agit d'un mélange d'hydrocarbures trouvé naturellement sous forme gazeuse. C'est la deuxième source d'énergie la plus utilisée dans le monde après le pétrole et son usage se développe rapidement. Le gaz naturel est principalement constitué de méthane et peut être trouvé en association avec

d'autres combustibles fossiles comme dans les veines de charbon et les clathrates de méthane. Le gaz naturel est créé dans deux classes de mécanismes: la création biogénique et la création thermogénique ([Roje et al., 1997](#)). Le pétrole produit et le gaz naturel vont migrer vers le haut et vont s'accumuler dans les structures réservoirs comme les anticlinaux ou des pièges failles. Le pétrole et le gaz naturel sont recherché par trouvant des signes de ces sédimentaires ou structures du réservoir.

Dans la première section, nous décrivons notre motivation et notre problème plus en détail. Ensuite, dans la seconde section, nous résumons les contributions principales de notre travail. Enfin, nous donnons un aperçu pour le reste de cette thèse dans la dernière section.

Motivation et description de la problématique

Il existe quatre techniques de levés géophysiques qui sont couramment utilisés dans l'exploration du pétrole et du gaz ([Ashcroft and Ashcroft, 2011](#)):

- le levé gravimétrique,
- le levé aéromagnétique,
- le levé électromagnétique,
- le levé sismique.

Le levé sismique est le programme pour cartographier la structure géologique par l'observation des ondes sismiques, notamment par la création des ondes sismiques en utilisant des sources artificielles et par l'observation du temps d'arrivée des ondes réfléchies à partir des contrastes d'impédance acoustique ou des réfractés par des membres à grande vitesse ([Sheriff, 1978](#)). Le levé sismique a une longue histoire d'utilisation dans le domaine de l'exploration pétrolière. Il est un principal outil pour délimiter la structure du sous-sol et détecter la présence d'hydrocarbures. Grâce aux données sismiques recueillies avant le forage, on pourrait, ainsi, optimiser les lieux de luis en place des forages des échantillons des épaisse accumulations de till ou, plus particulièrement, les établir sur le versant des élévations de roche en place oriente dans la direction de l'écoulement glaciaire, afin de tirer le maximum de chaque sondage. Depuis le premier profile sismique réalisé sur la terre long de la côte, qui a été réalisé dans les années 1920 ([Bakker, 2002](#)). La méthode de réflexion sismique a joué un rôle important dans l'exploration des ressources énergétiques. La méthode sismique est une puissante technique de télédétection, on peut imager le sous-sol depuis quelques dizaines de mètres jusqu'à quelques dizaines de kilomètres au maximum. Le premier levé sismique 3D a été réalisé par Exxon à Friendswood près de Houston au Texas en 1967. Les premiers levés

sismiques sont coûteux à acquérir et à traiter. Mais accompagné de progrès technologique, le coût, le processus et le temps d'interprétation de sismique 3D baissent. Au début des années 1980, plusieurs revues scientifiques ont publié un certain nombre d'articles concernant l'approche sismique 3D. Les levés sismiques 3D dans les autres zones littorales et de la terre sont également développés de plus en plus rapides. La technologie sismique 3D représente l'une des introductions technologiques les plus importantes dans les dernières décennies qui a permis d'améliorer les efficacités de la prospection de pétrole et de gaz significativement pour les compagnies pétrolière et gazière.

L'exploration sismique peut être divisée en trois principales étapes ([Yilmaz and Doherty, 1987](#)): i) l'acquisition de données (dans la terre et la mer), ii) le traitement (y compris le traitement du signal et le traitement de l'image), iii) l'interprétation (l'interprétation de structure, l'interprétation de faille, la classification de faciès sismiques, l'identification des hydrocarbures réservoirs, etc.). La méthode sismique commence avec l'acquisition qui consiste à collecter des données brutes directement à partir des récepteurs. Le but du traitement sismique est de traiter les données sismiques acquises dans une image qui peut être utilisée pour déduire la structure du sous-sol. Il existe un certain nombre d'étapes impliquées depuis l'acquisition de données sismiques jusqu'à l'interprétation de la structure du sous-sol. Quelques étapes les plus courantes sont résumées ci-dessous:

Les principales étapes de l'exploration sismique

Acquisition	Correction statique
Traitement	Analyse de la vitesse
	NMO/DMO
	Stacking
	Migration
Interprétation	Les données sismiques à la géologique du sous-sol

Pour travailler en utilisant les étapes ci-dessus, plusieurs opérations de traitement du signal sont nécessaires. Par exemple, l'échantillonnage des données, la récupération d'amplitude, la correction, la corrélation croisée, l'auto-corrélation, le filtrage, la transformée de Fourier, la transformée de Fourier discrète, la transformée Z, la convolution / déconvolution etc. Les données sismiques fournissent un outil le plus important pour les géoscientifiques à faire l'interprétation structurale. Néanmoins, non seulement ils contiennent des informations très

utiles pour l'interprétation structurale, mais ils contiennent ainsi des bruits aléatoires inutiles. Il est souhaitable de rehausser les structures et de réduire les bruits aléatoires. Mais, une seule donnée sismique ne permet pas de séparer le bruit à partir des caractéristiques sismiques réelles. Donc l'utilisation des cartes des attributs sismiques pour l'interprétation structurale détaillée a augmenté dans la dernière décennie. La présence de plus d'un levé sismique permettra à l'interpréteur d'accroître ses connaissances par les incertitudes dans l'interprétation structurale sismique détaillée. L'interprétation sismique exige également beaucoup de mathématiques, de la reconstruction des données, et de l'interprétation des données.

Les attributs sismiques sont des mesures spécifiques de géométrie, de cinématique, de dynamique ou de caractéristique statistique dérivé des données sismiques. Donc, il représente un sous-ensemble d'information totale ([Barnes, 2001](#)). Ils nous aident à mieux de visualiser ou de quantifier les caractéristiques d'interprétation ([Chopra and Marfurt, 2007](#)). L'application des attributs sismiques pour la détection de faille, la détermination de la distribution de fractures, l'identification des caractéristiques stratigraphiques et l'interprétation des autres événements géologiques est utilisée de plus en plus aujourd'hui en géosciences. Les attributs sismiques peuvent être divisés en deux grandes catégories: les attributs qui nous aident à quantifier la composante morphologique des données sismiques et les attributs qui nous aident à quantifier la composante de réflectivité des données sismiques. Les attributs morphologiques permettent d'extraire des informations sur le DIP de réflecteur, l'azimut, la forme, et la cessation, qui peuvent, à leur tour, affecter les failles, les canaux, les fractures, les karstiques, et les accumulations des carbonates. Les attributs de réflectivité donnent des informations sur l'amplitude des réflecteurs, la forme d'onde, et la variation de l'angle d'illumination, qui peuvent, à leur tour, influencer sur la lithologie, l'épaisseur de réservoir, la densité de fracturation et l'azimut de fracturation, et la présence d'hydrocarbures. Dans le mode de reconnaissance, les attributs sismiques nous aident à identifier rapidement les caractéristiques structurelles et les environnements de dépôt. Dans le mode de caractérisation des réservoirs, des attributs sismiques sont étalonnés par rapport aux données réelles et simulées du forage pour identifier les accumulations d'hydrocarbures et la compartimentation du réservoir. Lors des dernières années, beaucoup d'attentions ont été accordées à la prédiction des propriétés réservoirs et à l'extraction d'attributs sismiques pour rehausser la valeur de l'interprétation sismique.

Actuellement, les interprétations sismiques restent basées sur une utilisation intégrée des profils sismiques, tel que l'utilisation en ligne (Inline), en ligne transversale (Crossline), l'utilisation des tranches de temps (Time Slice), et les attributs des horizons. Le défi

aujourd'hui consiste à utiliser pleinement toutes les informations contenues dans les données sismiques. Pour cela, l'interpréteur doit combiner les connaissances dans les disciplines complexes telles que la géologie et la géophysique. Ce n'est pas une tâche facile, et assez souvent, l'absence d'une bonne compréhension géologique conduit le géophysicien à interpréter d'une façon erronée les objets géologiques. De même, le géologue peut facilement interpréter d'une façon erronée les caractéristiques sismiques.

L'interprétation sismique conventionnelle est un art qui exige des compétences et des expériences approfondies en géologie et en géophysique ([Brown, 2004](#); [Coleou et al., 2003](#); [Linari et al., 2003](#); [Marsh et al., 2005](#)). Ces dernières années, de nombreux aspects d'interprétation structurale des données sismiques ont été automatisés. Dorn et al ([2010](#)) ont introduit un nouveau flux de travail unique qui contient une combinaison de processus existants et de processus nouveaux, représentée pour l'interprétation assistée par ordinateur des systèmes de dépôt en volumes sismiques 3D. Ce flux de travail unique contient les étapes générales suivantes: la charge des données sismiques 3D, l'interprétation structurale, la transformation du domaine, le raffinement structurel optionnel, l'interprétation stratigraphique, l'inversement de la transformation du domaine, et la production de volumes stratigraphiques et d'organes stratigraphiques. Les étapes individuelles et les séries des étapes du flux de travail peuvent être appliqués récursivement au volume de donnée pour améliorer les résultats du processus général.

Depuis que la première trace sismique a été rendue par l'ordinateur, l'interprétation automatique a été la panacée promise de la communauté géoscientifique. Après plusieurs années de développement, les développeurs ont encore du mal à proposer une méthodologie d'interprétation automatique raisonnable. Les horizons sismiques correspondent à des objets géologiques stratifiés qui sont créés à travers un ensemble de processus sédimentaire complexe. La mesure de faille coupe et déplace des horizons. La reconstruction des structures de faille, dans leur espace 3D, est un défi majeur dans la géologie du sous-sol.

Dans le domaine de l'exploration sismique du sous-sol, l'incertitude et le non-unicité de l'interprétation géologique sont deux des problèmes importants à cause de la complexité de la géologie du sous-sol et de la dimension limitée des données disponibles. Dans les affichages traditionnels en 2D, il y a une limite de nombre de lignes sismiques ou de cartes sismiques, mais la technologie de l'imagerie sismique 3D fournit une couverture continue volumétrique sismique de la zone du levé qui permet d'étudier la structure sismique, la stratigraphie et des réservoirs d'hydrocarbures à partir de perspective 3D. Les données sismiques 3D offrent une

possibilité unique pour présenter l'observation et l'interprétation sismique géologique dans une espace 3D. Cependant, la plupart des données sismiques 3D sont affichées et interprétées en une manière 2D, laissant l'avantage essentiel et la valeur potentielle des données sismiques 3D non utilisé. Calcul numérique 3D à haut rendement, l'état-de-l'art visualisation de volume et les technologies d'interprétation ont joué des rôles importants en facilitant interprétation volume sismique 3D de manière interactive.

Les images sismiques sont caractérisées par des textures spécifiques qui peuvent fournir des informations précieuses pour localiser les réservoirs de pétrole potentiels. La texture est souvent présentée comme une structure hiérarchique à deux niveaux: le premier concerne les primitives, briques à partir desquelles est construite la texture; le second niveau est relatif aux arrangements spatiaux des primitives. Un problème essentiel dans le domaine de l'analyse des formes est la reconnaissance des objets indépendamment de leurs positions, de leurs tailles et de leurs orientations. Identifier ou reconnaître un contenu informatif par le biais de l'interprétation d'images implique la mise en oeuvre de mécanismes complexes correspondant à de nombreuses modalités visuelles. Parmi l'ensemble de ces modalités, la texture est une des plus importantes. Pour l'homme, elle constitue une excitation, source de phénomènes cognitifs allant du simple saillance visuelle à ceux plus complexes comme la spatialisation. Les descripteurs caractéristiques basés sur les moments ont évolué pour devenir un puissant outil pour l'application en analyse d'image.

Les moments peuvent être appliqués aux images binaires ou aux images en niveaux de gris, définies en 2D, en 3D et en dimension supérieure. Ils peuvent être appliqués aussi aux extraits de bords et de primitives par une étape prétraitement. Les moments et les fonctions moments ont été largement utilisées en analyse d'images pour reconnaissance des formes ([Flusser and Suk, 1993](#); [Hu, 1962](#)) avec des applications allant de la détection des contours ([Luo et al., 1993](#)), la classification et la segmentation d'image ([Yokoya and Levine, 1989](#)), l'analyse de texture ([Tuceryan, 1994](#); [Tuceryan and Jain, 1998](#)), l'estimation de la cohérence ([Li et al., 2010a](#)), l'identification des invariants ([Li et al., 2011](#); [Yang and Dai, 2011](#); [Yang et al., 2011](#)), la classification d'objets, le codage d'image ([Teague, 1980](#); [Teh and Chin, 1988](#)), la reconstruction d'image ([Liao and Pawlak, 1996](#); [Yang and Dai, 2012](#)), l'analyse de la scène ([Jerome, 2009](#); [Sadjadi and Hall, 1978](#)), l'analyse d'objets 3D ([Bronstein et al., 2005](#); [Sadjadi and Hall, 1980](#)). La description des images avec des moments signifie qu'on utilise les propriétés globales de l'image plutôt que ses propriétés locales.

Les moments géométriques sont apparus les premiers et ont été très utilisés essentiellement

pour leur simplicité et leur interprétation géométrique explicite. Néanmoins, les moments géométriques ne sont pas orthogonaux, il est alors difficile de reconstruire une image à partir de ces moments. Teague ([1980](#)) a montré qu'une grande efficacité pouvait être atteinte lorsque l'image était analysée par les moments orthogonaux de Legendre et de Zernike. En outre, il a été prouvé que les moments de Zernike pouvaient capturer l'information d'une image avec une redondance minimale et qu'ils ont la propriété d'invariance en rotation. Puisque les moments de Legendre et de Zernike sont tous les deux définis dans le domaine continu, des transformations appropriées des coordonnées image sont nécessaires pour l'implémentation de ces moments dans le cas discret. Le calcul des moments de Legendre nécessitent de transformer les coordonnées image dans l'intervalle $[-1, 1]$. D'autre part, les polynômes de Zernike sont définis seulement sur le disque de rayon unité ([Mukundan and Ramakrishnan, 1998](#)). De plus, l'erreur de discrétisation issue de l'approximation de l'intégral reste inévitable lors de leur implémentation, ce qui limite la précision des moments calculés ([Liao and Pawlak, 1996](#)). Liao et Pawlak ([1996](#)) ont conduit une analyse théorique sur l'erreur de discrétisation des moments continus et ont proposé une approche limitant l'erreur en dessous d'un certain niveau selon la règle de Simpson. D'autres travaux de recherche visant à améliorer la précision des moments continus se sont focalisés sur les moments géométriques et les moments de Legendre ([Hosny, 2007a, b](#)).

La reconnaissance de la forme d'objets dans une scène est facilement réalisée par des observations visuelles de l'homme, même si l'objet subit des transformations telles que la rotation, le changement d'échelle, la déformation, la vision en perspective etc. La reconnaissance invariante des formes est importante à l'homme pour une variété de tâches. Les moments invariants sont considérés comme des outils importants dans l'analyse d'images et la reconnaissance des formes. Au début des années 60 du siècle dernier, Hu ([1962](#)) a présenté pour la première fois ses sept fameux moments invariants géométriques. Comme ces invariants sont indépendants à la rotation, translation et facteur d'échelle, ils étaient rapidement utilisés comme descripteurs efficaces d'objets dans beaucoup d'applications. Par la suite, quelques nouveaux invariants de moments, toujours basés sur les moments géométriques, ont été développés et utilisés. Abu-Mostafa ([1985](#)) a proposé une méthode pour dériver des invariants de moments géométriques à partir de moments complexes et a analysé leurs propriétés en termes de redondance d'information et de sensibilité au bruit. De même, Reddi ([1981](#)) a fourni un contexte généralisé pour induire des invariants de type radial et angulaire. Un autre type de moments concerne les moments de Zernike à partir desquels des invariants en rotation peuvent être facilement dérivés, puisque les polynômes de Zernike sont orthogonaux à l'intérieur du disque de rayon unité et sont généralement définis en

coordonnées polaires. Les ensembles de type orthogonal et radial tels que les polynômes de Zernike ont une propriété spécifique: "forme-invariants" qui détermine directement l'invariance en rotation des moments correspondants ([Bhatia and Wolf, 1954](#)). Flusser ([Flusser and Suk, 1993](#)) et Reiss ([Reiss, 1991](#)) ont contribué de manière significative à la théorie des invariants de moments en corrigeant le théorème fondamental et en dérivant des invariants à la transformation affine générale. Malgré cela, un autre type important d'invariants appelé "*invariant flou*", qui est indépendant de la convolution, est aussi introduit à l'analyse d'images par le même groupe ([Suk and Flusser, 2003](#)). Les invariants flous apportent une contribution significative à l'analyse d'images, particulièrement les images de télédétection et aériennes. Il est à noter que tous les invariants de moments proposés par Flusser et ses collègues sont basés soit sur les moments géométriques ou les moments complexes. Certains travaux relatifs au développement d'invariants de moments à partir de moments orthogonaux sont apparus graduellement. Chong et al ([2003](#)) ont présenté les invariants en translation des moments de Zernike qui sont efficaces pour construire des invariants en rotation; et ils ont également proposés une méthode permettant de dériver les invariants en translation et en échelle en termes de moments de Legendre ([Chong et al., 2004](#)). Zhu et al ([2007b](#)) ont développés des invariants en translation et en échelle en utilisant les moments discrets de Tchebichef. Jusqu'ici, tous les moments invariants, qu'ils soient dérivés de moments géométriques, de Legendre, voire des moments discrets de Tchebichef, dérivent substantiellement de moments géométriques car les fonctions de base de ces moments sont des combinaisons linéaires de monômes. Par conséquent, certains invariants de moments peuvent être directement obtenus à partir d'invariants de moments géométriques. ([Yap et al., 2003](#); [Zhu et al., 2007c](#)).

Grâce au développement rapide de l'acquisition des données multi-dimensionnelles, il est possible de reconnaître directement des objets 3D. Maintenant, les modèles en 3D sont devenus de plus en plus populaire. Certaines applications, comme le suivi d'objet et la récupération de forme, nous demandent à réfléchir la manière de choix des descripteurs caractéristiques de formes 3D et la façon de mesure des similitudes entre les objets 3D. Sadjadi et Hall ([1980](#)) sont les pionniers du développement des moments invariants géométriques 3D à partir des moments 2D, ils ont construit une famille de trois moments invariants en utilisant un degré à l'ordre seconde. En utilisant la notion de moments complexes, Lo et Don ([1989](#)) ont construit une famille de douze moments invariants avec ordres à partir du premier degré jusqu'au troisième degré. Dans ces derniers travaux, des moments ont été utilisés principalement pour estimer les transformations 3D et leurs performances n'ont pas été évaluées pour les tâches de la classification. En outre, n'étant pas dérivés d'une famille de fonctions orthogonales, ces moments étaient soumis de la corrélation.

Reuze et al ([1993](#)) ont décrit une méthode basée sur les moments géométriques 3D pour le suivi 3D et la quantification des vaisseaux sanguins à partir de l'angiographie par résonance magnétique (ARM). Canterakis ([1997](#)) a étendu les moments de Zernike pour le cas 3D, mais leurs performances n'ont pas été mises à l'épreuve des moments. Werghi et Xiao ([2002](#)) ont proposé l'utilisation des coefficients de transformation par ondelettes (WTC). Sommer et al ([2007](#)) ont proposé une méthode pour comparer les sites de liaison sur les protéines. Ils utilisent moments invariants géométriques 3D comme des vecteurs caractéristiques pour la description de liaison. Xu et Li ([2006a](#)) ont généralisé les courbe des moments 2D dans l'espace euclidien 3D, et ont utilisé la méthode géométrique pour dériver les moments invariants courbe 3D aux différents ordres en vertu de transformation de similitude. Xu et Li ([2006b](#)) ont introduit des moments de surface qui peuvent être traité comme un nouveau type de descripteurs de forme de surfaces de forme libre et peuvent gérer la situation où la surface 3D des objets ne sont pas clos. Mademlis et al ([2006](#)) ont proposé une nouvelle méthode pour la recherche et la récupération basé sur le contenu 3D. Ils ont introduit les moments pondérés de Krawtchout 3D pour l'analyse 3D efficace qui conviennent pour la recherche et l'application de récupération basée sur le contenu. En utilisant le déplacement et les facteurs de l'échelle de polynômes de Legendre pour générer des invariants de la traduction et de l'échelle, Ong et al ([2007](#)) ont présenté un cadre théorique pour dériver la translation des invariants et l'échelle des invariants pour les moments de Legendre 3D.

Une autre série de moments orthogonaux, c'est les moments de Gauss-Hermite. L'analyse des images par les moments de Gauss-Hermite a été proposée par Shen il y a une décennie ([Shen, 1997](#)). Parmi les premiers travaux, on peut distinguer ceux de Shen et Wu sur la détection d'objets en mouvement en utilisant des moments de Gauss-Hermite unidimensionnels ([Shen et al., 2004](#); [Wu and Shen, 2005](#); [Wu et al., 2005](#)), la reconnaissance d'iris ([Ma et al., 2004](#)) et la classification d'empreintes digitales ([Wang and Dai, 2007](#)) basées sur les moments de Gauss-Hermite bidimensionnels. Cependant, ces applications n'utilisent qu'un filtrage dont le noyau est défini avec les fonctions de moments de Gauss-Hermite d'ordre inférieur. Il y a peu de recherche globale sur la capacité de représentation de l'image et de description de l'objet par les moments de Gauss-Hermite.

En ce qui concerne les moments orthogonaux, trois aspects importants sont pris en compte dans notre étude. Le premier est le calcul ou la mise en œuvre discrète. Le second est la reconstruction d'images, à partir de laquelle nous pouvons évaluer la capacité de représentation d'images par les moments. Le dernier est le développement des moments invariants. C'était sur ces axes que nous travaillions et quelques résultats significatifs ont été présentés dans nos publications ([Li et al., 2011](#); [Yang and Dai, 2011, 2012](#); [Yang et al., 2011](#)).

Contributions

Bien que la théorie du moment soit bien établie et appliquée largement dans un certain nombre de zones d'image numérique, elle reste relativement marginale en imagerie sismique. Nous avons appliqué avec succès les moments de Gauss-Hermite à l'analyse d'images sismiques. Avec la définition des moments de Gauss-Hermite 3D à partir du cas 2D, une nouvelle méthode d'interprétation sismique a été proposée dans la thèse. La recherche pour l'interprétation sismique basée sur les moments invariants de Gauss-Hermite a également été présentée dans la thèse. La thèse donne, ensuite, les contributions suivantes:

– **Définition des moments de Gauss-Hermite 3D et leur mise en œuvre discrète :**

Une définition des moments orthogonaux de Gauss-Hermite 3D est dérivée des moments orthogonaux de Gauss-Hermite 2D et de la définition générale des moments géométriques 3D. Sur la base de cette définition, les caractéristiques de l'image 3D peuvent être facilement réalisées à partir des moments orthonormales de Gauss-Hermite 3D. La mise en œuvre discrète de ces moments est détaillée.

– **Dérivation d'invariants 2D/3D par rotation et translation à partir des moments de Gauss-Hermite :**

La dérivation d'invariants pour les moments orthogonaux est généralement compliquée. Dans cette thèse, la dérivation d'invariants de moments de Gauss-Hermite est basée sur les propriétés des polynômes de Gauss-Hermite. Plus précisément, les invariants en translation sont construits avec les moments centraux des moments de Gauss-Hermite, dont on peut facilement prouver qu'ils ont une invariance en translation; les invariants en rotation, dérivent quant à eux d'une propriété des polynômes d'Hermite, ce qui indique que le produit de deux polynômes d'Hermite a une forme cohérente et similaire à celle de monômes. Une conclusion importante peut alors être émise: les invariants en rotation des moments de Gauss-Hermite ont une forme identique à celle des moments géométriques. Sans aucun doute, la combinaison de ces deux types d'invariants va générer un invariant de moment qui soit indépendant aussi bien de la translation que de la rotation. Quelques expérimentations visant à évaluer le potentiel de l'approche en termes de représentation et de classification d'images sont montrées. Les résultats confirment la supériorité des invariants des moments de Gauss-Hermite.

– **Applications des moments de Gauss-Hermite à l'analyse d'image et à l'analyse d'images sismiques :**

Nous proposons une application de l'estimation de la cohérence avec les moments de Gauss-Hermite dans l'espace spectral. L'algorithme présenté estime la cohérence au sein d'une petite fenêtre locale dans domaine de Fourier utilisant les moments du premier ordre et du second ordre. D'après les résultats, il est constaté que la taille de la fenêtre et la valeur σ sont importants dans la méthode d'estimation de la cohérence par les moments de Gauss-Hermite spectral. Plus la taille de fenêtre est grande, mieux les caractéristiques globales sont détectées.

Nous avons également présenté les moments invariants de Gauss-Hermite dans la correspondance de modèles. Dans le calcul des moments de Gauss-Hermite, σ (paramètre d'échelle) est paramètre très important. Etant donné un σ (paramètre d'échelle), nous avons pu obtenir un ensemble d'invariants. Par conséquent, nous définissons des ensembles différents des invariants avec de différent paramètre d'échelle et procédons à une analyse multi échelle qui nous permet d'obtenir plus d'informations sur l'image et mieux caractériser l'image.

– **Estimation de la cohérence de Dip Stepwise à Balayage des données sismiques 3D :**

La technologie de cohérence est un outil efficace pour l'interprétation sismique. Il détecte la discontinuité de l'événement sismique par analyse des signaux sismiques dans les traces adjacentes, afin d'identifier les phénomènes géologiques comme les failles, les objets géologique complexes, les formations fluviatiles, etc. La cohérence peut aussi être utilisée pour définir les caractéristiques stratigraphiques. Le troisième algorithme est plus robuste au bruit avec une meilleure résolution, mais il sera difficile de promouvoir en raison de ses coûts énormes de calcul. Nous proposons la procédure de base de l'algorithme de cohérence de Dip Stepwise à Balayage basé sur la structure.

– **Horizon 3D d'auto-suivi basée sur les moments, les moments invariants, et l'analyse de multi échelle :**

Il est relativement facile à extraire les caractéristiques d'une région locale au sein des données sismiques 3D à partir des moments géométriques 3D et de la nouvelle définition des moments de Gauss-Hermite 3D. Guidés par la nécessité impérative d'un outil de suivi fiable basé sur caractéristique locale 3D et des résultats très intéressants de travaux effectués dans le passé sur la performance des moments en traitement d'image, les moments géométriques 3D et les moments de Gauss-Hermite 3D sont proposés pour le suivi automatique d'un horizon 3D. Une approche multi échelle basée sur les moments invariants de Gauss-Hermite 3D a également été présentée pour suivre l'horizon sismique.

– **Analyse de faciès sismiques en utilisant les moments de Gauss-Hermite 3D :**

Pour un interpréteur sismique, l'analyse de faciès sismiques est une tâche monotone et fastidieuse car il reste encore à être fait manuellement par balayage des centaines de milliers de sections sismiques. Par conséquent, un processus est hautement nécessaire ce qui rend cette étape d'interprétation automatique. La description de la forme en 3D a évolué vers un domaine de recherche large au cours des dernières années. Les moments 3D permettent d'extraire des caractéristiques importantes de volume sismique. Une nouvelle méthode basée sur SOM, avec des techniques de visualisation de données Matrice U et le graphique PCP, en utilisant les moments de Gauss-Hermite 3D est présentée et utilisée pour l'analyse de faciès sismiques.

Structuration de la thèse

Pour exposer nos travaux, nous avons organisé le manuscrit en la façon suivante:

Le chapitre 1 introduit le sujet de la thèse. Dans la première section, nous décrivons notre motivation et notre problème plus en détail. Ensuite, dans la seconde section, nous résumons les contributions principales de notre travail. Enfin, nous donnons un aperçu pour le reste de cette thèse dans la dernière section.

Le chapitre 2 donne un aperçu sur les images sismiques ainsi que sur les attributs sismiques. Deux aspects sont abordés sur les images sismiques: l'acquisition des données sismiques, le traitement de l'image sismique. Tout d'abord, on présente l'acquisition des données sismiques. L'objectif de l'acquisition des données sismiques est de proposer des outils qui peuvent mettre en évidence des profils croisés. On décrit plusieurs méthodes typiques de traitement d'image incluant le lissage structural, le filtrage directionnel et l'analyse de texture. Une partie de ces approches relèvent du domaine de la géophysique où le traitement du signal est utilisé à des fins de caractérisation de signaux classiquement utilisés en géosciences. L'autre partie des méthodes concerne des méthodes proposées par la communauté des traiteurs d'image pour la détection de contours. Dans la deuxième partie, nous présentons la description des attributs sismiques. Nous introduisons également quelques classifications des attributs sismiques en fonction de différents critères, tel que les relations entre les attributs sismiques, les caractéristiques de domaine des attributs, les caractéristiques de calcul, et les caractérisations des réservoirs.

Le chapitre 3 présente l'analyse d'image sismique basée sur les moments. Un aperçu sur les moments géométriques ainsi que sur les moments orthogonaux a été donné. Cet aperçu est abordé à travers quelques moments orthogonaux typiques aussi bien continus que discrets,

dont les moments géométriques, les moments orthogonaux de Legendre et les moments de Zernike, les moments de Tchebichef discrets, et les moments de Krawtchouk. Nous présentons la définition des moments de Gauss-Hermite et quelques discussions sur leur base. L'implémentation discrète et le développement des invariants de ces moments sont détaillées. Au même temps, quelques applications utilisant les moments et les moments invariants de Gauss-Hermite sont exposées comme l'estimation de cohérence et la reconnaissance des formes.

Dans le chapitre 4, nous comparons deux principaux algorithmes qui sont utilisés sur l'attribut de cohérence: la cohérence et la différenciation. La méthode de cohérence originale a été présentée par Bahorich et Farmer. Marfurt et al ont développé cette méthode. Le troisième algorithme est plus robuste au bruit avec une meilleure résolution, mais il sera très difficile de promouvoir à cause des calculs coûteux. Nous proposons une procédure de l'algorithme de cohérence de Dip Stepwise à Balayage basé sur la structure.

Au chapitre 5, nous nous focalisons sur les aspects d'interprétation d'horizon sismique en 2D et en 3D. Nous présentons d'abord un bref aperçu de l'interprétation d'horizon. L'analyse de données sismiques pour l'étude du sous-sol est un travail long et difficile qui s'appuie sur l'expertise du géologue. Les interprétations manuelles sont coûteuses et subjectives. Cette tâche est heureusement facilitée par des techniques informatisées. En particulier, les méthodes de suivi automatique d'horizons sont d'une grande utilité pour l'interprétation structurale des données sismiques. Cependant, elles ont aujourd'hui encore de grandes difficultés à suivre parfaitement les horizons à travers un certain nombre de discontinuités, plus précisément à travers les failles, en raison de la prise en compte inadéquate d'informations locales très perturbées. Au cours des trois dernières décennies, un progrès considérable a été réalisé dans le domaine de la technique d'interprétation d'horizon. Les méthodes de l'interprétation d'horizon sismique incluent l'interprétation manuelle, la méthode d'interpolation, la méthode de suivi automatique, la méthode de suivi de voxel, et la tranche de surface. Selon les différents types de données sismiques, le suivi d'horizon peut être classé en suivi d'horizon 2D et en suivi d'horizon 3D. Dans ce chapitre, nous nous approchons de la méthode basée sur les moments géométriques et les moments de Gauss-Hermite pour la tâche du suivi d'horizon en 2D et en 3D. Les comparaisons sont faites entre la méthodologie de la corrélation, les statistiques d'ordre supérieur, et la méthode basée sur les moments en 2D et 3D. Nous avons également abordé la méthode basée sur les moments invariants de Gauss-Hermite pour l'horizon d'auto-suivi. Pendant ce temps, nous discutons l'analyse de multi-échelle basée sur les moments invariants de Gauss-Hermite pour l'horizon d'auto-suivi.

Le chapitre 6 présente l'analyse de faciès sismiques par les moments de Gauss-Hermite. Il y a deux problèmes majeurs dans l'analyse de faciès sismiques: le premier problème est de déterminer lesquelles paramètres sismiques sont discriminants pour caractériser les faciès sismiques; le deuxième problème est de veiller qu'il y a une liaison entre les paramètres sismiques et les faciès géologiques qui est étudiés par l'interpréteur. Dans l'analyse de faciès sismiques, il y a trois grandes méthodes de travail: les méthodes supervisées (il y a eu au moins un puits), les non-supervisées (sans puits: où les attributs sismiques peuvent être d'une grande utilité), et les modélisations (on simule le puits). En fin de ce chapitre, les exemples suffisants de la méthode proposée de l'analyse de faciès avec les moments de Gauss-Hermite peuvent être également trouvés.

Au chapitre 7, nous faisons attention à la technologie de traitement parallèle et à la technologie de visualisation. En comparant la taille de plusieurs dizaines de giga-octets des données sismiques, nous trouvons que la mémoire système et la mémoire de texture sur l'unité de traitement graphique restent maigres ressources. Avec la croissance de la taille du volume sismique, nous pouvons également constater la diminution rapide des performances du système d'application conventionnelle. Les processeurs multi-cœurs peuvent offrir une capacité aux développeurs de logiciels pour appliquer à un problème particulier. Pour utiliser cette nouvelle performance dans le domaine des données sismiques, nous calculons les attributs sismiques et suivons l'horizon avec la programmation parallèle. Donc, il y a eu un déclin spectaculaire de coûts de calcul des attributs, et l'interprétation sismique a été efficace. La technologie de visualisation de volume et la technologie de l'interprétation de volume peuvent aider l'interpréteur à mieux comprendre des données sismiques 3D et à accélérer le processus d'interprétation sismique. Dans ce chapitre, nous discutons également l'algorithme de rendu de volume basé sur le moteur Open-Scene-Graph qui permet de mieux comprendre la structure de données sismiques.

Finalement, le chapitre conclusion donne un bilan de cette thèse, propose des perspectives de travail sur l'interprétation sismique, et propose des perspectives de travail sur l'analyse des moments de Gauss-Hermite.

Contents

Remerciements	i
Résumé	iii
Contents	xvii
List of Figures.....	xxi
List of Tables.....	xxv
1 Introduction.....	1
1.1 Motivation and problem description	2
1.2 Contributions.....	8
1.3 Outline.....	11
2 Seismic image and seismic attributes	15
2.1 Seismic image	16
2.1.1 Seismic data acquisition	16
2.1.1.1 Seismic wave	16
2.1.1.2 Data acquisition	21
2.1.2 Seismic image processing and analysis	25
2.1.2.1 Image processing and analysis.....	26
2.1.2.2 Seismic image processing and analysis	31
2.2 Seismic attributes	37
2.2.1 Introduction of seismic attributes	39
2.2.2 Seismic attributes definition and classification	39
2.2.3 Some basic attribute characteristics.....	43
2.2.3.1 Coherence attribute.....	44
2.2.3.2 Average Energy attribute.....	45
2.2.3.3 Instantaneous phase attribute.....	47
2.2.3.4 Instantaneous frequency attribute	48
2.2.3.5 Curvature attributes	49
2.2.3.6 Dip and Azimuth attributes.....	51

2.3	Conclusion.....	51
3	Seismic image analysis by Gaussian-Hermite moments	53
3.1	Introduction of moments	54
3.1.1	Geometric moments.....	55
3.1.2	Legendre moment	56
3.1.3	Zernike moments	56
3.1.4	Discrete Tchebichef moments	57
3.1.5	Krawtchouk moments.....	58
3.1.6	Orthogonal Gaussian-Hermite moments	59
3.2	Coherency estimation based on spectral Gaussian-Hermite moments	60
3.2.1	Discrete implementation of Gaussian-Hermite moments	61
3.2.2	Representation program of 2D Gaussian-Hermite moments	61
3.2.3	Coherency estimation by spectral Gaussian-Hermite moments	63
3.2.4	Experimental results	64
3.3	Multi-scale image description with rotation invariants of Gaussian-Hermite moments	67
3.3.1	Central Gaussian-Hermite moments	68
3.3.2	Rotation Gaussian-Hermite moment invariants.....	68
3.3.3	Translation Gaussian-Hermite moment invariants	70
3.3.4	Multi-scale analysis	70
3.3.5	Experimental results	71
3.4	Seismic image analysis by moments	75
3.5	Conclusion.....	79
4	Stepwise dip scanning coherency estimation	81
4.1	Detection of seismic discontinuity	82
4.1.1	Coherency method.....	83
4.1.2	Difference method	85
4.2	Stepwise dip scanning coherence algorithm based on eigenstructure	86
4.2.1	Method of stepwise dip scanning	86
4.2.1.1	Select searching direction	86
4.2.1.2	Implement C2 algorithm to dip scanning	87
4.2.1.3	Algorithm statement	88
4.2.1.4	Implement C3 algorithm to dip scanning	88
4.2.2	Example result on a real 3D seismic data	89
4.3	Automatic Fault Detection for 3D Seismic Data.....	92
4.4	Conclusion.....	97
5	3D moments-based horizon auto-tracking.....	99
5.1	A review of horizon interpretation	100
5.1.1	Manual interpretation	101
5.1.2	Interpolation interpretation	102
5.1.3	Auto-tracking interpretation	104
5.1.4	Surface-slice interpretation.....	110
5.1.5	Voxel-based tracking.....	112
5.2	Moments-based method for horizon interpretation	112
5.2.1	2D Auto-Tracking of seismic horizon	115

5.2.2	The workflow for 2D horizon tracking using moments.....	116
5.2.3	Definition of 3D moments.....	118
5.2.3.1	3D geometric moments.....	118
5.2.3.2	3D Gaussian-Hermite moments.....	119
5.2.4	3D moments-Based estimation of local features.....	120
5.2.5	Representation program of 3D moments.....	120
5.2.6	Pattern matching algorithm of seismic horizon.....	122
5.2.7	The workflow for 3D horizon tracking using moments.....	122
5.3	Horizon auto-tracking in real seismic data sets.....	125
5.3.1	2D horizon tracking tasks.....	125
5.3.2	3D horizon tracking tasks.....	132
5.4	3D Gaussian-Hermite moment invariants-based approach for horizon interpretation.....	141
5.4.1	3D Gaussian-Hermite moment invariants.....	143
5.4.1.1	3D Gaussian-Hermite moment invariants to translation.....	143
5.4.1.2	3D Gaussian-Hermite moment invariants to rotation.....	143
5.4.1.3	3D Gaussian-Hermite moment invariants to contrast changes.....	144
5.4.2	3D Gaussian-Hermite moment invariants-based method for horizon auto-tracking.....	145
5.4.3	Multi-scale approach based on 3D Gaussian-Hermite moment invariants.....	145
5.5	Horizon self overlaps.....	150
5.6	Conclusion.....	155
6	Seismic facies analysis using 3D moments.....	157
6.1	Seismic Facies Analysis.....	158
6.1.1	Principal component analysis.....	161
6.1.2	The K-means clustering.....	162
6.1.3	Statistical analyses.....	164
6.1.4	Structure of Artificial Neural Networks.....	167
6.1.5	Self-Organizing Maps.....	170
6.2	3D moments-based approach for seismic facies analysis.....	172
6.2.1	3D Feature extraction of seismic traces.....	172
6.2.2	The workflow for seismic facies using 3D moments attribute.....	172
6.3	Example of seismic facies analysis.....	174
6.4	Conclusion.....	179
7	Parallel processing and Volume visualization.....	181
7.1	Parallel processing.....	182
7.1.1	General introduction of computer architecture.....	182
7.1.2	Typical threaded model.....	184
7.1.3	Parallel programming in seismic interpretation.....	186
7.1.3.1	Computing seismic attributes in parallel programming.....	189
7.1.3.2	Auto-tracking seismic horizon in parallel programming.....	194
7.2	Volume visualization and volume interpretation.....	195
7.3	Conclusion.....	202
8	Conclusion.....	203
	References.....	207

Notations	223
Publications of author	225

List of Figures

Figure 2.1 The seismic value chain.	15
Figure 2.2 2D seismic image.	17
Figure 2.3 3D seismic image.	17
Figure 2.4 Velocity of seismic waves in the Earth versus depth.	18
Figure 2.5 Propagation principle of seismic wave.	19
Figure 2.6 Snell's law.	20
Figure 2.7 Schematic representation of seismic data acquisition principle.	21
Figure 2.8 Seismic data acquisition.	22
Figure 2.9 An example of 3D seismic acquisition geometry.	23
Figure 2.10 Seismic reflections and record.	24
Figure 2.11 Seismic data processing chain.	25
Figure 2.12 A seismic section showing three different textures.	33
Figure 2.13 Overall approach of Tensor Voting.	37
Figure 2.14 Historical development of the attributes.	38
Figure 2.15 Basic flow chart of seismic pattern recognition (multi-attribute analysis).	42
Figure 2.16 Coherence of inline 350 section.	45
Figure 2.17 Average energy of inline 350 section.	46
Figure 2.18 Instantaneous phase of inline 350 section.	47
Figure 2.19 Instantaneous frequency of inline 350 section.	47
Figure 2.20 Mean curvature of inline 350 section.	50
Figure 2.21 Dip azimuth of inline 350 section.	50
Figure 3.1 Coherency estimation Results for first synthesized block.	65
Figure 3.2 Coherency estimation Results for second synthesized block.	65
Figure 3.3 Results for synthesized block with zero mean Gaussian white noise with variance 0.01.	66
Figure 3.4 Results for synthesized block with zero mean Gaussian white noise with variance 0.02.	66
Figure 3.5 The different rotation versions of image Mirage-2000.	72
Figure 3.6 Reference images (in first and second rows) and patterns to identify (in third row).	72

Figure 3.7 Weighted Euclidean distances with different scale parameters	73
Figure 3.8 Results of matching by using geometric moment invariants	75
Figure 3.9 Two original images for the SGMM experiments	77
Figure 3.10 The obvious fault detection for the seismic image.....	78
Figure 3.11 The slight fault detection for the seismic image.	79
Figure 4.1 Dip azimuth layout.....	86
Figure 4.2 TimeSlice. (Time = 400ms, analysis window format is 3*3*5)	90
Figure 4.3 InLine crosssection (InLine= 800, analysis window format is 3*3*5)	91
Figure 4.4 Workflow chart for the new fault detector.....	96
Figure 5.1 Manual interpretation.....	102
Figure 5.2 Lines interpretation before Interpolation interpretation.....	103
Figure 5.3 Map views of interpolation interpretation.....	103
Figure 5.4 Matching process of seed.....	107
Figure 5.5 Map views of a horizon auto-tracking interpretation based on cross-correlation.	108
Figure 5.6 Map views of a horizon auto-tracking interpretation based on higher order statistics.....	108
Figure 5.7 The conventional workflow chart of 2D horizon tracking.	113
Figure 5.8 The workflow chart of 2D horizon tracking using moments.	117
Figure 5.9 An example of selecting initial “seed point”.....	123
Figure 5.10 The workflow chart of 3D horizon tracking using moments.	124
Figure 5.11 First real seismic image for 2D horizon tracking.....	126
Figure 5.12 2D horizon tracking by correlation method in first seismic image.	126
Figure 5.13 2D Horizon tracking by higher order statistics in first seismic image.	127
Figure 5.14 2D Horizon tracking by geometrical moments in first seismic image.	127
Figure 5.15 2D Horizon tracking by Gaussian-Hermite moments in first seismic image.....	128
Figure 5.16 Second real seismic image for 2D horizon tracking.	129
Figure 5.17 2D Horizon tracking by correlation method in second seismic image.....	129
Figure 5.18 2D Horizon tracking by higher order statistics in second seismic image.....	130
Figure 5.19 2D Horizon tracking by geometrical moments in second seismic image.	130
Figure 5.20 2D Horizon tracking by Gaussian-Hermite moments in second seismic image.	131
Figure 5.21 3D horizon tracking tasks.	132
Figure 5.22 Moment feature vector around of First horizon seed.	133
Figure 5.23 Moment feature vectors around of 1 st seed for second horizon.	134
Figure 5.24 3D horizon tracking with first seed.....	136
Figure 5.25 Map views of 3D horizon tracking with second seed.	137
Figure 5.26 3D horizon tracking with second seed.	138
Figure 5.27 Map views of 3D horizon tracking with second seed.	139
Figure 5.28 Calculation feature vector two region using moments in a case.	142
Figure 5.29 Calculation feature vector two region using moments in rotational case.....	142

Figure 5.30 3D horizon tracking based on Gaussian-Hermite moment invariants under scale $7*7*7$	146
Figure 5.31 Maps for 3D horizon tracking based on Gaussian-Hermite moment invariants under scale $7*7*7$	146
Figure 5.32 3D horizon tracking based on Gaussian-Hermite moment invariants under scale $5*5*5$...	147
Figure 5.33 Maps for 3D horizon tracking based on Gaussian-Hermite moment invariants under scale $5*5*5$	147
Figure 5.34 3D horizon tracking based on Gaussian-Hermite moment invariants under scale $9*9*9$	148
Figure 5.35 Maps for 3D horizon tracking based on Gaussian-Hermite moment invariants under scale $9*9*9$	148
Figure 5.36 3D horizon tracking based on Gaussian-Hermite moment invariants under combining scale.....	149
Figure 5.37 Maps for 3D horizon tracking based on Gaussian-Hermite moment invariants under combining scale.....	149
Figure 5.38 Some surfaces with multiple reflection times.....	150
Figure 5.39 Tracking result of single reflection time.....	151
Figure 5.40 The modified workflow chart of 3D horizon tracking by moments.....	153
Figure 5.41 A real horizon auto-tracking has some self overlaps.....	154
Figure 5.42 The horizon auto-tracking by modified workflow.....	154
Figure 6.1 3D shapes of seismic facies units.....	159
Figure 6.2 Workflow for general seismic facies analysis.....	161
Figure 6.3 Structure of artificial neurons.....	168
Figure 6.4 Structure of multilayer artificial neurons.....	168
Figure 6.5 Workflow for nonsupervised seismic facies analysis based on SOM clustering using waveform attributes.....	171
Figure 6.6 Workflow for seismic facies analysis based on SOM clustering using 3D moments attribute.....	173
Figure 6.7 The interpretation of horizon for facies analysis.....	175
Figure 6.8 The map of horizon for facies analysis.....	175
Figure 6.9 The U-matrix display.....	176
Figure 6.10 The PCP graphic display.....	176
Figure 6.11 Automatic classification of U-matrix.....	177
Figure 6.12 The result of seismic facies analysis.....	178
Figure 6.13 The map result of seismic facies analysis.....	178
Figure 7.1 Four classifications of computer architectures by Flynn.....	183
Figure 7.2 Dual-core processor architecture.....	183
Figure 7.3 Single threaded model.....	185
Figure 7.4 Multiple threaded model.....	186
Figure 7.5 Interaction among Experiment, Theory and Computation.....	188
Figure 7.6 Representing 3D seismic data by grid.....	190
Figure 7.7 Representing 3D seismic data by multiple subvolume.....	191

Figure 7.8 Parallelization using multi-threading.....	191
Figure 7.9 Parallelization using multi-threading with thread pool pattern.....	193
Figure 7.10 The workflow chart of 3D horizon tracking using moments attribute volume.....	194
Figure 7.11 Surface visualization.....	197
Figure 7.12 Volume visualization.....	197
Figure 7.13 Volume visualization and interpretation workflow.....	198
Figure 7.14 Framework for the design of modular software system.....	199
Figure 7.15 An example of mapping display.....	200
Figure 7.16 A result of control alpha for volume visualization.....	200
Figure 7.17 Parameters adjustment of volume visualization.....	201
Figure 7.18 A nother result of control alpha for volume visualization.....	201

List of Tables

Table 1.1 Main stages of seismic exploration.	3
Table 2.1 Methods for computing post-stack seismic attributes.	40
Table 3.1 Pseudo code of Gaussian-Hermite polynomial computation.....	62
Table 3.2 Pseudo code of Gaussian-Hermite moments computation.....	62
Table 3.3 The Gaussian-Hermite moment invariants of figure.....	74
Table 3.4 Local structure conditions (GST).....	76
Table 4.1 Pseudo code of dip scanning computation.....	88
Table 4.2 Experimental results of coherence algorithms.....	90
Table 5.1 Pseudo code of 3D geometric moments computation.....	121
Table 5.2 Pseudo code of 3D Gaussian-Hermite moments computation.....	121
Table 5.3 Normalization coefficients of moments for Euclidean distance.	135
Table 5.4 Computation result of 3D horizon tracking with first seed.	140
Table 5.5 Performance result of 3D horizon tracking with second seed.....	141
Table 7.1 Pseudo code of master thread for attribute computation.....	192
Table 7.2 Pseudo code of worker thread for attribute computation.....	192

1 Introduction

Energy is one of the most important natural resources in modern societies. Over half of the world energy needs come from oil and gas ([Randen and Sønneland, 2005](#)). Increasing demands in world-wide energy consumption and oil and gas depletion of large reservoirs have resulted in the need for exploring smaller and more complex oil reservoirs. This results in high demands for hydrocarbon resources and makes their identification and extraction economically valuable. Oil and natural gas are two of the non renewable energy resources in the world, and they are main sources of the world's energy. Due to the high level of energy stored in oil, this energy source became and currently is one of the main pillars of our industrial societies. Because of their importance, Oil and natural gas have a deep impact in the world's economies and politics. Today, oil and natural gas account for 90% of the world's transportation fuels and are linked to many products that we use in our daily lives and activities.

Oil is a fossil fuel, and is created when organic material is deposited and then buried, followed by the application of pressure and heat over a long period of time ([Patel et al., 2008](#)). Natural gas also is a fossil fuel in gaseous state. Natural gas is mostly made up of methane and can be found associated with other fossil fuels such as in coal beds and with methane clathrates; and it is created in two mechanisms: biogenic creation and thermogenic creation ([Rojey et al., 1997](#)). The produced oil and natural gas will migrate upwards and accumulate in reservoir structures such as anticlines or fault traps. Oil and natural gas are searched for by looking for signs of these depositional or reservoir structures.

In Section 1.1, we describe our motivation and problem in greater detail. Next, in Section 1.2, we summarize the main contributions. Finally, we give an outline for the rest of the dissertation in Section 1.3.

1.1 Motivation and problem description

There are four geophysical survey techniques which are commonly used in the exploration for oil and gas: gravity survey, aeromagnetic survey, electromagnetic survey and seismic survey ([Ashcroft and Ashcroft, 2011](#)). Seismic survey is a program for mapping geological structure by observation of seismic wave, especially by creating seismic wave with artificial sources and observing the arrival time of the waves reflected from acoustic impedance contrasts or refracted through high velocity members ([Sheriff, 1978](#)). Seismic surveys have a long history of use in petroleum exploration and are the primary tool for delineating subsurface structure and detecting the presence of hydrocarbons prior to drilling. Since the first land seismic surveys along Gulf Coast, performed in the 1920's ([Bakker, 2002](#)), the seismic reflection method has played an important role in the exploration of energy resource. The seismic method is a powerful remote sensing technique that can image the subsurface over depths from tens of meters to tens of kilometres. In 1967, the first 3D seismic survey was shot by Exxon over the Friendswood field near Houston in Texas ([Robertson, 1989](#)). Early surveys were expensive to acquire and process, but as the industry gained familiarity with the needed technologies, then costs and processing and interpretation times for 3D seismic came down. By the early 1980s, trade journals had a number of articles confirming the 3D seismic approach. Likewise, 3D seismic surveying in other offshore areal and on land is growing rapidly. 3D seismic technology represents one of the more important technology introductions over the past decades in that it has allowed oil and gas companies to dramatically improve their oil and gas finding rates.

Seismic exploration can be divided into three main stages ([Yilmaz and Doherty, 1987](#)): data acquisition(both in land and in marine), processing (include signal processing and image processing), and interpretation (such as structure interpreting, fault interpreting, and seismic facies classification, hydrocarbons reservoirs identifying etc). The seismic method starts with the acquisition that consists of collecting raw data directly from the receivers. The purpose of seismic processing is to manipulate the acquired seismic data into an image that can be used to infer the subsurface structure. There are number of steps involved from seismic data acquisition to interpretation of subsurface structure. Some of the common steps are summarized below:

Table 1.1 Main stages of seismic exploration.

Acquisition	Static Correction
Processing	Velocity Analysis
	NMO/DMO
	Stacking
	Migration
Interpretation	Seismic data to subsurface geology

In order to work with above stages, a lot of signal processing operations are needed to accomplish the job. Some of them are sampling data, amplitude recovery, correction, cross-correlation, auto-correlation, filtering, Fourier transform, Discrete Fourier transform, Z-transform, convolution/deconvolution, and f-k analysis etc. Seismic data provides the geoscientist with the most important tool for structural interpretation. However, Seismic data often contain both useful structural information and useless random noise. It is desirable to enhance the structures and reduce the random noise. Seismic data alone do not allow for separating noise from real features. The use of seismic attribute maps for detailed structural interpretation has gained increasing popularity in the last decade. The presence of more than one seismic survey will allow the interpreter to increase his knowledge on uncertainties related to detailed structural interpretation of seismic. Seismic interpretation also requires a lot of math and the careful construction and interpretation of data.

Seismic attributes are specific measurements of geometric, kinematic, dynamic, or statistical features derived from seismic data. So it represents a subset of the total information([Barnes, 2001](#)). They help us better visualize or quantify features of interpretation interest ([Chopra and Marfurt, 2007](#)). Applying seismic attributes for fault detection, determination of fracture distribution, revealing stratigraphic features and interpretation of other geological events is a new technology which geoscientists use it overly nowadays. Seismic attributes can be divided into two broad categories: those that help us quantify the morphological component of seismic data and those that help us quantify the reflectivity component of seismic data. The morphological attributes extract information on reflector dip, azimuth, shape, and terminations, which can in turn be related to faults, channels, fractures, karst, and carbonate buildups. The reflectivity attributes extract information on reflector amplitude, waveform, and

variation with illumination angle, which can in turn be related to lithology, reservoir thickness, fracture density and azimuth, and the presence of hydrocarbons. In the reconnaissance mode, seismic attributes help us to rapidly identify structural features and depositional environments. In the reservoir characterization mode, seismic attributes are calibrated against real and simulated well data to identify hydrocarbon accumulations and reservoir compartmentalization. In the recent years, much attention has been given to the prediction of reservoir properties and to the extraction of seismic attributes to enhance the value of seismic interpretation.

Nowadays, most thorough seismic interpretations still remain based on an integrated use of seismic inline, cross-line, time slice, random line and horizon attributes. The challenge is to fully utilise all information contained in seismic data. To do this, the interpreter needs to combine knowledge within the complex disciplines of geology and geophysics. This is not an easy task, and quite commonly, the lack of a sound geological understanding leads the geophysicist to interpret unrealistic geological geometries. Similarly, the geologist may easily interpret features that the geophysicist would rapidly identify as being noise-related. The increasing demand for more and better data interpretation force the geoscientist to carry out very detailed interpretation without having time for the important and necessary quality control.

Conventional seismic interpretation is an art that requires skill and thorough experience in geology and geophysics. In recent years many aspects of the structural interpretation of seismic data have become automated and more rapid ([Brown, 2004](#); [Coleou et al., 2003](#); [Linari et al., 2003](#); [Marsh et al., 2005](#)). Dorn et al ([2010](#)) introduced a unique new workflow, which includes a combination of existing and new novel processes, is presented for computer-aided interpretation of depositional systems in 3D seismic volumes. This unique workflow includes the following general steps: Load (Input) 3D Seismic Volume, Structural Interpretation, Domain Transformation, Optional Structural Refinement, Stratigraphic Interpretation, Inverse Domain Transformation, and Output Stratigraphic Volumes and Bodies. Individual steps and series of steps of this workflow may be applied recursively to the data volume to improve the results of the overall process.

Since the first seismic trace was computer-rendered, automatic interpretation has been the promised panacea of the geoscience community. Many years later, developers are still struggling for a reasonable automatic interpretation methodology in structurally challenging areas. Seismic horizons are layered rocks which are created through a long time sedimentation process. A faulting process cuts and displaces horizons. Reconstructing structure and fault in

their accurate 3D space is a major challenge in subsurface geology. Accurate knowledge of the kinematics and geometry of the structure is essential for volumetric estimations of reservoirs and for the prediction of the orientation, distribution, and density of fractures that forms within this structural framework but are below seismic resolution. 3D seismic data has become the preferred tool for this task because it allows the interpreter to follow fault and folds throughout the seismic volume.

For subsurface seismic exploration, the uncertainty and nonuniqueness in geologic interpretation is one of the major problems because of the complexity of subsurface geology and the limited dimension of the data available. In traditional 2D displays there are a limited number of seismic lines or maps, often alias the interpretation of tectonic deformation, sediment deposition, and fluid flow occurring in three dimensions. 3D seismic imaging technology provides a continuous volumetric seismic coverage of the survey area that makes it possible to investigate seismic structure, stratigraphy, and hydrocarbon reservoirs from a 3D perspective. The 3D seismic data offer a unique opportunity to make seismic observations and geologic interpretations in 3D space; however, most 3D seismic data are displayed and interpreted in a 2D manner, leaving the critical advantage and potential value of 3D seismic data unused. High-performance 3D digital computing and state-of-the-art volume visualization and interpretation technologies have played an important role in facilitating 3D seismic volume interpretation in an interactive manner.

An essential issue in the field of pattern analysis is the recognition of objects and characters regardless of their positions, sizes, and orientations. Moment based feature descriptors have evolved into a powerful tools for image analysis applications. Moments can be applied to binary or grey level images, defined in 2D, 3D and higher dimensional space, but also to edges and primitives extracted through a pre-processing stage. Moments and functions of moments due to their capabilities to extract invariant global features have been extensively applied in the field of image processing: image analysis and pattern recognition ([Flusser and Suk, 1993](#); [Hu, 1962](#)) with applications ranging from edge detection ([Luo et al., 1993](#)), image understanding, image classification and segmentation ([Yokoya and Levine, 1989](#)), texture analysis ([Tuceryan, 1994](#); [Tuceryan and Jain, 1998](#)), coherency estimation ([Li et al., 2010a](#)), invariant identification ([Li et al., 2011](#); [Yang and Dai, 2011](#); [Yang et al., 2011](#)), target identification, object classification, image coding and reconstruction ([Teague, 1980](#); [Teh and Chin, 1988](#)), scene analysis ([Jerome, 2009](#); [Sadjadi and Hall, 1978](#)), image reconstruction ([Liao and Pawlak, 1996](#); [Yang and Dai, 2012](#)), and 3D object analysis ([Bronstein et al., 2005](#); [Sadjadi and Hall, 1980](#)). Describing images with moments instead of other more commonly used image features means that global properties of the image are used rather than

local properties.

Geometric moments are firstly proposed and have been extensively used due to their simplicity and explicit geometric meaning. However, geometric moments are not orthogonal, so it is difficult to reconstruct an image from them. Teague showed that great efficiency could be acquired when the image was analyzed by orthogonal Legendre and Zernike moments ([Teague, 1980](#)). Moreover, it was proven that Zernike moments could store image information with minimal redundancy and they have the property of being rotation invariants. As we know, the computation of Legendre moments needs to transform image coordinates over the interval $[-1, 1]$ and Zernike polynomials are only valid inside the unit circle ([Mukundan and Ramakrishnan, 1998](#)). Besides, the discretization error derived from approximating the integral is still inevitable during their implementations, which definitely limits the accuracy of computed moments ([Liao and Pawlak, 1996](#)). Liao and Pawlak conducted a theoretical analysis on the discretization error of continuous moments and they proposed an approach to keep the error under certain level according to Simpson's rule ([Liao and Pawlak, 1996](#)). Other researches aiming at improving the accuracy of continuous moments are accordingly focused on geometric and Legendre moments ([Hosny, 2007a, b](#)).

Recognition of the shape and form of objects in a scene is easily accomplished by human visual observations even if the object is translated, rotated, scaled, partially obscured, slightly distorted, or viewed in perspective. The invariant recognition of forms is important to humans for a variety of tasks, even though variant recognition is also necessary for some tasks as illustrated by the differentiation of the characters. Moment invariants are considered as important tools in image analysis and pattern recognition. In the early 60's of last century the pioneering work of Hu ([1962](#)) on moment invariants(his seven famous geometric moment invariants), moments and moment functions has opened many applications in the image field. Because these invariants are independent of rotation, translation and scaling, they were soon used in a lot of applications as efficient object descriptors. Thereafter, some new moment invariants, which are still based on geometric moments, have successively been developed and used. A large number of papers that have significant contributions to the application of the subject appeared afterward. Abu-Mostafa proposed a method to derive geometric moment invariants from complex moments and he analyzed their properties in terms of information redundancy and noise sensitivity as well ([Abu-Mostafa and Psaltis, 1985](#)). Correspondingly, Reddi also provided a generalized framework for deriving radial and angular invariants ([Reddi, 1981](#)). Another kind of moment is Zernike moment from which the rotation invariants can be easily derived, since Zernike polynomials are orthogonal inside unit circle and generally defined in polar coordinates. The radial orthogonal sets such as Zernike polynomials

have an congenital property “invariant in form” which directly determines the rotational invariance of corresponding moments ([Bhatia and Wolf, 1954](#)). Flusser ([Flusser and Suk, 1993](#)) and Reiss ([Reiss, 1991](#)) contributed significantly to the theory of moment invariants by correcting the fundamental theorem and deriving invariants to general affine transform. In spite of this, another important kind of moment invariant called blur invariant which is independent of convolution is also introduced to image analysis by the same group ([Suk and Flusser, 2003](#)). Blur invariants have the significant meaning to image analysis, especially to the analysis of remote sensing and aerial images. It should be noted that all moment invariants proposed by Flusser and his colleagues are based on either geometric moments or complex moments. Some work with respect to the development of moment invariants from orthogonal moments has been gradually introduced. Chong presented the translation invariants of Zernike moments which are efficient for constructing rotation invariants ([Chong et al., 2003](#)); and he also proposed a way to derive the translation and scale invariants in terms of Legendre moments ([Chong et al., 2004](#)). The researches in moment invariant can be also found in discrete orthogonal moments. Zhu has developed the translation and scaling invariants by using discrete Tchebichef moments ([Zhu et al., 2007b](#)). Hitherto, all moment invariants whatever they are derived from geometric moments, or Legendre moments, even or discrete Tchebichef moments, we can hold in a sense that they are substantially derived from geometric moments because the basis functions of these moments are linear combinations of monomials. Consequently, some moment invariants can be indirectly obtained from geometric moment invariants ([Yap et al., 2003](#); [Zhu et al., 2007c](#)).

With the rapid development of the acquisition of multi-dimensional data, it is possible to recognize 3D objects directly. Now, 3D shape models have become more and more common. Applications such as object tracking and shape retrieval require us to consider how to choose the feature descriptors of 3D shapes and how to measure the similarities between 3D objects. Sadjadi and Hall ([1980](#)) pioneered the development of 3D Geometric moment invariants from 2D moment. They built a family of three invariant moments with a degree up to the second-order. Using the notion of complex moments Lo and Don ([1989](#)) constructed a family of twelve invariant moments with orders up to the third degree. In these last works, moments were used mainly to estimate 3D transformations and their performances were not evaluated for classification tasks. Also, being not derived from a family of orthogonal functions, these moments were subject to correlation. Reuze et al ([1993](#)) described a method based on the 3D geometrical moments for the 3D tracking and the quantification of blood vessels from Magnetic Resonance Angiography (MRA). Canterakis ([1997](#)) extended Zernike moments to the 3D case, but their performances were not put into trial yet. In ([Werghe and Xiao, 2002](#)),

Werghi and Xiao proposed to investigate the wavelet transform coefficients (WTC). Sommer et al proposed a method for comparing protein-binding sites. They use 3D geometric moment invariants as feature vectors for the binding description. Xu and Li (2006a) generalized curve moments from 2D to 3D Euclidean space, and use geometrical method to derive 3D curve moments invariants of different orders under similarity transformation. In (Xu and Li, 2006b), the authors introduced the surface moments, a kind of moment can be treated as a new kind of shape descriptors of free-form surfaces and can handle the situation where 3D surface objects are not closed. Mademlis et al (2006) proposed a novel method for 3D content-based search and retrieval. They introduced weighted 3D Krawtchout moments for efficient 3D analysis which are suitable for content-based search and retrieval application. Ong et al (2007) present a theoretical framework to derive translation and scale invariants for 3D Legendre moments, by using generates 3D Legendre invariants from the existing 3D geometric moment invariants and eliminates the displacement and scale factors from Legendre polynomials to generate translation and scale invariants.

Another set of orthogonal moments, Gaussian-Hermite moments, was proposed by Shen a decade ago (Shen, 1997). However, the researches in this kind of moments are relatively less than those in other moments. The related records are countable: Shen and Wu detected moving objects by use of one-dimensional Gaussian-Hermite moments (Shen et al., 2004; Wu and Shen, 2005; Wu et al., 2005). Meanwhile, these moments were also used in iris recognition (Ma et al., 2004) and classification of fingerprint (Wang and Dai, 2007). In fact, the above applications are based on image filtering by some kernels defined with Gaussian-Hermite moment functions of low orders.

As far as the orthogonal moments are concerned, there are generally three important aspects on their study. The first one is the computation or discrete implementation. The second one is image reconstruction, from which we can evaluate image representation ability of the moments. The last one is the development of moment invariants. In those three aspects by Gaussian-Hermite moments, there are few researches about the image representation ability of Gaussian-Hermite moments. Some novel approaches are presented by Yang et al in recent works (Li et al., 2011; Yang and Dai, 2011, 2012; Yang et al., 2011).

1.2 Contributions

Although the moment theory is well established and widely applied in a number of digital image areas, it remains relatively marginal in seismic imaging. We have successfully applied

Gaussian-Hermite moments to seismic image analysis. With definition of Gaussian-Hermite moments from 2D case to 3D case, a new method of seismic interpretation has been proposed in the thesis. The research for seismic interpretation based on Gaussian-Hermite moment invariants has also been presented in the thesis. Taken these aspects into account, the thesis then gives the following contributions:

– **Definition of 3D Gaussian-Hermite moments and discrete implementation :**

A definition of 3D orthogonal Gaussian-Hermite moments is derived from orthogonal 2D Gaussian-Hermite moments and the general definition of 3D geometric moments. Based on this definition, 3D image features can be easily achieved from the orthonormal 3D Gaussian-Hermite moments. The discrete implementation of such moments is detailed.

– **Derivation of 2D /3D rotation and translation invariants from Gaussian-Hermite moments.**

The derivation of moment invariants for orthogonal moments is generally complicated and difficult. At present, there are two chief methods for achieving moment invariants of orthogonal moments: image normalization and expressing the orthogonal moments by a linear combination of geometric moment invariants. Image normalization needs many parameters to be computed; the indirect method, on the other hand, is substantially constructing moment invariants from geometric moments, which is not based on the property of orthogonal moments directly. In this thesis, the derivation of Gaussian-Hermite moment invariants is based on the properties of Gaussian-Hermite polynomials. To be more precise, the translation invariants are constructed by the central moments of Gaussian-Hermite moments, which can be readily proven to have translation invariance; the rotation invariants, on the other hand, are derived from a property of Hermite polynomial, which indicates that the product of two Hermite polynomials has the consistent and similar forms as that of monomials. A significant conclusion can then be drawn that the rotation invariants of Gaussian-Hermite moments have the identical forms to those of geometric moments. Undoubtedly, the combination of these two kinds of invariants will generate a moment invariant which is independent of both translation and rotation. Some experiments for testing feature representation and pattern classification ability have been given. The experimentation results confirm the superior ability of Gaussian-Hermite moment invariants.

– **Applications of Gaussian-Hermite moments to image analysis and seismic images analysis:**

We have offered application of spectral Gaussian-Hermite moments in coherency estimation. We present the way using the moments of the first order and the second order to estimate the coherency within a small local window in Fourier domain. From the experiments, it can be found that the size of the window and the value of σ are important in coherency estimation method by spectral Gaussian-Hermite moments. As the window size gets larger, more global features are detected.

We have also presented Gaussian-Hermite moment invariants in template matching. Since in the computation of Gaussian-Hermite moments, there is an important scale parameter σ . Given a σ , we could obtain a set of invariants. Therefore, we define different sets of invariants with the different scale parameter and perform a multi-scale analysis that allows us to obtain more information of the image and to better characterize the image.

– **Stepwise dip scanning coherency estimation of the 3D seismic data:**

Coherence technology is an effective tool for seismic interpretation. It detects the discontinuity of the seismic event by analyzing seismic signals in adjacent traces, so as to identify geological phenomena like faults, special lithologic bodies, river courses etc. Also coherence can be used to define stratigraphic features. Third algorithm is more robust to noise and with a better resolution, but it will be hard to promote due to its huge computational costs. We propose the basic procedure of the stepwise dip scanning coherence algorithm based on eigenstructure to solve these problems.

– **3D Seismic horizon auto-tracking based on moments and moment invariants, and multi scale analysis approach:**

With 3D geometric moments and the newly defined 3D Gaussian-Hermite moments, it is relatively easy to extract features of a local region within 3D seismic data from such moments. Guided by the imperative need for a reliable 3D local feature based tracking tool and the very interesting results of research work done in the past on the performance of moments in image processing, 3D geometric moments and 3D Gaussian-Hermite moments are proposed for efficient 3D horizon auto-tracking. 3D Gaussian-Hermite moment invariants also are proposed for efficient 3D horizon auto-tracking. A multiscale approach based on 3D Gaussian-Hermite moment invariants is presented to track seismic horizon.

– **Seismic facies analysis using 3D Gaussian-Hermite moments :**

For a seismic interpreter, seismic facies analysis is a monotonous and time consuming task

because it still has to be done manually by scanning through hundreds to thousands of seismic cross sections. Hence, a process is highly required which makes this interpretation step automatic. 3D shape description has evolved to a wide research area during the last years. 3D moments can extract important features of a volume. A novel method based on SOM, with data visualization techniques U-Matrix and PCP graphic, using 3D Gaussian-Hermite moments is introduced for seismic facies analysis.

1.3 Outline

The organization of this thesis is as follows:

Chapter 2 reviews two aspects of seismic data study: seismic image and seismic attributes. At the first, seismic data acquisition is introduced. The aim of seismic data acquisition and processing is to deliver products that mimic cross-sections through the earth. Focusing on the seismic image processing, we outline some typical image processing methods which include structure smooth, oriented filtering methods (be employed to enhance stratigraphic continuity and to preserve fault discontinuity for the applications that do not require actual fault surfaces), texture analysis (be used to extract patterns of common seismic signal character). The study and interpretation of attributes can provide us with some qualitative information of the geometry and the physical parameters of the subsurface. In the second part of this chapter, a brief description of seismic attributes is given. We introduce some classifications of seismic attributes according to different criteria such as relationship of the attributes, domain characteristics of the attributes, computational characteristics, or reservoir characterization. Some basic seismic attributes characteristics used in seismic object identifying are also introduced at the end of chapter.

In Chapter 3, we discuss image analysis based on moments. Moments based feature descriptors have evolved into a powerful tool for image analysis application. A basic overview of various types of moments which are currently in use is provided at the first section. We present a new orthogonal Gaussian-Hermite moment and derivation of its rotation and translation invariants from geometric moments invariants. Meanwhile, some diverse usages of Gaussian-Hermite moments and moment invariants in some applications are exhibited as: coherency estimation, pattern recognition. We also discuss seismic image analysis by moments in this chapter. It is shown that Gaussian-Hermite moments are effective tools for image analysis.

In chapter 4, we compare two main families of algorithms coherency and differencing used in

seismic attribute. Coherency method is firstly introduced by Bahorich and Farmer. Marfurt et al developed this method. First coherency method is not very robust to noise. The next algorithm is more robust to noise but with lower resolution and higher computational costs than first algorithm. Third algorithm is more robust to noise and with a better resolution, but it will be hard to promote due to its huge computational costs. To solve these problems, we propose the basic procedure of the stepwise dip scanning coherence algorithm based on eigenstructure. The dip scanning is conducted in two steps. In the first step, C_2 algorithm is employed to scan all dip directions; the resulted coherence values are sorted from small ones to large ones; dip directions of the larger coherence values will be kept for further use. In the second step, C_3 algorithm is implemented to search for the best dip directions among the ones we kept in the first step.

In Chapter 5, we specialize in the aspects of 2D and 3D seismic horizon interpretation. A brief review of horizon interpretation is firstly given. Over the last three decades, tremendous progress has been made in technique of horizon interpretation. These methods include manual interpretation, interpolation interpretation, auto-tracking interpretation, voxel tracking, and surface slicing. According the different kind of seismic data, the tracking of horizons can be classified into 2D horizon tracking and 3D horizon tracking. In this chapter, we approach method based on geometric moments and Gaussian-Hermite moments to the task of 2D/3D horizon tracking. The comparisons are made under both 2D and 3D conditions of correlation method, higher order statistics method, and moments-based method. We also approach method based on Gaussian-Hermite moment invariants to the task of 2D/3D horizon tracking. Meanwhile, we discuss multi-scale analysis based on Gaussian-Hermite moment invariants applying for horizon auto-tracking.

Chapter 6 presents the analysis of seismic facies by moments. There are two major problems in seismic facies analysis: the first problem is to determine which seismic parameters are discriminants for characterizing the seismic facies; the second problem is to be sure that there is a link between the seismic parameters and the geological facies which is investigated by interpreter. Still, the sufficient experiments of the proposed facies analysis with Gaussian-Hermite moments can be also found in this chapter.

In Chapter 7, we pay attention to parallel processing technology and visualization technology. Compared to the tens of gigabytes size of the seismic data sets, system memory and texture memory on the graphics processing unit remain scarce resources. With size of seismic volume increasing, we can also find that performance of conventional application system will decline rapidly. Multi-core processors can offer software developers the ability to apply more

resources at a particular problem. To take advantage of this new performance in seismic data field, we compute the seismic attributes and track the horizon with parallel program. It can be seen that there has been a dramatic decline in the calculation of attributes, and interpretation has been efficient. Interpreters can save their time and resources into others interesting tasks. Volume visualization technology and volume interpretation may help interpreter to insight into 3D seismic data and accelerate the interpretation process. In this chapter, we adapt high quality volume rendering algorithms based on Open-Scene-Graph (OSG) 3D engine, an open source high performance 3D graphics toolkit, to improve application efficiency in the imaging and visualization.

Finally, a chapter of conclusion gives a summary of this thesis and issues the future works and perspective study on seismic interpretation and application of Gaussian-Hermite moments.

2 Seismic image and seismic attributes

Seismic exploration can be divided into three main stages: data acquisition, processing (signal processing and image processing), and interpretation (structure interpreting, fault interpreting, and seismic facies classification, hydrocarbons reservoirs identifying etc). The seismic value chain ([Berkhout, 2004](#)) shows the procedure of seismic exploration in a conceptual way, making it easier to see Figure 2.1. The three nodes in the chain, coupled by a double loop, are seismic acquisition, structural imaging, and reservoir characterization. Insight is provided into the interactions between these nodes: the arrows in indicate the interactions that take place or that should take place between the different nodes. The arrows that point from left to right indicate ‘influence on’, and the arrows pointing from right to left indicate ‘imposing requirements on’.

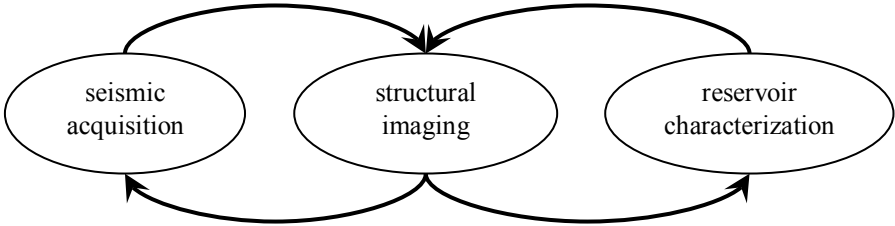


Figure 2.1 The seismic value chain.

One of the primary tasks in exploration seismology is to interpret seismic arrival patterns propagated from the source to receiver through the earth, and to map subsurface geological structure and stratigraphic features. The recorded seismic waves consist of a series of seismic events. The seismic event may be a reflection, refraction, surface wave, random signal, etc, which carries information about the earth’s subsurface.

2.1 Seismic image

Seismic imaging is a primary source of information used in the exploration of hydrocarbons. Seismic image is the process through which seismograms recorded on the Earth's surface are mapped into representations of its interior properties. Imaging methods are nowadays applied to a broad range of seismic observations: from near-surface environmental studies, to oil and gas exploration, even to long-period earthquake seismology. The characteristic length scales of the features imaged by these techniques range over many orders of magnitude.

2.1.1 Seismic data acquisition

In a sense, seismic images can be regarded as the reflections in the forms of image for the underground structures ([Bakker, 2002](#); [Pouliquen, 2003](#)). The images display the subsurface of the earth with geological structures evident in various layers. Figure 2.2 and Figure 2.3 are two typical seismic sample images. They are acquired in a certain time by an acoustic wave. This wave travels down the subsurface and partly reflects at locations where the acoustic rock properties change. Generally, seismic images are 3D images or called 3D block seismic image.

Seismic data acquisition consists of gathering and recording of continuous seismic signals from seismic stations. The aim of seismic data acquisition and processing is to deliver products that mimic cross-sections through the earth. In order to do this, the correct amount and types of data must be acquired, and processing applied to remove unwanted energy, and to place the required events in the correct location. At the same time, a balance needs to be struck between cost and timeliness of data, while attaining also the important objectives of safe operations and doing no harm to the environment.

Initially, seismic data were acquired along straight lines, known as 2D seismic; shooting a number of lines across an area gave us the data needed to make a map. Again the process is analogous to making a bathymetric map from echo soundings along a number of ship tracks. In 1980', it has been realised that there are big advantages to obtaining very closely spaced data. Instead of having to interpolate between sparse 2D lines, the result is very detailed information about the subsurface in a 3D cube, known as 3D seismic. 3D seismic can be used to improve our understanding of the subsurface.

2.1.1.1 Seismic wave

The theory of seismic wave propagation is the basis for seismic imaging. Seismic waves are generated when a stress is applied near or at the earth's surface. The generated seismic waves

propagate in all directions from the stress source, and they are governed by the mechanical properties of the rocks, such as incompressibility, rigidity, and density. Wave characteristics are also affected by the layering of the rocks and physical properties of the surface soil. The seismic reflection method deals with seismic waves that propagate through the earth's interior.

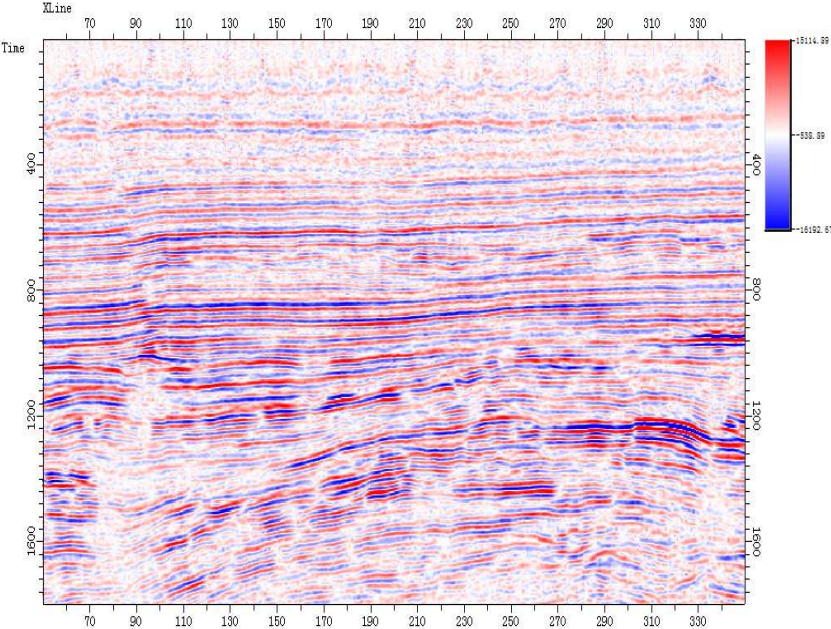


Figure 2.2 2D seismic image.

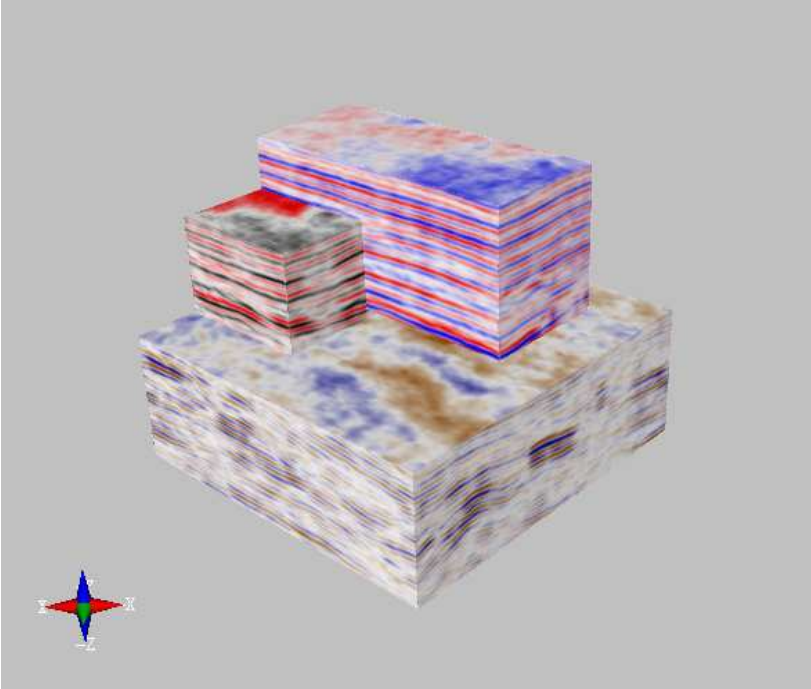


Figure 2.3 3D seismic image.

Seismic waves are divided into two types: body waves and surface waves. Body waves include P waves and S waves, these are the two types of waves that are used to determine the

internal structure of the Earth. Surface waves include Rayleigh waves and Love waves. On firing an energy source, a compressional force causes an initial volume decrease of the medium which the force acts. The elastic character of rock the caused an immediate rebound or expansion, followed by a dilation force. This response of the medium constitutes a primary “compressional wave” or P wave. P waves travel as a region of compression. P waves are the fastest kind of seismic wave. A longitudinal P wave has the ability to move through solid rock and fluid rock, like water or the semi-liquid layers of the earth. While P wave moves through, it pushes and pulls the rock in the same way sound waves push and pull the air. Shear strain occurs when a sideways force is exerted on a medium. S wave (shear wave) may be generated that travels perpendicularly to the direction of the applied force and travels like vibrations in a bowl of Jello. S wave is slower than a P wave and only moves through solid rock. This wave moves rock up and down, or side-to-side. Because P waves are compression waves, they can move through a liquid. However, S waves cannot move through a liquid such as water. This is possible because a liquid is not rigid enough to transmit S wave. P waves propagate by moving the particles in the medium parallel to the propagation direction while shear waves propagate by moving the medium particles perpendicular to the propagation direction.

The velocity of the seismic ray is described as a function of the elasticity of the medium in which the ray is travelling. Any medium that can support wave propagation may be described as having impedance. In dense rock, P wave can vary from 2500 to 7000 m/sec, while in spongy sand, from 300 to 500 m/sec.

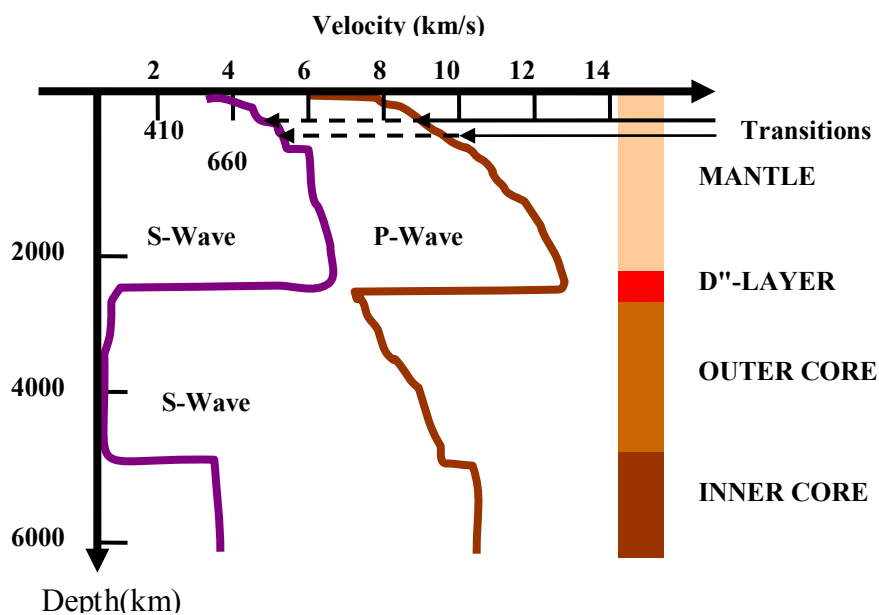


Figure 2.4 Velocity of seismic waves in the Earth versus depth.

A propagating seismic wave is understood by using principles from optics:

- **Huygens' Principle:** the wave front of a propagating wave of light at any instant conforms to the envelope of spherical wavelets emanating from every point on the wave front at the prior instant (with the understanding that the wavelets have the same speed as the overall wave). each point on a wave front (a seismic wave front is a constant phase surface) produces secondary spherical waves (called wavelets). After time t the spherical radius of each is $V * t$ (Figure 2.5 (a)). Huygens' Principle can be seen as a consequence of the isotropy of space.
- **Fermat's Principle:** or the principle of least time is the principle that the path taken between two points by a ray of light is the path that can be traversed in the least time. This principle is sometimes taken as the definition of a ray of light. However, this version of the principle is not general; a more modern statement of the principle is that rays of light traverse the path of stationary optical length. Fermat's principle can be used to describe the properties of light rays reflected off mirrors, refracted through different media, or undergoing total internal reflection. It follows mathematically from Huygens' Principle (at the limit of small wavelength), and can be used to derive Snell's law of refraction and the law of reflection. In a group of paths from source to receive, a seismic ray travels along the minimum-time path through the medium (Figure 2.5 (b)).

These principles help to locate a wave front after a certain time interval.

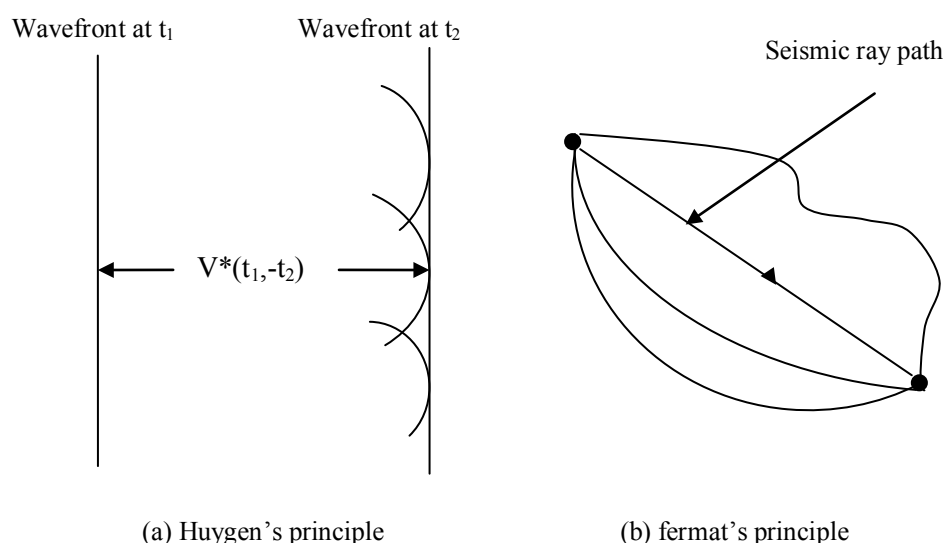


Figure 2.5 Propagation principle of seismic wave.

A change in velocity while a wave traverses through different media results in reflection and refraction (Figure 2.6). These events are governed by Snell's reflection and refraction laws:

- The law of reflection states that the angle of reflection equals the angle of incidence.
- The law of refraction relates velocity to the angle of incidence and to the angle of refraction,

$$\frac{\sin(\theta_1)}{\sin(\theta_2)} = \frac{V_1}{V_2} = \frac{n_2}{n_1}$$

where each θ as the angle measured from the normal, V as the velocity of wave in the respective medium (SI units are meters per second, or m/s) and n as the refractive index of the respective medium.

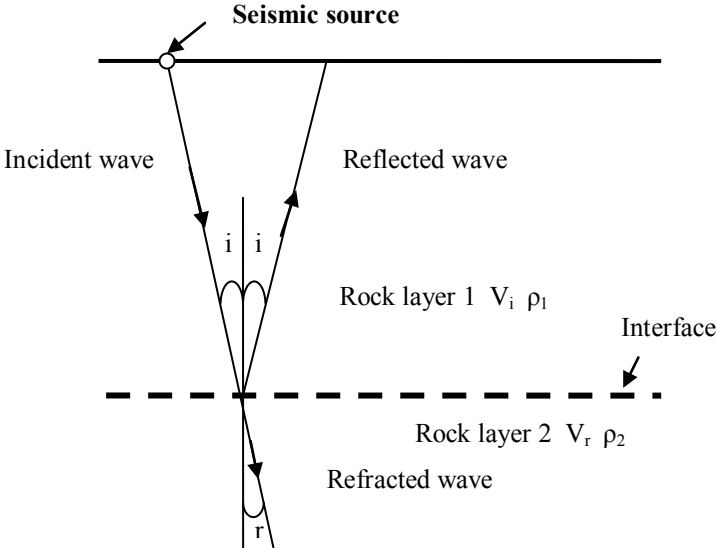


Figure 2.6 Snell's law.

Reflection and refraction occurs when a seismic wave passes through two media having different acoustic impedance. The angle of reflection is the same as the angle of incidence, while the angle of refraction is related to the angle of incidence through Snell's law.

In the seismic imaging theory, the subsurface geology is viewed as a stack of homogeneous rock layers with planar upper and lower surfaces. Each homogeneous layer supports wave propagation with different impedances. Seismic waves are generated from sources put on the surface, and structures are estimated by using travel times of seismic waves which get reflected at the boundaries between the layers. The reflections are recorded by recorder instruments put on the earth's surface close to the sources. After the recorder measured the precise arrival time of the wave, its velocity is calculated and used to determine the properties of the rock layer in which it travels.

Details of the seismic imaging theory are found in (Sheriff and Geldart, 1995). For details of the seismic wave propagation refer to (Claerbout, 1985; Treitel and Robinson, 1966). Figure 2.7 illustrates a seismic data acquisition principle.

The essential features of an exploration seismic data experiment are (Scales, 1997):

- Using controlled sources of seismic energy
- Illumination of a subsurface target area with downward propagating waves
- Reflection and refraction of the seismic waves by subsurface heterogeneities
- Detection of the reflected seismic energy on recorders on the earth's surface.

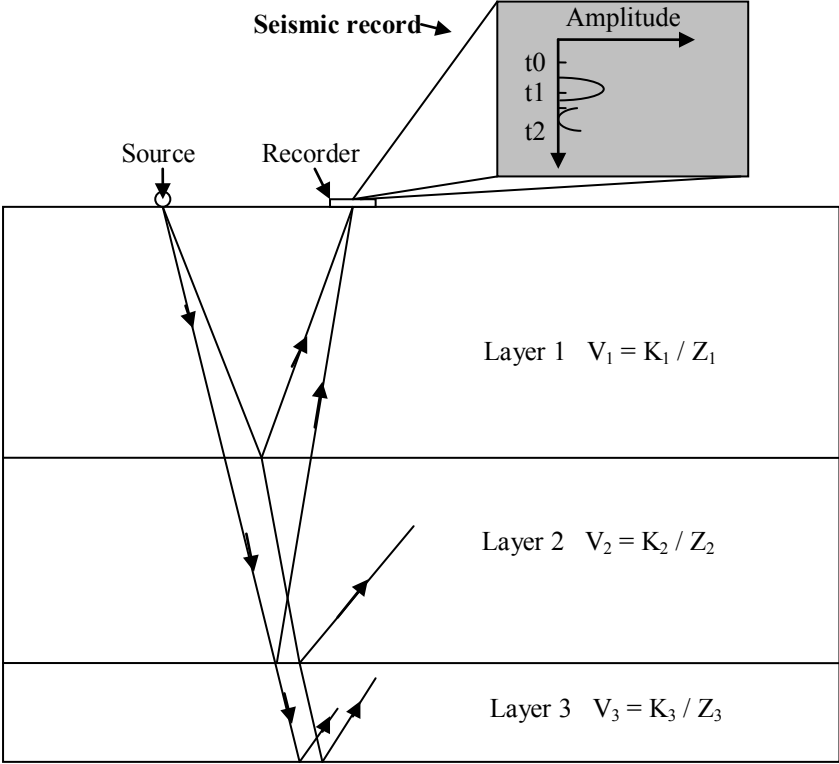


Figure 2.7 Schematic representation of seismic data acquisition principle.

A seismic wave originated from a source gets reflected and refracted while going down. The amplitude and the arrival time of the reflected waves are recorded by recorder put on the surface.

2.1.1.2 Data acquisition

Subsurface geologic structures containing hydrocarbons are found beneath either land or sea. So there are two methods for seismic data acquisition: land data acquisition and marine data acquisition. Both two methods have a common goal, imaging the earth. But because the environments is different, so each required unique technology and terminology.

In land acquisition (Figure 2.8 A), a shot is fired and reflections from the boundaries of various Lithological units within the subsurface are recorded at a number of fixed receiver stations on the surface. Geophones are used as recorders on land. Generally they work by measuring the motion of a magnet relative to a coil attached to a base implanted in the Earth. This motion produces a voltage which is proportional to the movement of the surface. These geophone stations are usually in-line although the shot source may not be. When the source is in-line with the receivers (at either end of the receiver line or positioned in the middle of the receiver line) a two-dimensional profile through the earth is generated. If the source moves around the receiver line causing reflections to be recorded from points out of the plane of the in line profile, then a three-dimensional volume is possible (the third dimension being distance, orthogonal to the in-line receiver-line). The majority of land survey effort is expended in moving the line equipment along and across farm field or through populated communities. Hence, land operations often are conducted only during daylight thus making it a slow process.

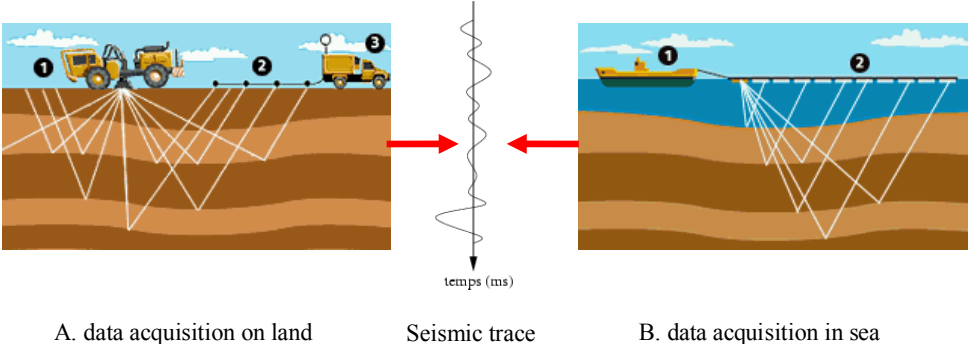


Figure 2.8 Seismic data acquisition.

For marine operation (Figure 2.8 B), a ship tows one or more energy sources fastened parallel with one or more towed seismic receiver lines. In this case, hydrophones are used to sense the instantaneous pressure in the water due to the seismic waves. The vessel moves along and fires a shot, with reflections recorded by the streamers. If a single streamer and a single source are used, a single seismic profile may be recorded in like manner to the land acquisition. If a number of parallel sources and streamers are towed at the same time, the result is a number of parallel lines recorded at the same time. If many closely spaced parallel lines are recorded, then a three-dimension seismic data volume is recorded.

Techniques have been developed to use both Geophones and Hydrophones in the surface area where the shore line / water edge is likely to migrate toward land and sea depending on the tide of sea a day. The combination of such hydrophones / geophones is called a “Dual Sensor”. The advantage of why this is to see that either of the receiver of Dual Sensor pickups the

surveyed from the slots recorded using a land or marine source and data gaps all along the coast within the area of prospect.

The receivers are deployed in clusters called groups; the signal from each receiver in a group is summed so as to: increase the signal to noise ratio and attenuate horizontally propagating waves. The individual receiver groups are separated from one another by distances of anywhere from a few dozen meters to perhaps 100 meters. The entire seismic line will be kilometres or more long.

Seismic sources come in different shapes and sizes. Sources such as dynamite, weight drops, large caliber guns and large resistive masses called vibrators are used on land, while vibrator, air guns, electric sparkers and confined propane-oxygen explosions are the most common sources for a marine survey ([Scales, 1997](#)).

For surveys related to the exploration of oil and gas, several sources and receivers are placed close to each other in order to illuminate the subsurface significantly. Their arrangement is guided by geometric and signal processing rules. The typical distance between the sources is 50-100 meters (m) and the distances between sources and recorders are within the range of 25 m. Figure 2.9 shows an example of seismic acquisition geometry. In this figure, the recorders are put in stations with separation of 3 m. The distance of the first recorder from a shot source is 15 m. Additional acquisition geometries are discussed in ([Cordson et al., 2000](#)).

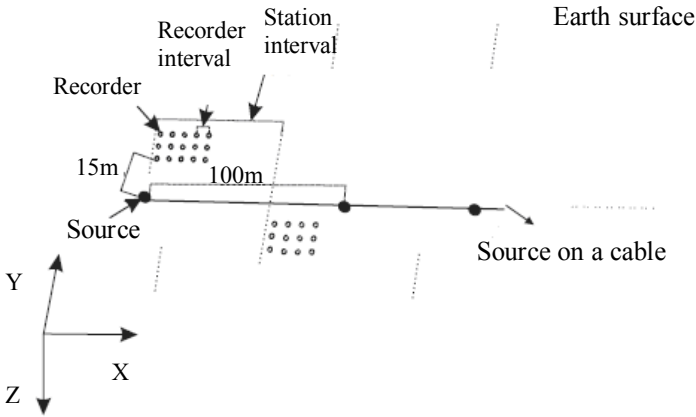


Figure 2.9 An example of 3D seismic acquisition geometry.

The group of recorders (stations) are placed in interval distances of 25 meters. Within the station, recorders are placed at distance of 3 meters from each other. The sources are aligned on a cable at distances of 100 meters apart.

Seismic recordings store geophone's impulses as functions of time and positions of the source and the recorder. Figure 2.10 shows reflections at different layers and their corresponding recorded reflection section. Each line of the reflection section is called a seismic trace and

shows a time varying seismic signal recorded by a single receiver. The x-coordinate measures the distances of the receivers from the source. Time increases in units of milliseconds downwards. The horizontal coordinate for each line represents the amplitude of the recorded signal (voltage, in principle). The amplitude provides the change in velocity perturbation at the reflector while moving from one media to another. It oscillates indicating changes from a lower acoustic impedance to higher and vice versa.

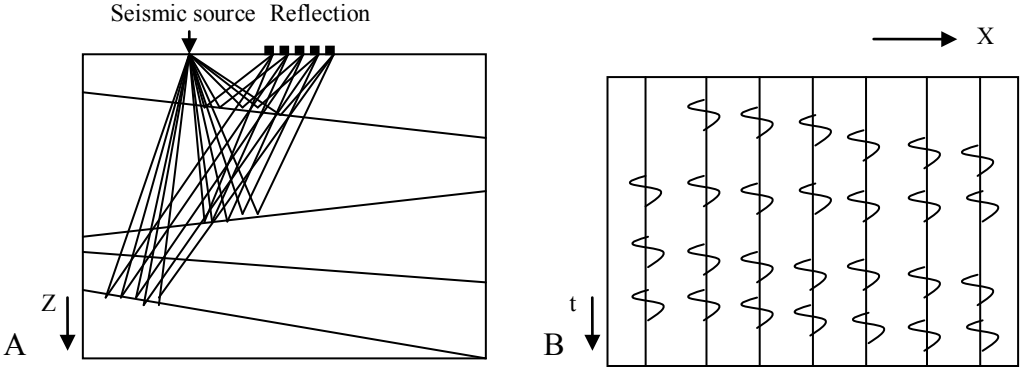


Figure 2.10 Seismic reflections and record.

A. Seismic reflections at different layers. B. Recorded seismic reflection section.

The time-series, or seismogram, recorded by each receiver group is called a trace. The set of traces recorded by all the receivers for a given source is called a common source gather. Seismic traces are sampled in interval time. The sampling interval affects the quality and size of the resulting data. A lower sampling interval results in a higher resolution, but also in a larger data size. A typical sampling interval is 2 milliseconds for the duration of 6 seconds. A seismic survey may have 210 records, each record having 256 traces, resulting in about 230 time samples.

As an interpretation of towards to the subsurface earth structures, seismic images are powerful tools for us in the understanding the underground. However, in practice, there will be several difficulties in achieving this, since the acquisition of the underground scenes and the processing of the seismic images are all involved in influences. The first difficulty lies in the methods by which we acquire the information underground.

Over the years Seismic Data Acquisition has become more important then ever for many companies and industries around the globe. During the coming years and into the future this important work will continue. It is vital for many companies to have an accurate database of the most current information on underwater geography. For those industries that use this type of information, the accuracy and the quality of this seismic data must be at very high levels. Modern technology has made seismic data acquisition quicker, simpler, and more accurate. It

is still used for many of the same purposes, including locating oil, natural gas, or valuable minerals. The Seismic Data Acquisition information will help the geoscientists to make accurate maps of the subsurface both the land and the marine areas. With this information the geoscientists can then predict the value of the area and make it more profitable for use in any capacity. Recent advances in seismic acquisition will help Apache gather more higher-quality data at a lower cost and at a staggeringly faster rate.

2.1.2 Seismic image processing and analysis

After the seismic data has been recorded, it is processed through the three main stages of deconvolution, stacking, and migration, resulting in a post-processed data volume. Deconvolution acts on the data along the time axis and increase temporal resolution by filtering and trace correction. Stacking compresses the data volume in the offset direction and yields the planes of stacked sections. Migration then moves dipping events to their true subsurface positions and collapses diffractions, thus increasing lateral resolution. Figure 2.11 shows a processing chain of seismic data.

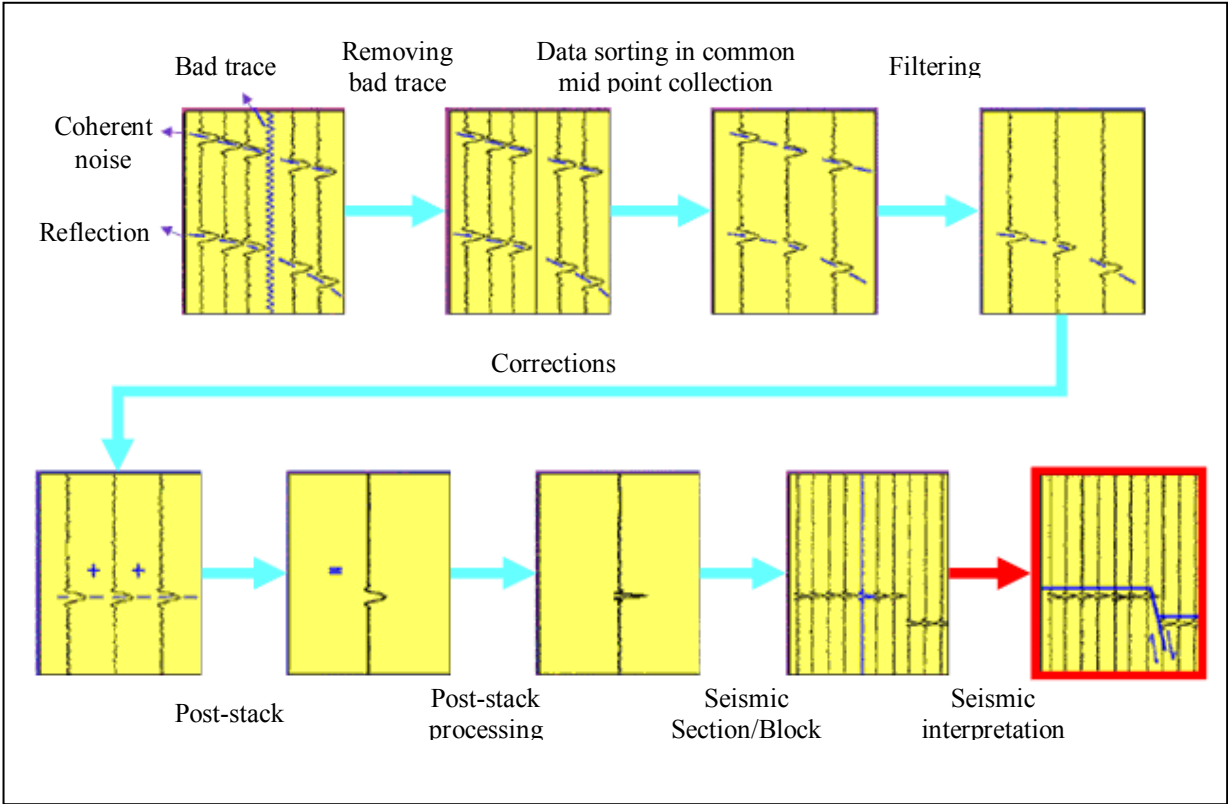


Figure 2.11 Seismic data processing chain.

The purpose of seismic processing is to manipulate the acquired data into an image that can be used to infer the sub-surface structure. Only minimal processing would be required if we had a perfect acquisition system. Processing consists of the application of a series of computer

routines to the acquired data guided by the hand of the processing geophysicist. The interpreter should be involved at all stages to check that processing decisions do not radically alter the interpretability of the results in a detrimental manner.

The origin of digital signal processing techniques (DSP) can be traced back to the seventeenth century when finite difference methods, numerical integration methods and numerical interpolation methods were developed to solve physical problems involving contiguous variables. Signal processing is the science of extracting, enhancing, storing, and transmitting useful information carried by a signal. DSP is the mathematics, the algorithms, and the techniques used to manipulate these signals after they have been converted into a digital form. Digital signal processing is concerned with the design and application of generic methods for representing and manipulating digital signals.

2.1.2.1 Image processing and analysis

Image is the major focus of research interest in digital image processing and image understanding. Image processing can be defined as the Signal processing of two-dimensional signals (Images). This includes a wide variety of goals. Image processing methods have:

- Image Enhancement;
- Image Restoration;
- Image Compression;
- Image reconstruction;
- Image Texture analysis;
- Morphological image processing;
- Feature extraction and recognition.

Image enhancement improves the quality of images for human viewing. Removing blurring and noise, increasing contrast, and revealing details are examples of enhancement operations. For example, an image might be taken of an endothelial cell, which might be of low contrast and somewhat blurred. Reducing the noise and blurring and increasing the contrast range could enhance the image. The original image might have areas of very high and very low intensity, which mask details. An adaptive enhancement algorithm reveals these details. Adaptive algorithms adjust their operation based on the image information (pixels) being

processed. In this case the mean intensity, contrast, and sharpness (amount of blur removal) could be adjusted based on the pixel intensity statistics in various areas of the image.

In image analysis, the texture analysis is an efficient tool for identifying object and matching pattern. Although there is no strict definition of the image texture, it is easily perceived by humans and is believed to be a rich source of visual information. Generally speaking, textures are complex visual patterns composed of entities, or sub patterns, which have characteristic brightness, colour, slope, size, etc. Thus texture can be regarded as a similarity grouping in an image ([Rosenfeld and Kak, 1982](#)). The local sub pattern properties give rise to the perceived lightness, uniformity, density, roughness, regularity, linearity, frequency, phase, directionality, coarseness, randomness, fineness, smoothness, granulation, etc., of the texture as a whole ([Levine, 1985](#)). There are four major issues in texture analysis:

- Feature extraction: to compute a characteristic of a digital image able to numerically describe its texture properties;
- Texture discrimination: to partition a textured image into regions, each corresponding to a perceptually homogeneous texture (leads to image segmentation);
- Texture classification: to determine to which of a finite number of physically defined classes (such as normal and abnormal tissue) a homogeneous texture region belongs;
- Shape from texture: to reconstruct 3D surface geometry from texture information.

Feature extraction is the first stage of image texture analysis. Results obtained from this stage are used for texture discrimination, texture classification or object shape determination. Approaches to texture analysis are usually categorised into structural ([Chen and Dougherty, 1994](#); [Haralick, 1979](#); [Levine, 1985](#); [Serra, 1982](#)), statistical ([Julesz, 1975](#)), model-based ([Cross and Jain, 1983](#); [Strzelecki and Materka, 1997](#)) and transform methods (such as Fourier, Gabor, wavelet transforms).

Many image processing publications report on methods for analyzing the orientation in images. Known methods include Gabor filters, windowed Fourier analysis, the local gradient, local Radon (Hough) transform, and correlation techniques. Oriented smoothing as part of image processing has been documented only since the 1990s, notably reflecting on a method called anisotropic diffusion, pioneered by Weickert ([1996](#)).

Most people have an intuitive impression of diffusion as a physical process that equilibrates concentration differences without creating or destroying mass. This physical observation can

be easily cast in a mathematical formulation. The equilibration property is expressed by *Fick's* law:

$$j = -D \cdot \nabla u \quad (2.1)$$

This equation states that a concentration gradient ∇u causes a flux j which aims to compensate for this gradient. The relation between ∇u and j is described by the *diffusion tensor* D , a positive definite symmetric matrix.

Diffusion equation is firstly proposed by Koenderink ([Koenderink, 1984](#)). It has form as:

$$\frac{\partial I}{\partial t} = \text{div}(c \nabla I) = \nabla \cdot (c \nabla I) = c \Delta I + \nabla c \cdot \nabla I \quad (2.2)$$

where I : function of the image; ∇ : gradient; Δ : Laplacian; *div* : divergence; c : diffusion coefficient.

If c is constant, it will be isotropic diffusion

$$\frac{\partial I}{\partial t} = c \Delta I \quad (2.3)$$

Otherwise, it will be anisotropic diffusion.

The image at the instant $(t + I)$ deduce from the instant t :

$$I_{t+1} = I_t + \frac{\partial I_t}{\partial t} = I_t + \nabla \cdot (c \nabla I_t) = I_t + c \Delta I_t + \nabla c \cdot \nabla I_t \quad (2.4)$$

For the isotropic diffusion ($c = \text{constant}$) :

$$I_{t+1} = I_t + \frac{\partial I_t}{\partial t} = I_t + c \Delta I_t \quad (2.5)$$

From above equations, we can get diffusion in three cases:

– 1D diffusion filtering:

$$\frac{\partial}{\partial t} I(x, t) = \frac{\partial}{\partial x} \left[(c(x, t) \cdot \frac{\partial}{\partial x} I(x, t)) \right], \quad (2.6)$$

$$\begin{aligned}
\frac{\partial}{\partial t} I(x, t) &\approx \frac{1}{\Delta x} \left[c(x, t) \cdot \frac{1}{\Delta x} (I(x + \frac{\Delta x}{2}, t) - I(x - \frac{\Delta x}{2}, t)) \right] \\
&\approx \frac{1}{(\Delta x)^2} \left[\begin{array}{l} c(x + \frac{\Delta x}{2}, t) \cdot (I(x + \Delta x, t) - I(x, t)) \\ -c(x - \frac{\Delta x}{2}, t) \cdot (I(x, t) - I(x - \Delta x, t)) \end{array} \right] \\
&= \Phi_{right} + \Phi_{left} \mid \Delta x = 1
\end{aligned} \tag{2.7}$$

– 2D diffusion filtering:

$$\begin{aligned}
\frac{\partial}{\partial t} I(x, y, t) &=+ \frac{\partial}{\partial x} \left[c(x, y, t) \cdot \frac{\partial}{\partial x} I(x, y, t) \right] - \frac{\partial}{\partial y} \left[c(x, y, t) \cdot \frac{\partial}{\partial y} I(x, y, t) \right] \\
&= \Phi_E + \Phi_W + \Phi_N + \Phi_S \mid \Delta x = \Delta y = 1
\end{aligned} \tag{2.8}$$

$$I(x, y, t + \Delta t) \approx I(x, y, t) + \Delta t \cdot (\Phi_E + \Phi_W + \Phi_N + \Phi_S) \tag{2.9}$$

– 3D diffusion filtering:

$$\begin{aligned}
I(x, y, z, t + \Delta t) &\approx I(x, y, z, t) + \Delta t \cdot \left[\frac{1}{(\Delta x)^2} (\Phi_E(\Delta x) + \Phi_W(\Delta x)) \right. \\
&\quad \left. + \frac{1}{(\Delta y)^2} (\Phi_N(\Delta y) + \Phi_S(\Delta y)) + \frac{1}{(\Delta z)^2} (\Phi_{UP}(\Delta z) + \Phi_{DOWN}(\Delta z)) \right]
\end{aligned} \tag{2.10}$$

Based on the anisotropic diffusion, Weickert introduced anisotropic diffusion filtering ([Weickert, 1998](#)). Using the diffusion tensor to steer the filtering process allows for directional, anisotropic smoothing. The eigenvectors of the diffusion tensor define the principal directions of smoothing and the corresponding eigenvalues define the amount of smoothing. Weickert based the diffusion tensor on the structure tensor ([Estepar, 2005](#); [Weickert, 1997](#)), which describes structures in the image using first order derivative information. Therefore the principal directions of smoothing are based on the description of the structures.

Two specializations of anisotropic diffusion were introduced by Weickert, edge-enhancing diffusion (EED) and coherence-enhancing diffusion (CED) ([Weickert, 1998](#)). Both were initially defined in two dimensions. EED was designed to smooth noise while enhancing edges and CED was designed to enhance line-like textures. CED is essentially one dimensional diffusion ([Weickert, 1999](#)), since there is either diffusion in one direction or almost no diffusion at all. EED in 3D becomes plate enhancing diffusion, it filters noise from homogeneous areas and enhances plate-like structures. 3D CED preserves small structures

and enhances tubular structures; we use the ratio between the second and the third eigenvalue of the structure tensor to decide whether diffusion should be performed. In tubular structures the ratio between these eigenvalues is large, while in small almost spherical structures the ratio is small.

Often image smoothing is a pre-processing step toward image segmentation. Edge preserving image smoothing plays an important role in image processing and computer vision. Edge-preserving oriented smoothing has been implemented in Shell in two fashions. A first algorithm extracts a 2D platelet of seismic amplitudes from 3D seismic data, following the local structure. Edge-preserving smoothing is then applied to the data of this platelet, writing the result back into a 3D output cube. In edge-preservation tests, it was found that simple median filters become inadequate when increasing the filter size. Among the oldest ideas in edge preserving image smoothing methods is introduced by Graham ([1962](#)), pixels corrupted by impulse noise were detected and replaced by an estimate based on local average. Since then, several solutions have been proposed to limit the effect of untypical or outlier samples in the filtering window. Better edge preservation performance was achieved with Kuwahara-type methods ([Kuwahara et al., 1976](#)). The general idea behind Kuwahara filter is to divide the filter kernel into four rectangular sub-regions which overlap by one pixel. The filter response is then defined by the mean of a sub-region with minimum variance. A possible edge is detected by computing the statistics over a set of sub regions; sub regions showing deviating statistics are likely to contain edges and are assigned smaller weights in filtering. Based on local area flattening, the Kuwahara filter properly removes details even in a high-contrast region, and protects shape boundaries even in low-contrast regions. The Kuwahara filter produces clearly noticeable artifacts. The sub-region selection process is unstable if noise is present or sub-regions have the same variance.

The second generation of edge preserving oriented smoothing was developed in 1999. It is based on a 3D implementation of the anisotropic diffusion technique and has been called the van Gogh filter. The advantage of this method is that it can be carried much further than SOF-EP filtering. In first instance, filtering suppresses incoherent noise and small stratigraphic features. The continuity of events is enhanced while the acuity of faults is preserved or even improved. By applying more diffusion steps, the van Gogh filter simplifies the structural image: Undulating reflections are gradually straightened and minor fault-like features vanish—whether real or not. Ultimately, the structure is simplified to its most rudimentary form.

The recent works in edge preserving oriented smoothing have been made to address the

limitations of the Kuwahara filter. Papari et al ([2007](#)) defined a new criterion to overcome the limitations of the unstable sub-region selection process. Instead of selecting a single sub-region, the result is defined as the weighted sum of the means of the sub-regions. The weights are defined based on the variances of the sub-regions. Even though this improves the output quality significantly, clustering artifacts are still noticeable. Kyprianidis et al ([2009](#)) presented anisotropic Kuwahara filter. It is based on a generalization of the Kuwahara filter that is adapted to the local shape of features, derived from the smoothed structure tensor. The anisotropic Kuwahara filter replaces the weighting functions defined over sectors of a disc by weighting functions defined over ellipses. Due to this adaptation of the filter to the local structure, directional image features are better preserved and emphasized. In ([Kyprianidis et al., 2010](#)), the authors presented a modification of the anisotropic Kuwahara filter, a new weighting functions that are not based on convolution. The proposed weighting functions are parameterizable. The eccentricity and expansion can be adjusted, which allows to control the overlapping areas to adjacent sectors.

2.1.2.2 Seismic image processing and analysis

The seismic image is one of the most important sources to understand the earth subsurface, e.g., the properties and orientation of rock layers, without having to drill it. The image is acquired by collecting the reflected sound waves by the rock layers, and stratigraphic structures are shown as horizontal line-like flow patterns.

Seismic data processing routines generally fall into one of the following categories (Seismic Data Processing and Interpretation):

- Enhancing signal at the expense of noise;
- Providing velocity information;
- Collapsing diffractions and placing dipping events in their true subsurface locations (migration);
- Increasing resolution.

Because drilling a well is extremely expensive, seismic image processing and interpretation becomes one of the most important processes in the upstream sector of the petroleum industry. Seismic image analysis is a complex and subjective process requiring a wide range of interdisciplinary knowledge in geology, physics, and engineering. Traditionally, seismic image analysis has been done by manual interpretation of processed 2D slices. With the

advent of the rapid increasing computational power, direct processing of 3D seismic images with the help of computer programs is becoming more practical.

Seismic images often show patterns with a layered structure due to the depositional nature of the subsurface. In image processing a pattern with a certain regularity or structure is called a texture. The description of the 'layered' textures in seismic images can be split up in two parts. One part is the geometrical description of the structure; the other part is the description of the signal perpendicular to the layered structure. Examples of geometrical properties are the orientation and the curvature of the layered structure. An example of a property of the perpendicular signal is its characteristic frequency. In the case of a seismic image, the perpendicular signal is determined by the change in the acoustic impedance of the subsurface rock, convolved with the seismic wavelet. This convolved signal is usually described by using a time-frequency representation. The main subject of this thesis is the geometrical description of the structure of layered textures.

Seismic data contains both useful structural information and useless random noise. In seismic image, from the interpreter's point of view, there are two types of noise ([Chopra and Marfurt, 2008](#)): noise the interpreter can address through some relatively simple process applied to the migrated data volume, and noise that require reprocessing of prestack data. The interpreter can address noise spikes, a limited degree of migration operator aliasing, small-velocity errors, and backscattered noise that can result in acquisition footprint, as well as overall "random noise" through band pass, k_x - k_y , and structure-oriented filtering. In contrast, significant velocity errors will result in overlapping reflector signals, producing discontinuity and tuning artifacts that may overwhelm corresponding events associated with the subsurface geology. Surface and interbed multiples result in similar strong artifacts.

In image processing, it is desirable to enhance the structures and reduce the random noise. It is commonly known that smoothing is an effective way of reducing random noise. Hall summarized eight smoothing methods and discusses their effects in the article ([Hall, 2007](#)). Gaussian and mean filters are structure in-distinguishable and smear the edges and texture boundaries. After these filters are applied, the resolution of horizons, faults, and unconformities are reduced or even lost. Edge-preserving smoothing, such as the known Kuwahara filter, is able to keep edges in 2D, but its 3D counterpart, as described in ([AlBinHassan et al., 2006](#)), is designed to preserve body segmentation and cannot keep planar structures, such as faults.

To better image and interpret seismic data, two different ways have been approached. The first

approach is to improve the signal-to-noise ratio of the seismic data so that the traditional horizon-based interpretation method can be better followed. The second approach is to highlight specific geologic features that have a 3D extent, and the geometry of which may have little in common with the orientation of the 3D grid of seismic data.

Seismic images are characterised by specific textures which can provide valuable information for locating potential oil reservoirs. Figure 2.12 shows an example image of a seismic cross-section. A non-specialist can easily identify three texture areas in this image: parallel, chaotic and mixed. An expert may identify several structures of interest in the image, such as a mound indicating a carbonate built-up, horizon terminations indicating the location of a prehistoric coastline, faults, etc.

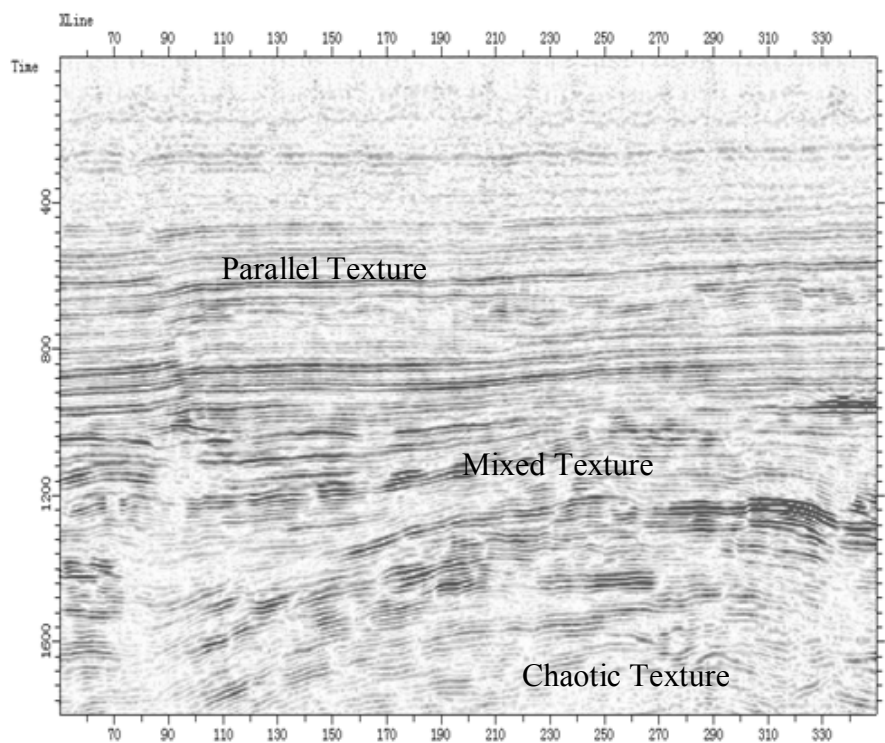


Figure 2.12 A seismic section showing three different textures

Successful application of oriented smoothing to seismic data requires three ingredients:

- orientation analysis: determination of the local orientation of the reflections
- edge detection: determination of possible reflection terminations
- smoothing with edge preservation: smoothing of the data in the direction of the local orientation, without filtering across detected edges

Each step can be performed in a multitude of ways and has been explored in the academic realm, however, without optimization for noise suppression in seismic data.

Image processing and computer vision play a crucial role in computer-assisted interpretation of seismic images. A variety of effective image processing techniques for seismic image analysis have been developed in the fields of geophysics, mathematics, and computer science. Many geological features produce discontinuous seismic signal across their boundaries, and therefore measuring seismic attributes, such as coherence or discontinuity, has been an active research area. A seminal work by Bahorich and Farmer ([1995](#)) first proposed using coherency of pixel intensities to detect faults and other geological features in 3D seismic volumes. In ([Bahorich and Farmer, 1995](#)), coherency is measured by the geometric mean of maximum time-lagged cross-correlation along x and y directions in a 3D volume. Because voxel intensities indicate sharp contrasts across fault surfaces, those regions become distinct in the coherence cube. Marfurt et al ([1998](#)) proposed a robust coherence estimation algorithm based on multiple traces with locally adapted similarity (or semblance) measure. Another variant of coherence cube, based on eigenanalysis of covariance matrix, is proposed by Gersztenkorn and Marfurt ([1999](#)). A practical survey of several variants of the coherence cube algorithm can be found in ([Chopra, 2002](#)). Cohen and Coifman ([2002](#)) proposed a more efficient discontinuity measure computation method using a normalized trace of a small correlation matrix. Lu et al ([2005](#)) employed higher-order statistics and a supertrace technique for more accurate coherence estimation. A recent survey of state-of-the-art seismic attribute processing techniques can be found in ([Chopra and Marfurt, 2008](#)).

Structure tensors have been shown to work well in segmenting and locating structures of specific shape. Several books published in the recent years present extensive literature reviews on structure tensors and their applications ([Bakker, 2002](#); [Bakker et al., 1999](#); [Florack, 1997](#); [Weickert, 1998](#)). The first and second order structure tensors, simply estimated by differencing the image, can be used to quantify the local structure of seismic data and their departure from laminar structure. They can be used to distinguish chaotic regions as well as regions of interest, like mounds and horizon terminations from stratified regions. This tensor is known by many different names: gradient structure tensor, second-moment matrix, scatter matrix, interest operator and windowed covariance matrix. It is defined in terms of the first derivative of the image and has been introduced for the detection of lines, edges and corners.

Bakker ([2002](#)) detected channels and faults in 2D and 3D seismic images by using the gradient structure tensor for detecting the position of these structures. More specifically, the author estimated their orientation by using the eigenvectors of the tensor and used steered

adaptive anisotropic filters, elongated according to the shape of the structure under examination along the estimated orientation. These filters enhanced the structure by noise removal without degrading it. Furthermore, the gradient structure tensor was modified into a curvature corrected structure tensor, to account for plane-like and line-like curvilinear structures. Meanwhile, others have been successfully employed some oriented filtering methods to enhance stratigraphic continuity and to preserve fault discontinuity ([Bakker et al., 1999](#); [Fehmers and Hocker, 2003](#); [Weickert, 1999](#)) for the applications that do not require actual fault surfaces. Randen et al ([1999](#)) measured fault strength using the norm of the projected gradient vector onto the local orientation plane computed using a least-square axis fitting method([Bigun et al., 1991](#)), which is in fact similar to a structure tensor method introduced by Bakker ([2002](#)). Gibson et al ([2003](#)) also proposed a structure tensor approach, but the semblance value, a measure for similarity with neighbor pixels, is estimated using a user-defined oriented window. A major difference from ([Bakker et al., 1999](#)) is that ([Gibson et al., 2003](#)) creates 3D polygons instead of binary voxels for the resulting geometry. Pedersen et al ([2002](#)) proposed a statistical method based on the idea borrowed from the behaviour of a group of social insects to enhance fault responses. Jacquemin and Mallet ([2005](#)) used a Hough transform, one of the traditional feature detection algorithms, to automatically extract 3D fault surfaces. Dip-steered mean filters work well on prestack data in which discontinuities appear as smooth diffractions, but smear faults and stratigraphic edges on migrated data.

Dip-steered median and alpha-trimmed mean filters work somewhat better but will still smear faults. Fehmers and Hocker ([Fehmers and Hocker, 2003](#); [Hocker and Fehmers, 2002](#)) address this problem through an “anisotropic diffusion” smoothing algorithm. The anisotropic part is so named because the smoothing takes place parallel to the reflector, while no smoothing takes place perpendicular to the reflector. The diffusion part of the name implies that the filter is applied iteratively, much as an interpreter would apply iterative smoothing to a time-structure map. Most important, no smoothing takes place if a discontinuity is detected, thereby preserving the appearance of major faults and stratigraphic edges. Luo et al ([2002](#)) proposed a noise-reduction method, edge-preserving smoothing (EPS), that uses a multi-window (Kuwahara) filter to address the same problem. EPS is also described by Hall ([2007](#)). In the application of EPS, a set of predefined neighbourhood sub-windows are used and the best result, which is usually the one with minimum deviation, is selected for smoothed output. Both approaches use a mean or median filter applied to data values that fall within a spatial analysis window with a thickness of one sample. In ([Jeong et al., 2006](#)), Jeong et al propose a semi-automated interactive 3D fault detection method using graphics hardware. The proposed method implements the time-consuming computing components entirely on the GPU to

extract 3D faults from seismic images at interactive rates.

Medioni and colleagues used the tensor voting technique in different applications of image analysis ([Medioni et al., 2000](#); [Tang and Medioni, 2002](#); [Tang et al., 2001](#); [Tong et al., 2001](#); [Tong et al., 2004](#)). Tensor voting is an approach of extracting salient structures by encoding data and corresponding uncertainties in the Hessian matrix. An overall illustration of Tensor Voting method([Medioni et al., 2000](#)), summarizing its different components, is shown in Figure 2.13. The methodology is grounded on two elements: tensor calculus for data representation, and linear tensor voting for data communication. David also used the tensor voting technique in seismic image analysis to detect seismic fault ([David, 2008](#)).

Lavialle et al ([2007](#)) presented an approach called SFPD (Seismic Fault Preserving Diffusion) based on the CED model, dedicated to 3D seismic blocks processing. Their pre-processing step based on a non linear diffusion filtering leading to a better detection of seismic faults. The non linear diffusion approaches are based on the definition of a partial differential equation that allows us to simplify the images without blurring relevant details or discontinuities. Computing the structure tensor which provides information on the local orientation of the geological layers, authors propose to drive the diffusion along these layers. In SFPD, the eigenvalues of the tensor are fixed according to a confidence measure that takes into account the regularity of the local seismic structure. The filtering consists in a data pre-processing method, which takes into consideration the enhancing of relevant discontinuities.

After obtaining seismic images, the following operation is the interpretation of seismic images. Seismic interpretation begins with mapping the large scale structure of the area. This structural interpretation mainly consists of creating horizons and fault planes. Horizons are surfaces that are created by the interpreter by selecting a reflector and following it over the volume ([Bakker, 2002](#)). They are important information towards to the structure of underground. And the tracing of horizon therefore is still an objective in the analysis of seismic image. The creation of horizons will be discontinued when the appearances of faults. The faults will cause great difficulties in locating and tracing the horizons. Of course, the detection and accurate location of faults is another important task in analysis of seismic images.

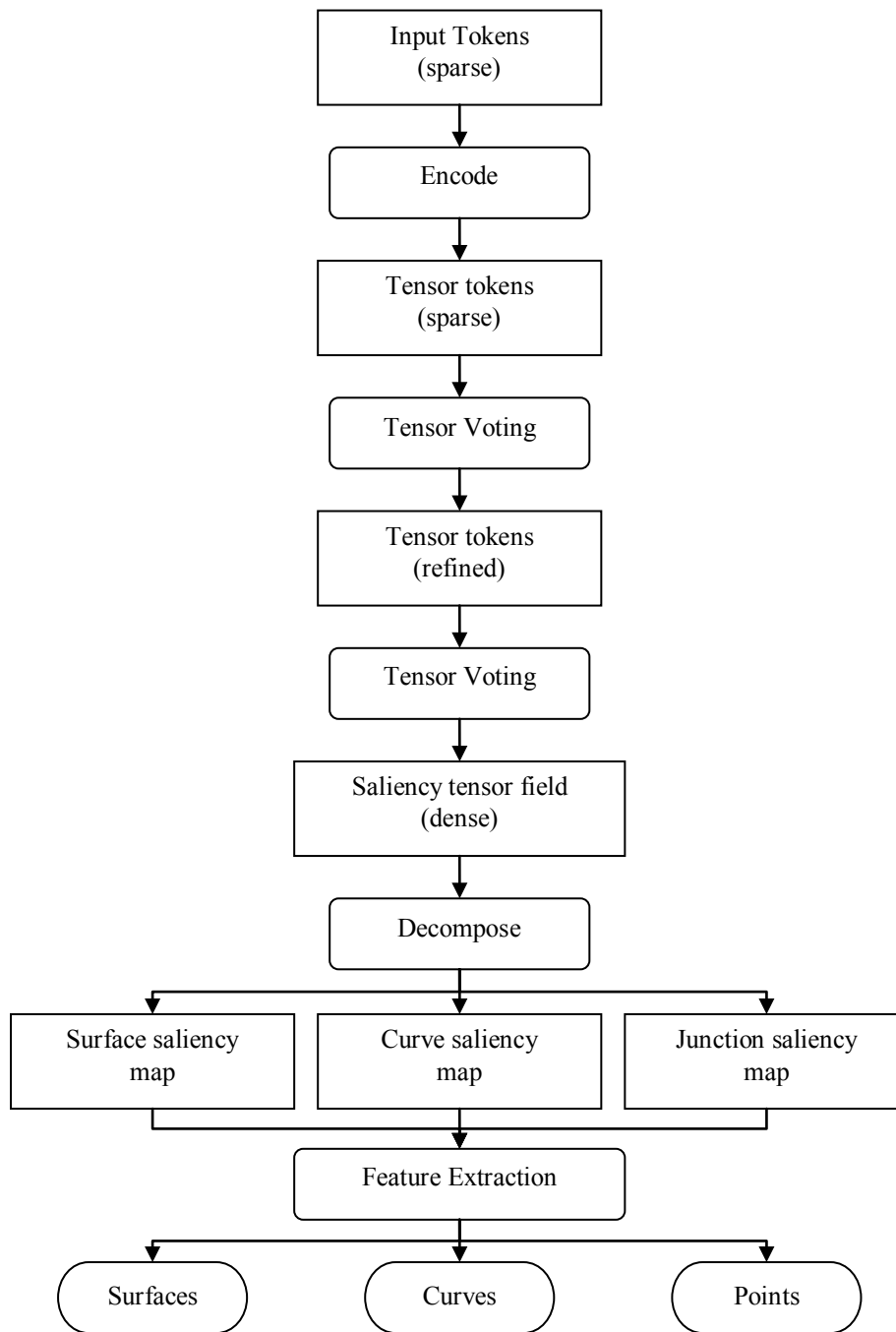


Figure 2.13 Overall approach of Tensor Voting.

2.2 Seismic attributes

A seismic attribute is a quantitative measure of a seismic characteristic of interest ([Chopra and Marfurt, 2005](#)). Analysis of attributes has been integral to reflection seismic interpretation since the 1930s when geophysicists started to pick travel times to coherent reflections on seismic field records. Seismic attributes are the fundamental pieces of information contained within a recorded seismic trace: time, amplitude, frequency, and attenuation ([Brown, 2001](#)).

The analysis of seismic attributes allows the identification of petrophysical and structural aspects of a buried volume of rock that would typically be beneath the resolution of traditional seismic amplitude data. In the petroleum industry, seismic attributes are used to identify areas of high porosity or permeability, lateral changes in the aspect or dip direction of a horizon, continuity of reflectors, stratigraphic pinch-outs, and a multitude of other properties of use in petroleum exploration and field development(Siguaw et al., 2001). In the recent years, much attention has been given to the prediction of reservoir properties and to the extraction of seismic attributes to enhance the value of seismic interpretation. Many new signal-processing methods are being developed and entering commercial packages, exploiting properties of local curvature, local frequency variability, and seismic textures.

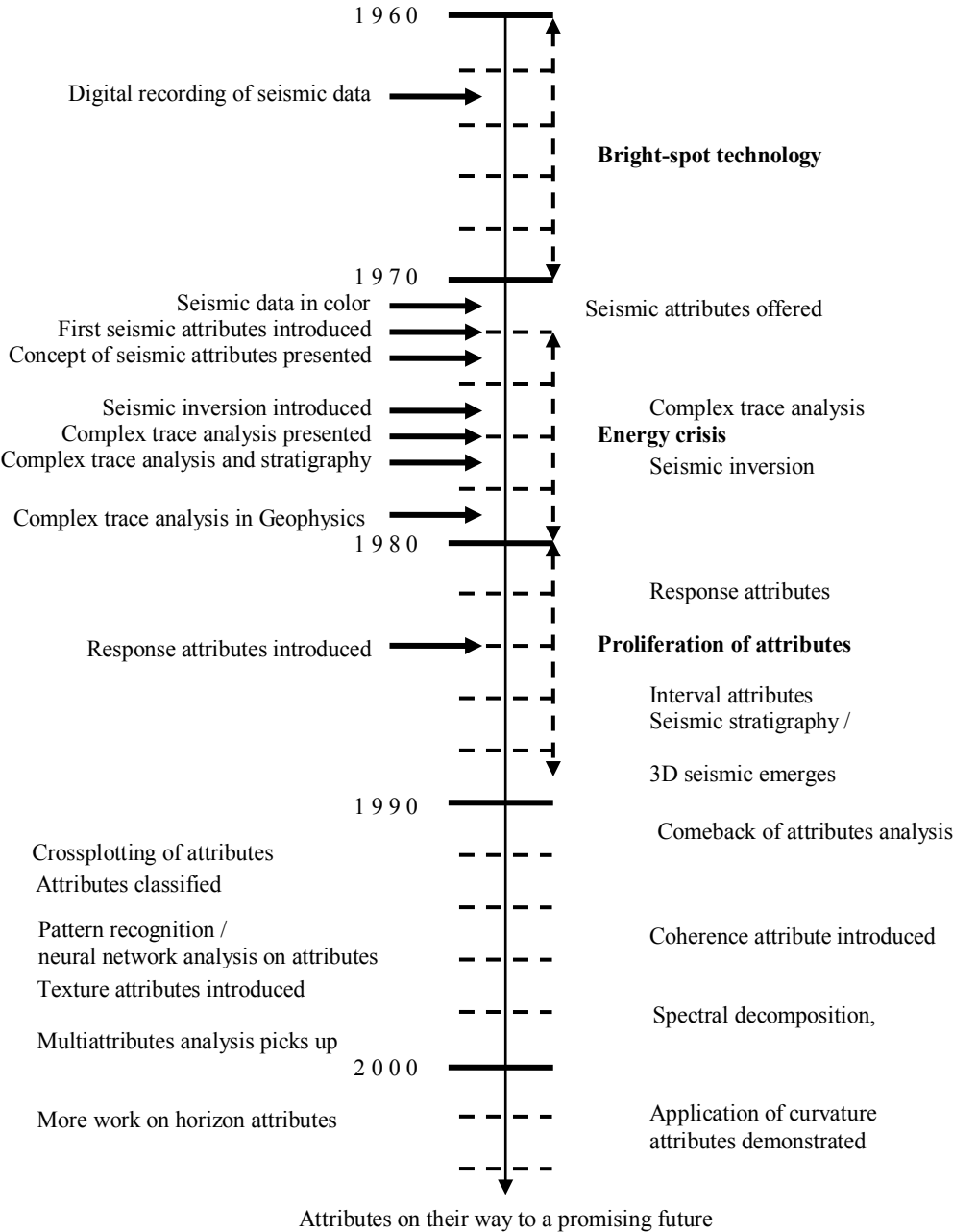


Figure 2.14 Historical development of the attributes.

2.2.1 Introduction of seismic attributes

Seismic attributes are specific measurements of geometric, kinematic, dynamic, or statistical features derived from seismic data. There are now more than 50 different seismic attributes generated from a given seismic data set and applied to the interpretation of geologic structure, stratigraphy, and rock/pore fluid properties.

Some of seismic attributes are more sensitive than others to specific reservoir environments, some are better at revealing subsurface anomalies not easily detectable, and some have been used as direct hydrocarbon indicators. The evolution of seismic attributes is closely linked to advances in computer technology. The introduction of colour printers in the early 1970s allowed colour displays of reflection strength, frequency, phase, and interval velocity to be overlain routinely on black-and-white seismic records. Interpretation workstations in the 1980s provided interpreters with the ability to interact quickly with data to change scales and colors and to easily integrate seismic traces with other information such as well logs. Today, very powerful computer workstations capable of integrating large volumes of diverse data and calculating numerous seismic attributes are a routine tool used by seismic interpreters seeking geologic and reservoir engineering information from seismic data. Historical development of seismic attribute is shown in Figure 2.14 ([Chopra and Marfurt, 2005](#)).

2.2.2 Seismic attributes definition and classification

Seismic attributes describe seismic data and are defined as quantitative derivatives of a basic seismic measurement that may be extracted along a seismic trace, a horizons surface, or summed over a time window ([Brown, 1996](#)). Geometry is probably the most important information that seismic data immediately provides after initial processing.

Attributes can be divided into eight additional categories: pre-stack attributes, post-stack attributes, instantaneous attributes, wavelet attributes, physical attributes, geometrical attributes, reflective attributes, and transmissive attributes([Taner, 2001](#)). Indeed, any quantity calculated from seismic data can be considered an attribute. Consequently, attributes are of many types: prestack, inversion, velocity, horizon, multi-component, 4-D, and, the most common kind and subject of this review, attributes derived from conventional stacked data (showed in Table 2.1) ([Barnes, 2001](#)).

Table 2.1 Methods for computing post-stack seismic attributes.

Method	Representative Attributes
complex trace	amplitude, phase, frequency, polarity, response phase, response frequency, dip, azimuth, spacing, parallelism
time-frequency	dip, azimuth, average frequency, attenuation, spectral decomposition
correlation/covariance	discontinuity, dip, azimuth, amplitude gradient
interval	average amplitude, average frequency, variance, maximum, number of peaks, % above threshold, energy halftime, arc length, spectral components, waveform
horizon	dip, azimuth, curvature
miscellaneous	zero-crossing frequency, dominant frequencies, RMS amplitude, principal components, signal complexity

Attributes can be computed effectively from pre-stack and post-stack data, before or after time migration. The procedure is the same in all of these cases. Attributes can be classified in many different ways. Several authors have given their own classification. Here we give a classification based on the domain characteristics of the attributes:

- **Pre-Stack Attributes:** Input data are CDP or image gather traces. They will have directional (azimuth) and offset related information. These computations generate huge amounts of data; hence they are not practical for initial studies. However, they contain considerable amounts of information that can be directly related to fluid content and fracture orientation. AVO, velocities and azimuthal variation of all attributes are included in this class.
- **Post-Stack Attributes:** Stacking is an averaging process which eliminates offset and azimuth related information. Input data could be CDP stacked or migrated. One should note that time migrated data will maintain their time relationships, hence temporal variables, such as frequency, will also retain their physical dimensions. For depth migrated sections, frequency is replaced by wave number, which is a function of propagation velocity and frequency. Post-stack attributes are a more manageable approach for observing large amounts of data in initial reconnaissance investigations. For detailed studies, pre-stack attributes may be incorporated.

Attributes may be further classified by their computational characteristics:

- **Instantaneous Attributes:** are computed sample by sample, and represent instantaneous variations of various parameters. Instantaneous values of attributes such as trace envelope, its derivatives, frequency and phase may be determined from complex traces.
- **Wavelet Attributes:** This class comprises those instantaneous attributes that are computed at the peak of the trace envelope and have a direct relationship to the Fourier transform of the wavelet in the vicinity of the envelope peak. For example, instantaneous frequency at the peak of the envelope is equal to the mean frequency of the wavelet amplitude spectrum. Instantaneous phase corresponds to the intercept phase of the wavelet. This attribute is also called the “response attribute”(Bodine, 1984).

These attributes may be sub-classified on the basis of the relationship of the attributes to the geology:

- **Physical Attributes:** relate to physical qualities and quantities. The magnitude of the trace envelope is proportional to the acoustic impedance contrast; frequencies relate to bed thickness, wave scattering and absorption. Instantaneous and average velocities directly relate to rock properties. Consequently, these attributes are mostly used for lithological classification and reservoir characterization.
- **Geometrical Attributes:** describe the spatial and temporal relationship of all other attributes. Lateral continuity measured by semblance is a good indicator of bedding similarity as well as discontinuity. Bedding dips and curvatures give depositional information. Geometrical attributes are also of use for stratigraphic interpretation since they define event characteristics and their spatial relationships, and may be used to quantify features that directly assist in the recognition of depositional patterns, and related lithology.

Reservoir characterization is the process of mapping a reservoir's thickness, net-to-gross ratio, pore fluid, porosity, permeability and water saturation. Within the past few years, it has become possible to make some of these maps using seismic attributes when those attributes are calibrated with available well control. Some of these attributes are much better than others for reservoir characterization, but there has not been much discussion of this in the geophysical literature. One way to organize and understand seismic attributes is to separate them into the following categories(Cooke et al., 1999):

- **Qualitative attributes** such as coherency - and perhaps instantaneous phase or instantaneous frequency - are very good for highlighting spatial patterns such as faults or

facies changes.

- **Quantitative attributes:** The simplest quantitative attributes are the amplitude (of a peak or a trough) on zero phase data, relative impedance data or absolute impedance data. These three attributes (zero phase amplitude, relative impedance and absolute impedance) are the most useful for quantitative reservoir characterization.
- **Interval attributes** are those that are used to quantify a window of seismic data usually containing more than one peak or trough. Most seismic attributes fall into this category. Examples of interval attributes are number of zero crossings, average energy and dominant frequency.
- **AVO attributes** are those that are generated using a reflection's pre-stack amplitudes.

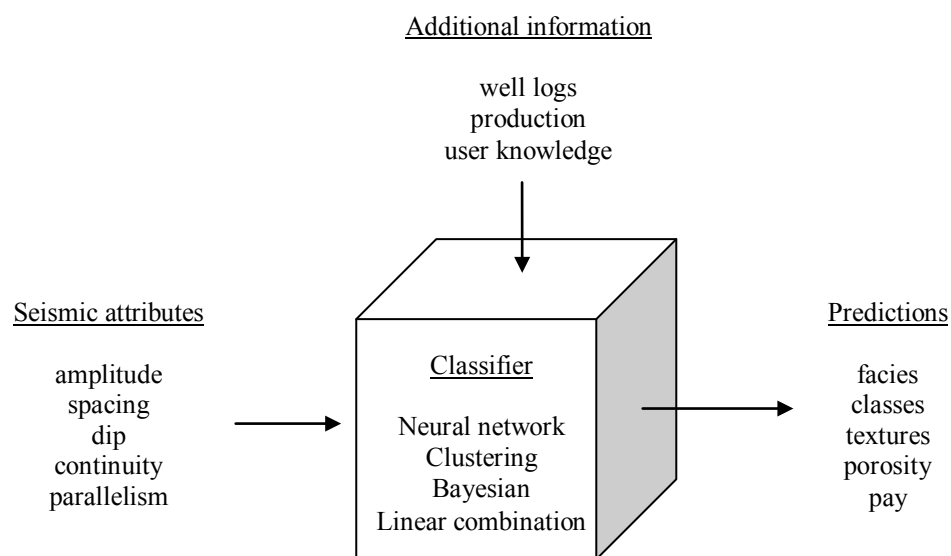


Figure 2.15 Basic flow chart of seismic pattern recognition (multi-attribute analysis).

Seismic attributes work also began on seismic pattern recognition or “multi-attribute analysis” ([Barnes, 2001](#)). It illustrates in Figure 2.15. While the driving force was to automatically determine seismic facies, there also arose the curious idea that attributes might somehow make sense in combination even if they didn’t make any sense individually.

Most of the attributes are a function of the characteristics of the reflected seismic wavelet. We consider the interfaces between two beds. However, velocity and absorption are measured as quantities occurring between two interfaces, or within a bed. Therefore we can divide the attribute into basis categories based on their origin:

- **Reflective attributes** correspond to the characteristics of interfaces. All instantaneous and

wavelet attributes can be included under this category. Pre-stack attributes such as AVO are also reflective attributes.

- **Transmissive attributes** relate to the characteristics of a bed between two interfaces. Interval, RMS and average velocities, Q, absorption and dispersion come under this category.

2.2.3 Some basic attribute characteristics

The Trace Envelope is a physical attribute and it can be used as an effective discriminator for the following characteristics:

- Mainly represents the acoustic impedance contrast, hence reflectivity,
- Bright spots, possible gas accumulation,
- Sequence boundaries,
- Thin-bed tuning effects
- Major changes in depositional environment,
- Spatial correlation to porosity and other lithologic variations,
- Indicates the group, rather than phase component of the seismic wave propagation.

For the remainder of the discussion on seismic attribute analysis, let us assume a complex seismic trace with a real component.

$$g(t) = A(t) \cos 2\pi vt \quad (2.11)$$

where $A(t)$ is the amplitude envelope of the signal $g(t)$ and v is the frequency of the seismic signal. Application of a Hilbert transform to the above seismic trace yields the quadrature, or imaginary component, of the trace. The quadrature of $g(t)$ is given by

$$g(t) \leftrightarrow g_{\perp}(t) = A(t) \sin 2\pi vt \quad (2.12)$$

where $g_{\perp}(t)$ is the imaginary component of the complex trace $g(t)$ ([Sheriff and Geldart, 1995](#); [Taner et al., 1979](#)).

2.2.3.1 Coherence attribute

Analysis of horizon attributes began with the examination of coherence values of interpreted horizons. Coherence is the measure of the similarity in appearance and shape of waveforms between neighboring vertical traces.

Bahorich and Farmer (1995) introduced the attribute of coherence in 1995. The coherence cube calculates localized waveform similarity in both inline and cross-line directions and estimates of 3D seismic coherence are obtained. Small regions within the seismic volume containing stratigraphic anomalies such as channels have a different seismic character compared to the corresponding regions of neighbouring traces. This attribute is given by equation:

$$c_1 = \sqrt{\frac{C_{f_1 f_2}}{\sqrt{C_{f_1 f_1} C_{f_2 f_2}}} \frac{C_{f_1 f_3}}{\sqrt{C_{f_1 f_1} C_{f_3 f_3}}}} \quad (2.13)$$

where f_1 and f_2 are two consecutive tracks the direction and inline f_1 and f_3 and the direction cross-line $C_{f_1 f_2}$ is the maximum correlation between f_1 and f_2 .

To involve a larger number of traces, Marfurt et al (1999; 1998) introduced the covariance matrix of traces. The new attribute of coherence is then given by:

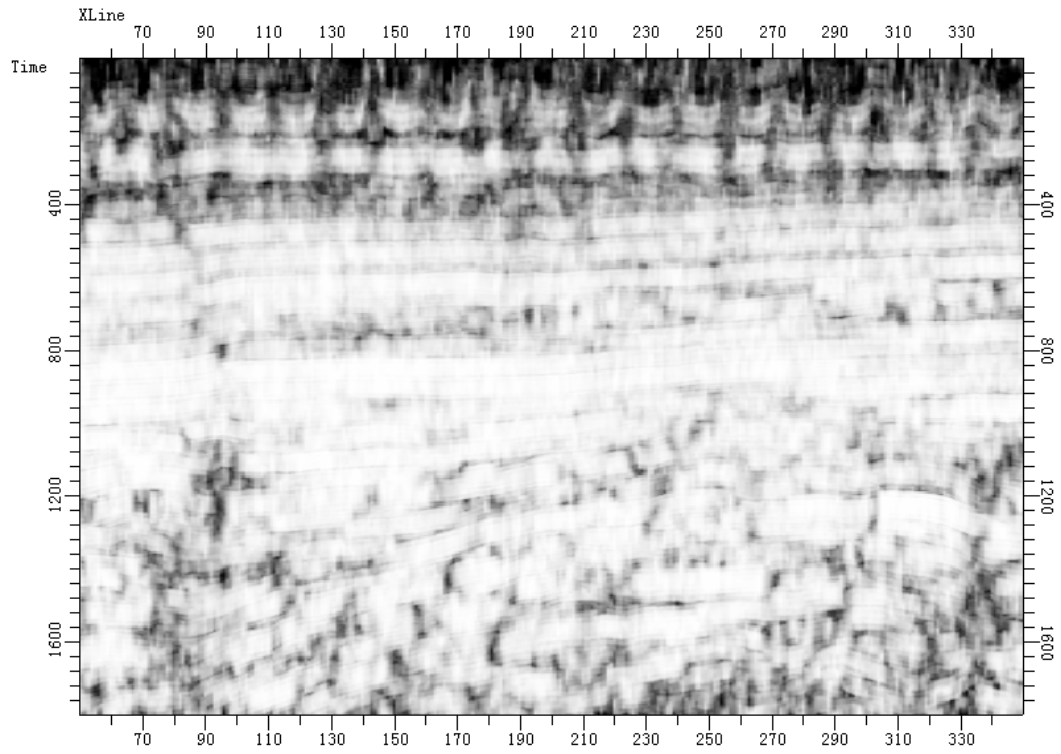
$$c_2 = \frac{\sum_{i,j} C_{ij}}{\sum_i C_{ii}} \quad (2.14)$$

For through reducing the level of noise introduced by the calculation of the covariance matrix trace, we can use only the dominant component, which gives us the attribute C_3 :

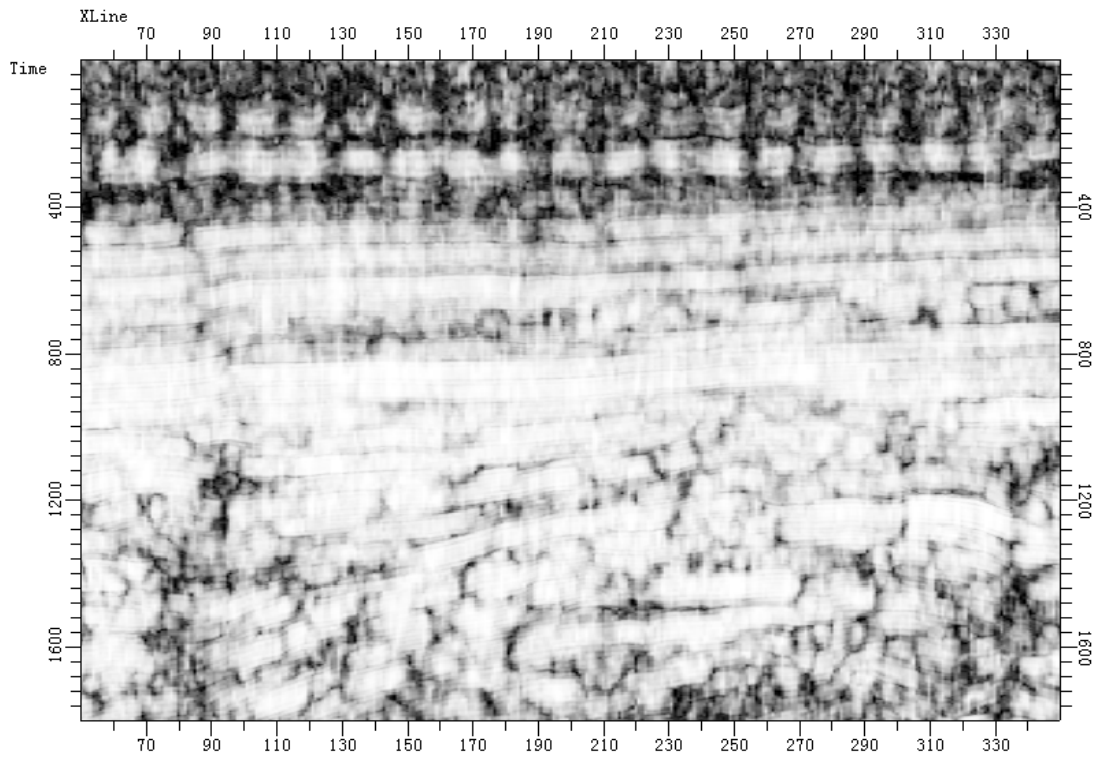
$$c_3 = \frac{\lambda_1}{\sum_i \lambda_i} \quad (2.15)$$

where λ_j is the eigenvalues of C . λ_1 is the largest eigenvalue. This measure was presented as an estimate of seismic coherency in (Gersztenkorn and Marfurt, 1999).

The technique of coherent cube is a new technique for seismic interpretation. It has great advantages in recognizing faults and fractures, interpreting ancient channels, edge detection of oil-gas reservoir, or other discontinuous features, etc. The method of coherent cube may be applied in oil exploration, coal exploration and study of natural earthquakes.



(a) C2 algorithm



(b) C3 algorithm

Figure 2.16 Coherence of inline 350 section.

2.2.3.2 Average Energy attribute

The average amplitude of the stacked trace over time window t to $t+m\Delta t$ is [\(Sheriff and](#)

[Geldart, 1995](#)):

$$C_A = \frac{\sum_t^{t+m\Delta t} \left| \sum_{i=1}^N g_{ti} \right|}{t + m\Delta t} \quad (2.16)$$

The average energy of a seismic signal is proportional to the sum of the amplitudes of the signal squared. Referring to equation (2.16), this can be illustrated for a single trace i as

$$\langle E \rangle = C_A^2 \quad (2.17)$$

where g_{ti} is the amplitude of channel i at time t and $\langle E \rangle$ is average energy.

The average provides a measure of reflectivity and allows one to map direct hydrocarbon indicators within a zone of interest.

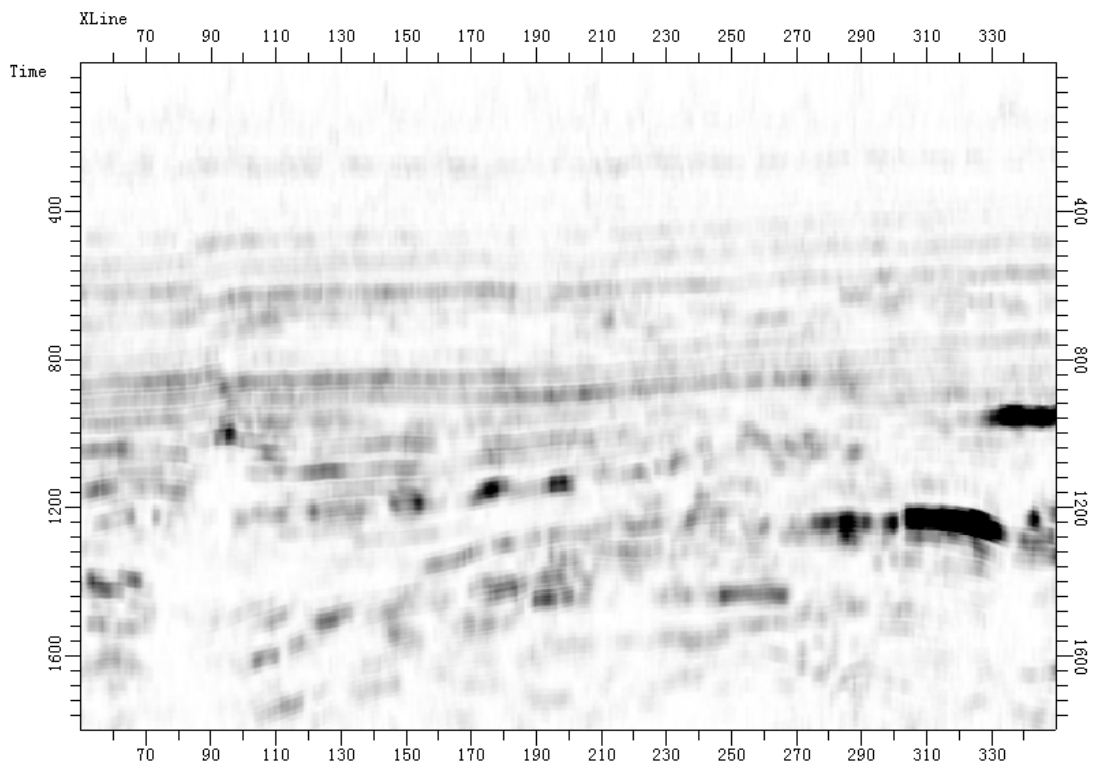


Figure 2.17 Average energy of inline 350 section.

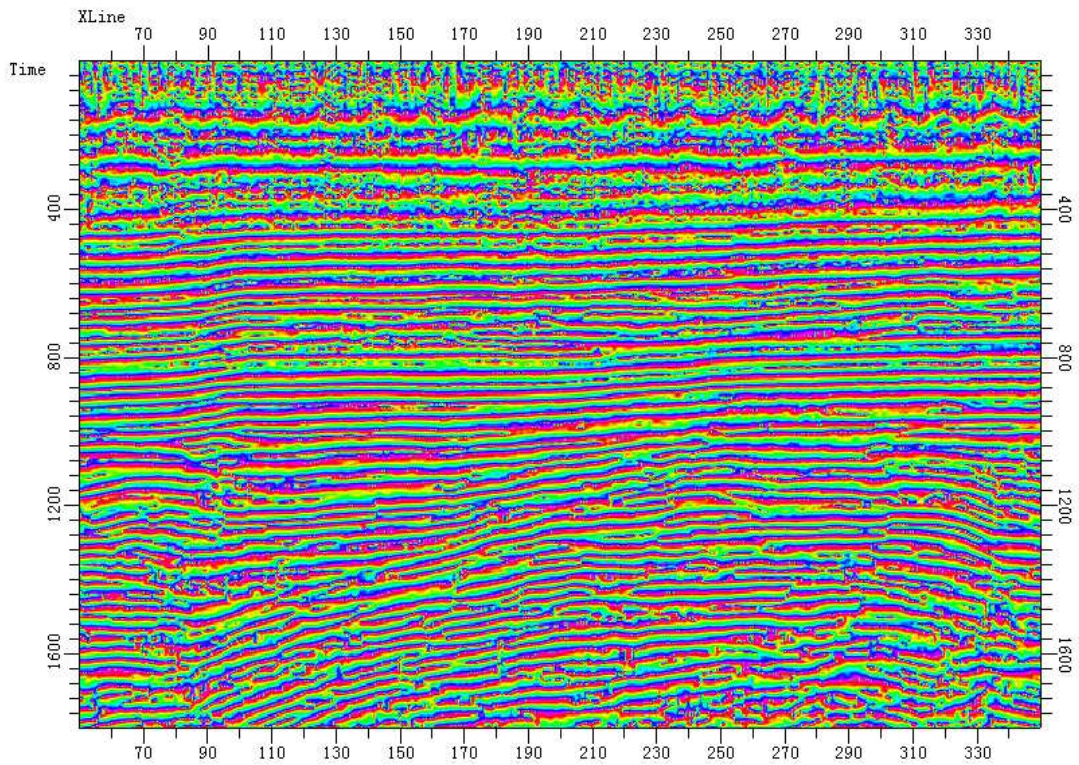


Figure 2.18 Instantaneous phase of inline 350 section.

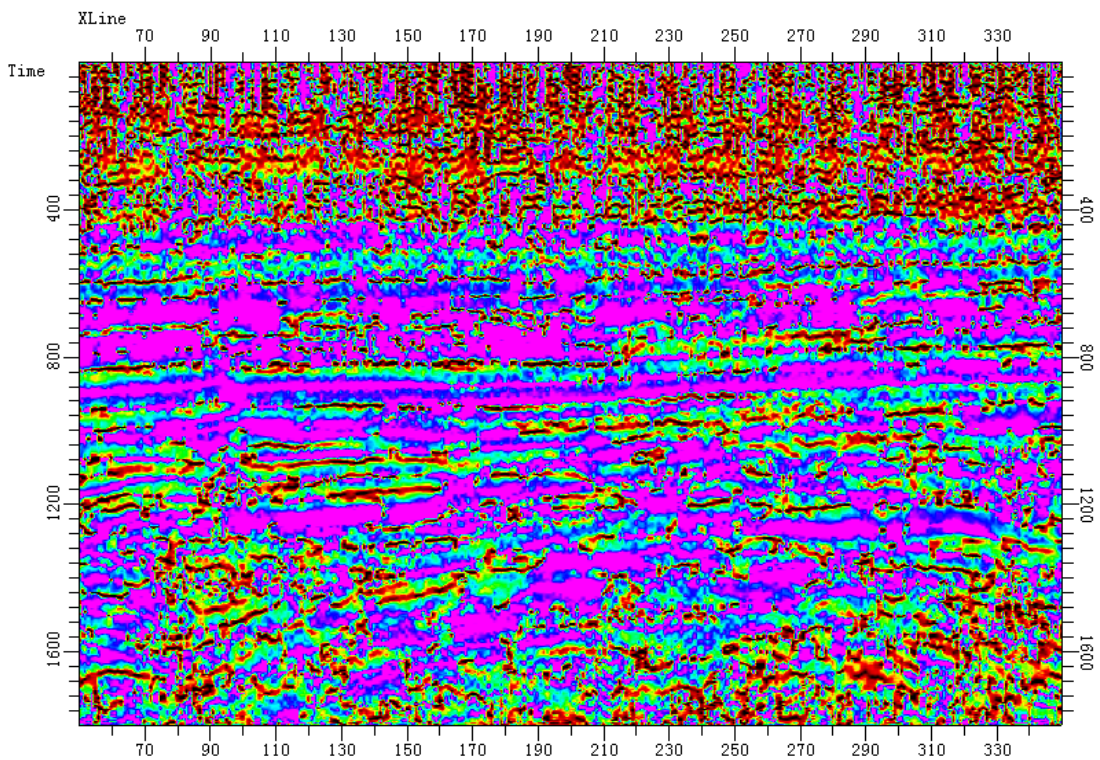


Figure 2.19 Instantaneous frequency of inline 350 section.

2.2.3.3 Instantaneous phase attribute

Instantaneous phase is the angle of lag or lead of the harmonic components of a seismic pulse

with respect to a reference. For example, a zero-phase wave would be symmetric whereas a 90° phase wave would be perfectly asymmetric. Phase is measured from -180° to +180°. After Sheriff and Geldart ([1995](#)), instantaneous phase is given by:

$$\gamma(t) = 2\pi vt = \tan^{-1} \left[\frac{g^H(t)}{g(t)} \right] \quad (2.18)$$

where $g(t)$ is the measured seismic data, and $g^H(t)$ is its Hilbert transform.

The instantaneous phase, shows in Figure 2.18, enhances the continuity of events where amplitude information related with the reflection strength can be variable. Often, it makes weak coherent events appear more clearly. Instantaneous phase is intrinsically related to instantaneous frequency at time t ; therefore, phase anomalies should overlap with areas of lowered instantaneous frequency and in turn low coherence. Phase displays can be used for the regional visualization of stratigraphic features such as faults, angularities, onlaps, and in some cases fluid contacts.

Instantaneous phase attribute is a physical attribute and can be effectively used as a discriminator for geometrical shape classifications:

- Best indicator of lateral continuity;
- Relates to the phase component of the wave-propagation;
- Can be used to compute the phase velocity;
- Has no amplitude information, hence all events are represented;
- Shows discontinuity, but may not be the best;
- Sequence boundaries;
- Detailed visualization of bedding configuration;
- Used in the computation of instantaneous frequency and acceleration.

2.2.3.4 Instantaneous frequency attribute

Instantaneous frequency describes the duration of a seismic pulse and it is commonly subequal to the centroid of the power spectrum of the seismic wavelet ([Taner, 2001](#)). The instantaneous frequency is the time derivative of instantaneous phase if the frequency of the seismic energy is not constant but varies slowly over time. Instantaneous frequency of trace i

at time t is ([Sheriff and Geldart, 1995](#)):

$$v_i(t) = \frac{1}{2\pi} \frac{d}{dt} [\gamma(t)] \quad (2.19)$$

where $\gamma(t)$ is phase. It has been shown that instantaneous frequency (Figure 2.19), computed as the time derivative of instantaneous phase, relates to the centroid of the power spectrum of the seismic wavelet.

Instantaneous frequency relates the wave propagation and depositional environment, hence it is physical attribute and it can be used as effective discriminator:

- Corresponds to the average frequency if the power spectrum of the seismic wavelet;
- Seismic character correlator in lateral direction;
- Indicates the edges of low impedance thin beds;
- Hydrocarbon indicator by low frequency anomaly;
- Fracture zone indicator;
- Chaotic reflection zone indicator;
- Bed thickness indicator;
- Sand/Shale ratio indicator in a clastic environment.

2.2.3.5 Curvature attributes

Curvature attributes are a useful set of attributes that provide images of structure and stratigraphy that complement those seen by the well-accepted coherence algorithms. Being second order derivative measures of surfaces, they can be quite sensitive to noise.

Curvature attributes are a group of post-stack attributes that are computed from the curvature of a specified horizon. These attributes include: magnitude or direction of maximum curvature, magnitude or direction of minimum curvature, magnitude of curvature along the horizon's azimuth (dip) direction, magnitude of curvature along the horizon's strike direction, magnitude of curvature of a contour line along a horizon, and mean curvature (Figure 2.20). Instead of using maximum and minimum curvature, or most-positive and most-negative curvature, attributes which are intuitively easy to understand, simply the use of principal curvatures to image can subtle faults, folds, incised channels, differential compaction, and a

wide range of other stratigraphic features ([Chopra and Marfurt, 2010](#)).

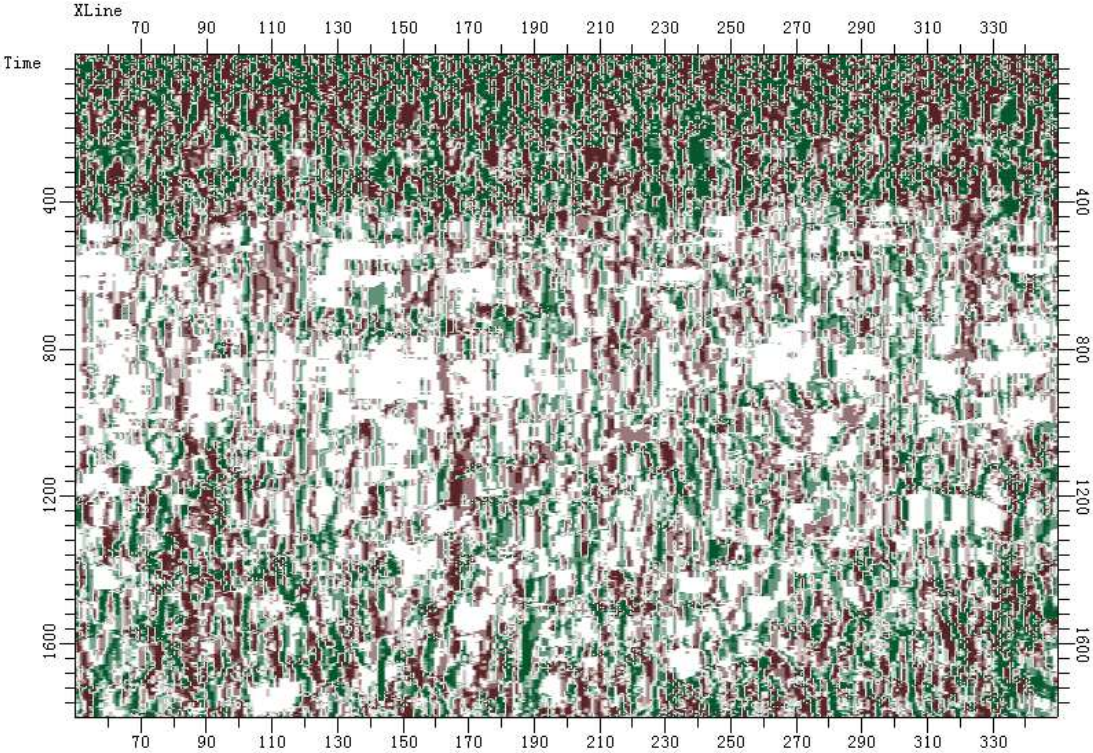


Figure 2.20 Mean curvature of inline 350 section.

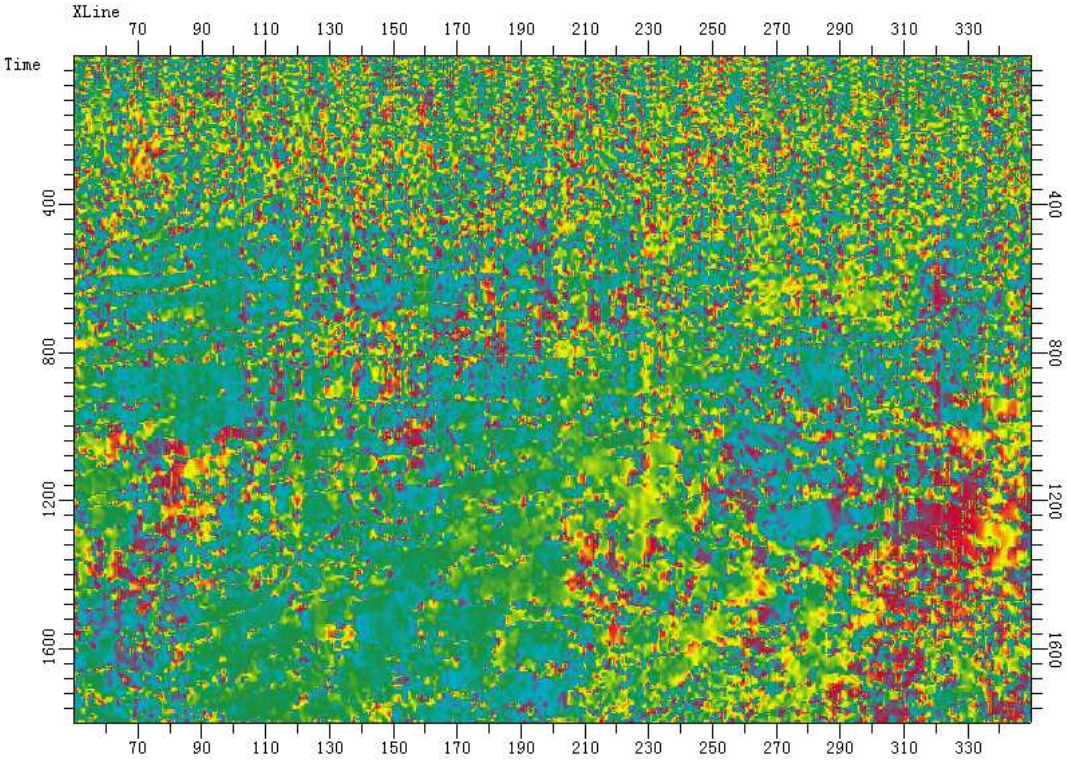


Figure 2.21 Dip azimuth of inline 350 section.

2.2.3.6 Dip and Azimuth attributes

Dip attribute is a post-stack attribute that computes, for each trace, the best fit plane (3D) or line (2D) between its immediate neighbour traces on a horizon and outputs the magnitude of dip (gradient) of said plane or line measured in degrees. It can be used to create a pseudo paleogeologic map on a horizon slice.

Azimuth attribute, shows in Figure 2.21, is a post-stack attribute that computes, for each trace, the best fit plane (3D) between its immediate neighbour traces on a horizon and outputs the direction of maximum slope (dip direction) measured in degrees, clockwise from north. This is not to be confused with the geological concept of azimuth, which is equivalent to strike and is measured 90° counter-clockwise from the dip direction.

2.3 Conclusion

This chapter introduces seismic image and seismic attributes. Over the years Seismic Data Acquisition has become more important than ever for many companies and industries around the globe. During the coming years and into the future this important work will continue. The Seismic Data Acquisition information will help the geoscientists to make accurate maps of the subsurface both the land and the marine areas. With this information the geoscientists can then predict the value of the area and make it more profitable for use in any capacity.

Analysis of the seismic image is powerful tools for us in the understanding the underground. Many methods of image processing and analysis can be used in seismic data; and a lot of new signal processing methods have been developed and applied to exploit properties. Some of the methods are also presented to enhance the structures and reduce the random noise.

Seismic attributes describe seismic data. They are specific measurements of geometric, kinematic, dynamic, or statistical features derived from seismic data. Hundreds of seismic attributes have been invented, computed by a wide variety of methods, including complex trace analysis, interval statistics, correlation measures, Fourier analysis, time-frequency analysis, wavelet transforms, principal components, and various empirical methods. Regardless of the method, attributes are used like filters to reveal trends or patterns, or combined to predict a seismic facies or a property such as porosity. With vast array of seismic attribute volumes, classification and neural network analysis are natural solutions for extraction or identification of seismic objects.

3 Seismic image analysis by Gaussian-Hermite moments

An essential issue in the field of pattern analysis is the recognition of objects and characters regardless of their positions, sizes, and orientations. Moments and functions of moments due to their capabilities to extract invariant global features have been extensively applied in the field of image processing: image analysis and pattern recognition ([Flusser and Suk, 1993](#); [Hu, 1962](#)) with applications ranging from edge detection ([Luo et al., 1993](#)), image classification and segmentation ([Yokoya and Levine, 1989](#)), texture analysis ([Tuceryan, 1994](#)), coherency estimation ([Li et al., 2010a](#)), invariant identification ([Li et al., 2011](#); [Yang and Dai, 2011](#); [Yang et al., 2011](#)), target identification, object classification, image coding and reconstruction ([Teague, 1980](#); [Teh and Chin, 1988](#)), scene analysis ([Jerome, 2009](#); [Sadjadi and Hall, 1978](#)), image reconstruction ([Liao and Pawlak, 1996](#); [Yang and Dai, 2012](#)), and 3D object analysis ([Bronstein et al., 2005](#); [Sadjadi and Hall, 1980](#)).

Generally, global features are invariant under image translation, scale change, and rotation only when they are computed from the original non-distorted analog 2D image ([Liao and Pawlak, 1996](#)). In practice, we observe the digitized, quantized, and often noisy version of the image and the invariance properties are satisfied only approximately. Among all kinds of moments, geometric moments are firstly proposed and have been extensively used due to their simplicity and explicit geometric meaning. However, geometric moments are not orthogonal, so it is difficult to reconstruct an image from them. Teague showed that great efficiency could be acquired when the image was analyzed by orthogonal Legendre and Zernike moments ([Teague, 1980](#)). Moreover, it was proven that Zernike moments could store image information with minimal redundancy and they have the property of being rotation invariants. Since both Legendre and Zernike moments are defined in the continuous domain, the suitable transformations of image coordinates are needed when we implement these moments in the discrete case. As we know, the computation of Legendre moments needs to transform image

coordinates over the interval $[-1, 1]$ and Zernike polynomials are only valid inside the unit circle ([Mukundan and Ramakrishnan, 1998](#)). Besides, the discretization error derived from approximating the integral is still inevitable during their implementations, which definitely limits the accuracy of computed moments ([Liao and Pawlak, 1996](#)). Liao and Pawlak conducted a theoretical analysis on the discretization error of continuous moments and they proposed an approach to keep the error under certain level according to Simpson's rule ([Liao and Pawlak, 1996](#)). Other researches aiming at improving the accuracy of continuous moments are accordingly focused on geometric and Legendre moments ([Hosny, 2007a, b](#)).

Meanwhile, the computational inconvenience of continuous moments encourages the researches in the discrete orthogonal moments. Mukundan first introduced a set of moments to analyze the image basing on the discrete Tchebichef polynomials ([Mukundan et al., 2001](#)). Some techniques for efficiently computing this kind of moment were also provided soon after ([Mukundan, 2004](#)). Another kind of discrete orthogonal moment widely used is Krawtchouk moments, which are based on the discrete classical Krawtchouk polynomials ([Yap et al., 2003](#)). Krawtchouk moments can be employed to extract local features of image unlike other orthogonal moments which generally capture the global features. More recently, the discrete orthogonal Racah and dual Hahn moments were also proposed and introduced to image analysis ([Zhu et al., 2007a](#); [Zhu et al., 2007c](#)). The computation of discrete orthogonal moments does not need any numerical approximations and image coordinates transformations, which generally makes the discrete orthogonal moments superior to conventional continuous orthogonal moments in terms of image representation ability.

3.1 Introduction of moments

The moments have been proposed initially in the theory of statistics. The different orders of moment indicate the different statistical features of a piece-wise continuous function. So, as far as their definitions are concerned, the moments are the representations of the global information of the related function. They are corresponding to the whole information rather than the local or the fixed parts of the function. Here, our discussion is conducted when the object is limited to 2D images. For a 2D image $f(x,y)$ where the function value denotes the intensity at the pixel location (x,y) , we assume ζ is the image region of the x - y plane, or the definition domain of image function $f(x,y)$.

A complete characterization of moment functionals over a class of univariate functions was given by Hausdor ([1921a, b](#)). These results were extended to the 2D case by Hildebrandt and

Schoenberg (1933). The general 2D moment Φ_{pq} of order $(p+q)$ definition, using a moment weighting kernel $\psi_{pq}(x, y)$ (also known as the basis function), and an image intensity function $f(x, y)$, is given by:

$$\Phi_{pq} = \iint_{\zeta} \psi_{pq}(x, y) f(x, y) dx dy, \quad p, q = 0, 1, \dots \quad (3.1)$$

The indices p, q usually denote the degrees of the coordinates x, y respectively, as defined inside the function ψ . So we can construct a *basis set* with all of p and q . According to the equation (3.1), different basis sets can then define different kinds of moment, such as geometric moments, Legendre moments, complex moments, rotational moments, and etc. It is clear that the moments can be regarded as the mapping of the original image function into moment kernels, and this mapping is global and the information represented by each pixel in the function will contribute to the moments. Therefore, the moments can be used to be the feature descriptors of the original image or the concerned objects.

3.1.1 Geometric moments

Geometric moments are defined with the monomial basis set $[x^p, y^q]$. The $(p+q)$ order moment of an image with the intensity function $f(x,y)$ has the definition as

$$m_{pq} = \iint_{\zeta} x^p y^q f(x, y) dx dy \quad (3.2)$$

where ζ denotes the definition domain of $f(x,y)$. A set of moments up to order N consists of all moments m_{pq} such that $0 \leq p+q \leq N$ and if (p,q) are non-negative integers then the set contains $\frac{(N+1)(N+2)}{2}$ elements. Some basic geometric characters can be found in geometric moments.

The zeroth order moment m_{00} generally defines the total mass of $f(x,y)$; The two first order moments, (M_{10}, M_{01}) , provide the position of the center of mass. The second order moments, (M_{20}, M_{11}, M_{02}) , can be used to determine several useful image features such as the principal axes, the image ellipse and the radii of gyration. The centroid coordinates can also be represented by the geometric moments of order 0 and 1 as following:

$$\bar{x} = \frac{m_{10}}{m_{00}} = \frac{\sum_{i=0}^{K-1} \sum_{j=0}^{K-1} x \cdot I(i, j)}{\sum_{i=0}^{K-1} \sum_{j=0}^{K-1} I(i, j)}, \quad \bar{y} = \frac{m_{01}}{m_{00}} = \frac{\sum_{i=0}^{K-1} \sum_{j=0}^{K-1} y \cdot I(i, j)}{\sum_{i=0}^{K-1} \sum_{j=0}^{K-1} I(i, j)}. \quad (3.3)$$

Another character called radius of gyration which often appears in mechanics can be derived

form (m_{00}, m_{20}, m_{02}) . It is a description as the distance from the axis to a line where all the mass may be assumed to be concentrated ([Mukundan and Ramakrishnan, 1998](#)). The central moments corresponding to m_{pq} are defined as follows

$$\mu_{pq} = \iint_{\zeta} (x - \bar{x})^p (y - \bar{y})^q f(x, y) dx dy \quad (3.4)$$

The central moments are substantially the regular geometric moments which correspond to the moments of the image with the origin being shifted to the centroid. The central moments are generally characterized to be translation invariants in general.

3.1.2 Legendre moment

Legendre moment is a set of typical continuous orthogonal moments. Since firstly proposed by Teague in 1980, this kind of moments has demonstrated several superiorities over the traditional geometric moments. It is shown that image reconstruction from Legendre moments is much easier than from geometric moments. The kernels of Legendre moments are products of Legendre polynomials defined along rectangular image coordinate axes inside a square. Legendre moment of order $(p+q)$ is defined as ([Mukundan and Ramakrishnan, 1998](#)):

$$L_{pq} = \frac{(2p+1)(2q+1)}{4} \int_{-1}^1 \int_{-1}^1 P_p(x) P_q(y) f(x, y) dx dy \quad p, q = 0, 1, \dots \quad (3.5)$$

where $P_p(x)$ denotes Legendre polynomial of p^{th} degree

$$P_p(x) = \frac{1}{2^p p!} \frac{d^p}{dx^p} (x^2 - 1)^p \quad (3.6)$$

Certainly, Legendre polynomial can be also expressed as a series of monomials, which has the form as:

$$P_p(x) = \sum_{k=0}^p (-1)^{(p-k)/2} \frac{1}{2^p} \frac{(p+k)! x^k}{\left(\frac{p-k}{2}\right)! \left(\frac{p+k}{2}\right)! k!} \quad |x| \leq 1, (p-k) \text{ is even} \quad (3.7)$$

3.1.3 Zernike moments

Teague first proposed Zernike moments basing on the orthogonal functions called Zernike polynomials. Though computationally very complicated compared to geometric and Legendre moments, Zernike moments have been proved to be superior in terms of their feature

representation capability and low noise sensitivity ([Teh and Chin, 1988](#)). The kernels of Zernike moments are orthogonal Zernike polynomials defined over polar coordinates inside a unit circle. The Zernike moments of order p are defined as:

$$Z_{pq} = \frac{(p+1)}{\pi} \int_0^{2\pi} \int_0^1 V_{pq}^*(r, \theta) f(r, \theta) r dr d\theta, \quad r \leq 1 \quad (3.8)$$

The equation requires p is a non-negative integer and q satisfies the condition $p-|q|$ is even and $|q| \leq p$. Zernike polynomials $V_{pq}(r, \theta)$ of order p are complex functions defined over polar coordinate

$$V_{pq}(r, \theta) = R_{pq}(r) e^{iq\theta}$$

where $R_{pq}(r)$ is a real-valued radial polynomial given by

$$R_{pq}(r) = \sum_{s=0}^{(p-|q|)/2} (-1)^s \frac{(p-s)!}{s! \left(\frac{p-2s+|q|}{2}\right)! \left(\frac{p-2s-|q|}{2}\right)!} r^{p-2s} \quad (3.9)$$

3.1.4 Discrete Tchebichef moments

Discrete Tchebichef moments are the first kind of discrete orthogonal moments. This kind of moments has been proved to be a powerful tool in image analysis and pattern recognition. The discrete Tchebichef polynomials have the explicit expression as ([Mukundan et al., 2001](#))

$$t_p(x) = p! \sum_{k=0}^p (-1)^{p-k} \binom{K-1-k}{p-k} \binom{p+k}{p} \binom{x}{k} \quad p, x = 0, 1, \dots, K-1 \quad (3.10)$$

The polynomials satisfy the orthogonality with $\rho(p, K)$ being defined as

$$\rho(p, K) = (2p)! \binom{K+p}{2p+1} \quad (3.11)$$

Mukundan proposed to normalize the polynomials by the magnitude K^p and still normalize $\rho(p, K)$ by such factor to achieve the orthonormal polynomials as

$$\tilde{t}_p(x) = \frac{t_p(x)}{\beta(p, K)} \quad (3.12)$$

where $\beta(p, K)$ is a suitable constant which is independent of x . With the introduction of $\beta(p, K)$ the corresponding changes are necessary in weight function

$$\tilde{\rho}(p, K) = \frac{\rho(p, K)}{\beta(p, K)^2} \quad (3.13)$$

Then the Tchebichef moments are subsequently defined as

$$T_{pq} = \frac{1}{\tilde{\rho}(p, K)\tilde{\rho}(q, K)} \sum_{x=0}^{K-1} \sum_{y=0}^{K-1} \tilde{t}_p(x) \tilde{t}_q(y) f(x, y) \quad (3.14)$$

3.1.5 Krawtchouk moments

Compared with discrete Tchebichef moments, another kind of discrete orthogonal moments named Krawtchouk moments are widely used. The definition of the p order classical Krawtchouk polynomials is defined as

$$K_n(x; p, K) = \sum_{k=0}^K a_{k,n,p} x^k = {}_2F_1\left(-n, -x, -K; \frac{1}{p}\right) \quad (3.15)$$

where $x, n=0,1,2,\dots,K$. $p \in (0,1)$. ${}_2F_1$ is hypergeometric function and $(a)_k$ is Pochhammer symbol.

Krawtchouk polynomials form a complete set of discrete basis functions with weight function

$$w(x; p, K) = \binom{K}{x} p^x (1-p)^{K-x} \quad (3.16)$$

and the orthogonality can be expressed by the equation

$$\sum_{x=0}^K w(x; p, K) K_n(x; p, K) K_m(x; p, K) = \rho(n; p, K) \delta_{nm} \quad (3.17)$$

With

$$\rho(n; p, K) = (-1)^n \left(\frac{1-p}{p}\right)^n \frac{n!}{(-K)_n} \quad (3.18)$$

Yap firstly introduced Krawtchouk moments which base on a weighted version of Krawtchouk polynomials

$$\hat{K}_n(x; p, K) = K_n(x; p, K) \sqrt{\frac{w(x; p, K)}{\rho(n; p, K)}} \quad (3.19)$$

The weighted Krawtchouk polynomials are orthonormal because they satisfy the condition

$$\sum_{x=0}^K \hat{K}_n(x; p, K) K_m(x; p, K) = \delta_{nm} \quad (3.20)$$

The Krawtchouk moments of order $(n+m)$ in terms of weighted Krawtchouk polynomials, for an image with intensity function $f(x,y)$ is defined as:

$$Q_{nm} = \sum_{x=0}^{K-1} \sum_{y=0}^{L-1} \hat{K}_n(x; p_1, K-1) K_m(y; p_2, L-1) f(x, y) \quad (3.21)$$

3.1.6 Orthogonal Gaussian-Hermite moments

Gaussian-Hermite moments, which were firstly proposed by Shen(1997), are also a kind of orthogonal moments and their applications in image analysis have been also explored in the past decade.

The p^{th} order of Hermite polynomial defined as:

$$H_p(x) = (-1)^p \exp(x^2) (d^p / dx^p) \exp(-x^2) \quad (3.22)$$

Or in a form of series

$$H_p(x) = \sum_{k=0}^{\lfloor p/2 \rfloor} \frac{(-1)^k p!}{k!(p-2k)!} (2x)^{p-2k} \quad (3.23)$$

Hermite polynomials are orthogonal with respect to the weight function $w(x)=\exp(-x^2)$. Their orthogonality is presented by:

$$\int_{-\infty}^{\infty} \exp(-x^2) H_p(x) H_q(x) dx = 2^p p! \sqrt{\pi} \delta_{pq} \quad (3.24)$$

The recursive equation is available for fast computation of the polynomials:

$$H_{p+1}(x) = 2x \cdot H_p(x) - 2p \cdot H_{p-1}(x) \text{ for } p \geq 1 \quad (3.25)$$

with the initial conditions $H_0(x)=1$ and $H_1(x)=2x$. Eq. (3.24) shows that Hermite polynomial is orthogonal but not orthonormal. Its weighted form is then proposed as:

$$\hat{H}_p(x) = (2^p p! \sqrt{\pi})^{-1/2} \exp(-x^2/2) H_p(x) \quad (3.26)$$

According to Equation (3.22), Equation (3.26) is then orthonormal and it is substantially a Hermite polynomial modulated by a Gaussian function with the variance equal to 1.0. For a general case, Gaussian-Hermite polynomial with scale parameter σ has the following

definition:

$$\hat{H}_p(x; \sigma) = (2^p p! \sqrt{\pi} \sigma)^{-1/2} \exp(-x^2 / 2\sigma^2) H_p(x / \sigma) \quad (3.27)$$

and it is not difficult to verify that Gaussian-Hermite polynomial keeps the orthogonality

$$\int_{-\infty}^{\infty} \hat{H}_p(x; \sigma) H_q(x; \sigma) dx = \delta_{pq} \quad (3.28)$$

The equation indicates that Gaussian-Hermite polynomials are not only orthogonal but also orthonormal. Besides the orthonormal property, Gaussian-Hermite polynomial also inherits the symmetry property of Hermite polynomial. To the p^{th} degree Hermite polynomial, it satisfies the symmetry condition

$$H_p(-x) = (-1)^p H_p(x) \quad (3.29)$$

According Equation(3.29), it is obvious that Gaussian-Hermite polynomial also satisfies the corresponding condition

$$\hat{H}_p(x; \sigma) = (-1)^p H_p(x; \sigma) \quad (3.30)$$

3.2 Coherency estimation based on spectral Gaussian-Hermite moments

The process of identifying regions with similar texture and separating regions with different texture is an essential step towards identifying surfaces and objects. Texture analysis has been studied for a long time using various approaches. Various methods perform texture analysis directly upon the gray levels in an image. Coherency estimation in local region is one of the methods to identify regions. Mihran Tuceryan proposes a method of obtaining texture features directly from the gray-level image by computing the geometric moments of the image in local regions ([Tuceryan, 1994](#)). Some acceptable techniques for measuring coherence are based on cross correlation ([Bahorich and Farmer, 1995](#)), eigenstructure of the covariance matrix techniques ([Gersztenkorn and Marfurt, 1999](#); [Marfurt et al., 1999](#)), semblance based coherency ([Marfurt et al., 1998](#)), gradient structure tensor ([Bakker, 2002](#)). These methods, however, typically suffer from a lack of robustness, especially when dealing with noisy data ([Marfurt et al., 1999](#)). Randen et al. address an approach exploiting the spatial derivatives of the data. They measure the disorder of the gradient vector field caused by discontinuities ([Randen et al., 2000](#)).

3.2.1 Discrete implementation of Gaussian-Hermite moments

The Gaussian-Hermite moments of order (p, q) can be defined over the domain $(-\infty \leq x, y \leq \infty)$ as:

$$\eta_{p,q} = \int_{-\infty}^{\infty} \int_{-\infty}^{\infty} \hat{H}_p(x/\sigma) H_q(y/\sigma) f(x, y) dx dy \quad (3.31)$$

where $f(x, y)$ is the image intensity function.

The Gaussian-Hermite functions are orthogonal over the domain $(-\infty, \infty)$. For a digital image $I(i, j)$ defined over a square $[0 \leq i, j \leq K-1]$, in order to choose easily a comparable standard variation value σ for the Gaussian envelope, the image coordinates would be normalized to be within $[-1 \leq x, y \leq 1]$ firstly by

$$\begin{cases} x = (2i - K + 1) / (K - 1) \\ y = (2j - K + 1) / (K - 1) \end{cases} \quad (3.32)$$

Equation is therefore modified with a scale coefficient $1/\sqrt{(K-1)/2}$ as follows:

$$\begin{cases} \hat{H}_p(i) = [(K-1)/2]^{-1/2} H_p(x/\sigma) [2^{p-1}(K-1)p!\sqrt{\pi}\sigma]^{-1/2} \exp(-x^2/2\sigma^2) H_p(x/\sigma) \\ \hat{H}_q(j) = [(K-1)/2]^{-1/2} H_q(y/\sigma) [2^{q-1}(K-1)q!\sqrt{\pi}\sigma]^{-1/2} \exp(-y^2/2\sigma^2) H_q(y/\sigma) \end{cases} \quad (3.33)$$

Given the discrete Gaussian-Hermite moments, $\eta_{p,q}$, of a gray scale image $I(i, j)$ as follows:

$$\eta_{p,q} = \sum_{i=0}^{K-1} \sum_{j=0}^{K-1} \hat{H}_p(i) H_q(j) I(i, j) \quad (3.34)$$

or

$$\eta_{p,q} = \frac{4}{(K-1)^2} \sum_{i=0}^{K-1} \sum_{j=0}^{K-1} \hat{H}_p(x/\sigma) H_q(y/\sigma) I(i, j) \quad (3.35)$$

3.2.2 Representation program of 2D Gaussian-Hermite moments

Computing the discrete version of Gaussian-Hermite polynomials is the key step of discrete implementation. When represented by the program, the polynomial computation is illustrated by the following pseudo-code.

The algorithm for computing the moments is also illustrated by similar pseudo-codes. It should be noted that these algorithms can be more efficiently facilitated by matrix form supported by the software as MATLAB.

Table 3.1 Pseudo code of Gaussian-Hermite polynomial computation

```


$$C_0 = 1 / \sqrt{\sqrt{\pi} \sigma_N (K-1) / 2}$$

For  $i = 0$  to  $K-1$ 
     $x_i = (2i - K + 1) / (K - 1) / \sigma_N$ 
     $\hat{H}_0(i) = C_0 \cdot \exp(-x_i^2 / 2)$ 
     $\hat{\hat{H}}_1(i) = 2x_i H_0(i)$ 
For  $p = 2$  to  $N$ 
     $\hat{\hat{H}}_p(i) = 2x_i H_{p-1}(i) - 2(p-1)H_{p-2}(i)$ 
End for
End for
 $c = 1$ 
For  $p = 1$  to  $N$ 
     $c = c / \sqrt{2^p}$ 
For  $i = 0$  to  $K-1$ 
     $\hat{\hat{H}}_p(i) = c \cdot H_p(i)$ 
End for
End for

```

Table 3.2 Pseudo code of Gaussian-Hermite moments computation

```

For  $q = 0$  to  $N$ 
    For  $i = 0$  to  $K-1$ 
         $Sum = 0.0$ 
        For  $j = 0$  to  $K-1$ 
             $Sum = Sum + Img(i, j) \times \hat{H}_q(j)$ 
        End for
        For  $p = 0$  to  $N$ 
             $Mom(p, q) = Mom(p, q) + Sum \times \hat{H}_p(i)$ 
        End for
    End for
End for

```

With the appearance of more powerful computers, it becomes practical to compute and use

the higher order moments. However, the computation of moments, specifically, if the higher order moments are involved, is still a time consuming procedure. Moment computation can still be efficiently accomplished by separate property of basis functions. For example, when a set of moments of order (0,0) up to (N, N) is required, it generally needs a quadruple loop to traverse all pixels (0 to K-1) and moment depth (0 to N) in both x and y directions. However, the separate property enables us to compute the moment by firstly calculating the moment of each row and then obtaining the final moment value from the pixels of each column and the weighted moment of each row. Besides, the loop computation for the moments of order 0 to N in x direction is independent of that for traversing all pixels (0, K-1) in y direction; so does the loop computation of order in y direction and all pixels in x direction. The moment computation for all moments of order 0 to N in x direction can be therefore calculated cascadelly in the same loop degree where the moment of each row is executed. The great efficiency is acquired for computing the moments because the method actually needs a triple loop instead of quadruple one to accomplish the computation. The moments up to order (N, N) can be computed by the algorithm below.

According to the above algorithms, we can conclude that moment computation has the same computational complexity and they generally contain the same number of addition and multiplication operations.

3.2.3 Coherency estimation by spectral Gaussian-Hermite moments

We regard the intensity image as a function of two variables: $I(x,y)$. For each pixel in the image, we select a small local window around it. The local image is firstly converted from spatial domain into frequency domain using 2D discrete fast Fourier transform (FFT) function:

$$I_f(u,v) = FFT\{I(x,y)\} \quad (3.36)$$

Energy of Fourier transform can be calculated by:

$$E(u,v) = |I_f(u,v)|^2 \quad (3.37)$$

Then the spectrum Gaussian-Hermite central moments is computed as follows:

$$\tilde{\eta}_{p,q} = \sum_u \sum_v \hat{H}_p(u-\bar{u})H_q(v-\bar{v})E(u,v) \quad (3.38)$$

where denote centroid's coordinates of the image given by:

$$\bar{u} = \frac{m_{1,0}}{m_{0,0}}, \bar{v} = \frac{m_{0,1}}{m_{0,0}}$$

Now, we compute the lower order moments $\tilde{\eta}_{1,1}$, $\tilde{\eta}_{0,2}$ and $\tilde{\eta}_{2,0}$. Constructed the spectral Gaussian-Hermite moments matrix (SGMM) form as:

$$C = \begin{bmatrix} \tilde{\eta}_{2,0} & \tilde{\eta}_{1,1} \\ \tilde{\eta}_{1,1} & \tilde{\eta}_{0,2} \end{bmatrix} \begin{bmatrix} \sum_u \sum_v E(u,v) \cdot u^2 & \sum_u \sum_v E(u,v) \cdot u \cdot v \\ \sum_u \sum_v E(u,v) \cdot u \cdot v & \sum_u \sum_v E(u,v) \cdot v^2 \end{bmatrix} \quad (3.39)$$

We assume that the eigenvalues of matrix C are ordered, i.e. . We use the following contrast coefficient to measure coherency:

$$C_{coh} = \frac{\lambda_2}{\lambda_1} \quad (3.40)$$

It takes value between 0 and 1, meanwhile indicates how much the local data resembles a linear structure. The more isotropic a structure becomes ($C_{coh} \rightarrow 1$), the more difficult it becomes to estimate the orientation of that structure. We use C_{coh} as the coherency measure of the orientation estimation. Since a linear structure can also be viewed of as an anisotropic structure, C_{coh} is also referred to as the anisotropy.

3.2.4 Experimental results

We use two synthesized images to test the method. Both two synthesized images we select small local window at 9 by 9 and 17 by 17. Meanwhile we contrast the coherency of results from based on geometric moments and from based on Gaussian-Hermite moments.

The scale parameter of Gaussian envelope is selected 0.2681 in small local window at 9 by 9, and 0.1468 in another case. Figure 3.1 shows the coherency results of the first synthesized image. Then another synthesized image is showed in Figure 3.2. On two synthesized images we add noises to test the method. Figure 3.3 (a) and (d) are added zero mean Gaussian white noise with variance 0.01. Figure 3.4 (a) and (d) are added zero mean Gaussian white noise with variance 0.02. In all the cases we calculate local coherency with window 17 by 17. The σ is selected 0.1468.

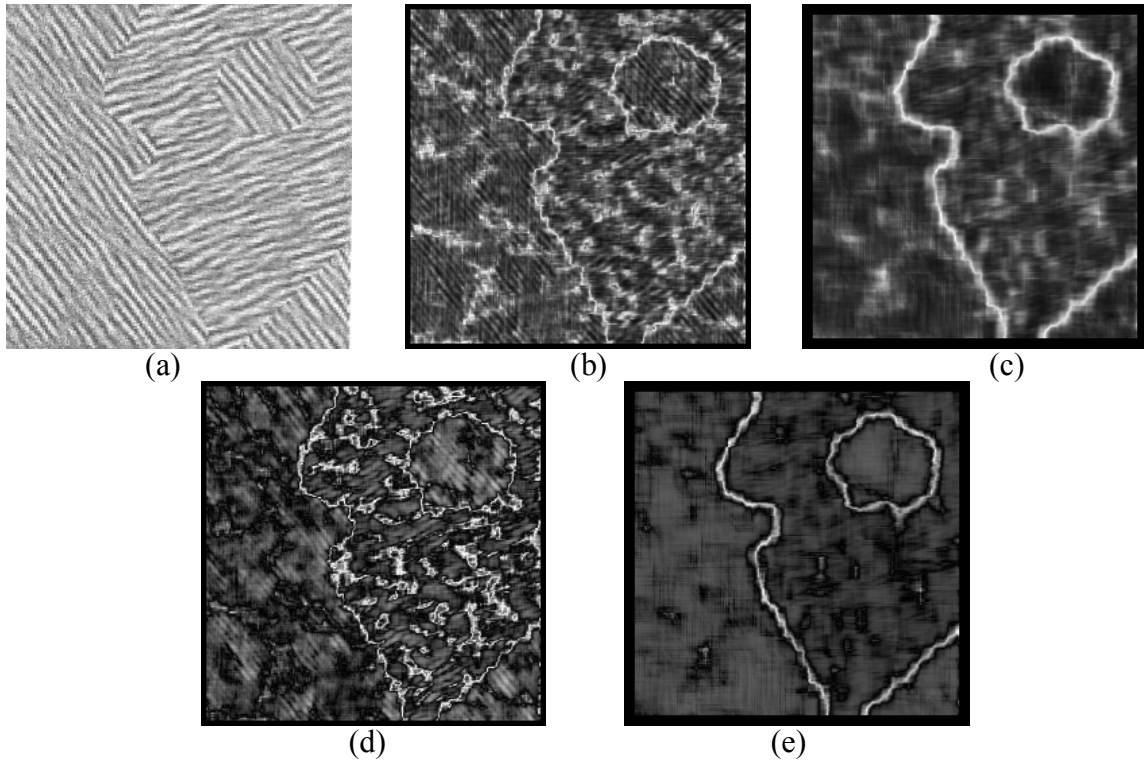


Figure 3.1 Coherency estimation Results for first synthesized block.

(a) Original image ; (b) local window 9×9 and (c) local window 17×17 are computed the coherency based on geometric moments; (d) local window 9×9 and (e) local window 17×17 are computed the coherency based on Gaussian-Hermite moments.

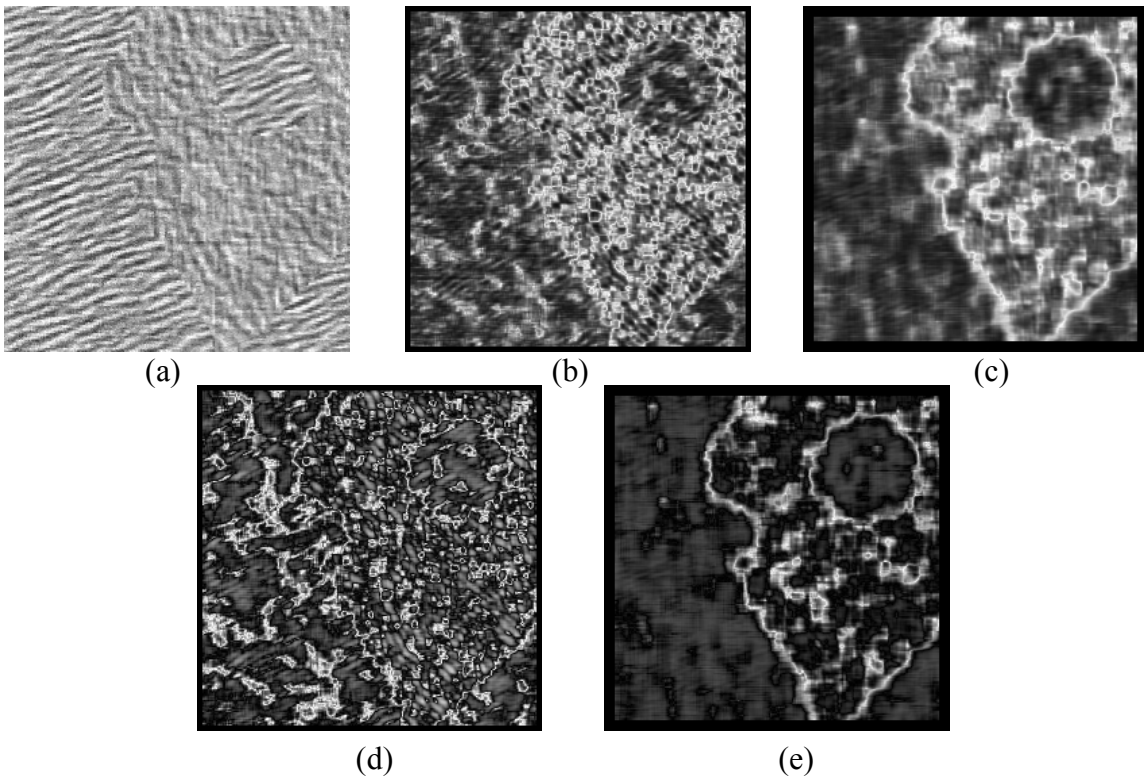


Figure 3.2 Coherency estimation Results for second synthesized block.

(a) Original image , (b) local window 9×9 and (c) local window 17×17 are computed the coherency based on geometric moments ; (d) local window 9×9 and (e) local window 17×17 are computed the coherency based on Gaussian-Hermite moments.

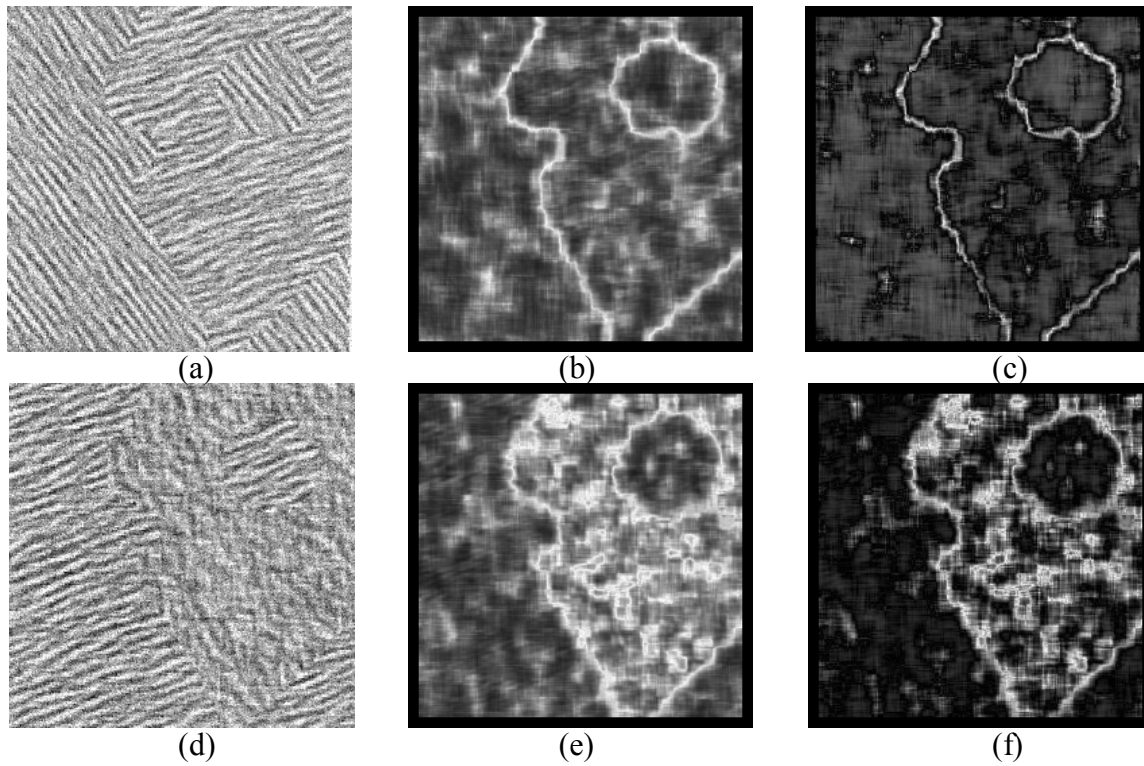


Figure 3.3 Results for synthesized block with zero mean Gaussian white noise with variance 0.01.

(a) and (d) are added noise, (b) and (e) are Coherency based on geometric moments computing, (c) and (f) is Coherency based on Gaussian-Hermite moments computing.

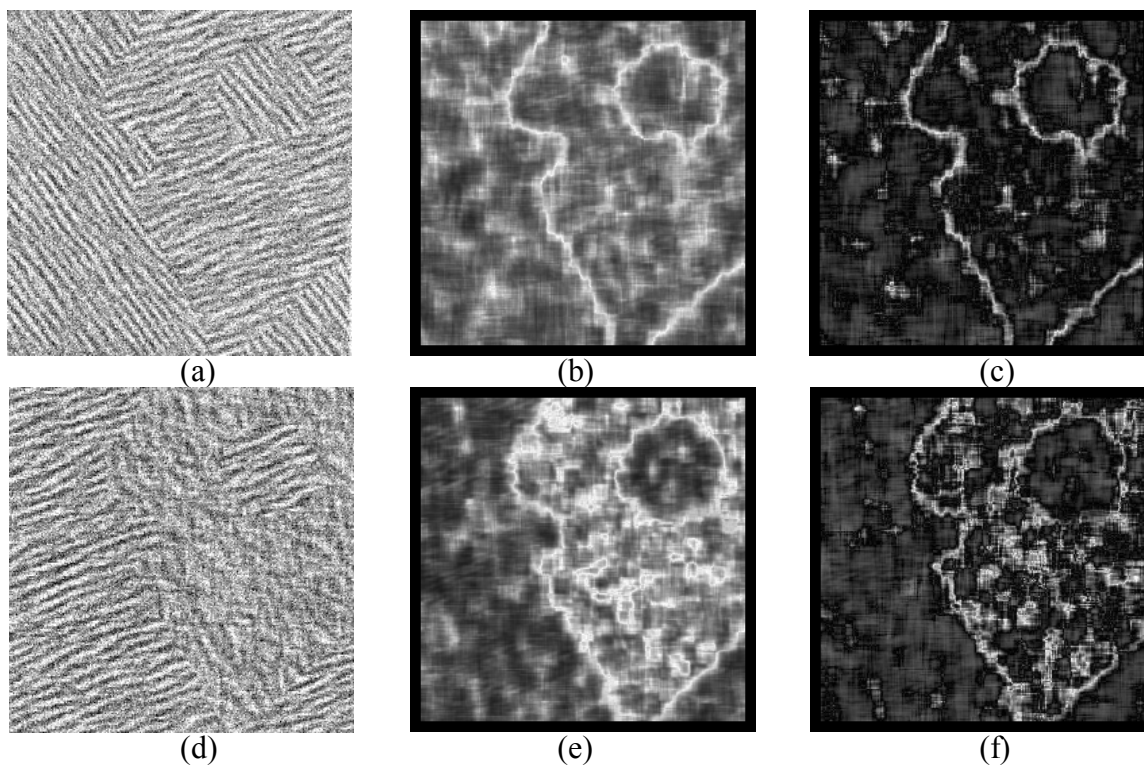


Figure 3.4 Results for synthesized block with zero mean Gaussian white noise with variance 0.02.

(a) and (d) are added noise , (b) and (e) are Coherency based on geometric moments computing, (c) and (f) is Coherency based on Gaussian-Hermite moments computing.

In this section, we have proposed an approach for estimating the coherency of texture that is based on the spectrum Gaussian-Hermite moments. We give an introduction of the Gaussian-Hermite moments and its discrete implementation. And then present the way using the moments of the first order and the second order to estimate the coherency within a small local window in Fourier domain. Finally we test the competence of the approach with the synthesized images and the images added Gaussian noise. In this new method the size of the window and the value of σ are important. As the window size gets larger, more global features are detected. This suggests that the choice of window size could possibly be tied to the contents of the image. The images with larger texture tokens would require larger window sizes whereas finer textures would require smaller windows.

3.3 Multi-scale image description with rotation invariants of Gaussian-Hermite moments

Since the early 1960s of the last century, the moment invariants play an important rule in image analysis and pattern recognition. As we all know, the 7 famous Hu's invariants based on second and third-order geometric moments are widely used as a good feature set to represent an object pattern or an image ([Dudani et al., 1977](#); [Hu, 1962](#); [Wong and Hall, 1978](#)). So far, the most popular moment invariants are still derived from geometric moments ([Li, 1992](#); [Wong et al., 1995](#)). A few years ago, Flusser has proved how to find the independent and complete set of geometric moment invariants corresponding to a given order ([Flusser et al., 2009](#)). It looks to be an almost perfect answer to the derivation of geometric moment invariants.

The problem of image reconstruction from its statistical moments is particularly interesting to researchers in the domain of image processing and pattern recognition. Compared to geometric moments, the orthogonal moments offer the ability to recover much more easily the image due to their orthogonality, which allows reducing greatly the complexity of computation in the phase of reconstruction. Gaussian-Hermite moments is proposed for image analysis recently. For example, the image reconstruction from its orthonormal Gaussian-Hermite moments has already been studied ([Wang and Dai, 2007](#)); Yang and Dai focus their attention on image reconstruction from the Gaussian-Hermite moment ([Yang and Dai, 2012](#)). We introduce a new image analysis and representation method by Gaussian-Hermite rotation and translation moment invariants from geometric moments ([Li et al., 2011](#); [Yang and Dai, 2011](#); [Yang et al., 2011](#)). It is proved that if we have a rotation invariant derived from the geometric moments, we can simply substitute Gaussian-Hermite moments instead of the

geometric moments into it and its rotation invariance remains preserved. Moreover, in the Gaussian-Hermite moment definition, there is a scale parameter which allows us to perform a multi-scale analysis and use more information to represent the object or image.

Translation, rotation and scaling (TRS) are the simplest transformations of spatial coordinates. TRS, sometimes called similarity transform, is a four-parameter transform, which can be described as:

$$\mathbf{x}' = s\mathbf{R} \cdot \mathbf{x} + \mathbf{t}, \quad (3.41)$$

where \mathbf{t} is a translation vector, s is a positive scaling factor (note that here we consider uniform scaling only, i.e. s is the same, both in horizontal and vertical directions), and \mathbf{R} is a rotation matrix:

$$\begin{bmatrix} \cos \theta & -\sin \theta \\ \sin \theta & \cos \theta \end{bmatrix}$$

where θ is the angle of rotation.

Invariance with respect to TRS is required in almost all practical applications, because the object should be correctly recognized, regardless of its position and orientation in the scene and of the object-to-camera distance. On the other hand, the TRS model is a sufficient approximation of the actual image deformation if the scene is flat and perpendicular to the optical axis. Therefore, much attention has been paid to TRS invariants. While translation and scaling invariants can be derived in an intuitive way, derivation of invariants to rotation is far more complicated.

3.3.1 Central Gaussian-Hermite moments

From the equation (3.3) and equation (3.35), we could define the central Gaussian-Hermite moments of $I(i,j)$ as following by

$$\tilde{\eta}_{pq} = \frac{4}{(K-1)^2} \sum_{i=0}^{K-1} \sum_{j=0}^{K-1} \hat{H}_p \left(\frac{x-\bar{x}}{\sigma} \right) H_q \left(\frac{y-\bar{y}}{\sigma} \right) I(i,j) \quad (3.42)$$

3.3.2 Rotation Gaussian-Hermite moment invariants

Given an image rotated by an arbitrary angle, the new Cartesian coordinates after rotation are satisfied with the following equation:

$$\begin{bmatrix} x' \\ y' \end{bmatrix} = \begin{bmatrix} \cos \theta & -\sin \theta \\ \sin \theta & \cos \theta \end{bmatrix} \begin{bmatrix} x \\ y \end{bmatrix} \quad (3.43)$$

After this rotation, Gaussian-Hermite moments have the form as:

$$M_{pq}^\theta = \int_{-\infty}^{\infty} \int_{-\infty}^{\infty} f(x, y) H_p(x'/\sigma) H_q(y'/\sigma) \exp\left(-\frac{x'^2 + y'^2}{2\sigma^2}\right) dx dy. \quad (3.44)$$

It should be noted here that the image intensity function remains unchanged during image rotation, 2D Gaussian function and integral element also. From (12) and (13), the relation between and can be derived. Here we give them only for the 3 first orders:

$$\begin{aligned} M_{00}^\theta &= M_{00}, \\ M_{01}^\theta &= \sin \theta M_{10} + \cos \theta M_{01}, \\ M_{10}^\theta &= \cos \theta M_{10} - \sin \theta M_{01}, \\ M_{02}^\theta &= \sin^2 \theta M_{20} - 2 \sin \theta \cos \theta M_{11} + \cos^2 \theta M_{02}, \\ M_{20}^\theta &= \cos^2 \theta M_{20} + 2 \sin \theta \cos \theta M_{11} + \sin^2 \theta M_{02}, \\ M_{11}^\theta &= \sin \theta \cos \theta (M_{20} - M_{02}) + (\cos^2 \theta - \sin^2 \theta) M_{11}, \\ M_{03}^\theta &= \sin^3 \theta M_{30} - 3 \sin^2 \theta \cos \theta M_{21} + 3 \sin \theta \cos^2 \theta M_{12} + \cos^3 \theta M_{03}, \\ M_{30}^\theta &= \cos^3 \theta M_{30} + 3 \cos^2 \theta \sin \theta M_{21} - 3 \cos \theta \sin^2 \theta M_{12} + \sin^3 \theta M_{03}, \\ M_{12}^\theta &= \sin \theta \cos \theta (\sin \theta M_{30} - \cos \theta M_{03}) + (2 \sin \theta \cos^2 \theta - \sin^3 \theta) M_{21} \\ &\quad + (\cos^3 \theta - 2 \sin^2 \theta \cos \theta) M_{12}, \\ M_{21}^\theta &= \sin \theta \cos \theta (\cos \theta M_{30} + \sin \theta M_{03}) + (\cos^3 \theta - 2 \sin^2 \theta \cos \theta) M_{21} \\ &\quad + (\sin^3 \theta - 2 \sin \theta \cos^2 \theta) M_{12}. \end{aligned} \quad (3.45)$$

The rotation invariants, therefore, can be obtained by eliminating the angle factor θ in the combination of above equations. Some invariants can be easily found with simple form such as M_{00} and $M_{10}^2 + M_{01}^2$. Other invariants of order 2 and 3 which we have derived are given as follows:

$$\begin{aligned} I_1 &= M_{20} + M_{02}, \\ I_2 &= (M_{30} + M_{12})^2 + (M_{03} + M_{21})^2, \\ I_3 &= (M_{20} - M_{02}) \left[(M_{30} + M_{12})^2 - (M_{03} + M_{21})^2 \right] \\ &\quad + 4M_{11}(M_{30} + M_{12})(M_{03} + M_{21}), \\ I_4 &= M_{11} \left[(M_{30} + M_{12})^2 - (M_{03} + M_{21})^2 \right] \\ &\quad - (M_{20} - M_{02})(M_{30} + M_{12})(M_{03} + M_{21}), \\ I_5 &= (M_{30} - 3M_{12})(M_{30} + M_{12}) \left[(M_{30} + M_{12})^2 - 3(M_{03} + M_{21})^2 \right] \\ &\quad + (M_{03} - 3M_{21})(M_{03} + M_{21}) \left[(M_{03} + M_{21})^2 - 3(M_{30} + M_{12})^2 \right], \\ I_6 &= (M_{30} - 3M_{12})(M_{03} + M_{21}) \left[(M_{03} + M_{21})^2 - 3(M_{30} + M_{12})^2 \right] \\ &\quad + (3M_{21} - M_{03})(M_{30} + M_{12}) \left[(M_{30} + M_{12})^2 - 3(M_{03} + M_{21})^2 \right]. \end{aligned} \quad (3.46)$$

From above derivation, we have found an interesting fact: these invariants have the exact form of the geometric ones. Is it true for all invariants of all orders? In other words, can we replace the geometric moments with the Gaussian-Hermite ones in any geometric moment invariant and its rotation invariance remains preserved? The answer is positive and it can be proved by mathematical induction ([Yang et al., 2011](#)). The rotation Gaussian-Hermite invariants of order 4 are then given as follows:

$$\begin{aligned}
I_7 &= M_{40} + 2M_{22} + M_{04}, \\
I_8 &= (M_{40} - M_{04}) \left[(M_{30} + M_{12})^2 - (M_{21} + M_{03})^2 \right] + 4(M_{31} + M_{13})(M_{30} + M_{12})(M_{03} + M_{21}), \\
I_9 &= (M_{31} + M_{13}) \left[(M_{30} + M_{12})^2 - (M_{03} + M_{21})^2 \right] - (M_{40} - M_{04})(M_{30} + M_{12})(M_{03} + M_{21}), \\
I_{10} &= (M_{40} - 6M_{22} + M_{04}) \left[(M_{30} + M_{12})^4 - 6(M_{30} + M_{12})^2(M_{03} + M_{21})^2 + (M_{03} + M_{21})^4 \right] \\
&\quad + 16(M_{31} - M_{13})(M_{30} + M_{12})(M_{03} + M_{21}) \left[(M_{30} + M_{12})^2 - (M_{03} + M_{21})^2 \right], \\
I_{11} &= (M_{40} - 6M_{22} + M_{04})(M_{30} + M_{12})(M_{03} + M_{21}) \left[(M_{03} + M_{21})^2 - (M_{30} + M_{12})^2 \right] \\
&\quad + (M_{31} - M_{13}) \left[(M_{30} + M_{12})^4 - 6(M_{30} + M_{12})^2(M_{03} + M_{21})^2 + (M_{03} + M_{21})^4 \right].
\end{aligned} \tag{3.47}$$

3.3.3 Translation Gaussian-Hermite moment invariants

It is well known that under the translation of coordinates on the Cartesian plan

$$\begin{cases} x' = x + a \\ y' = y + b \end{cases} \text{ with } a, b : \text{ constants} \tag{3.48}$$

The central moments do not change whatever the basis function of moments. Therefore, if $a = -\bar{x}$ and $b = -\bar{y}$, the rotation and translation Gaussian-Hermite moment invariants could be easily obtained by use of the central Gaussian-Hermite moments $\tilde{\eta}_{pq}$ instead of η_{pq} in (3.46) and (3.47).

3.3.4 Multi-scale analysis

In the computation of Gaussian-Hermite moments, there is an important scale parameter σ . Given a σ , we could obtain a set of invariants. Therefore, we can define different sets of invariants with the different scale parameter and perform a multi-scale analysis that allows us to obtain more information of the image and to better characterize the image.

3.3.5 Experimental results

Figure 3.5 shows the 8 versions of image Mirage2000 rotated by different angles and translated in different positions in the background. Their 11 invariants are computed with different scale parameter respectively and recorded in Table 3.3. The percentage spread from the corresponding means of invariants $\xi/|\mu|$ is used to evaluate the numerical stability. Here, ξ and μ represent respectively the standard deviation and the mean of the computed values of an invariant for different versions of the image. Small value of $\xi/|\mu|$ shows the better stability of invariants; on the contrary, great value indicates the increment of instability. In this example all deviations are less than 5%, the Gaussian- Hermite moment invariants show a good stability.

In Figure 3.6 the two first rows show the reference images of fight planes CY47, F22, F35, J10, MIG1.44 and Mirage2000, in the third row, there are three patterns to identify. We try to match P1, P2 and P3 respectively on the reference images. Each image is characterized by a feature vector composed of its Gaussian-Hermite moment invariants.

Finally, the weighted Euclidean distance (WED) is used to evaluate the results of matching. The WED between two vectors is defined as

$$d(\mathbf{V}', \mathbf{V}^{(k)}) = \sqrt{\sum_{n=1}^N \rho_n (I'_n - I_n^{(k)})^2} \quad (3.49)$$

Where \mathbf{V}' is the feature vector of a pattern to identify, $\mathbf{V}^{(k)}$ is the feature vector of k-th reference image with

$$\rho_n = K / \sum_{k=1}^K (I_n^{(k)} - \bar{I}_n)^2 \quad \text{and} \quad \bar{I}_n = \sum_{k=1}^K I_n^{(k)} / K,$$

here $N=11$ and $K=3$. The pattern will be identified as a certain fight plane in the reference if their WED is the minimum. The different scale parameters ($\sigma = 0.2, 0.4$ and 0.7) used in Gaussian-Hermite moment computation.

The matching results are reported in Figure 3.7, from which we know that with three different scale parameters, all three patterns are identified correctly as P1 = F22, P2 = J10 and P3 = MIG1.44.

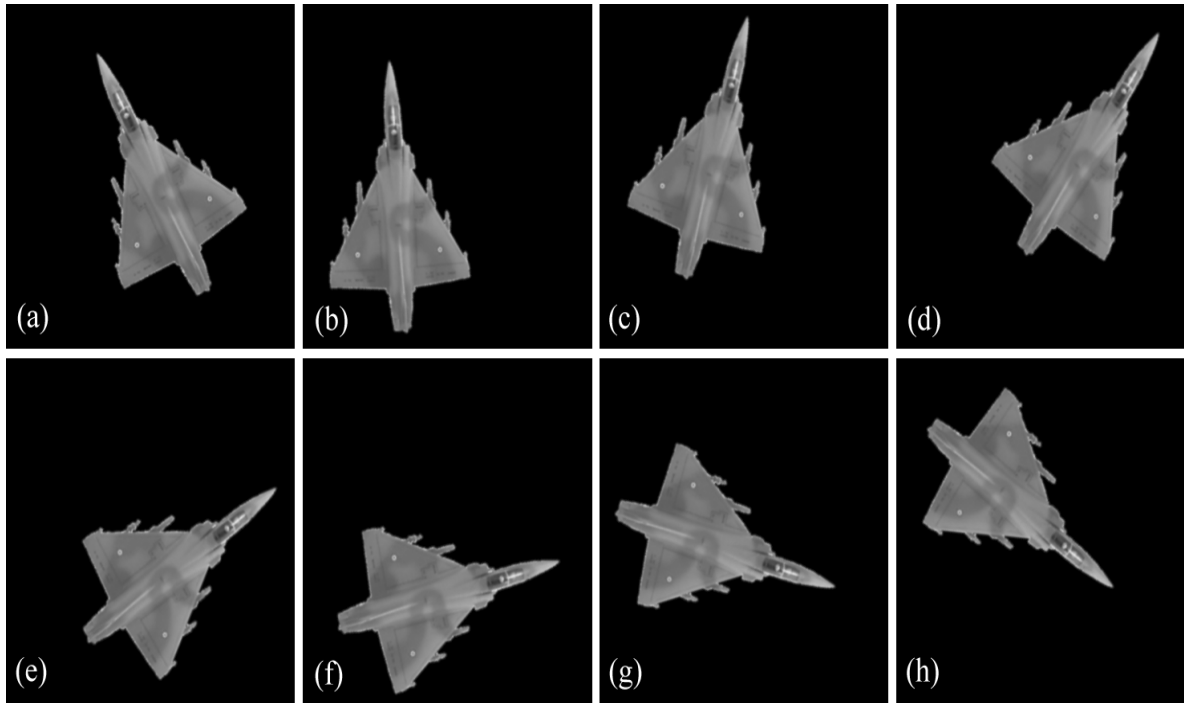


Figure 3.5 The different rotation versions of image Mirage-2000

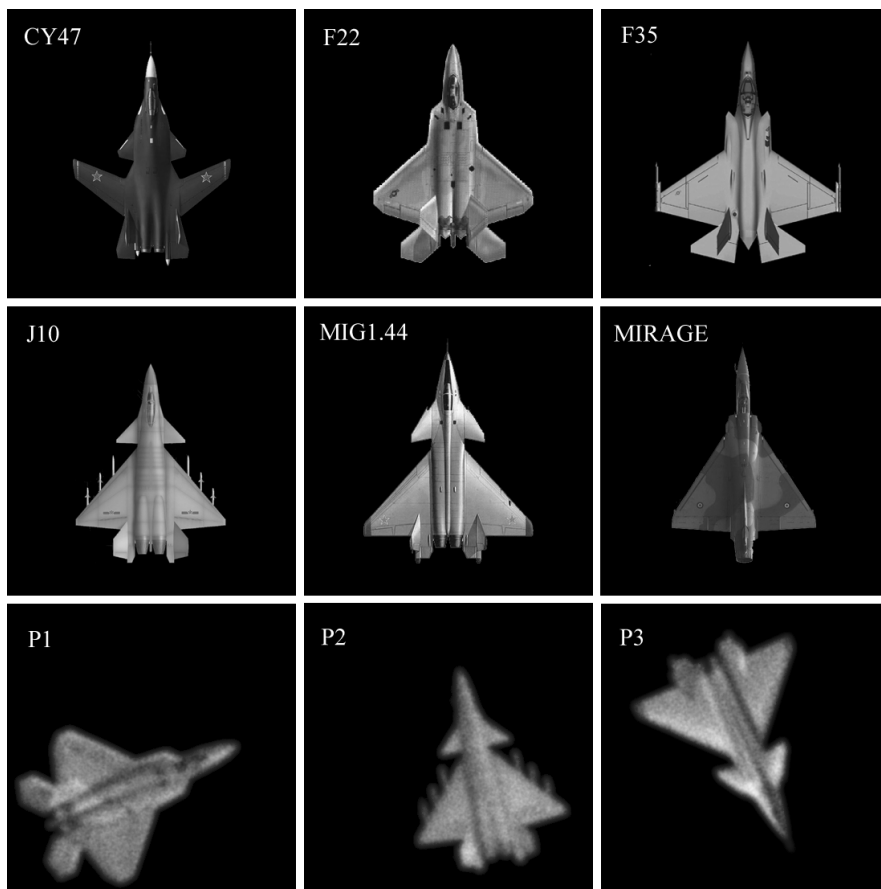


Figure 3.6 Reference images (in first and second rows) and patterns to identify (in third row)

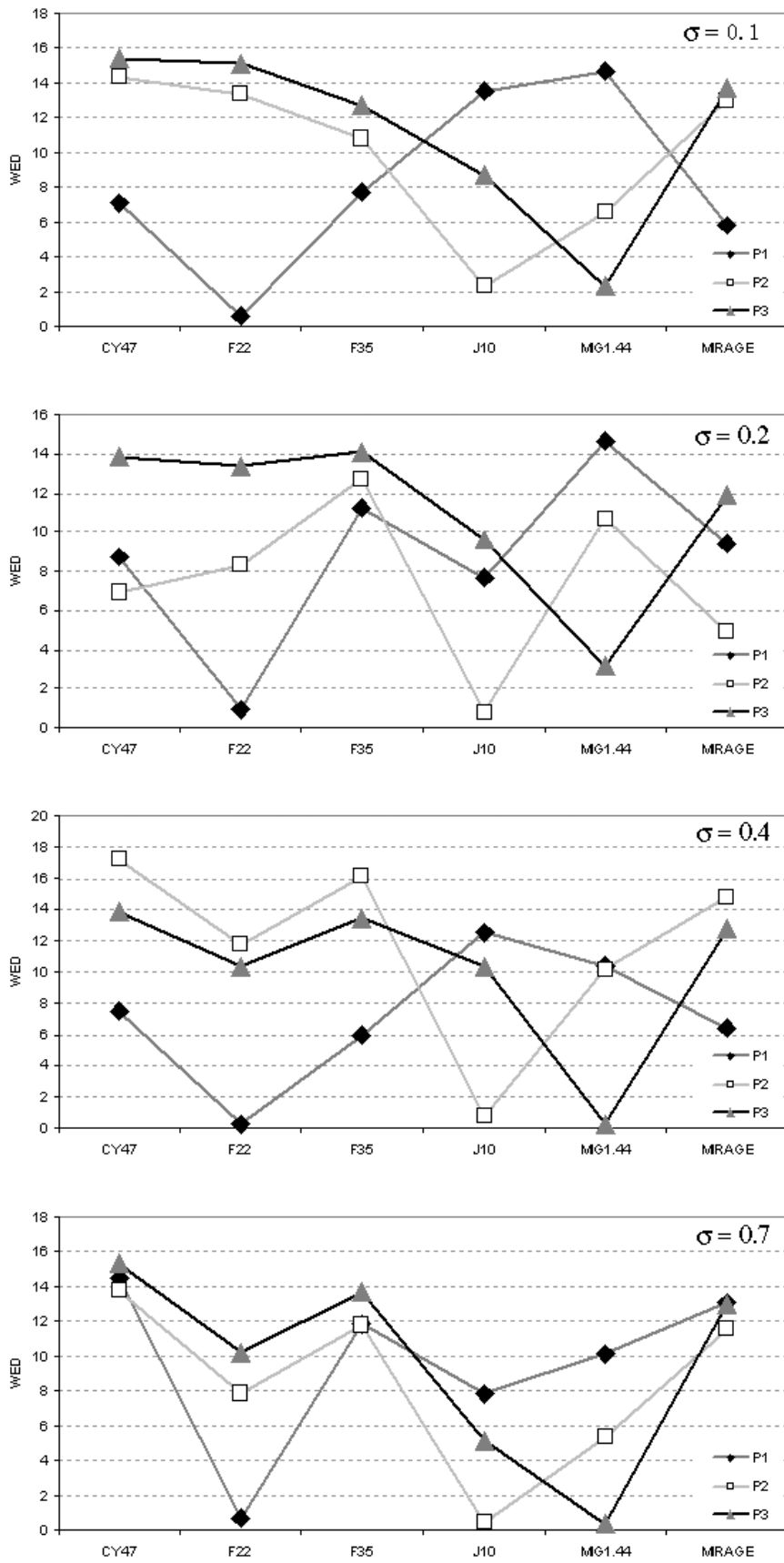


Figure 3.7 Weighted Euclidean distances with different scale parameters

Table 3.3 The Gaussian-Hermite moment invariants of figure

Figure	(a)	(b)	(c)	(d)	(e)	(f)	(g)	(h)	$\xi / \mu $
I_1	3.0511E+01	3.0511E+01	3.0511E+01	3.0509E+01	3.0509E+01	3.0511E+01	3.0511E+01	3.0509E+01	0.00%
I_2	2.3875E+00	2.3744E+00	2.3859E+00	2.3892E+00	2.3890E+00	2.3803E+00	2.3859E+00	2.3892E+00	0.22%
I_3	-5.8788E+00	-5.8605E+00	-5.8717E+00	-5.8924E+00	-5.9008E+00	-5.8675E+00	-5.8715E+00	-5.8924E+00	0.24%
I_4	1.0670E+00	1.0339E+00	1.0636E+00	1.0484E+00	1.0408E+00	1.0507E+00	1.0635E+00	1.0484E+00	1.12%
I_5	-1.1118E+01	-1.0871E+01	-1.1077E+01	-1.1021E+01	-1.0972E+01	-1.1030E+01	-1.1078E+01	-1.1021E+01	0.69%
$\sigma = 0.1$ I_6	-1.2344E+01	-1.2424E+01	-1.2366E+01	-1.2516E+01	-1.2497E+01	-1.2385E+01	-1.2367E+01	-1.2516E+01	0.58%
I_7	2.1460E+02	2.1458E+02	2.1457E+02	2.1457E+02	2.1457E+02	2.1457E+02	2.1457E+02	2.1457E+02	0.01%
I_8	-3.9057E+01	-3.8902E+01	-3.9071E+01	-3.9111E+01	-3.9151E+01	-3.8987E+01	-3.9072E+01	-3.9111E+01	0.20%
I_9	2.5349E+00	2.3433E+00	2.5146E+00	2.3967E+00	2.3767E+00	2.4571E+00	2.5146E+00	2.3967E+00	3.00%
I_{10}	1.9812E+02	1.9787E+02	1.9779E+02	1.9998E+02	2.0008E+02	1.9792E+02	1.9779E+02	1.9998E+02	0.55%
I_{11}	-2.9816E+01	-2.8545E+01	-2.9666E+01	-2.9198E+01	-2.9053E+01	-2.9221E+01	-2.9663E+01	-2.9198E+01	1.41%
I_1	-1.5335E+01	-1.5330E+01	-1.5330E+01	-1.5330E+01	-1.5329E+01	-1.5334E+01	-1.5330E+01	-1.5330E+01	0.01%
I_2	1.9369E+02	1.9364E+02	1.9349E+02	1.9374E+02	1.9382E+02	1.9378E+02	1.9349E+02	1.9374E+02	0.07%
I_3	4.1696E+03	4.1670E+03	4.1646E+03	4.1666E+03	4.1732E+03	4.1691E+03	4.1644E+03	4.1666E+03	0.07%
I_4	-1.6740E+03	-1.6743E+03	-1.6722E+03	-1.6758E+03	-1.6748E+03	-1.6757E+03	-1.6722E+03	-1.6758E+03	0.09%
I_5	1.6251E+05	1.6228E+05	1.6225E+05	1.6218E+05	1.6270E+05	1.6235E+05	1.6223E+05	1.6218E+05	0.11%
$\sigma = 0.3$ I_6	-2.9475E+05	-2.9465E+05	-2.9424E+05	-2.9504E+05	-2.9495E+05	-2.9505E+05	-2.9423E+05	-2.9504E+05	0.12%
I_7	-9.7844E+01	-9.7834E+01	-9.7826E+01	-9.7817E+01	-9.7833E+01	-9.7793E+01	-9.7826E+01	-9.7817E+01	0.02%
I_8	-3.7698E+03	-3.7651E+03	-3.7619E+03	-3.7628E+03	-3.7753E+03	-3.7679E+03	-3.7618E+03	-3.7628E+03	0.13%
I_9	5.7030E+02	5.7076E+02	5.7008E+02	5.6938E+02	5.6964E+02	5.7131E+02	5.7011E+02	5.6938E+02	0.12%
I_{10}	1.4350E+06	1.4291E+06	1.4325E+06	1.4226E+06	1.4387E+06	1.4279E+06	1.4321E+06	1.4226E+06	0.40%
I_{11}	-2.1174E+06	-2.1162E+06	-2.1124E+06	-2.1188E+06	-2.1200E+06	-2.1192E+06	-2.1122E+06	-2.1188E+06	0.14%
I_1	-1.3322E+02	-1.3322E+02	-1.3322E+02	-1.3322E+02	-1.3321E+02	-1.3322E+02	-1.3322E+02	-1.3322E+02	0.00%
I_2	2.1586E+03	2.1581E+03	2.1582E+03	2.1585E+03	2.1580E+03	2.1584E+03	2.1582E+03	2.1585E+03	0.01%
I_3	6.3477E+04	6.3459E+04	6.3461E+04	6.3464E+04	6.3460E+04	6.3466E+04	6.3460E+04	6.3464E+04	0.01%
I_4	-3.3988E+03	-3.4002E+03	-3.3977E+03	-3.4035E+03	-3.3977E+03	-3.4009E+03	-3.3977E+03	-3.4035E+03	0.07%
I_5	8.0571E+06	8.0530E+06	8.0543E+06	8.0560E+06	8.0525E+06	8.0552E+06	8.0542E+06	8.0560E+06	0.02%
$\sigma = 0.5$ I_6	-1.3859E+06	-1.3859E+06	-1.3851E+06	-1.3877E+06	-1.3855E+06	-1.3870E+06	-1.3851E+06	-1.3877E+06	0.08%
I_7	5.8786E+02	5.8782E+02	5.8780E+02	5.8780E+02	5.8779E+02	5.8782E+02	5.8780E+02	5.8780E+02	0.00%
I_8	-3.8695E+05	-3.8682E+05	-3.8682E+05	-3.8682E+05	-3.8686E+05	-3.8686E+05	-3.8682E+05	-3.8682E+05	0.01%
I_9	1.9386E+04	1.9397E+04	1.9381E+04	1.9414E+04	1.9376E+04	1.9398E+04	1.9381E+04	1.9414E+04	0.08%
I_{10}	6.8459E+08	6.8417E+08	6.8425E+08	6.8447E+08	6.8410E+08	6.8437E+08	6.8424E+08	6.8447E+08	0.02%
I_{11}	-3.6238E+07	-3.6228E+07	-3.6205E+07	-3.6270E+07	-3.6223E+07	-3.6249E+07	-3.6205E+07	-3.6270E+07	0.07%

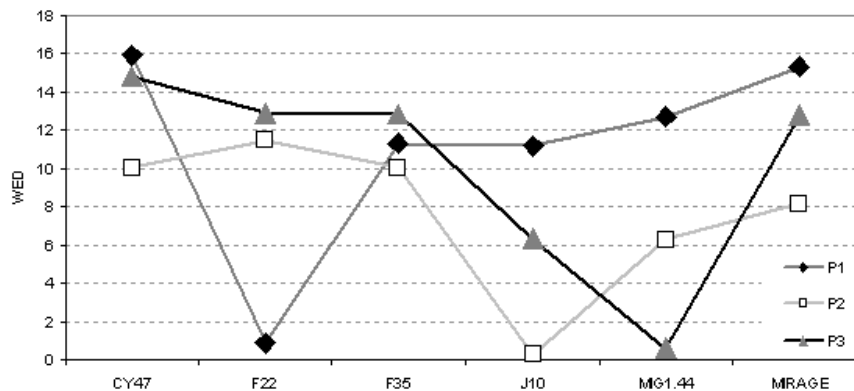


Figure 3.8 Results of matching by using geometric moment invariants

In order to compare with geometric moment invariants, we give also the results of matching by using their geometric moment invariants to constitute the feature vectors of images (Figure 3.8). The results show that the method by use of Gaussian-Hermite moment invariants has almost the same ability of the method by use of geometric moment invariants. In general, the numerical stability of the orthogonal moments with respect to the geometric ones increases with the order. More precisely, it decreases, but that of the geometric moments decreases much faster. Because the 11 first invariants are based on the moments of orders 2–4, this advantage is not obvious.

3.4 Seismic image analysis by moments

The seismic data can be considered volume with texture. Seismic images are also characterised by specific textures which can provide valuable information for locating potential oil reservoirs. Texture is an important feature for human perception of visual objects along with shape, color, and motion features ([du Buf et al., 1990](#)). Various feature representations of visual objects and similarity measures based on these descriptors have been investigated for texture recognition and similarity-based retrieval applications ([Chang and Kuo, 1993](#); [Miyamoto et al., 2000](#); [Sim et al., 2004](#)).

Textures can be classified into two categories: inhomogeneous and homogeneous textures. Homogeneous textures such as pictures of wall of bricks or sands have the uniform statistical characteristics over the whole area of an image whereas inhomogeneous textures such as pictures of clouds or flowers in a vase do not even have a quasi-periodic structure. Usually, a

lot of conventional algorithms have focused on investigation of homogeneous textures. On the contrary, inhomogeneous textures have been investigated recently. Especially, the Hurst parameters of fractal Brownian motion have been used for representation of inhomogeneous textures.

Some properties make it possible to use the moments to be the unique features of image and hence represent the image in feature space. Since the moments are uniquely determined by the image, the uniqueness of moments will then ensure their discriminative ability. On the other hand, the feature is always described as global information which can be also demonstrated from the definition of moment. Therefore, the introduction of moments in the feature space to represent the image has then become an efficient way in image analysis. We obtain a significant reduction of dimensionality without losing important information about the original image or object through such feature representation. If the representation is carefully chosen, we can obtain the features which are relatively insensitive to noise and occlusion. Furthermore, the feature representation with moment-based techniques provides a complete object representation which is invariant to some transformations. In pattern recognition, the moment invariants are taken as the features which maintain the invariance of some image transformations such as rotation, translation and scaling of the original image. This advantage is the most important reason for which the moments can be used as good features in image analysis. Apart from image analysis, moment-based techniques have been also widely used in the fields of computer vision, machine learning and pattern recognition.

So far, there are several ways for anisotropy detection in an image. The most used method for anisotropy detection is based on gradient structure tensor (GST) ([Bakker, 2002](#)). The information about anisotropy can be well reflected according to the analysis of the eigenvalues of GST matrix. The eigenvalues λ of the image structure tensor can be used to detect lines, corners or constant grey value regions.

Table 3.4 Local structure conditions (GST)

Local Structure	Eigenvalues
constant intensity	$\lambda_1 \approx \lambda_2 \approx 0$
Linear structure	$\lambda_1 \geq 0, \lambda_2 \approx 0$
The underlying structure deviates from the linear structure model	$\lambda_1 \geq 0, \lambda_2 \geq 0$

Here we take a 2D structure tensor as an example. We assume that the eigenvalues are sorted

so that $\lambda_1 > \lambda_2$. In two dimensions we can distinguish three different cases, corresponding to different types of local neighbourhoods. They are given in the table above.

Contrast independent measures can be constructed dividing the eigenvalues by the total energy. The anisotropy or isotropy can be measured by a confidence which is calculated by these two eigenvalues:

$$C_{an} = \frac{\lambda_1 - \lambda_2}{\lambda_1 + \lambda_2} \quad (3.50)$$

Another method is still based on matrix analysis; however, unlike with the mentioned above, this method uses Fourier transform to extract the desire information. To be more precise, it uses the spectral moment instead of the gradient to be the elements of the matrix. Since this method is related greatly to the spectral geometric moments, we then call this as spectral moment matrix method (SMM) ([Miguel, 1995](#)). Likewise, SMM also detects anisotropy or isotropy information depending on its two eigenvalues. Since the two eigenvalues are both non-negative, a non-negative confidence defined by

$$C_{an} = \frac{\min(\lambda_1, \lambda_2)}{\max(\lambda_1, \lambda_2)} \quad (3.51)$$

can be used to judge anisotropy or isotropy of the neighbourhood. if C_{an} is great which indicates the higher degree of anisotropy; on the other hand, if C_{an} is little, which shows a linear texture of image and the orientation in the region trends to be the same.

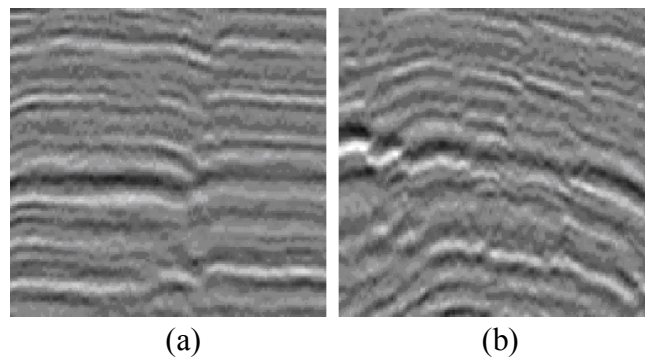


Figure 3.9 Two original images for the SGMM experiments
(a) a seismic image with obvious fault; (b) a seismic image with slight faults.

Inspired by the SMM, we try to construct the corresponding SMM which is based on Gaussian-Hermite moments other than geometric moments. The corresponding SMM is so-called spectral Gaussian-Hermite moments matrix (SGMM) is has the form equation(3.39) in section 2.2.2.2 and a non-negative confidence defined by equation(3.40).

The experiments are carried out for evaluating the proposed. For comparison, both GST and SMM are also used to detect the isotropy. Two experiments are conducted. The first experiment is carried out on a real seismic image which is shown in Figure 3.9(a). We can observe that this image contains an obvious fault which locates right and passes through vertically in the image. Three methods are used for locating this fault. The results are well shown in Figure 3.10, (a) and (b) show the result from GST with $\sigma_T=2.0$ and 4.0 respectively. Apparently, $\sigma_T=4.0$, this parameter setting produces much obvious faults location than the first one; (c) and (d) show the results from SMM with different window size 16×16 and 32×32 pixels respectively. We can observe that small window size causes the unsmooth location of faults. From (e) to (h), we can see the results from SGMM. (e) and (f) show the results with window size 16×16 . The difference lies in the σ selection. $\sigma=4.0$ for (e) and 5.0 for (f). We make an improvement by increasing window size to 32×32 . (g) shows the detection results with $\sigma=6.0$, the result is almost as good as (d) from SMM. When σ is increased to 9.0, as can be seen in (h), the clear and obvious location of isotropy is found. We can learn from this figure that GST gives a much coarse location of fault. SMM produces a much better location when the window size is 32×32 . SGMM, on the other hand, shows the most clear and obvious location when the bigger window is used, as can be seen from (g) and (h), the white parts are relatively narrow and located exactly the place where the fault exists. With the increase of σ the influence from other parts on the main fault detection has efficiently eliminated.

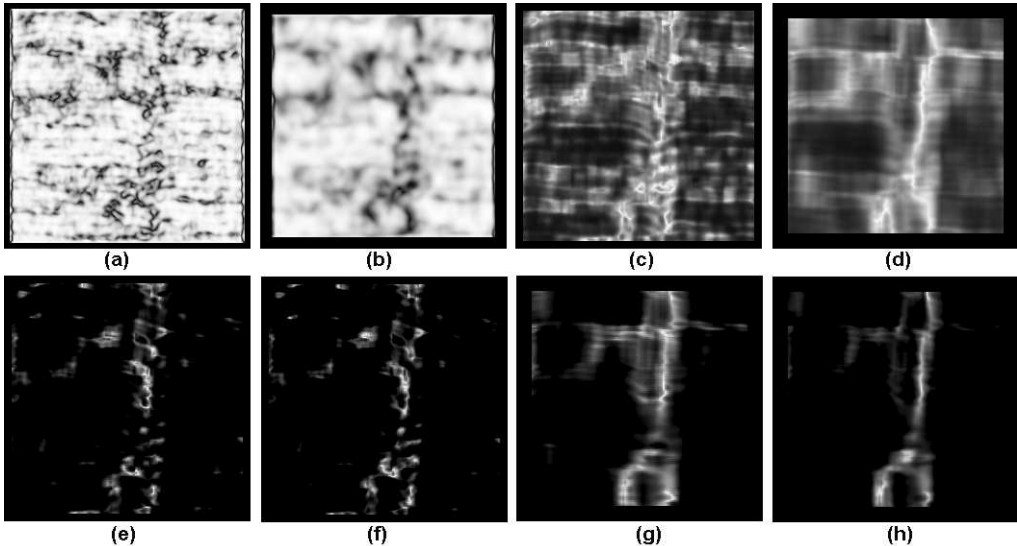


Figure 3.10 The obvious fault detection for the seismic image.
(a-b) are the results from GST;
(c-d) are the results from SMM;
(e-h) are the results from SGMM.

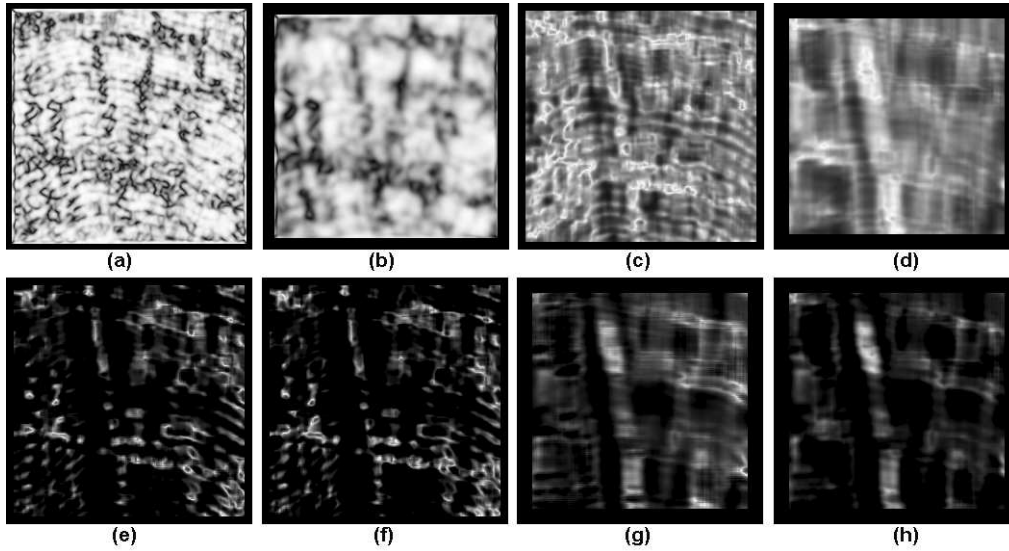


Figure 3.11 The slight fault detection for the seismic image.

- (a-b) are the results from GST;
- (c-d) are the results from SMM;
- (e-h) are the results from SGMM.

Figure 3.11 shows the result for Figure 3.9(b) which contains several faults; however, these faults are relatively slight so that it is difficult to detect them. The parameter setting is as the same as that of Figure 3.10. The figure shows generally lower qualified detection of these faults by three methods mentioned above. The main fault located around the center image crossing vertically can be successfully detected by both SMM and SGMM. The other faults, as can be seen from the figure are slightly stood out. Most of them are even discontinuous. However, generally speaking, among three methods, SGMM relatively perform better than other methods. This is supported by the (g) and (h) in the figure.

Finally, it should be noted here that the method based on spectral moments can be used for detection isotropy, however, for some texture appears in seismic images, as can be seen from the results of Figure 3.11, huge variations have been produced not only in their orientation, but also in their frequency, and grey-level. These factors all influence the final results of detection. This can be learned from Figure 3.10 and Figure 3.11. Hence, the methods are generally used with some pre-processing of the original images so that the certain properties can be well stood out. Then the better results can be expected on these pre-processed images.

3.5 Conclusion

In this chapter, we introduce the ways of analyzing image by moments, from which the advantages of moments are obviously exhibited. The different kinds of moments, the non-orthogonal moments such as geometric moments and the orthogonal moments, are introduced

in the chapter. From the summary of the different kinds of moments, we have learned that geometric moments are the simplest ones that can be easily used to develop moment invariants. Invariants of Gaussian-Hermite moments are discussed and constructed in this chapter. The translation invariants are constructed by the corresponding Gaussian-Hermite central moments accordingly. The rotation invariants are derived from a theorem which indicates that Hermite polynomials keep the similar linear relations to monomials when image coordinates are rotated. Based on this theorem the rotation invariants of Gaussian-Hermite moments are achieved and tested by related images. The combined invariants are finally introduced which are independent of both translation and rotation.

We have proposed an approach for estimating the coherency of texture that is based on the spectrum Gaussian-Hermite moments in this chapter. We present the way using the moments of the first order and the second order to estimate the coherency within a small local window in Fourier domain. In this new method the size of the window and the value of σ are important. As the window size gets larger, more global features are detected. This suggests that the choice of window size could possibly be tied to the contents of the image.

The experiments are designed for testing feature representation and pattern classification abilities in the chapter. The experimental results show that Gaussian-Hermite moment invariants have better feature representation abilities and perform better in the task of pattern classification than geometric moment invariants. They are potential tools for image analysis and pattern recognition.

In the end of chapter, we design the experiments for analysis of seismic image. The experimental results show that Gaussian-Hermite moments have better representation abilities and perform efficiently in the task of coherence estimation.

4 Stepwise dip scanning coherency estimation

Coherence technology is an effective tool for seismic interpretation. It detects the discontinuity of the seismic event by analyzing seismic signals in adjacent traces, so as to identify geological phenomena like faults, special lithologic bodies, river courses etc. Also coherence can be used to define stratigraphic features.

Seismic trace coherence is a measure of lateral changes in the seismic trace pattern and is based on a cross-correlation measurement. Coherence algorithm has been developed rapidly since Bahorich and Farmer firstly introduced the coherence technology in 1995. At present, there are mainly three types of coherence algorithms, the cross-correlation based the first generation of algorithm (C_1 algorithm) ([Bahorich and Farmer, 1995](#)), multi-trace semblance second generation of algorithm (C_2 algorithm) ([Marfurt et al., 1998](#)), and eigenstructure based third generation of algorithm (C_3 algorithm) ([Gersztenkorn and Marfurt, 1999](#)). The C_1 algorithm is the simplest one with the highest computational efficiency among the three algorithms, but it only allows three traces to participate the computation at one time. It's not very robust to noise either. The C_2 algorithm is more robust to noise but with lower resolution and higher computational costs than C_1 algorithm. Compared with C_2 algorithm, Eigenstructure based C_3 algorithm is more robust to noise and with a better resolution. Since the original C_3 algorithm did not implement dip scanning, it could not provide good coherence estimation in areas with strong structural dips. If dip scanning is employed in C_3 algorithm, it will be hard to promote due to its huge computational costs.

3D coherent cube is an extremely effective new technique for interpreting seismic data. It has obvious advantages in many aspects compared with the conventional 3D data volume, such as recognizing faults and fractures, interpreting ancient channels, and edge detection of oil and gas reservoir. Coherent cube is to condense and extract information around a certain point in

3D data volume, and then highlight the original characteristics of the geologic body at this point. Therefore, in terms of its essence, coherent cube is a special seismic attribute cube and those points having rather small coherent value are related to the discontinuity of geologic body. In practical production, people often interpret horizontal slices or layer slices of coherent cube, and this provides advantageous foundations for resolving special problems in exploration of oil and gas.

In normal seismic interpretation, the seismic amplitude data is used. We can use inline, crossline, horizontal time slices or layer time slices, and we can also use 3D data volumes. Whatever kind of data is used, however, it just shows the information of single point, single section and single surface. It is not enough for recognizing and describing some special geologic bodies such as faults, fractures and old channels. In coherent cube, with seismic traces combined in space, attribute values of each spatial point reveal the information of lines, traces and points of initial data volume. The fact is that the common attribute of abnormal bodies is embodied on each point. It is a special kind of space weighting.

In this chapter, the basic procedure of the stepwise dip scanning coherence algorithm based on eigenstructure ([Li et al., 2010b](#)) is as follows: The dip scanning is conducted in two steps. In the first step, C_2 algorithm is employed to scan all dip directions; the resulted coherence values are sorted from small ones to large ones; dip directions of the larger coherence values will be kept for further use. In the second step, C_3 algorithm is implemented to search for the best dip directions among the ones we kept in the first step. As a matter of application results to real data set, the newly proposed algorithm remains a resolution as good as C_3 algorithm does, while it can also provide good coherence estimation in areas with strong structural dips. As the dip scanning is mainly conducted in C_2 algorithm in which we employ a fast algorithm, the algorithm proved to be highly efficient.

4.1 Detection of seismic discontinuity

Seismic imaging of discontinuities is a relatively geophysical technique. We compare two main families of algorithms, coherency ([Bahorich and Farmer, 1995](#); [Gersztenkorn and Marfurt, 1999](#); [Marfurt et al., 1998](#)) and differencing ([Luo et al., 1996](#)). Both of these algorithms image discontinuities using different mathematical techniques.

4.1.1 Coherency method

The C_1 coherency algorithm utilizes cross-correlation, $\rho(t)$, between two seismic signals, \vec{A} and \vec{B} , and is shown mathematically to be:

$$\rho(t) = \sum_{\tau} A_{t+\tau} B_{\tau} \quad (3.52)$$

where A and B are vectors containing seismic trace time sequences $\vec{A} = (A_0, A_1, \dots, A_n)$ and $\vec{B} = (B_0, B_1, \dots, B_n)$, and where t is the displacement of \vec{B} relative to \vec{A} . The C_1 algorithm computes the cross-correlation of traces in the x direction, denoted by ρ_x and the cross-correlation of traces in the y direction, denoted by ρ_y . The C_1 algorithm normalizes these cross-correlations with respect to trace energies and then computes the maximum values for lags in the x and y directions. The coherency measure ρ_{xy} , is given by the square root of these maximum values, that is

$$\rho_{xy} = \max(\rho_x) * \max(\rho_y) \quad (3.53)$$

Bahorich and Farmer (1995) introduced the attribute of coherence in 1995. The coherence cube calculates localized waveform similarity in both inline and crossline directions and estimates of 3D seismic coherence are obtained. Small regions within the seismic volume containing stratigraphic anomalies such as channels have a different seismic character compared to the corresponding regions of neighboring traces. This attribute is given by equation

$$c_1 = \sqrt{\frac{C_{f_1 f_2}}{\sqrt{C_{f_1 f_1} C_{f_2 f_2}}} \frac{C_{f_1 f_3}}{\sqrt{C_{f_1 f_1} C_{f_3 f_3}}}} \quad (3.54)$$

where f_1 and f_2 are two consecutive tracks the direction and inline f_1 and f_3 and the direction crossline $C_{f_1 f_2}$ is the maximum correlation between f_1 and f_2 .

To account for the dip, the attribute C_1 is computed for several values of the dip, the maximum value of C_1 corresponds to the proper value of the dip of the reflectors.

To involve a larger number of traces, Marfurt et al (1999; 1998) introduced the covariance matrix of traces following

$$C = \sum \begin{pmatrix} f_j^1 f_j^1 & f_j^1 f_j^2 & \dots & f_j^1 f_j^q \\ f_j^2 f_j^1 & f_j^2 f_j^2 & \dots & f_j^2 f_j^q \\ \vdots & \vdots & \vdots & \vdots \\ f_j^q f_j^1 & f_j^q f_j^2 & \dots & f_j^q f_j^q \end{pmatrix} \quad (3.55)$$

where f^0, f^1, \dots, f^q are known traces of a vertical window of size $2n + 1$.

The new attribute of coherence is then given by:

$$c_2 = \frac{\sum_{i,j} C_{ij}}{\sum_i C_{ii}} \quad (3.56)$$

For through reducing the level of noise introduced by the calculation of the covariance matrix trace, we can use only the dominant component, which gives us the attribute C_3 :

$$c_3 = \frac{\lambda_1}{\sum_i \lambda_i} \quad (3.57)$$

where λ_j is the eigenvalues of C . λ_1 is the largest eigenvalue. This measure was presented as an estimate of seismic coherency in ([Gersztenkorn and Marfurt, 1999](#)).

Another method of coherence estimation using the gradient structural tensor(GST) is introduced by Bakker ([2002](#)). A seismic image of a single constant planar reflector is just a stack of isophote planes, and it therefore has a plane-like linear structure. Since the confidence value C_{plane} of the GST is a measure for the resemblance of an image structure to a plane-like linear structure, it can be used as an estimate of coherence as well. The gradient structure tensor T is defined as the averaged dyadic product of the gradients g :

$$T = \overline{gg^T} \quad (3.58)$$

The eigenvalues of this tensor indicate the gradient energy in the orientations defined by the corresponding eigenvectors. In the case of a planar reflector the tensor has only one non-zero eigenvalue, and the corresponding eigenvector is the normal vector of the reflector. Any deviation of the data from a constant planar reflector leads to an increase of the gradient energy in the lateral direction. The coherency of the GST could therefore be estimated by :

$$\hat{c}_{gst} = \frac{\lambda_1}{tr(T)} \quad (3.59)$$

The eigenvalues of the covariance matrix represent the correlation between seismic traces and

the eigenvalues the GST represent the gradient energies of a geometrically ordered set of traces. This means that the reflector continuity is measured with the correlation between traces by the C_3 method, while the GST method uses the gradient energy in the lateral direction as a measurement for continuity.

4.1.2 Difference method

The difference method is a simpler technique which subtracts seismic signals (signal A on the target trace and signal B on an adjacent trace) and is given by:

$$\vec{d} = \frac{\vec{A} - \vec{B}}{|\vec{A}| + |\vec{B}|} \quad (3.60)$$

where \vec{d} is the difference at the center sample of the window on the target trace ([Luo et al., 1996](#)).

In version of the differencing algorithm Carter and Lines ([1999](#)) average the absolute differences of a grid point and its neighbours. The differencing method is somewhat similar to the use of second derivative computations that are used to enhance high wave number variations in data.

Consider the wavefield at some particular time slice and at some specific map location at grid (i, j). Denote this wavefield value at some given time by $u_{i,j}$. It can be shown that this second derivative value is closely related to a variation of the differencing algorithm. An average of absolute differences with surrounding traces in the differencing algorithm would consider:

$$d_{i,j} = \left(|u_{i+1,j} - u_{i,j}| + |u_{i-1,j} - u_{i,j}| + |u_{i,j+1} - u_{i,j}| + |u_{i,j-1} - u_{i,j}| \right) \quad (3.61)$$

By comparing the previous two equations, the differencing expression for the second derivative map would be equivalent to the expression for the average absolute differences, d_{ij} , if all the quantities within the absolute value signs of d_{ij} were positive. Therefore, differencing and second derivative maps have a somewhat similar appearance. Also, both the differencing and second derivative measures generally have a higher frequency content than the C_1 coherency algorithm since, in the Fourier domain, differentiation will multiply the Fourier transformed wavefield by spatial frequency while producing 90 degree phase shift.

4.2 Stepwise dip scanning coherence algorithm based on eigenstructure

The C_3 algorithm requires estimating the eigenvalue of the covariance matrix of the data trace volume within the analysis window. Therefore, with the increase of the seismic traces in the analysis window, the exponent number of the covariance matrix also increase, which would lead to a dramatic rise of computational costs. That is the reason why C_3 algorithm doesn't implement dip scanning. In contrast, the C_2 algorithm includes dip scanning in it and the algorithm is robust to noise. Currently commercial software mainly uses C_2 algorithm. Both theory and practice proves that C_3 algorithm has higher horizontal and vertical resolution than C_2 algorithm has.

4.2.1 Method of stepwise dip scanning

The stepwise dip scanning algorithm we presented in the paper comprehensively combines the merits of C_2 and C_3 algorithm to process coherence estimation. The details of our proposed algorithm are as follows.

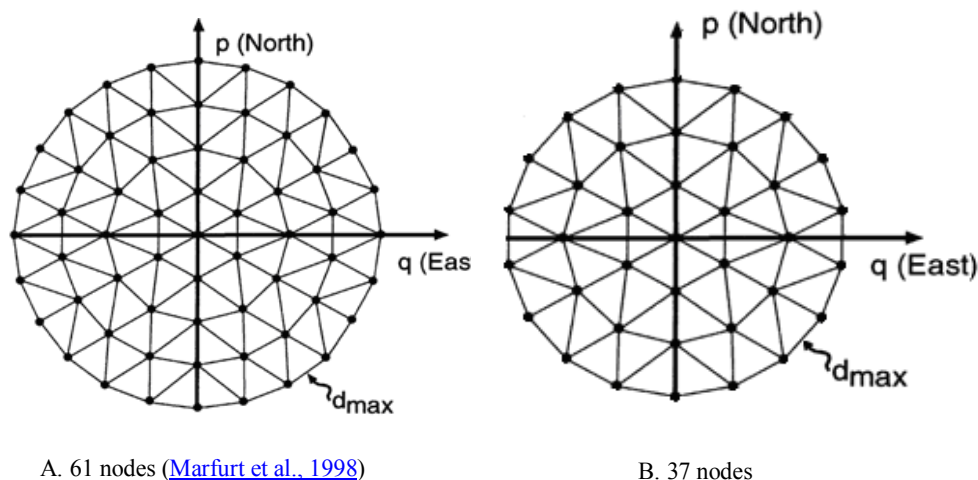


Figure 4.1 Dip azimuth layout

4.2.1.1 Select searching direction

Set d_{\max} as the largest estimated value of the stratigraphic dip, if $d_{\max} \geq 0.25 \text{ms/m}$, the dip azimuth layout of 61 nodes (Figure 4.1(a)) will be employed; if $d_{\max} < 0.25 \text{ms/m}$, the dip azimuth layout of 37 nodes (Figure 4.1 (b)) will be employed. In figure 1, p and q are the apparent dips in the x and y directions; d_{\max} is the largest dip value estimated by interpreters. Its unit is ms/m . Suppose the position of the i^{th} node is (p_i, q_i) , then

$$\sqrt{p_i^2 + q_i^2} \leq d_{\max} \quad (3.62)$$

where $i = 0, 1, \dots, 60$ (or $i = 0, 1, \dots, 36$).

4.2.1.2 Implement C2 algorithm to dip scanning

Suppose there are J seismic traces included in the analysis window, then we apply the following equation to the seismic data $u(t, x, y)$, as well as to the data of each direction (p_i, q_i)

$$\sigma(\tau, p_i, q_i) = \frac{\sum_{k=-K}^{+K} \left[\sum_{j=1}^J u(\tau + k\Delta t - p_i x_j - q_i y_j, x_j, y_j) \right]^2}{J \sum_{k=-K}^K \sum_{j=1}^J \left[u(\tau + k\Delta t - p_i x_j - q_i y_j, x_j, y_j) \right]^2} \quad (3.63)$$

where K is half length of the vertical length of the analysis window; $K = w / \Delta \tau$, where $\Delta \tau$ is the sampling interval of the seismic data; then we estimate the average mean similarity of $2K+1$ sampling points. Out of all $\sigma(\tau, p_i, q_i)$ data, m (3~5) largest ones are selected and denoted by (\hat{p}_i, \hat{q}_i) $i = 1, \dots, m$.

The 3D seismic data volume is arranged according to traces, and the data volume of each trace is arranged according to the sequence of the sampling points. The coherence algorithm of 3D seismic data volume is also estimated in accordance with the traces. If we assume:

$$S_u[i][k] = \left[\sum_{j=1}^J u(\tau + k\Delta t - p_i x_j - q_i y_j, x_j, y_j) \right]^2$$

$$S_d[i][k] = \sum_{j=1}^J \left[u(\tau + k\Delta t - p_i x_j - q_i y_j, x_j, y_j) \right]^2 \quad (3.64)$$

Then from equation (4.12), we have:

$$\sigma(\tau, p_i, q_i) = \frac{\sum_{k=-K}^{+K} S_u[i][k]}{J \sum_{k=-K}^K S_d[i][k]} \quad (3.65)$$

$$\begin{aligned}
\sigma(\tau + \Delta t, p_i, q_i) &= \frac{\sum_{k=-K}^{+K} \left[\sum_{j=1}^J u(\tau + (k+1)\Delta t - p_i x_j - q_i y_j, x_j, y_j) \right]^2}{J \sum_{k=-K}^K \sum_{j=1}^J \left[u(\tau + (k+1)\Delta t - p_i x_j - q_i y_j, x_j, y_j) \right]^2} \\
&= \frac{\sum_{k=-K}^{+K} S_u[i][k] - S_u[i][-K] + S_u[i][K+1]}{J \sum_{k=-K}^{+K} S_d[i][k] - J * S_d[i][-K] + J * S_d[i][K+1]}
\end{aligned} \tag{3.66}$$

It is clear that as the estimated results of $\sigma(\tau, p_i, q_i)$, $S_u[i][k]$ and $S_d[i][k]$ can also be used in the estimation of $\sigma(\tau + \Delta t, p_i, q_i)$, so if we keep and carry on the estimated results of $\sigma(\tau, p_i, q_i)$, the following estimation work of $\sigma(\tau + \Delta t, p_i, q_i)$ can be dramatically lessened.

4.2.1.3 Algorithm statement

if nTraceNum is seismic trace number and nSampleIndex is Index number of the sampling points, the method can be written as follow:

Table 4.1 Pseudo code of dip scanning computation

```

if (nSampleIndex == 0) //the first sampling point
{
    // DipNum is the number of scanning dips
    For(i=0; i<DipNum; i++)
    {
        estimate  $S_u[i][k]$ ,  $S_d[i][k]$ ;
        estimate the coherence value of the point;
    }
}
else if (nSampleIndex > 0) //is not first sampling point
{
    // update the data retention
    estimate  $S_u[i][2K]$  and  $S_d[i][2K]$ ;
    estimate the coherence value of the point;
}

```

4.2.1.4 Implement C3 algorithm to dip scanning

At the position (t, x, y) , we read the data volume of the J^{th} seismic trace in each dip direction (\hat{p}_i, \hat{q}_i) in the analysis window.

$$U_{ij} = u(\tau - \hat{p}_i x_j - q_i y_j, x_j, y_j) \tag{3.67}$$

where $i = 1, 2, \dots, m$; $j = 1, 2, \dots, J$. Let $D_i = [U_{i1}, U_{i2}, \dots, U_{iJ}]$ estimate the largest eigenvalue of $D_i^T D_i$, denoted by $\lambda_{i \max}$.

$$\sigma(t, x, y) = \lambda \max = \max_i \{ \lambda_i \max \} \quad (3.68)$$

The complete equation of equation (4.12) is displayed in equation (4.18), where superscript H indicates the Hilbert transform of the real seismic trace. During the dip scanning process of the proposed algorithm, application results to the real data shows that there are no significant change between the calculation results of equation (4.12) and equation (4.18), whereas equation (4.12) requires much less calculation time.

$$\sigma(\tau, p_i, q_i) = \frac{\sum_{k=-K}^{+K} \left\{ \left[\sum_{j=1}^J u(\tau + k\Delta t - p_i x_j - q_i y_j, x_j, y_j) \right]^2 + \left[\sum_{j=1}^J u^H(\tau + k\Delta t - p_i x_j - q_i y_j, x_j, y_j) \right]^2 \right\}}{J \sum_{k=-K}^K \sum_{j=1}^J \left\{ \left[u(\tau + k\Delta t - p_i x_j - q_i y_j, x_j, y_j) \right]^2 + \left[u^H(\tau + k\Delta t - p_i x_j - q_i y_j, x_j, y_j) \right]^2 \right\}} \quad (3.69)$$

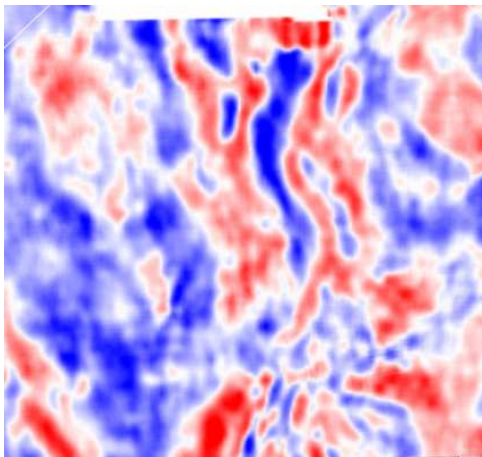
4.2.2 Example result on a real 3D seismic data

This section illustrates the efficiency of our approach on real seismic blocks. The real seismic data is from middle China. The time interval is 4 ms, and inline and cross-line trace spacing are 25m.(InLine 700~900,XLine 650~850,Time 0~800 ms). The algorithm is tested with environment: cpu: Intel core2 duo P8400, memory: 2G PC. The result of the algorithm is showed in Table 4.2. From the coherence slices in Figure 4.2, we can see that the C3 algorithm leads to higher resolution than C2 algorithm does, as Figure 4.2 (A) and (D) are clearer than (B). Because of dip scanning, (D) eliminates the invalid coherence values caused by structural dips. In cross-section Figure 4.3, there are two strong structural dips on the blue circled area of the vertical cross-section through the original seismic data volume (Figure 4.3 (A)).As dip scanning is included in the corresponding algorithms of Figure 4.3 (B) and Figure 4.3 (C), the blue circled area has relatively larger coherence value. However, the algorithm used in Figure 4.3 (C) doesn't include dip scanning, thus the coherence value of the circled area decreases due to the structure dips.

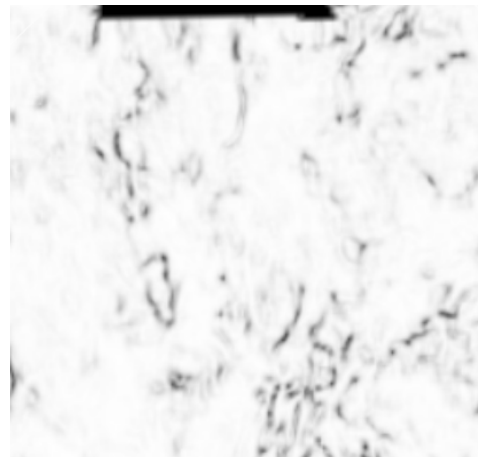
Although C₃ algorithm has higher horizontal and vertical resolution than C₂ algorithm, as the original C₃ algorithm did not implement dip scanning, it could result to distortional coherence value in areas with strong structural dips. However, if dip scanning is employed in C₃ algorithm, there is too much time cost, especially when the size of the analysis window increases. In our newly proposed stepwise dip scanning coherence algorithm based on eigenstructure, dip scanning is mainly done by C₂ algorithm, in which we implement its fast algorithm to improve the algorithm with higher quality and less time cost.

Table 4.2 Experimental results of coherence algorithms

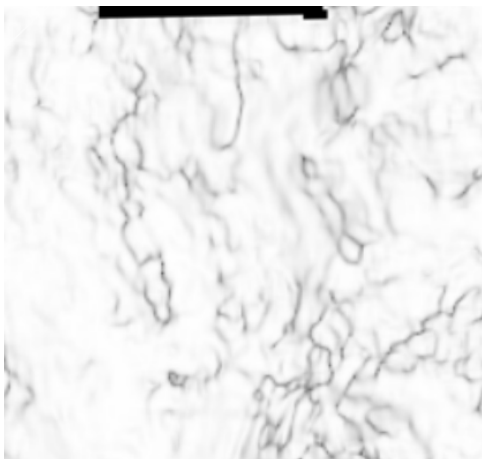
Coherence algorithm	Size of analysis window	Time (s)
C ₂ algorithm*	3*3*5	230
C ₂ algorithm*	5*5*5	335
C ₃ algorithm	3*3*5	20
C ₃ algorithm	5*5*5	180
C ₃ algorithm (with dip scanning)	3*3*5	3360
C ₃ algorithm (with dip scanning)	5*5*5	11467
Algorithm proposed in the thesis	3*3*5	346
Algorithm proposed in the thesis	5*5*5	831
*Note: The fast algorithm proposed in the paper is employed in the C ₂ algorithm.		



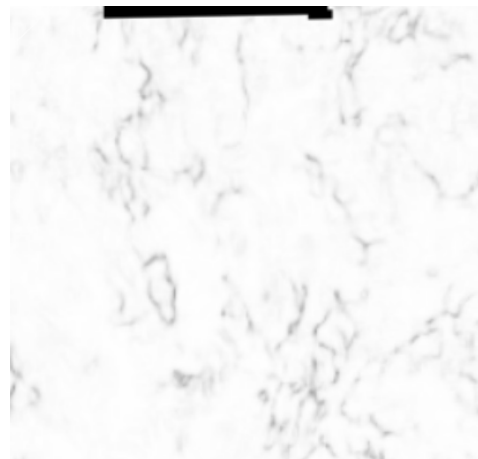
A. Horizontal slice through the original seismic data volume



B. Horizontal slice through C₂ coherence volume

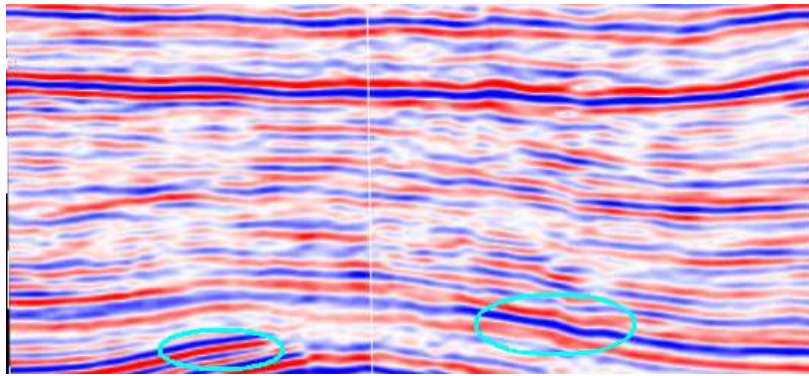


C. Horizontal slice without dip scanning through C₃ coherence volume

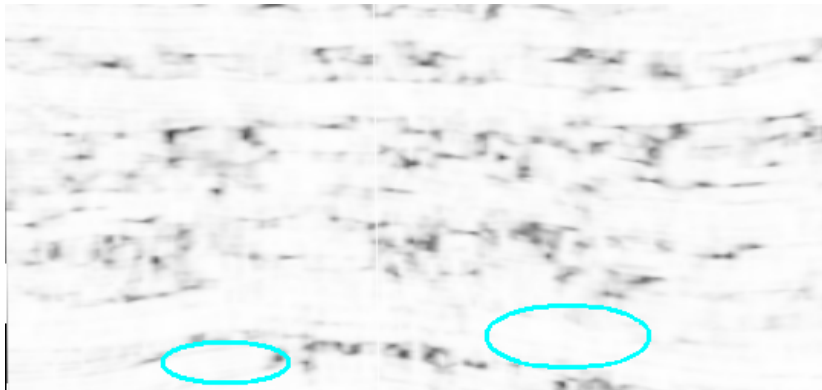


D. Horizontal slice with 61 dip scanning through the coherence volume obtained by our algorithm volume

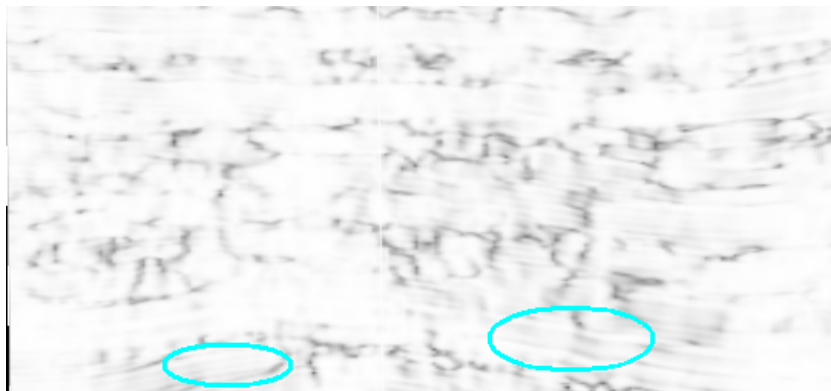
Figure 4.2 TimeSlice. (Time = 400ms, analysis window format is 3*3*5)



A. Vertical crosssection through the original seismic data volume



B. Vertical crosssection through C_2 coherence volume



C. Vertical crosssection without dip scanning through C_3 coherence volume



D. Vertical crosssection with 61 dip scanning through the coherence volume obtained by our algorithm

Figure 4.3 InLine crosssection (InLine= 800, analysis window format is 3*3*5)

4.3 Automatic Fault Detection for 3D Seismic Data

Seismic data sets typically contain a large number of faults at many different spatial scales. Knowledge of the location of the faults is critical to understanding a geological system. One effect that faults have, which is of real commercial significance, is that they act as membranes to the movement of hydrocarbons. Therefore having a good understanding of the fault positions is critical for the effective planning of drilling sites in order to maximize output efficiency. However, despite the significant progress in the development of horizon autotrackers, computer-aided interpretation of fault surfaces is significantly less advanced than horizon interpretation. Fault interpretation is more difficult as it involves especially detection of faults and correlation of horizons across faults. Current approaches for picking faults are largely manual, and involve laborious handpicking of discontinuities on a slice-by-slice basis, one fault at a time. This is time consuming resulting in hundreds of man-hours of work, performed by trained geologists. It is estimated that for every six months saved in the work leading up to the onset of production from a new oilfield, 5% will be saved from the total production bill. Hence, there is a strong financial imperative for this work.

Faults are important subsurface features that are often of interest to the geologist. According to conventional techniques, the identification of faults in coherent 3D seismic volumes is typically performed by human analysts, through manual identification and interpretation (i.e., "picking") of potential faults from seismic amplitude data. Of course, manual fault picking is an extremely time consuming process, and is thus quite costly. Additionally, manual interpretation is to a large extent dependent upon the skill, experience, and subjectivity of the individual analyst, resulting in imprecise results.

The automatic tracking of seismic horizons has been widely available in commercial software since the early 1990s providing first insight into the problem of interpretation automation for geologic faults. What is immediately obvious with a horizon auto-tracker is that the tracking frequently breaks down at fault boundaries. Depending on the tracker, and the parameter settings, we observe gaps in the resulting interpreted surface and possible large time jumps where the auto-tracker picks an erroneous event.

The automated calculation of correlation or coherency values from 3D seismic amplitude data is known in the art. According to this approach, geologic discontinuities such as faults are directly imaged from non-correlation or non-coherency events in the 3D seismic volume. However, this approach and other conventional methods do not provide any sort of automatic or quantitative interpretation of faults, but instead simply image the location of discontinuities

in the dataset.

An early effort for semi-automatic fault interpretation came from Simpson and Howard (1996). This technique allowed users to begin their fault interpretation task by simply “seeding” one or more fault segments (sticks) on a vertical seismic section, and the automatic operation would perform a cross-correlation on a series of slanted traces derived parallel to the seeded fault segment. The method could be used for both tracking, where no previous fault interpretation existed, and snapping, where an existing fault interpretation would be corrected based on the slant trace cross-correlation algorithm. Each fault surface extracted would need an initial seed point.

Coherence measures such as cross correlation (Bahorich and Farmer, 1995) semblance (Marfurt et al., 1998), or eigenstructure-based (Gersztenkorn and Marfurt, 1999) are applied to seismic data for imaging geological discontinuities like faults or stratigraphic features. . However, they produce only potential fault pixels, but do not generate the actual fault lines or surfaces. There exist methods for fault autotracking which use the same basic approach as horizon trackers, but with limited success.

Gibson et al (2003) introduced a method has been presented to tackle the difficult and resource consuming task of fault detection in 3D seismic datasets. Based on a multi-stage approach, it first detects points of horizon discontinuity, and progressively groups these points into larger surfaces. The final surface representation is a combined parametric and residual field model, which allows for a highly flexible surface representation. Comparative results with manually labelled faults show promising results.

Crawford and Medwedeff (1999) described an automated method of processing a fault enhanced 3D seismic volume to locate and interpret faults. The method includes processing of individual lateral slices of the 3D seismic volume wherein for each lateral slice, stripe artifacts are eliminated by adjusting pixel values to account for lines that are unduly bright or dim (and thus artifacts of processing). The linear features are enhanced by applying a modified Gumeys-Vanderburg algorithm, such that the intensity value of each pixel is enhanced according to the extent to which the pixels reside in a line. Detection of lines in the enhanced lateral slice is then performed by summing pixel intensities over a window at varying directions, and associating, with a center pixel, an amplitude value corresponding to the maximum sum and a direction value associated with this sum. The amplitude and direction values are then used to trace lines in the data. The tracing of lines is performed by locating a maximum pixel and examining adjacent pixels of high amplitude in directions similar to the direction values of

locally maximum amplitude values. The resulting vectors are then linked among lateral slices into surfaces that are representative of geologic faults.

Neff et al ([2000b](#)) described another method related to a computer implemented method and apparatus for automatically picking faults in a recorded three-dimensional seismic trace data volume. The method employs test planes, which are mathematically inserted into the seismic data volume to approximate dip and azimuth of a potential fault plane surface. A large number of data points, which are selected points on the seismic traces, are defined within the seismic volume, such that each test plane positioned in the seismic volume contains data points corresponding to at least a significant portion of a trace. The method then determines a factor for each data point which is representative of the probability that the point resides on a fault plane. This probability is based on planar discontinuity and average amplitude difference between corresponding traces in adjacent parallel test planes. The method selects locations, in an x, y grid, of a strip of locations having high probability of residing on a fault surface. The strip of the selected locations is smoothed to a line and used to construct fault lineament displays in seismic sections or time slices. The fault lineaments are stored in a computer data file, and conventional, stratigraphically enhanced, or other seismic data enhanced for seismic attributes is merged with the fault lineament files to create consolidated displays to aid interpretation of the data volume.

Neff et al ([2000b](#)) introduced a method that uniquely combine many of these elements by estimating a probability factor that a fault exists at a specific spatial location using parallel estimation planes within the seismic volume, and then following this procedure with an orientation and extraction method based on linear feature detection on time slices.

Randen et al ([2000](#)) proposed a seismic signal feature, exploiting its spatial and temporal derivatives. He proposed measuring the gradient vector field disorder caused by the fault crossing. The disorder of the gradient vector field attribute evaluates the local disorder in seismic data based on the orientation and magnitude of the gradient vector field. Areas without faults have a smooth gradient vector field, whereas areas with faults give a disrupted gradient vector field. The disorder of the gradient vector field attribute is obtained using the eigenvalue properties of the structure tensor. Explicitly, a strong variation of the eigenvalue magnitude shows the variation of spectral density projected on both the principal direction and the orthogonal ones. For faults and stratigraphic features, eigendecomposition of the structure tensor gives very close eigenvalues, so the attribute is near to one. In contrast, for layered zones, it tends towards zero.

Pedersen et al ([2002](#)) introduced a method known as ant-tracking, based on artificial swarm intelligence. The Ant Tracking algorithm follows an analogy of ants finding the shortest path between their nest and their food source by communicating using pheromones, a chemical substance that attracts other ants. The shortest path will be marked with more pheromones than the longest path and so the next ant is more likely to choose the shortest route, and so on. The idea is to distribute a large number of these electronic "ants" in a seismic volume; and let each ant move along what appears to be a fault surface while emitting "pheromone." Ants deployed along a fault should be able to trace the fault surface for some distance before being terminated. Surfaces meeting expectations will be strongly marked by "pheromone." Surfaces unlikely to be faults will be unmarked or weakly marked. It is important to note that the ant-tracking attribute will not only enhance faults in the data; other discontinuities, like processing effects, acquisition foot prints, channel boundaries, chaotic responses and internal reflector amplitude variations, will also be enhanced. The Ant Tracking workflow consists of four independent steps:

- Enhance the spatial discontinuities in seismic data using any edge detection algorithm (variance, chaos, edge detection)
- Generate the Ant Track Cube and extract the fault patches
- Validate and edit the fault patches
- Create final fault interpretation model

Goff et al ([2003](#)) described a method for extracting geologic faults from a 3D seismic attribute cube. The present method is directed to a semi-automated process for interpreting faults from a fault-enhanced 3D seismic attribute cube. The process operates in three dimensions on groups of time or horizontal slices throughout the 3D seismic cube. The faults in the input data are represented by either the high or the low end of the seismic attribute range. The general process for interpreting faults from a fault-enhanced 3D seismic attribute cube has five distinct processing steps. The first four steps are automatic. The last step is semi-automatic. The steps are as follows:

- Calculate a minimum path value at each voxel of the input 3D seismic cube to enhance the local strength of the geologic faults and to determine the local azimuthally trend of any fault passing through that voxel;
- Extract a fault network skeleton from the 3D seismic attribute cube by utilizing the

minimum path value at each voxel together with the input seismic attribute 3D cube;

- Flood fill individual fault networks, label them, and create a vector description of the fault network skeletons;
- Subdivide the fault network skeletons into the smallest, non-intersecting, non-bifurcating patches that lie on only one geologic fault;
- Correlate the individual fault patches into realistic representations of geologic faults.

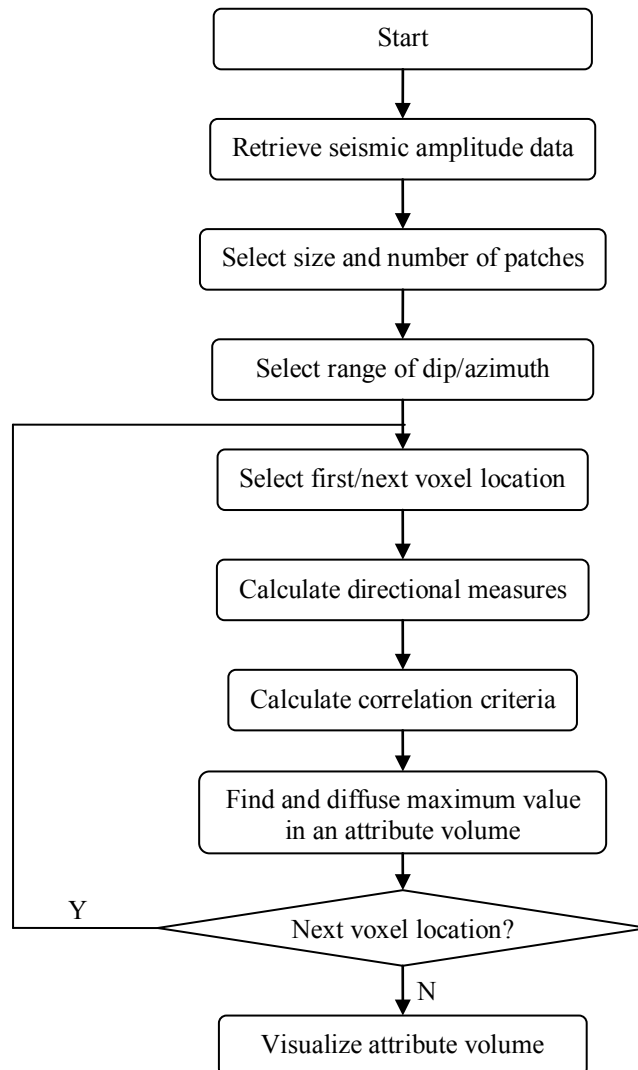


Figure 4.4 Workflow chart for the new fault detector.

In (Donias et al., 2007), Donias et al. presented a steered data-analysis approach to measure coherence for fault detection. In contrast with conventional coherence, which detects discontinuities without distinction, their approach aims to identify faults only. Assuming the local linearity of fault geometry, the method performs a continuity test using a steered data-analysis window over a set of dip/azimuth directions. A robust, selective directional continuity

test is achieved by combining measures of coherence computed from a few aligned, steered windows. Finally, fault detection consists of finding the maximum directional response and accumulating it into an attribute volume. The workflow of this approach is showed as Figure 4.4.

Seismic signal process advanced rapidly during the 1990s, allowing us to approach the problem of fault interpretation automation in a similar vein as we attack horizon interpretation. Advances in edge-detection algorithm have allowed direct illumination of faulting and seismically detectable fracture. These techniques improve manual interpretation. For some geologic plays, re-sampling of the enhanced edge attribute into a geologic model property is a simple and effective method of un-biased automated fault interpretation. Explicit methods to extract fault surfaces can utilize an automatically picked horizon indirectly through analysis of “non-picks” and gradient trend, followed by spatial correlation for vertical connectivity. Alternatively, using the familiar techniques of seeded auto-tracking, on an edge volume, shows great promise.

4.4 Conclusion

In this chapter, we propose a method of stepwise dip scanning coherence algorithm based on eigenstructure. The dip scanning of the method is conducted in two steps. In the first step, C_2 algorithm is employed to scan all dip directions; the resulted coherence values are sorted from small ones to large ones; dip directions of the larger coherence values will be kept for further use. In the second step, C_3 algorithm is implemented to search for the best dip directions among the ones we kept in the first step. As a matter of application results to real data set, the newly proposed algorithm remains a resolution as good as C_3 algorithm does, while it can also provide good coherence estimation in areas with strong structural dips. As the dip scanning is mainly conducted in C_2 algorithm in which we employ a fast algorithm, the algorithm is proved to be highly efficient.

5 3D moments-based horizon auto-tracking

Energy resources are becoming more difficult to find and develop. It has been recognized for many years that the majority of new oil and gas reserves are a function of a complex combination of geological, structural and stratigraphic elements. While the problems of exploration and the efficient development of hydrocarbon reserves have become more difficult, the volume of data to be interpreted for each project has become orders of magnitude greater over the past 30 years. Simultaneously, both the number of interpreters and the time allowed for interpretation have been substantially reduced. This drives the need for more advanced computer-aided processes that can support the interpreter by enabling more efficient, precise and effective interpretation of 3D seismic data volumes.

Visually, a seismic array is a layered image, as it reflects the stratiform structure of the earth's crust ([Blinov and Petrou, 2005](#)). The Earth subsurface consists of material layers with distinct mineral densities and porosity characteristics. The interfaces between these layers are called horizons. They are seen as bright or dark lines in gray-level reflection data and are central structures for interpretation. Other structures such as faults, channels, salt bodies, and gas chimneys are mainly identifiable by their interaction with horizons. Faults are generally sub-vertical fractures which have shifted horizons on either side; they are thus identified as discontinuity in horizons. Salt bodies are homogeneous units of salt. Due to the high seismic wave velocity of homogeneous salt, such structures can have strong reflections at their boundaries and low or no internal reflections. Areas void of horizons can thus indicate the presence of salt bodies having the property of shadowing the underlying seismic. Subsurface leakages of gas, called gas chimneys, can be indicated by the up-bulging of horizons around them and the fragmentation of the horizons in their path. A reservoir in a porous rock formation can be accurately pinpointed by identifying its upper and lower boundary. The different rock materials at the boundaries give rise to horizons in the reflection data. Therefore

horizons can be central in delineating reservoirs. In addition to these descriptive properties of horizons, horizons are perhaps the most easily identifiable objects in the seismic volume and thus of the most important objects during interpretation. As opposed to most other seismic structures, horizons can directly be identified with image processing techniques such as ridge and valley detection.

Strong reflection events visible in seismic images indicate boundaries between rock formations or strata while faults are discrete fractures across which there is measurable displacement of rock layering. Reflection seismic data images consist of adjacent time series indicating the arrival of artificially created sound waves reflected from interfaces between rock formations with differing physical properties. By analysing these traces, hypotheses about the underground structure can be developed which should merge into a consistent subsurface model.

Interpretation of horizons and faults are the backbone of seismic data interpretation. Computer-aided structural interpretation of 3D seismic data volumes has been embodied in tools in interactive seismic interpretation for a number of years. Since the early 1980s, horizon autotracking tools have been available to help increase the speed and consistency of horizon interpretation in 3D seismic surveys([Dorn, 1998](#)). More recently, techniques have been developed to provide computer-aided interpretation of horizons and automatic tracking horizon.

In this chapter, a general approach for seismic horizon auto-tracking by moments is proposed. We describe the methods in 2D case and in 3D case. The method in 2D Case is similar to cross-correlation. In 3D case, the 3D moments based method of horizon interpreting approach makes use of a two-step process: first step is computation 3D properties of the region around seed selected; second step an optimization tracking algorithm is designed for the horizon auto-tracking. The approach offers an alternative to structural methods for seismic horizon description and recognition. Experimental results are provided to illustrate the method.

5.1 A review of horizon interpretation

Horizon tracking with traditional tools can be a very time consuming task since conventional autotrackers can't jump across faults and other discontinuities and need reseeded. A seismic attribute based seismic pattern can be learnt by a neural network in order to track horizons across faults. Alberts et al ([2000](#)) use seismic attributes like instantaneous amplitude or variance to compute characteristic patterns for the horizons which interpreters are interested

in. then a neural network is trained to distinguish these patterns and work as a classifier. Intelligent search methods exclude is classifications from the result in order to track the desired horizon. The method can track several horizons simultaneously and works on 3D seismic data.

Over the last three decades, tremendous progress has been made in technique of horizon interpretation. Most of the approaches to horizon picking have concentrated in the past on treating the seismic data as 2D images ([BondÁR, 1992](#); [Maroni et al., 2001](#)). These are largely edge linking algorithms. Maroni et al use a multi-resolution approach based on wavelet analysis, followed by edge linking. There are some works done on the simultaneous 3D seismic horizon picking ([Bienati and Spagnolini, 1998](#); [Keskes et al., 1983](#); [Lavest and Chipot, 1993](#)). Lavest and Chipot ([1993](#)) built the 3D horizons by refining an initial triangulation representation. In ([Bienati and Spagnolini, 1998](#)) horizon estimation is performed by integration of local time shifts (dips) along the 3D volume. The integration procedure is simple with no global correction of accumulated error and in ([Lomask et al., 2006](#)) it is performed either in the Fourier or in the real domain. The Fourier-based approach was found to be inadequate. The problem of noise reduction as a preprocessing step of 3-D data analysis is considered in ([Fehmers and Hocker, 2003](#)). The authors use filtering based on anisotropic diffusion in order to reduce noise.

Most of the ideas in identifying the horizons in seismic data are based on the hypothesis that the seismic signal is repeated from trace to trace with only slight changes. In this case the procedure of horizon extraction consists of finding similar fragments of the signal along neighbouring traces. These methods include manual interpretation, interpolation interpretation, auto-tracking interpretation, voxel tracking, and surface slicing.

5.1.1 Manual interpretation

Traditionally, picking was done manually by drawing with pencils on paper. Manual picking is simply the manual interpretation of horizons on lines, cross-lines, time slices, and traverses. On a noisy background Human eyes have a strong capability to recognize seismic events. This is the technique with which we are all most familiar. It is also, by far, the least efficient horizon interpretation technique in terms of interpreter time and effort. While interpreting manually, the interpreter is looking for some degree of local continuity in the data, and local similarity of character to identify the event to be picked. However, manual picking has the disadvantage of being inaccurate in estimating the parameters of events, and is inefficient and expensive.

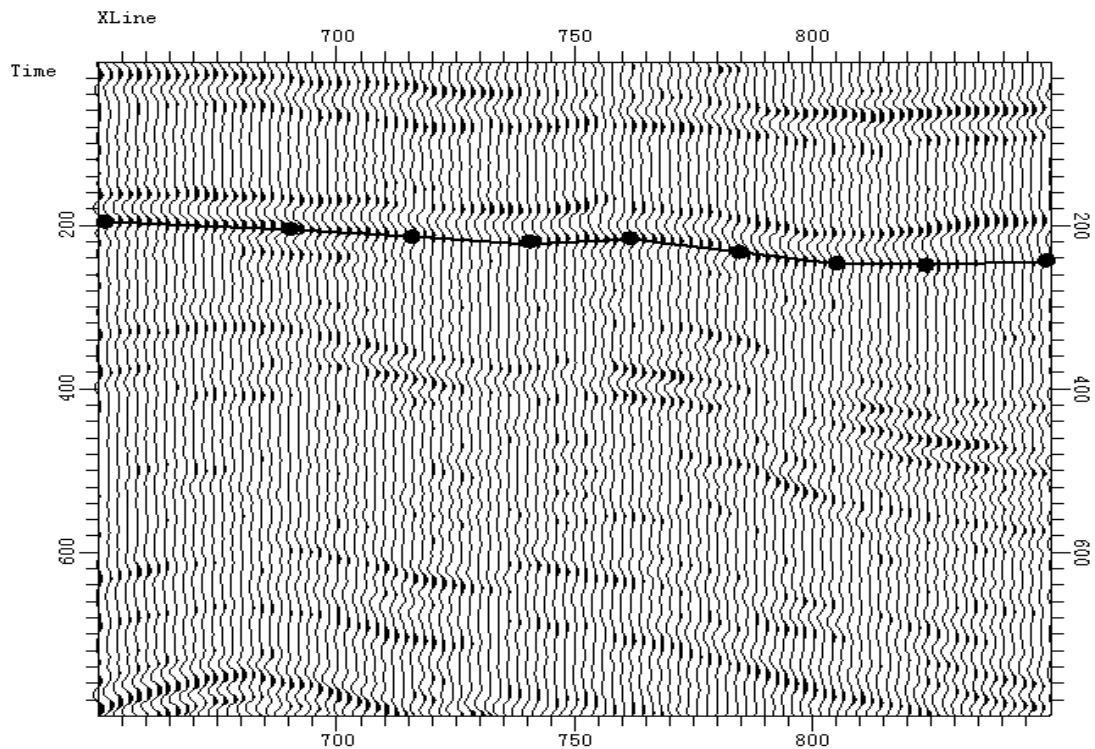


Figure 5.1 Manual interpretation

5.1.2 Interpolation interpretation

Interpolation interpretation, or semi-automated interpretation, is a horizon picking technique that is somewhat more efficient than manual interpretation. When discussing manual interpretation of horizons, the reference is to traditional line-by-line interpretation in which the interpreter is picking on specific inlines sections or cross-lines sections, usually at some specific interval (e.g. every 10 line or 20 line), as shown in Figure 5.2. Within a 3D survey, arbitrary lines may also be defined and be interpreted to get a better image of a given feature. Picks on time slices are also part of the manual interpretation process. Along with larger data volumes and better computing resources, interpretation tools have evolved to improve the reliability and speed of manual interpretation. These advances include bilinear interpolation techniques, the use of seed lines as input for various auto-pickers, and the auto-tessellation of horizon surfaces during the interpretation process. While these tools improve speed, there are still the same issues associated with manual interpretation. Each of these techniques is susceptible to error due to sampling, obliquity, intersections, relays and curved structures.

Bilinear interpolation of horizons merely interpolates values between picked seed lines, and can fail to honour faults or subtle geological changes if sampled too coarsely.

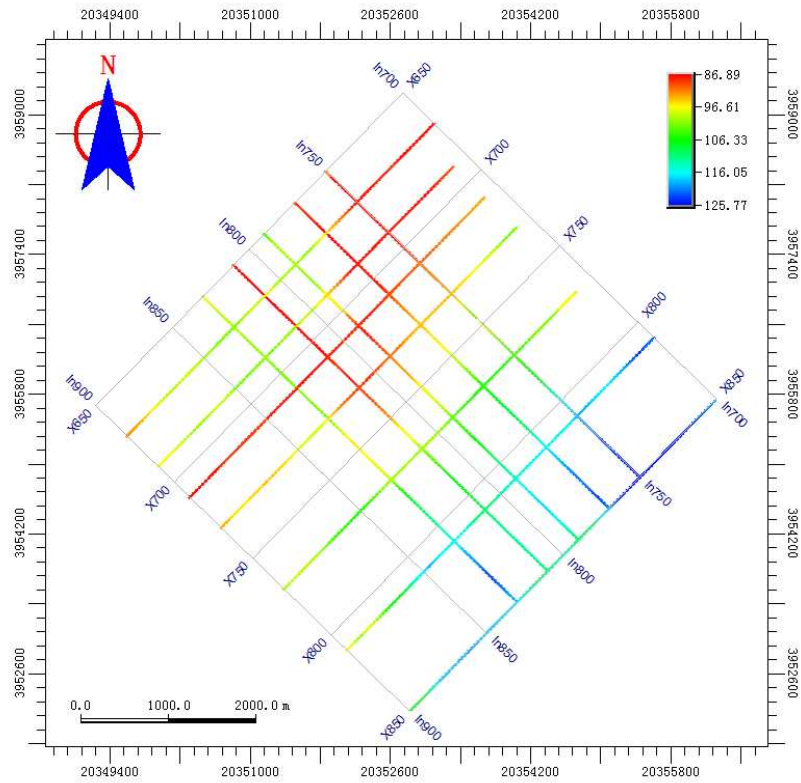


Figure 5.2 Lines interpretation before Interpolation interpretation

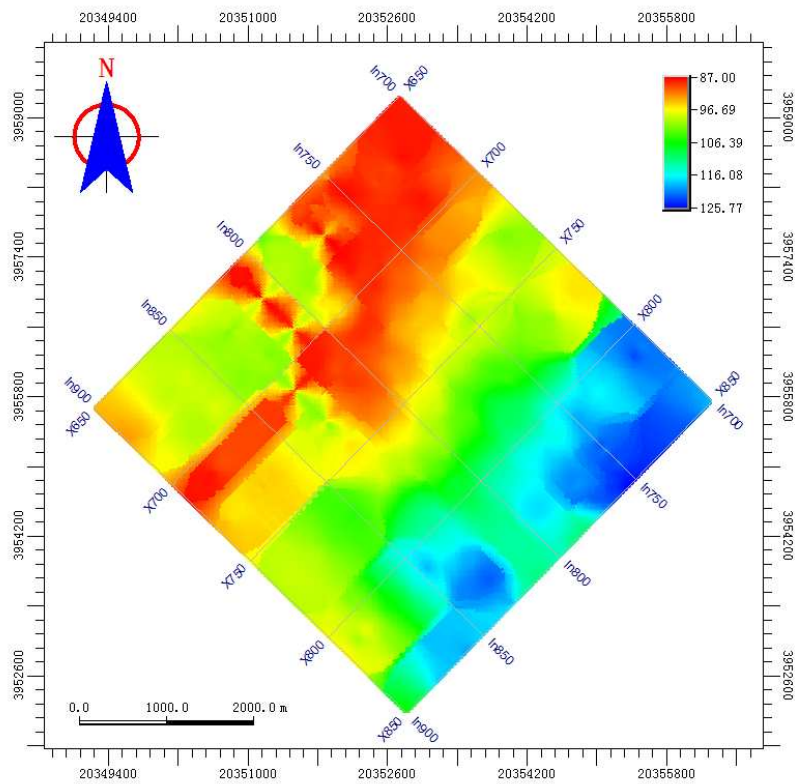


Figure 5.3 Map views of interpolation interpretation

The interpolation process can be improved if the interpreter is able to snap to the event

(minimum, maximum, zero-crossing, etc.) during the interpolation process, but behaviour at fault intersections can still be problematic. The same is true of auto-picking tools using seed lines as input. Mispicks on the initial seed lines cause erroneous surfaces, which can be difficult or time-consuming to edit. Figure 5.3 shows the result of interpolation process from Figure 5.2. Although the use of auto-tessellation to build solid surfaces while moving through the volume is valuable, it faces the same sampling issues and resultant accuracy problems between picked lines. The auto-tessellation performed in 3D visualization applications can reduce errors associated with increment sampling. For example, when interpreting faults the interpreter adjusts the line sampling as the character or orientation of the fault changes, rather than interpreting lines at a set increment.

The use of interpolation, however, assumes that the horizon is locally very smooth, and perhaps linear (or planar in two dimensions) between control points. If this assumption is violated between control points (e.g., there is a fault between the interpreted lines), then the results will be poor.

5.1.3 Auto-tracking interpretation

Since the early 1980s, auto-tracking is the most commonly employed technique for horizon tracking and has been around in interactive interpretation systems. The concept behind auto-picking is simple. A similar feature is searched on a neighbouring trace; if the feature has been found in specified constraints, the tracker moves on to the neighbouring trace.

In one prior art automatic system for tracking a horizon in a substantially horizontal direction through a 3D volume of data, a user selected at least one "seed point", which then "expanded" in all four directions within the 3D data volume until it reached the boundaries of a user specified zone. Users had the option of tracking seismic data in one of two modes.

A "seed point" is specified by its x and y location and its time or depth. It is also specified by a characteristic or attribute of the reflection at that point. Such characteristic is usually the maximum amplitude of the reflection at that location in the volume of the data. Other attributes or characteristics, such as minimum amplitude, phase, frequency, etc., of the reflection at the x, y, z point may be used. Non-iterative tracking searched the seismic traces adjacent seed points for similar amplitude values, picked the best one, then proceeded to the next available trace without double-checking the accuracy of the pick.

An iterative picking mode verified an adjacent trace as a pick by cross-referencing the previous trace. Once verified, the adjacent trace was treated as a seed point and the picking of

adjacent traces from it proceeded. Verification means that if the amplitude of the picked trace is within the limits of tolerance set by the user, the pick is accepted. Users could specify (on a scale of 1-10) the degree of amplitude similarity they would allow. If a pick did not pass this acceptance test, it was designated "dead" until at least one directly adjacent trace matched sufficiently to accept it.

Most automatic horizon tracking applications include cross-correlation or waveform based tracking algorithms to capture the seismic character over a user controlled window length. These methods also compute a "quality factor" attribute associated with the horizon pick position. Feature trackers and correlation trackers are two major classes of auto-tracking ([Dorn, 1998](#)).

- **Feature trackers:** the feature tracker will search for a similar configuration of samples within the dip window but does not perform any correlations between traces. It simply tries to track a configuration of samples on the seismic trace that defines a peak, trough, zero crossing, etc., from trace to trace.
- **Correlation trackers:** a correlation-based auto-tracker takes a portion of the seismic trace around the seed pick and correlates it with a neighbouring trace through a set of lag times that are constrained by the specified dip search window. If a lag time is found with an acceptable correlation quality factor, then the pick on the new trace is accepted, and the picker moves on to the next trace. Clearly the correlation auto-picker is much more computationally intensive than the feature tracker; it is also typically more robust in its picking.

The most effective way to detect a known signal embedded in a time series is by means of a correlation detector ([Anstey, 1964](#)). In such a detector, the signal template is correlated with the continuous data stream and at any sample where the correlation coefficient is sufficiently high, a detection is declared. Note that such detections are also classifications. The source that produced the detection must be substantially similar in location and mechanism to the source used to create the template. The auto-correlation function of a waveform is a graph of the similarity between the waveform and a time-shifted version of itself, as a function of this time-shift; and the cross-correlation function of two waveforms is a graph of the similarity between the two waveforms as a function of the time shift between them ([Anstey, 1964](#)). Cross-correlation is a linear operation, so that when it is associated with other linear operations the order in which these operations are performed does not affect the final result.

In signal processing, the cross-correlation is a measure of similarity of two signals, commonly

used to find features in an unknown signal by comparing it to a known one. Cross-correlation is essentially the same process but instead of comparing a sequence with a time shifted version of itself, it compares two different sequences. The cross-correlation function (CCF) of two sequences $x[n]$ and $y[n]$, and the cross-covariance function are defined in terms of time averages by

$$\phi_{xy}[m] = E\{x[n]y[n-m]\} \quad (4.1)$$

$$\gamma_{xy} = E\{(x[n] - \overline{x[n]})(y[n+m] - \overline{y[n]})\} \quad (4.2)$$

Both of these functions are second-order measures, with the CCF providing a statistical comparison of two sequences as a function of the time-shift between them. Cross-covariance is the same as the CCF, except that the mean values of the two sequences are removed. The CCF reflects the various frequency components held in common between the two sequences $x[n]$ and $y[n]$. In addition, it also holds vital information about the relative phases of shared frequency components. Unfortunately, when the cross-correlation of two sequences is performed, sometimes the fine detail of the shared frequency components is hard to interpret. If a detailed spectral analysis of the signals is required then it is better to use the cross-spectrum approach. However from a practical point of view there is one situation where the CCF is useful – namely when there are timing differences between two sequences. For example, suppose that $x[n]$ and $y[n]$ are identical white noise sequences which differ only in the time origin. Their CCF will then be zero for all values of m , except the one which corresponds to the timing difference.

Now let us suppose that the two signals $x[n]$ and $y[n]$, are completely uncorrelated with each other. From Equation(5.1), it can be shown that their CCF is a product of the expectation of each signal, as illustrated below.

$$\phi_{xy}[m] = E\{x[n]\} \cdot E\{y[n+m]\} \quad (4.3)$$

In an autocorrelation, which is the cross-correlation of a signal with itself, there will always be a peak at a lag of zero. Sometimes it is preferable to express the cross correlation of two signals in terms of the cross-correlation coefficient ([Oliver, 2011](#)). It is calculated by normalizing the cross-correlation of the two signals with the power of the two signals i.e. by setting $m = 0$, as illustrated in Equation(5.1). The cross-correlation coefficient lies between -1 and +1, with zero indicating no correlation between the two signals.

$$l_{xy}[m] = \frac{\phi_{xy}[m]}{\sqrt{\phi_{xx}[0] \cdot \phi_{yy}[0]}} \quad (4.4)$$

In order to make a simple implementation of cross-correlation method, we should firstly study Figure 5.4, in which the tracking principle is well shown.

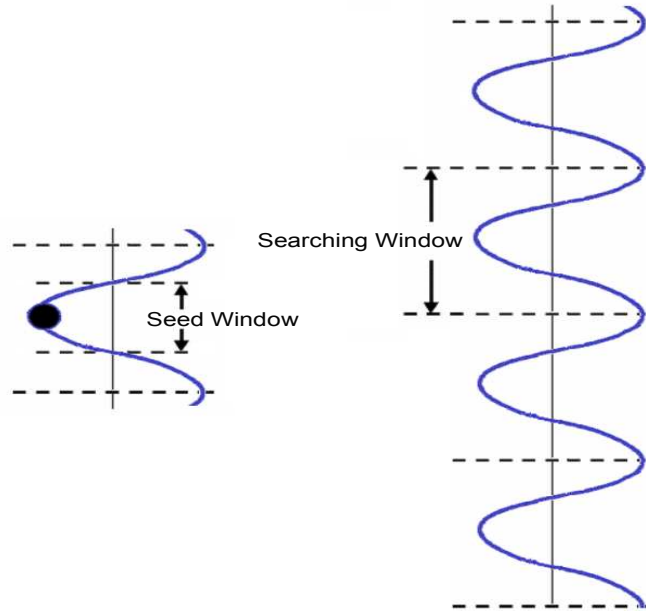


Figure 5.4 Matching process of seed.

We assume that the selected “seed” in the figure can be expressed by a k dimension vector. “ $k=2w$ ” is also actually the window size of seed. In different seismic profile, generally from the next one to the profile from which the seed is selected, the tracking is commencing. Given a search window, whose size is generally bigger than that of seed, a processing of matching is then scanned from the entire search window.

$$C(t) = \frac{\sum_{i=1}^k (\text{Seed}(i) \cdot \text{Search}(t+i))}{\sqrt{\sum_{i=1}^k (\text{Seed}(i)^2) \cdot \sum_{i=1}^k (\text{Search}(t+i))^2}} \quad (4.5)$$

If search window has the size of “ l ”, in order to look through all elements in the search window, it is necessary to calculate “ $l-k+1$ ” number of cross-correlation. Among all these “ $l-k+1$ ” cross-correlations, the maximum will be taken as the potential point which have the huge possibility of being derived from the same horizon. This processing is repeated to the next profile and continued; finally we can obtain a complete horizon tracking which appears a curve determined by the seed. An example shows the result of auto-tracking horizon by cross-correlation method in Figure 5.5.

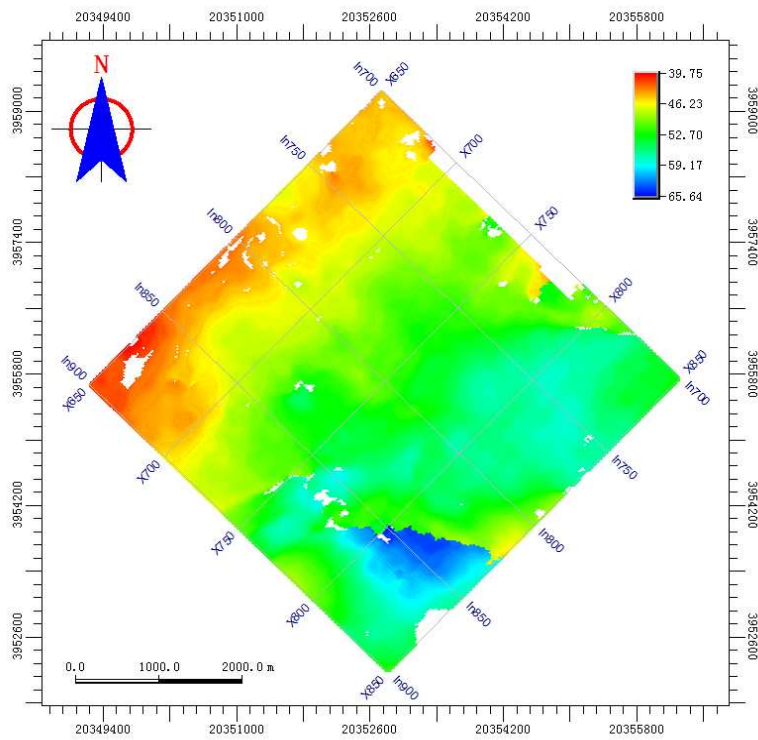


Figure 5.5 Map views of a horizon auto-tracking interpretation based on cross-correlation.

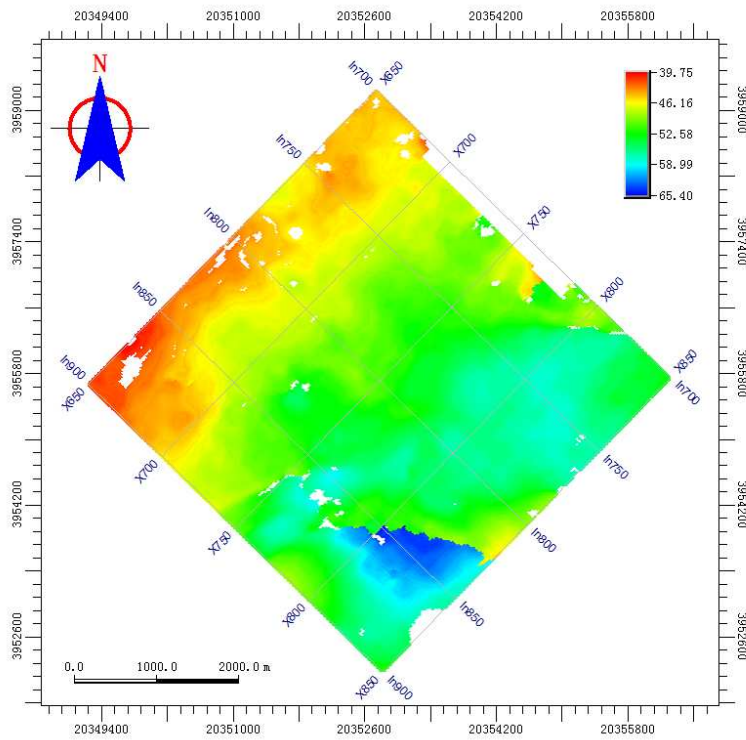


Figure 5.6 Map views of a horizon auto-tracking interpretation based on higher order statistics.

Another method recently introduced to the tracking of horizon is higher order statistics (HOS). High order statistics is widely used in system identification and the analysis of time delay etc. The horizon tracking can be therefore regarded as issue with time delay of adjacent channels which brings due to the different kinds of seismic structure. Then high order statistics can be consistent in this task. Once the time delay between the adjacent channels, we can then locate the corresponding potential points which are in fact in the same horizon.

Assume $x(t)$ and $y(t)$ are respective the statistic descriptions for “seed” and for the candidate seeds in search window:

$$\begin{aligned} x(t) &= s(n) + w_1(n) \\ y(t) &= s(n-d) + w_2(n) \end{aligned} \quad (4.6)$$

In Equation (5.6) $s(n)$ is original signal, d represents the time delay. $w_1(n)$, $w_2(n)$ are the noise. The seismic horizon tracking, therefore, is reduced to a problem to evaluate time delay d according to $x(t)$ and $y(t)$. The function based on the fourth order cumulant is then used for computing the time delay d . The desire d is generally make the function produce the maximum ([Tugnait, 1993](#); [Zhang, 1996](#)).

$$J_1(d) = \frac{|c_H [x(n-d), x(n-d), y(n), y(n)]|}{\sqrt{|c_H [x(n)]| |c_H [y(n)]|}} \quad (4.7)$$

where

$$c_H [x(n)] = \frac{1}{N} \sum_{i=1}^N x^4(n) - 3 \left(\frac{1}{N} \sum_{i=1}^N x^2(n) \right)^2 \quad (4.8)$$

$$\begin{aligned} &c_H [x(n-d), x(n-d), y(n), y(n)] \\ &= \frac{1}{N} \sum_{n=N_1}^{N_2} x^2(n-d) y^2(n) - 2 \left(\frac{1}{N} \sum_{n=N_1}^{N_2} x(n-d) y(n) \right)^2 - \left(\frac{1}{N} \sum_{n=N_1}^{N_2} x^2(n) \right) \left(\frac{1}{N} \sum_{n=N_1}^{N_2} y^2(n) \right) \end{aligned} \quad (4.9)$$

these equations seem to be complicated, in actual implementation, we just take $x(i)$ as the “seed” and $y(j)$ as the search window, then set d parameter for adjusting the location of counterpart of $x(i)$ in $y(j)$. The d which makes Equation (5.7) give the maximum value will be the desire one. Figure 5.6 shows an example of auto-tracking of horizon by HOS.

Interpretation algorithms for horizons are typically semi-automatic and require a detailed and time consuming user involvement. User steered horizon growing is a standard method. The user manually places a seed point on a horizon in a seismic slice and adjusts growing parameters before starting a growing process of the horizon. This method is not fully

interactive due to the need to set parameters and to wait for the growing to finish.

The main disadvantage of auto-tracking algorithms is that they are unable to track horizons across discontinuities. A lateral change in polarity within an event will not be recognized during auto-tracking. Also, in areas of poor signal-to-noise ratio or where a single event splits into a doublet, the auto-picking may fail to track the correct horizon. Whenever any of the search criteria are not met, the auto-tracker stops at that trace. However, an auto-tracking can be more efficient and accurate if the interpreter holds tight control over the track. This requires user-machine interaction.

5.1.4 Surface-slice interpretation

Surface slice is a technique that is a conventional approach to interpreting seismic horizons. This technique involves visualizing and interpreting really finite portions of horizons on time slice slabs of the data. The slab thickness used is a weak function of the bandwidth of the data and a stronger function of the dip of the reflections.

Surface slice approach is described in Stark ([Stark, 1991, 1996](#)), Surface-slice interpretation is an automated approach in which the analyst selects a thin slab of the seismic volume, for example at a selected depth or time, in which the automated computer system identifies potential reflective events. For example, seismic signal amplitudes above a certain threshold may be identified as reflective events. Reflective events are then similarly identified in the next incremental slab in time or depth, and are "joined" to those reflective events in the previous slice that can be considered as part of the same horizon. A set of surfaces are thus generated through the repetition of this process; for example, an anticline would appear as a set of concentric shells. The surface-slice interpretation system is often referred to as "2.5-dimensional", due to its linking of events from two-dimensional slices. While the surface-slice interpretation approach is somewhat more efficient than the volume autotracking approach, this process can be time-consuming and difficult when the geologic structure is complex or when the seismic signal is weak. In addition, discontinuities and faults encountered in complex geology can also result in ambiguities when interpreted by the surface-slice method.

A lightweight representation of volumetric data is often necessary for real-time rendering, for the segmentation of interpreted data, and for reducing visual clutter. A new Surface Wrapping technique has also been developed in accordance with an exemplary embodiment of this invention, and is described herein. For example, it allows, for example, the user to create a 3D polygonal mesh that conforms to the exterior boundary of geobodies (such as stream channels)

that offers significant improvements over existing techniques.

An inspiration for this Surface Wrapping approach was the Surface Draping algorithm ([Dorn, 1999](#)), which allows a polygonal mesh to be defined that reflects the geometry of an interpreted horizon. The surface draping algorithm is based on the metaphor of laying an elastic sheet over a contoured surface: gravity pulls the sheet down, causing it to conform to the surface beneath it, and the tension of the elastic material allows the sheet to smoothly cover small gaps in the surface while preserving the important features.

Dorn's Surface Draping allows the user to view seismic data and define a series of points slightly above the desired horizon. These points define the initial shape of the 3D mesh, which corresponds to the elastic sheet described above. When the user has completed this stage, the actual mesh is computed, generally using one vertex per voxel. These vertices are then iteratively “dropped” onto the horizon. At each step, the value of the voxel at each vertex's position is compared to a range that corresponds to the values found in an interpreted horizon. If the value falls within that range, the vertex is fixed in place.

The Surface Draping concept would have benefits if adapted to work on geobodies and other 3D volumes. Other approaches have been used to define a mesh that surrounds and conforms to the shape of a volume. Acosta et al ([2006a](#), [2006b](#)) propose a technique where the bounding surface is defined slice-by-slice by a user as a set of spline curves or general polylines that are then connected in 3D. Kobbelt et al ([1999](#)) describes a technique based on successive subdivision of an initially simple mesh that completely surrounds the volume. The above algorithms work by moving each vertex to the nearest point in the volume.

The Dorn's method comprising the steps of:

- retrieving digital data from memory corresponding to the seismic survey signals, and arranged as a plurality of traces, each trace associated with a surface location of the survey and representative of a plurality of values of at least one attribute along a depth-related dimension;
- displaying the plurality of traces as a survey representation;
- receiving inputs corresponding to a first initial surface in the survey representation;
- for each of the plurality of traces, evaluating the attribute at a plurality of points in the depth-related dimension near the first initial surface relative to a selected draping criterion;

- responsive to the evaluated attribute at one of the plurality of points meeting the draping criterion, setting a first interpreted horizon point along the depth-related dimension for each of the plurality of traces; and
- Outputting an interpreted survey representation including the first interpreted horizon points for each of the plurality of traces.

5.1.5 Voxel-based tracking

In general, auto-pickers are sensitive to variations in signal-to-noise ratio in the data; assume that the data are locally continuous, smooth, and consistent. The type of control the interpreter picks in the volume prior to auto-picking should in part be dependent on the type of algorithm being used and the path it follows through the data. A technique called voxel tracking has become available with the advent of volume rendering and visualization. (A voxel is a “volume element.” In a 3D seismic volume, it is a sample). Voxel tracking is conceptually related to auto-picking in the sense that an “event” or feature is tracked through the volume starting from seed control points which are picked by the interpreter. Voxel trackers, however, tend to follow a true three-dimensional path through the data. Starting at the seed voxel, the voxel tracker will search for connected voxel that satisfy the search criteria specified by the user. The search is typically conducted in line, cross-line, and time directions.

Like auto-picking, voxel tracking assumes that the data are locally continuous, consistent, and connected or smooth. The interpreter needs to choose the technique that will allow the best interpretation to be achieved in the most efficient manner possible. In terms of interpretive efficiency, techniques would typically be ordered, from most efficient to least efficient: voxel tracking, surface slicing, auto-picking, interpolating, and manual interpretation.

5.2 Moments-based method for horizon interpretation

As we have reviewed in section 5.1, the most commonly employed technique for horizon tracking is the so called auto-tracking or auto-picking ([Dorn, 1998](#)). These algorithms require manually selected seed points and search for similar features on neighbouring traces. The main disadvantage of auto-tracking algorithms is that they are unable to track horizons across discontinuities ([Aurnhammer and Tonnie, 2002](#)). The reason for this is the difficulty involved in locating non-ambiguous local correlation features as a result of the small amount of local information contained in seismic reflection images. When implement these algorithms, it is

necessary to select some primitive information which is called “seeds”. Once the “seeds” are chosen, the second step is tracing the horizons by the computer in the windows with the fixed sizes. The tracking is conducted according to the information of “seeds”. This processing can substantially be described as a matching processing. The tracking is achieved by matching the “seeds” in each of potential points in the searching windows.

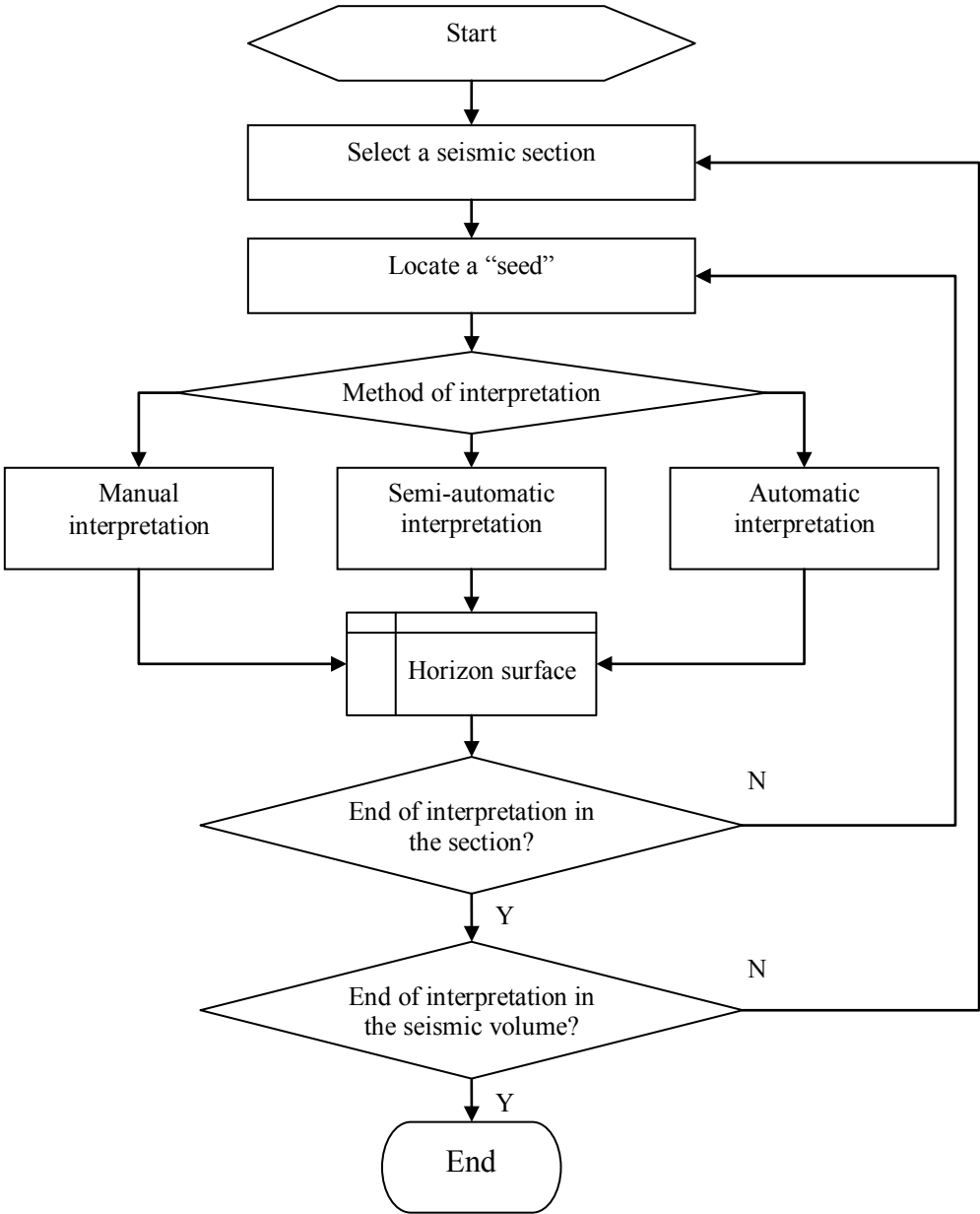


Figure 5.7 The conventional workflow chart of 2D horizon tracking.

According to the different kind of seismic data, the tracking of horizons can be classified into 2D horizon tracking and 3D horizon tracking. 2D tracking, as the name suggests, is tracking horizons in a 2D image which is the slice of original 3D seismic data. The track of horizons finally appears to be a curve in the 2D image; 3D tracking, on the other hand, is tracking a

curved surface in the 3D seismic data. In this section, we mainly discuss 2D horizon tracking and introduce Gaussian-Hermite moments to this task. The conventional workflow chart for 2D horizon tracking is denoted in Figure 5.7. As can be seen from this figure, 2D horizon tracking in fact is a loop operation which repeats the seeking of the potential point with huge relation to the seeds in the different seismic profiles. The introduction of 3D horizon propagation brings numerous advantages over traditional horizon interpretation techniques. The most recognizable advantage is speed. Another benefit is a much higher degree of accuracy in the interpretation. A third benefit, and a very important one for mapping and solid model building, is a much sharper definition of fault edges.

The moments are features of the object, which allow a geometrical reconstruction of the object. They do not have a direct understandable geometrical meaning, but usual geometrical parameters can be derived from them. The moment features have been extensively used in image analysis and description. Moments and moment functions have been widely used in image analysis and pattern recognition ([Flusser and Suk, 1993](#); [Hu, 1962](#)) with applications ranging from edge detection ([Luo et al., 1993](#)), image segmentation ([Yokoya and Levine, 1989](#)), texture analysis ([Tuceryan, 1994](#)), invariant identification, object classification, image coding and reconstruction ([Teague, 1980](#); [Teh and Chin, 1988](#)) to computer vision ([Abu-Mostafa and Psaltis, 1984](#); [Lo and Don, 1989](#)).

With the rapid development of the acquisition of multi-dimensional data, it is possible to recognize 3D objects directly. Now, 3D shape models have become more and more common. Applications such as object tracking and shape retrieval require us to consider how to choose the feature descriptors of 3D shapes and how to measure the similarities between 3D objects. In early works, moments were used mainly to estimate 3D transformations and their performances were not evaluated for classification tasks. Also, being not derived from a family of orthogonal functions, these moments were subject to correlation. Reuze et al ([1993](#)) described a method based on the 3D geometrical moments for the 3D tracking and the quantification of blood vessels from Magnetic Resonance Angiography (MRA). Canterakis ([1997](#)) extended Zernike moments to the 3D case, but their performances were not put into trial yet. In ([Werghi and Xiao, 2002](#)), Werghi and Xiao proposed to investigate the wavelet transform coefficients (WTC). The authors suggest the WTC as 3D shape descriptors of the Human body posture. Integrated within a Bayesian classification framework and compared with other standard moments, the WTC showed great capabilities in discriminating between close postures. Xu and Li ([2006a](#)) generalized curve moments from 2D to 3D Euclidean space, and use geometrical method to derive 3D curve moments invariants of different orders under similarity transformation. In ([Xu and Li, 2006b](#)) the authors introduced the surface moments,

a kind of moment can be treated as a new kind of shape descriptors of free-form surfaces and can handle the situation where 3D surface objects are not closed.

5.2.1 2D Auto-Tracking of seismic horizon

It is well-known that moments have been widely used in pattern recognition and image processing, especially in various shape-based applications. Here, Gaussian-Hermite moments are used for feature representation due to their mathematical orthogonality and effectiveness for characterizing local details of the signal ([Shen et al., 2000](#)). They provide an effective way to quantify the signal variation. We will introduce geometrical moments and Gaussian-Hermite moments to the task of horizon tracking. The principle of the usage of moments set in the task is alike as the cross-correlation. Given a seed, we compute its feature represented by geometrical moments or Gaussian-Hermite moments, of course, since the seed here is a vector; geometrical moments or Gaussian-Hermite moments used are 1D dimension. Taking the seed's feature as the reference, we then search the most matched template in the search window for each seismic profile. As we know, the processing is sustainably a template matching in the search window. The matching result is determined by the minimum of Euclidean distance.

Here, we should present the 1D geometrical moments

$$\eta_p = \int_{-w}^w x^p f(x) dx \quad (4.10)$$

and the 1D Gaussian-Hermite moments

$$\eta_p = \int_{-w}^w f(x) \hat{H}(x; \sigma) dx \quad (4.11)$$

We first define a metric to describe the feature of each sample with a 1D vector by several order of moment. We should take the seed size into account when select moment to construct the feature. When seed window is small such as 7 or 9 pixels, the moment with order greater than the number is meaningless. In the actual implementation, before we use geometrical moments or Gaussian-Hermite moments, we should construct the feature vector to represent the original seed or the seeds in the search window. The feature vector is constructed by

$$\mathbf{V} = [\eta_0, \eta_1, \eta_2, \dots, \eta_p] \quad (4.12)$$

Of course, it is not necessary to construct the feature vector with all order of moments. We

can arbitrarily select the moment with certain orders however, different order of moment constructing the feature vector, the different representation ability will exhibit. Finally, we can get a distance for each sample region i :

$$D_{t,t+1}^i = D_e(P_t, P_{t+1}^i) \quad (4.13)$$

Among the candidates sample P_{t+1}^i , the point with lowest value of $D_{t,t+1}^i$, is selected as potential candidate:

$$\hat{P}_{t,t+1}^i = \min\{D_{t,t+1}^i\} \quad (4.14)$$

5.2.2 The workflow for 2D horizon tracking using moments

Figure 5.8 illustrates a workflow chart of 2D horizon tracking using moments. The workflow begins with initial horizon surface placement process. Once the initial horizon surface is complete, horizon tracking by moments process is performed to iteratively move each point of the surface toward a reflective event. Firstly an initial seismic section is selected. In this seismic section, a first trace $T_{(x,y)}$ of the survey upon which the searching is to take place, where the values of the indices x and y indicate the position of the trace in the x and y surface directions in the survey. Following initial trace process, one pattern “seed point” is selected from human analysis. The “seed point” is also specified by a characteristic or attribute of the reflection at that point. In order to match pattern, we define a queue to store the candidate “seed”.

We compute the feature vector by geometrical moments or Gaussian-Hermite moments, and push the potential candidates from neighbour traces of the initial trace $T_{(x,y)}$ in this section. Then we pop a candidate “seed” from seed queue. In the range of searching window, we can evaluate a serial of features upon determination of the candidate “seed”. By Equation (5.13) we get the Euclidean distance between the feature of the pattern “seed” and each feature. The candidate with lowest value is draped as potential candidate “seed”. If this “seed” is verified and satisfied, it is recorded in horizon surface and pushed to seed queue. Verification means that if the matching result is within the limits of tolerance set by the interpreter, the tracking is accepted. We continue “pop-evaluate-push” process until the queue of the candidate seeds is empty.

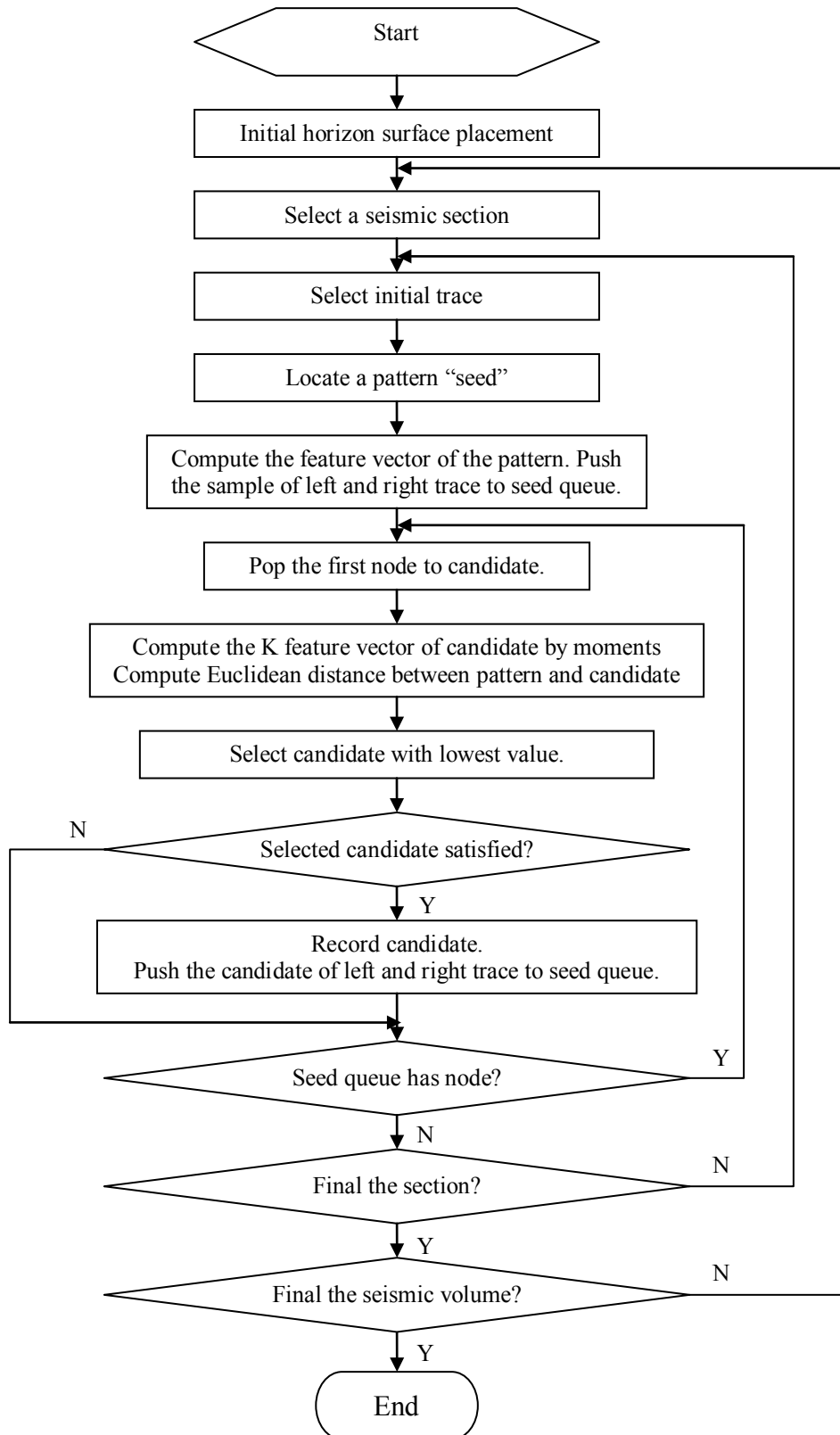


Figure 5.8 The workflow chart of 2D horizon tracking using moments.

When the seed queue is empty, another decision is performed to determine if the horizon tracking is final in the seismic section. If tracking is not over the section, another initial trace is selected to continue; otherwise a new seismic section is checked out to continue process.

5.2.3 Definition of 3D moments

With the rapid development of the acquisition of three-dimensional information, it is possible for us to recognize the shapes of 3D objects directly. Applications such as object tracking and shape retrieval require us to consider how to choose the feature descriptors of 3D shapes and how to measure the similarities between 3D objects. Although recognition of objects from 1D projection (i.e. seismic trace correlation) and 2D projections has been widely studied among the horizon auto-tracking, little research has been devoted to recognition using 3D information.

5.2.3.1 3D geometric moments

In order to describe the 3D geometric moments algorithm we are interested in here, we first reformulate the 2D version of the geometric moments and then proceed to its 3D generalization. The definition of the geometric moments m_{pq} in equation (3.2) of a 2D discrete field $f(i,j)$ is:

$$M_{pq} = \sum_{i=0}^{N_x-1} \sum_{j=0}^{N_y-1} i^p j^q f(i,j) \quad (4.15)$$

For any non-negative integers p , q and r , the 3D moments of order $p + q + r$ of a density distribution function $f(x, y, z)$ are defined in terms of the Riemann integrals as:

$$M_{pqr} = \iiint_{xyz} x^p y^q z^r f(x, y, z) dx dy dz. \quad (4.16)$$

It is assumed that $f(x, y, z)$ is a piecewise continuous and therefore bounded and it is non-zero only in a finite part of R^3 space, moments of all orders exist and their sequence M_{pqr} is uniquely determined by $f(x, y, z)$. In the same way $f(x, y, z)$ is uniquely determined by M_{pqr} ([Sadjadi and Hall, 1980](#)).

The moment generating function for 3D moments may be defined as

$$M(u_1, u_2, u_3) = \iiint_{xyz} \exp[u_1 x + u_2 y + u_3 z] f(x, y, z) dx dy dz. \quad (4.17)$$

which can be expanded into a power series,

$$M(u_1, u_2, u_3) = \iiint_{xyz} \sum_{p=0}^{\infty} \frac{1}{p!} (u_1 x + u_2 y + u_3 z)^p f(x, y, z) dx dy dz. \quad (4.18)$$

Their formulation in the discrete case is:

$$M_{pqr} = \sum_{i=0}^{N_x-1} \sum_{j=0}^{N_y-1} \sum_{k=0}^{N_z-1} (i \Delta x)^p (j \Delta y)^q (k \Delta z)^r f(i \Delta x, j \Delta y, k \Delta z). \quad (4.19)$$

where $N_x, N_y, N_z, \Delta x, \Delta y, \Delta z$ define the 3D local region. The centroid of the 3D region can be determined from the zeroth and the first-order moments by

$$\bar{x} = \frac{M_{100}}{M_{000}}, \quad \bar{y} = \frac{M_{010}}{M_{000}}, \quad \bar{z} = \frac{M_{001}}{M_{000}}. \quad (4.20)$$

Then 3D central geometric moments are defined as:

$$\mu_{pqr} = \iiint_{xyz} (x - \bar{x})^p (y - \bar{y})^q (z - \bar{z})^r f(x, y, z) dx dy dz. \quad (4.21)$$

Trivially, when the center of mass $(\bar{x}, \bar{y}, \bar{z})$ is at the origin, the raw moments become the central moments.

5.2.3.2 3D Gaussian-Hermite moments

In order to describe the 3D Gaussian-Hermite moments algorithm, we also proceed 2D definition to its 3D generalization. From the 2D Gaussian-Hermite moments defined in section 3.2.1, the 3D Gaussian-Hermite moments for solids of order $p+q+r$ of a 3D density function are defined by Riemann integrals

$$\eta_{pqr} = \int_{-\infty}^{\infty} \int_{-\infty}^{\infty} \int_{-\infty}^{\infty} \hat{H}_p(x/\sigma) \hat{H}_q(y/\sigma) \hat{H}_r(z/\sigma) f(x, y, z) dx dy dz. \quad (4.22)$$

If the density function is piecewisely continuous and bounded in a finite region in 3D Euclidean space, then moments of all orders exist. Their formulation in the discrete case is:

$$\eta_{pqr} = \sum_{i=0}^{N_x-1} \sum_{j=0}^{N_y-1} \sum_{k=0}^{N_z-1} \hat{H}_p(i) \hat{H}_q(j) \hat{H}_r(k) f(i, j, k). \quad (4.23)$$

or

$$\eta_{pqr} = \frac{8}{(N_x - 1)(N_y - 1)(N_z - 1)} \sum_{i=0}^{N_x-1} \sum_{j=0}^{N_y-1} \sum_{k=0}^{N_z-1} \hat{H}_p(\Delta x / \sigma) \hat{H}_q(\Delta y / \sigma) \hat{H}_r(\Delta z / \sigma) f(i \Delta x, j \Delta y, \Delta z). \quad (4.24)$$

where $N_x, N_y, N_z, \Delta x, \Delta y, \Delta z$ define the 3D local region. Then 3D central Gaussian-Hermite moments are defined as:

$$\tilde{\eta}_{pqr} = \int_{-\infty}^{\infty} \int_{-\infty}^{\infty} \int_{-\infty}^{\infty} \hat{H}_p(x/\sigma - \bar{x}) H_q(y/\sigma - \bar{y}) H_r(z/\sigma - \bar{z}) f(x, y, z) dx dy dz. \quad (4.25)$$

where $\bar{x}, \bar{y}, \bar{z}$ is defined in equation (5.20) and discrete case has form:

$$\tilde{\eta}_{pqr} = \frac{8}{(N_x - 1)(N_y - 1)(N_z - 1)} \sum_{i=0}^{N_x-1} \sum_{j=0}^{N_y-1} \sum_{k=0}^{N_z-1} \hat{H}_p(\Delta x/\sigma - \bar{x}) H_q(\Delta y/\sigma - \bar{y}) H_r(\Delta z/\sigma - \bar{z}) f(\Delta x, \Delta y, \Delta z) \quad (4.26)$$

5.2.4 3D moments-Based estimation of local features

The local characteristics of the structure are expressed in terms of geometry and intensity information. They are computed from the 3D moments up to the order 2 inside a cube window centred on the point of interest.

It is possible to compute from the ten moments up to order 2 ($M_{000}, M_{100}, M_{010}, M_{001}, M_{110}, M_{101}, M_{011}, M_{200}, M_{020}, M_{002}$):

- the position of the centre of the local region:

$$C = (\bar{x}, \bar{y}, \bar{z}). \quad (4.27)$$

- two angles, α, β , as angles maximizing the Z inertia and minimizing the X and Y inertia of the cube windows rotated first by α around the OZ axis and then by β around the OY axis:

$$\alpha = \frac{1}{2} \arctan\left(\frac{2M_{110}}{M_{200} - M_{020}}\right) \quad k \frac{\pi}{2}, \quad (4.28)$$

$$\beta = \frac{1}{2} \arctan\left(\frac{2M_{101} \cos \alpha + M_{011} \sin \alpha}{M_{002} - M_{200} \cos^2 \alpha - M_{020} \sin^2 \alpha - M_{110} \sin 2\alpha}\right) \quad k \frac{\pi}{2}. \quad (4.29)$$

5.2.5 Representation program of 3D moments

The algorithm for computing the 3D geometric moments is illustrated by pseudo-codes in Table 5.1. Computing the discrete version of Gaussian-Hermite polynomials and 2D Gaussian-Hermite moments are given in section 3.2.2. 2D Gaussian-Hermite moments are

easily extended to the 3D case. The moments up to order (M, N, L) can be computed by the algorithm in Table 5.2.

Table 5.1 Pseudo code of 3D geometric moments computation.

```

For  $p = 0$  to  $M$ 
  For  $q = 0$  to  $N$ 
    For  $r = 0$  to  $L$ 
      For  $x = 0$  to  $N_x - 1$ 
        For  $y = 0$  to  $N_y - 1$ 
          For  $z = 0$  to  $N_z - 1$ 
             $Mom(p, q, r) += Img(x, y, z) * x^p * y^q * z^r$ 
          End for
        End for
      End for
    End for
  End for
End for

```

Table 5.2 Pseudo code of 3D Gaussian-Hermite moments computation.

```

For  $p = 0$  to  $M$ 
  For  $q = 0$  to  $N$ 
    For  $r = 0$  to  $L$ 
      For  $x = 0$  to  $N_x - 1$ 
        For  $y = 0$  to  $N_y - 1$ 
          For  $z = 0$  to  $N_z - 1$ 
             $Mom(p, q, r) += Img(x, y, z) * \hat{H}(p, x) * \hat{H}(q, y) * \hat{H}(r, z)$ 
          End for
        End for
      End for
    End for
  End for
End for

```

According to the algorithms, we can get the 3D moments parameters of the local region around the seed sample.

5.2.6 Pattern matching algorithm of seismic horizon

Tracking of seismic horizon is initiated interactively, selecting a point, P_t , on the seismic volume. An iterative multi-resolution algorithm is applied to adjust this position on the seismic track. The local characteristics of region are then estimated accurately.

The matching, between the referent region centred on P_t and each region centred on point around P_t , is performed using the characteristic of the second order moments. We can get a distance for each region i :

$$D_{t,j+1}^i = \frac{0.5}{\alpha_1} D_e(\mu_{2(1)} P_t, \mu_{2(1)} P_{t+1}^i) + \frac{0.5}{\alpha_2} D_e(\mu_{2(2)} P_t, \mu_{2(2)} P_{t+1}^i). \quad (4.30)$$

where D_e is the Euclidean distance, α_1, α_2 are normalization coefficients, $\mu_{2(1)}$ designates the second order moments μ_{110}, μ_{101} , and μ_{011} , and $\mu_{2(2)}$ designates the second order moments μ_{200}, μ_{020} , and μ_{002} . the second order moments are split in two groups because their stand deviations differ.

Among the candidates P_{t+1}^i , the point with lower value of $D_{t,j+1}^i$, is selected as potential candidate:

$$\hat{P}_{t,j+1}^i = \min \{ D_{t,j+1}^i \} \quad 1 \leq i \leq K \quad (4.31)$$

where K is difference between the searching windows and the sample windows.

5.2.7 The workflow for 3D horizon tracking using moments

3D seismic interpretation often involves the picking of horizon surface to characterize the subsurface for the delineation of underground features relevant to the exploration, identification and production of hydrocarbons. The workflow begins with initial horizon surface placement process. Once the initial horizon surface is complete, 3D horizon tracking by moments process is performed to iteratively move each point of the surface toward a reflective event.

Firstly an initial trace $T_{(x,y)}$ of the survey upon which the searching is to take place, where the values of the indices x and y indicate the position of the trace in the x and y surface directions in the survey. Following initial trace process, one pattern “seed point” at time or depth s is selected from human analysis.

The difficulty for automatic horizon extraction exists at least in two fold:

- the selection of picks in a trace usually ignores lateral continuity;
- the trace traversal order can result in significantly different horizons so that the resulting picks in the same horizon often conflict with each other.

So the selections of initial “seed point” and initial trace are important to achieve a desired result of 3D horizon tracking. As shown (Figure 5.9), among several candidate seeds, Seed B or C is an optimal initial candidate.

In order to match pattern, we define a queue to store the candidate “seed point”. We compute the feature vector by geometrical moments or Gaussian-Hermite moments, and push the “seed” to queue. candidates from eight initial trace $T_{(x,y)}$ in this section.

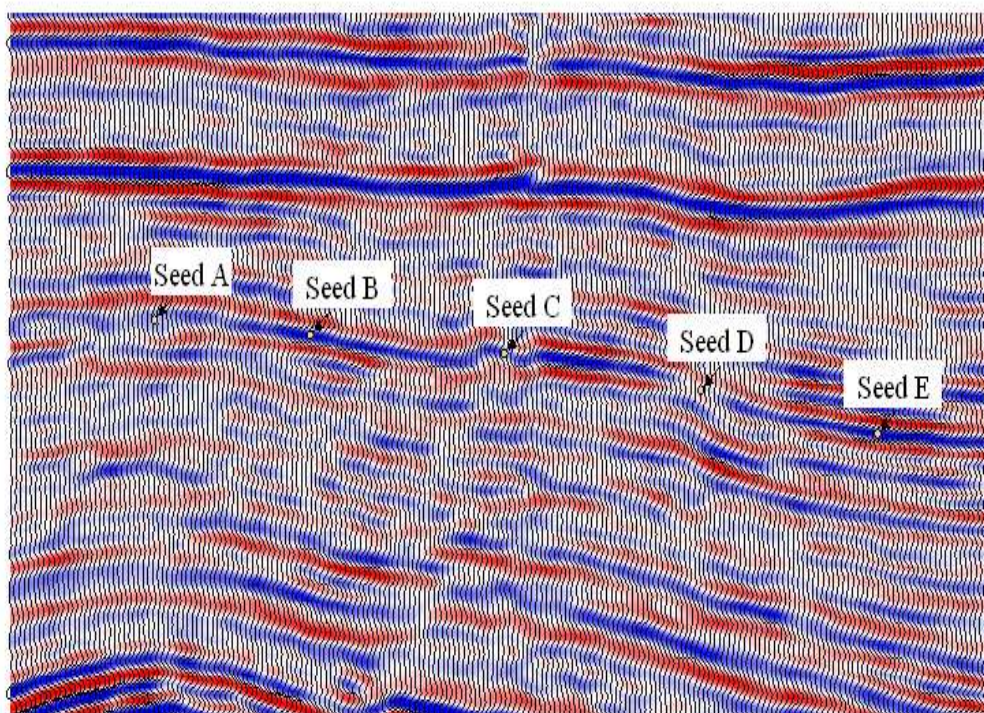


Figure 5.9 An example of selecting initial “seed point”.

Then we sort the queue in ascending order upon the distance value and pop first candidate “seed” from the queue. For each of eight neighbour traces of the trace which candidate seed is within, we can evaluate a serial of features upon determination of the candidate “seed” in the range of searching window. By Equation (5.30) we get the Euclidean distance between the feature of the pattern “seed” and each feature. The candidate with lowest value is selected as potential candidate “seed”. If this candidate “seed” is verified and satisfied, it is recorded in

horizon surface and pushed to queue. We continue “pop-evaluate-push” process until the queue of candidate seeds is empty.

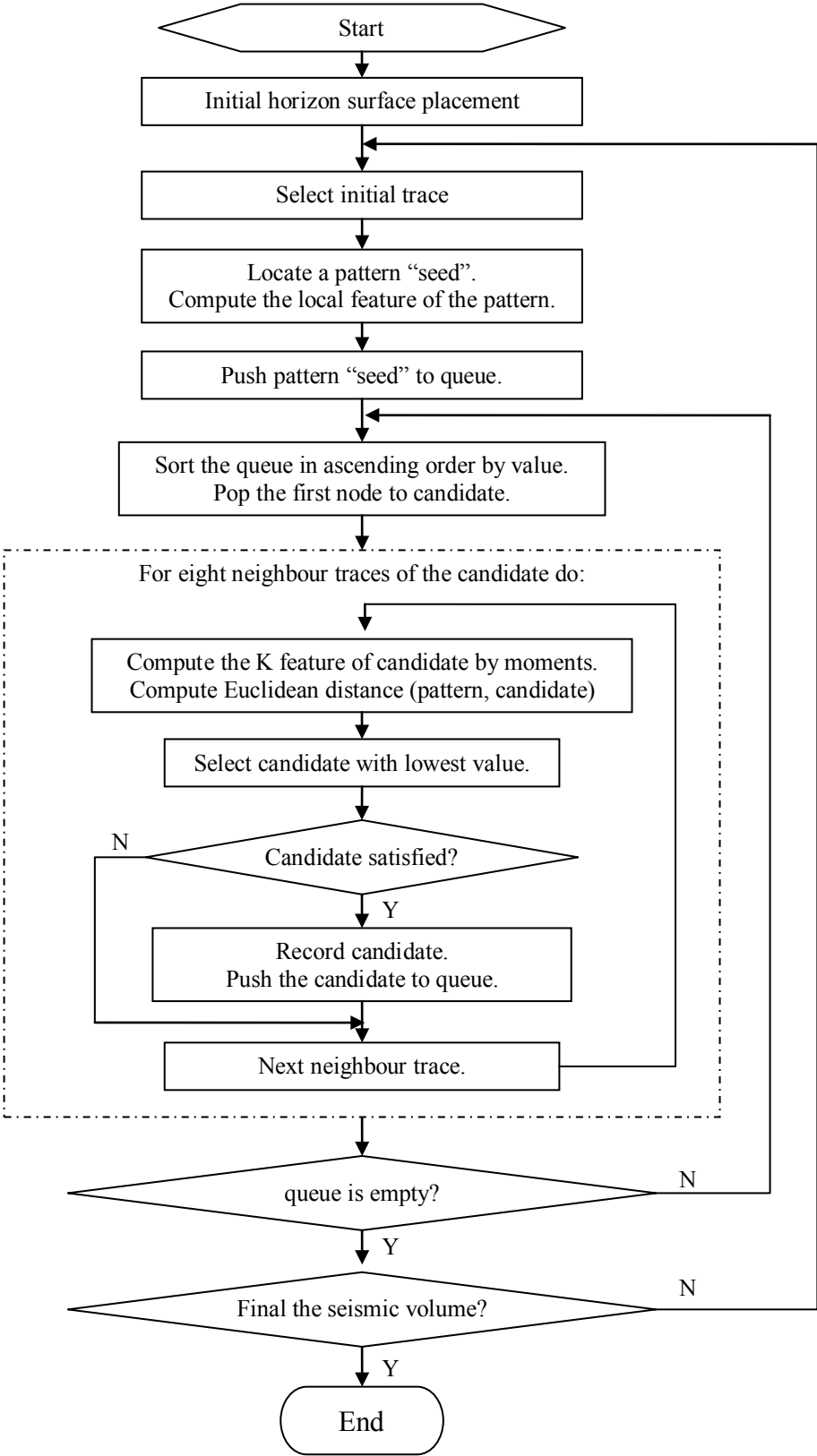


Figure 5.10 The workflow chart of 3D horizon tracking using moments.

When the seed queue is empty, another decision is performed to determine if the horizon tracking is final in the seismic volume. If tracking is not over the volume, another initial trace is selected to continue; otherwise the tracking end. The workflow chart shows in Figure 5.10.

5.3 Horizon auto-tracking in real seismic data sets

The described algorithm was tested on 2D seismic images and 3D seismic volume from 3D seismic data. 2D seismic images include one without fault and another with some seismic faults. Auto-tracking within 3D volume we also test two different environments, one has few of faults and another has much faults.

5.3.1 2D horizon tracking tasks

Two seismic images extracted from a 3D seismic slice data are used for horizon tracking task. These two images are extracted from the different regions in which the definitely different geologic properties are exhibited.

The first image is shown in Figure 5.11. We can observe that some horizons in the image are very obvious and most of them are continuous, because there are no faults, horizon tracking in this image will be more satisfy. Cross-correlation, and higher order statistics, geometrical moments, and Gaussian-Hermite moments are carried out for such aim. The two horizons are tracked. The results are respectively shown as follows. Auto-tracking starts with selection of initial seed. Two seeds are manually selected for the tracking mission. These seeds are derived from either “peak” or “through” and they are taken from the different regions of the image. In our experiment, we give an obvious mark on these seeds; a black cross in a little circle is used to stand out these seeds. The tracked horizons are labelled by the green lines.

The parameters for this experiment are: 9 pixels for seed window and 15 pixels for search window. The threshold is 80%. For geometrical moments and Gaussian-Hermite moments, σ is set to 0.5, the feature is represented by the vector $[\eta_0, \eta_1, \eta_2, \eta_3, \eta_4, \eta_5, \eta_6]$.

As can be seen from the Figure 5.12 to Figure 5.15, for the top one and the bottom one, four methods all give the relatively satisfactory tracking results. It should be noted here that for the seed located in the bottom of the image, cross-correlation and higher order statistics give the few smoothing tracking lines, because the tracking lines have the apparent echelonments.

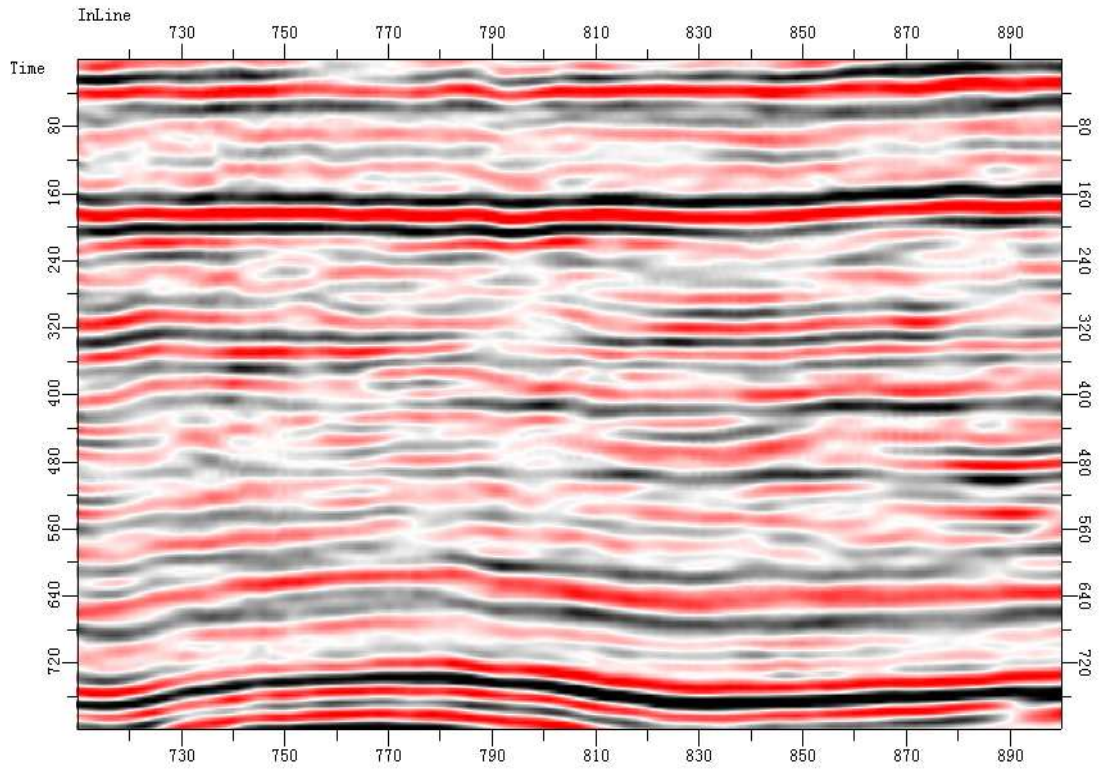


Figure 5.11 First real seismic image for 2D horizon tracking.

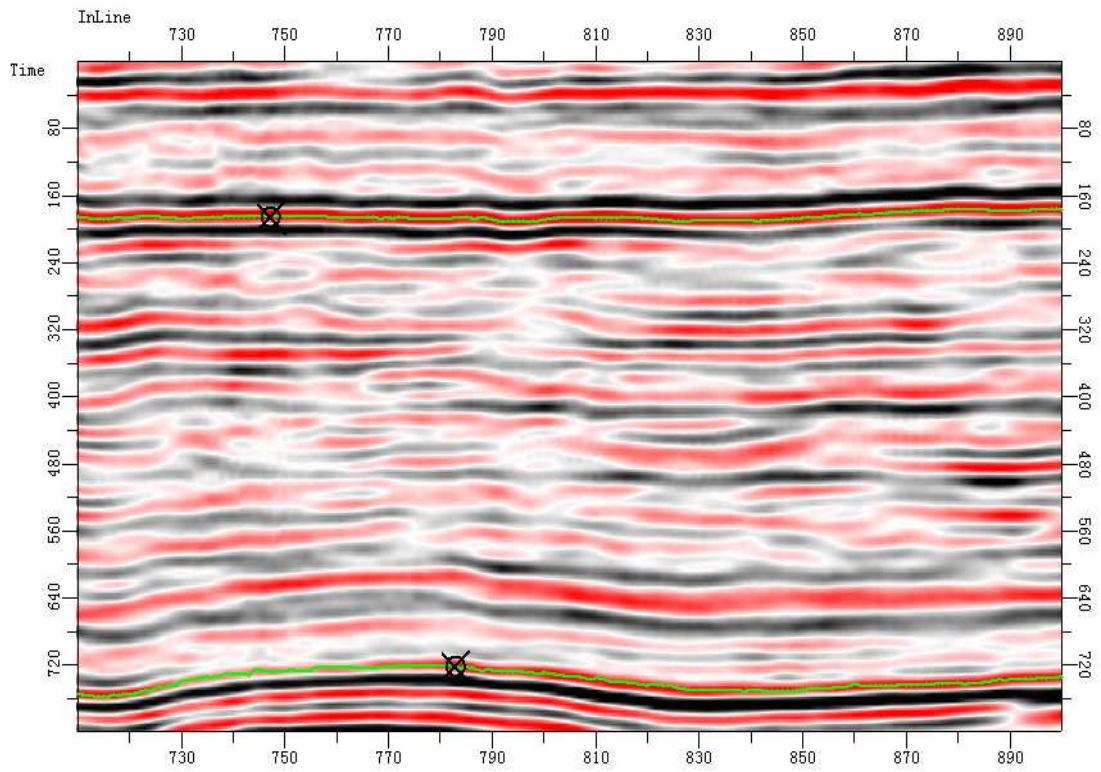


Figure 5.12 2D horizon tracking by correlation method in first seismic image.

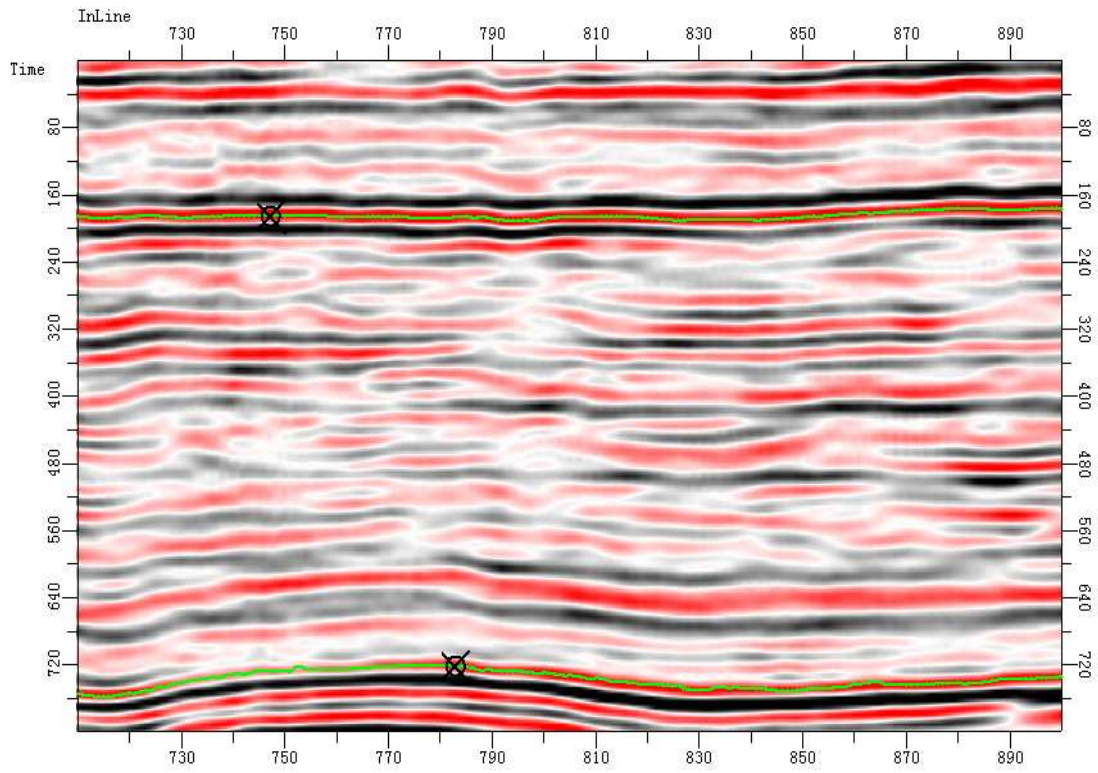


Figure 5.13 2D Horizon tracking by higher order statistics in first seismic image.

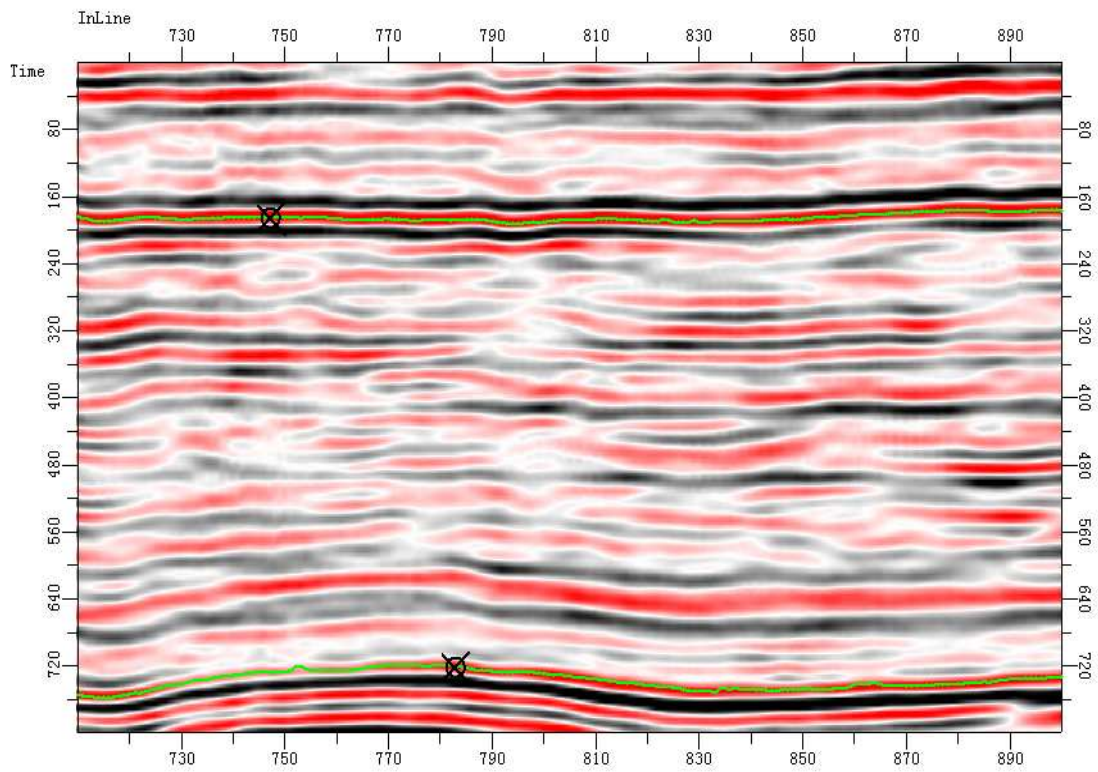


Figure 5.14 2D Horizon tracking by geometrical moments in first seismic image.

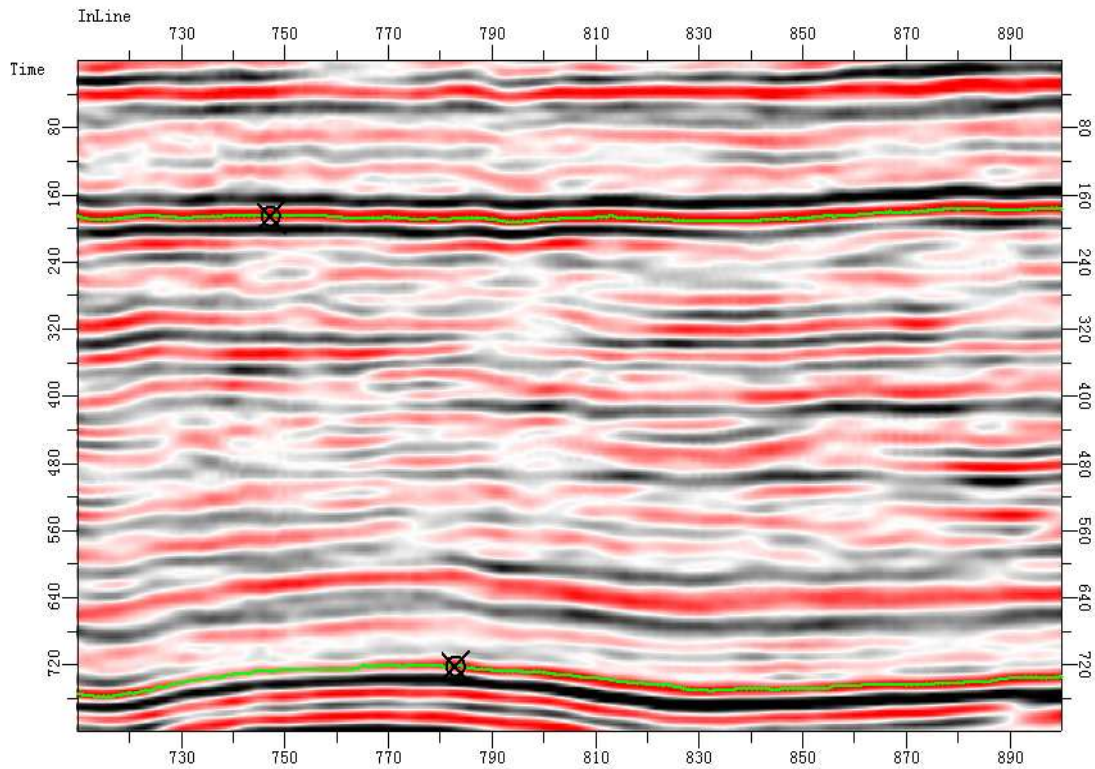


Figure 5.15 2D Horizon tracking by Gaussian-Hermite moments in first seismic image.

We can observe from these four figures, compared with correlation higher order statistic, and geometrical moments, Gaussian-Hermite moments gives a more exactly tracking than those from the other two methods. They offer more reasonable tracking around the discontinuous areas, which can be learned from the two discontinuities located in the left and the middle of the images.

The second experiment is carried out on a seismic image which contains a obvious fault. In general, horizon tracking can be hardly continued when the faults are in presence. So, under this condition, the tracking results also reflect the performance of the proposed methods. As can be seen in Figure 5.16, both the fault and the other influences make the horizons discontinuous and obscuring. And the effects have the different degrees in the different locations. The corresponding tracking results are shown in Figure 5.17 to Figure 5.20.

The parameters are updated for this task: seed window has 9 pixels and the search has 15 pixels. For Gaussian-Hermite method, all parameters are the same as those in the first experiment. From up to bottom, the first seed is selected clearly in the horizons with the faults. The seed has the narrow discontinuation which means the relatively easy tracking of this horizon. All methods show the correct tracking for the first seed. The second seed located in the bottom of the image distinguish four methods greatly.

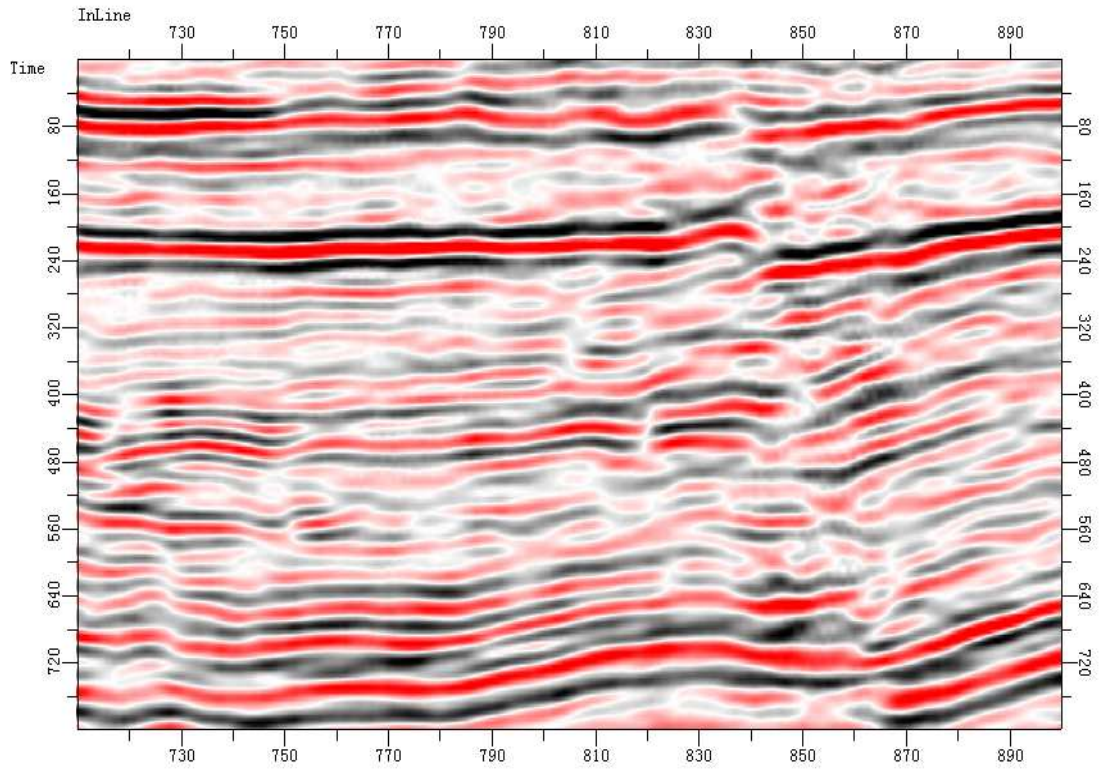


Figure 5.16 Second real seismic image for 2D horizon tracking.

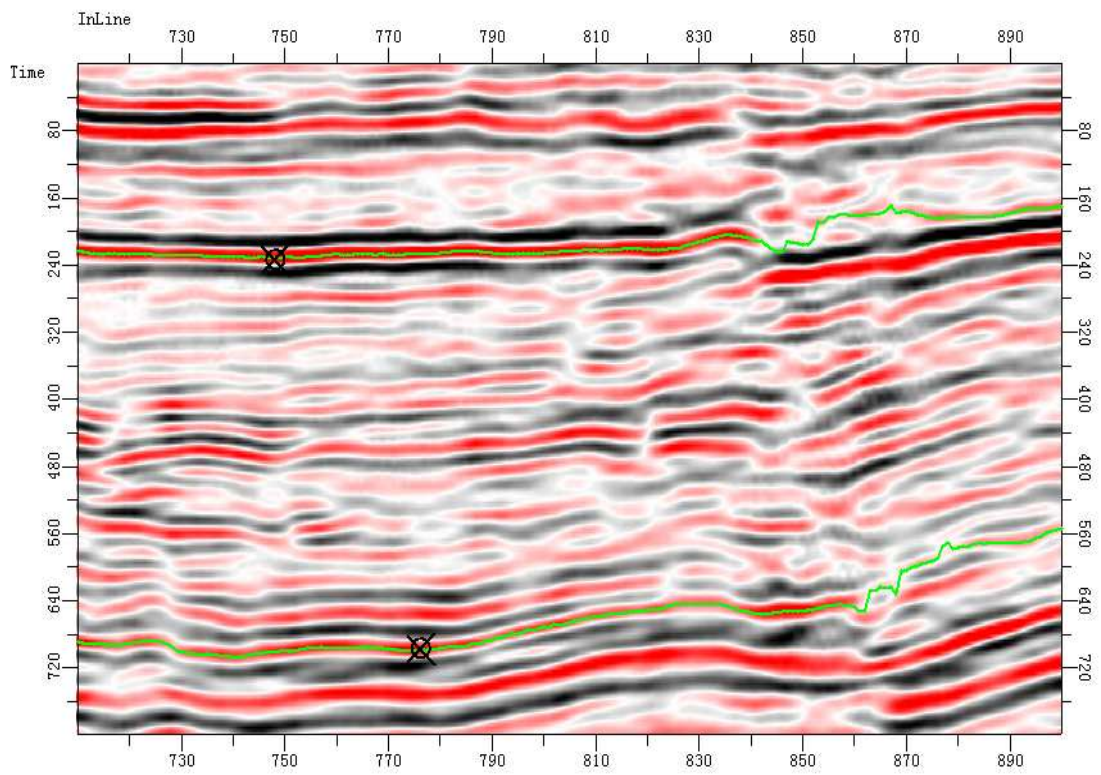


Figure 5.17 2D Horizon tracking by correlation method in second seismic image.

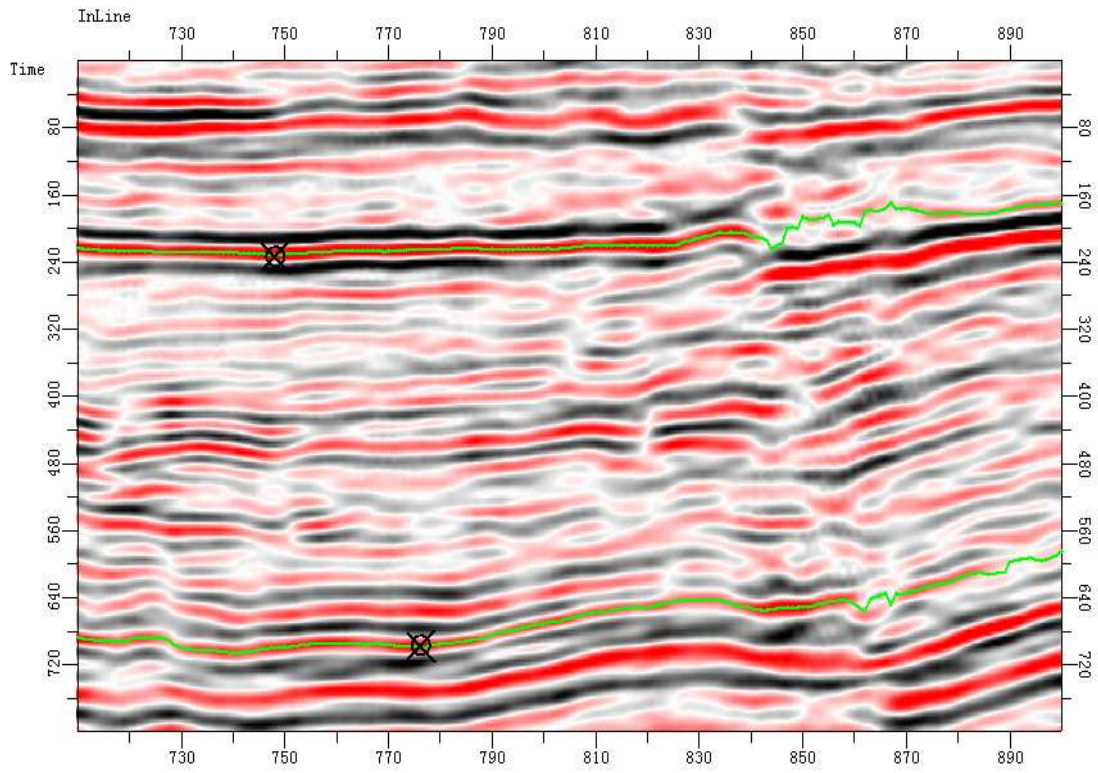


Figure 5.18 2D Horizon tracking by higher order statistics in second seismic image.

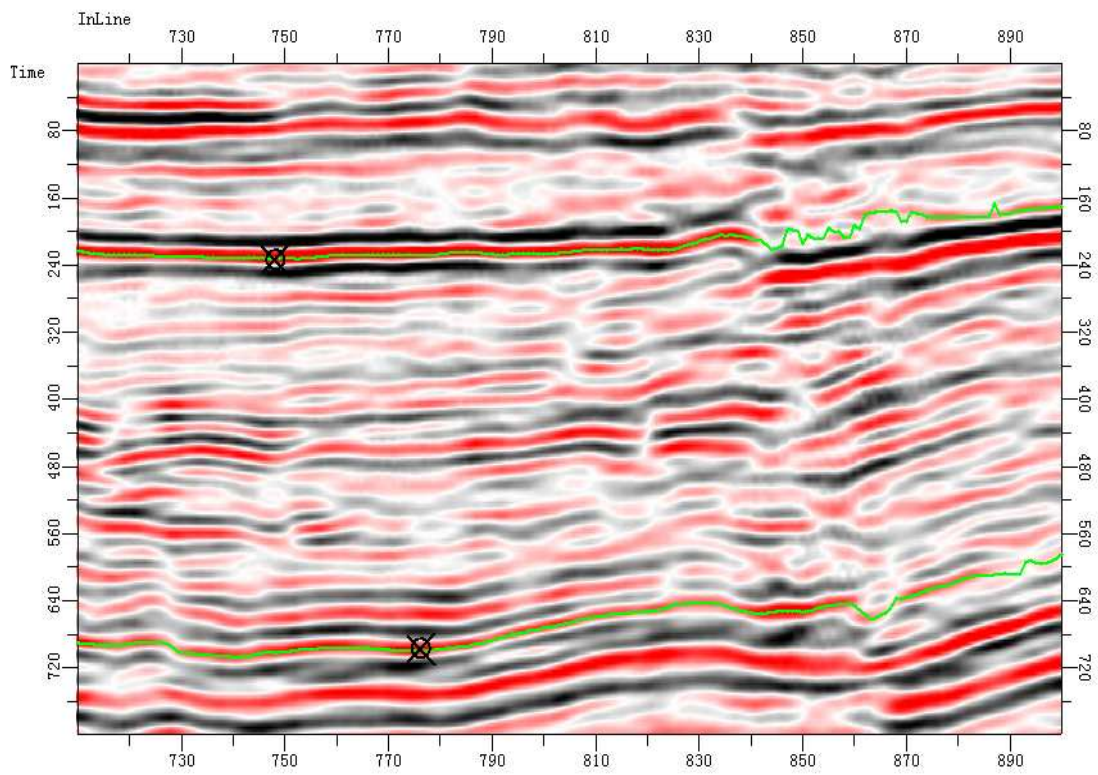


Figure 5.19 2D Horizon tracking by geometrical moments in second seismic image.

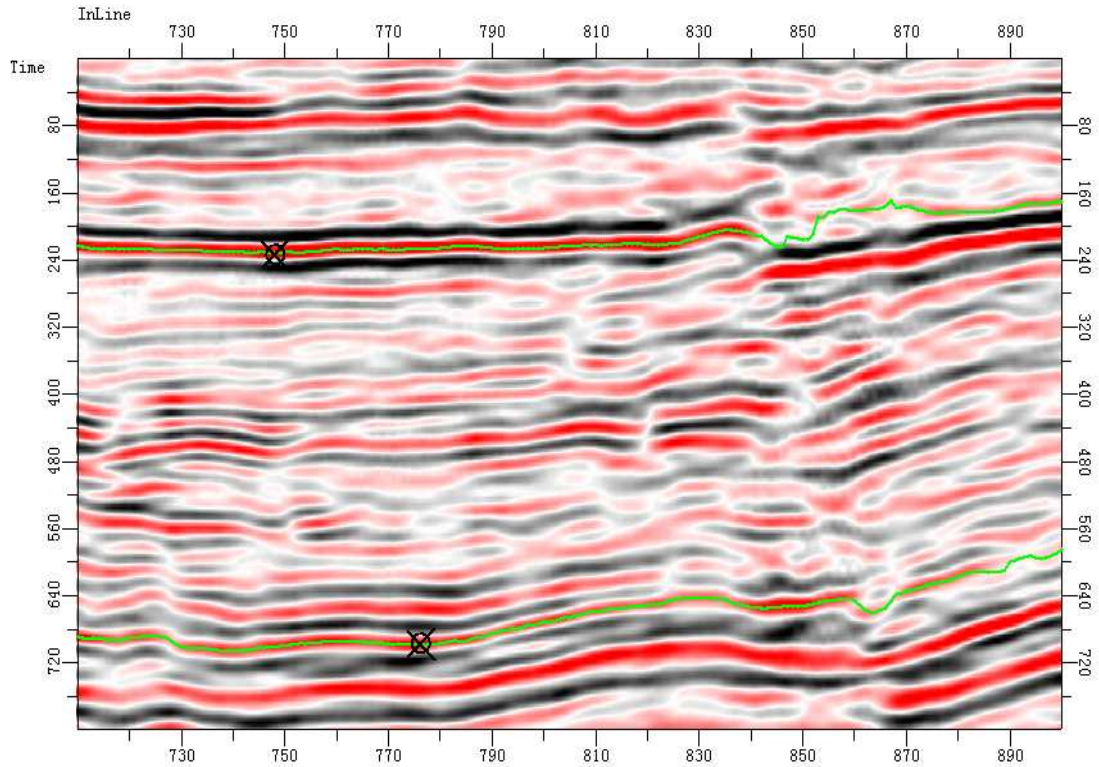


Figure 5.20 2D Horizon tracking by Gaussian-Hermite moments in second seismic image.

As can be seen from the figure, correlation outputs a wrong tracing as the seed across the fault; higher order statistics outputs a slight jitter tracing as the seed across the fault; geometrical moments and Gaussian-Hermite moments direct a reasonable tracking for this seed. Since it is much obscuring for the areas near to the fault, the tracking can be hardly judged correctly or wrongly for this seed; however, it still can be seen from the images, geometrical moments and Gaussian-Hermite moments give a directly opposite tracking, they track down after the fault compared with correlation and higher order statistics which track with a up tendency.

We have discussed the tracking results of the methods mention above. On the whole, Gaussian-Hermite moments show better tracking results than the other three. Here, it should also consider the complexity and time for implement the methods. According to equation (5.5) and equation (5.7), the detailed multiplication and addition involved in both correlation and high order statistic can be well evaluated. As for geometric moments and Gaussian-Hermite moments, it should generate the moment kernel first. The moment kernel is independent of the image as long as the size of seed window does not change, and need to be computed alone and be saved for the future usage. From this viewpoint, the implementation of moments in horizon tracking is neither expensive in complexity nor in time.

5.3.2 3D horizon tracking tasks

A seismic cube clipped from a seismic survey, the map of volume is 190*200 and samples are 200, is used for 3D horizon tracking tasks. We have tracked two horizons in different regions the different regions in which the definitely different geologic properties are exhibited. 3D scene is shown in Figure 5.21. We can observe that first horizon in the seismic cube is very obvious is continuous, because there are no faults, or the obvious faults in the image. However, another horizon is discontinuous due to faults and noises. So, 3D auto-tracking of second horizon will have different degree of difficulties. Correlation, higher order statistics, 1D and 3D geometric moments, 1D and 3D Gaussian-Hermite moments are carried out for such aim. The horizons both continuous and discontinuous are tracked. The results are respectively shown as follows. The one seed are manually selected for first tracking task. The two seed are manually selected for the second tracking mission. The parameters for this experiment are: 7 pixels for seed window and 13 pixels for search window. For 1D geometric moments and 1D Gaussian-Hermite moments, σ is set to 0.26 and the feature is represented by the vector $[\eta_0, \eta_1, \eta_2, \eta_3, \eta_4, \eta_5, \eta_6]$.

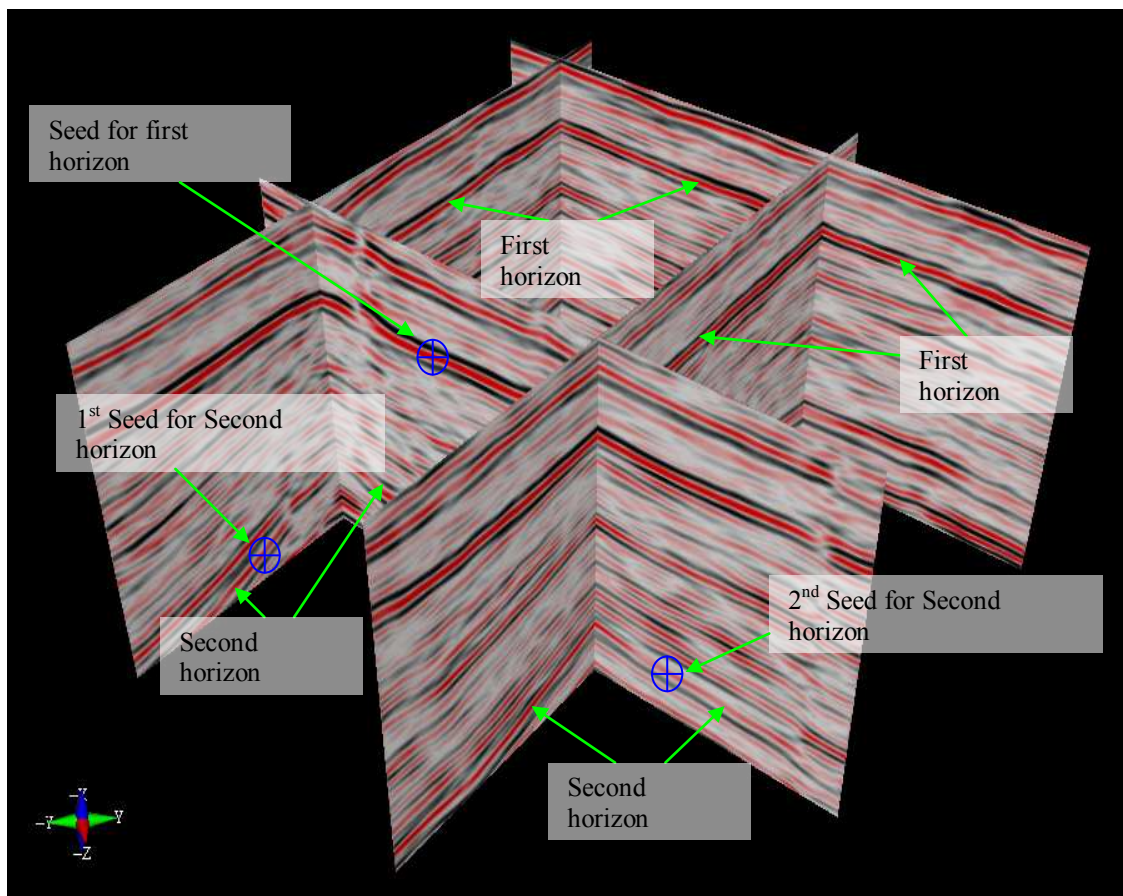
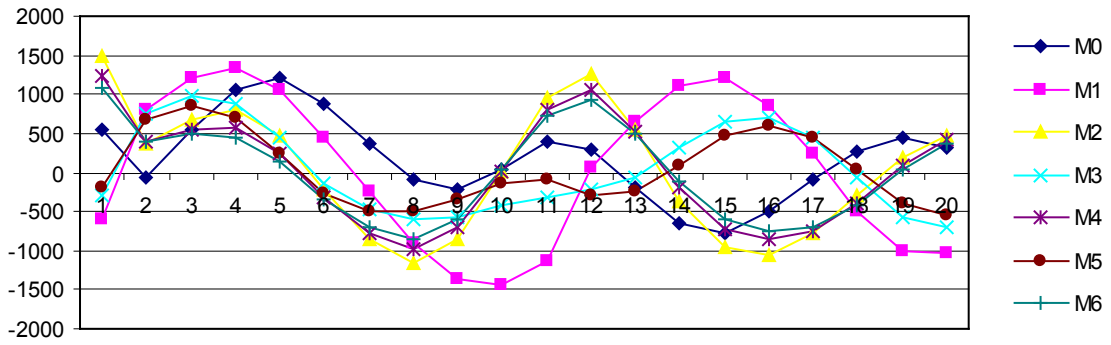
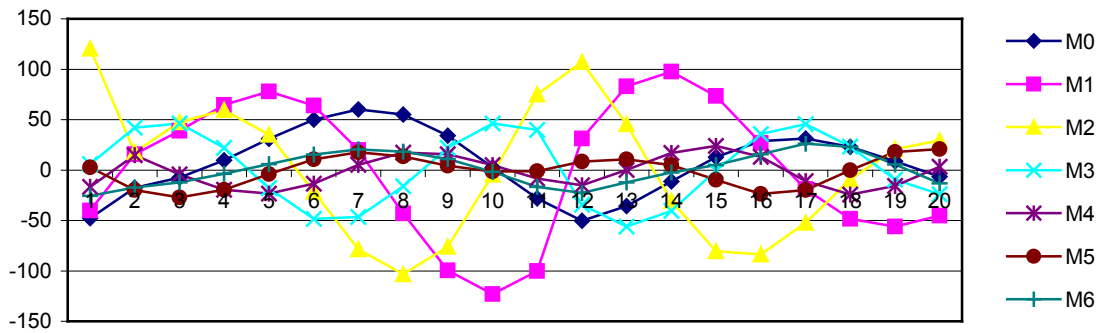


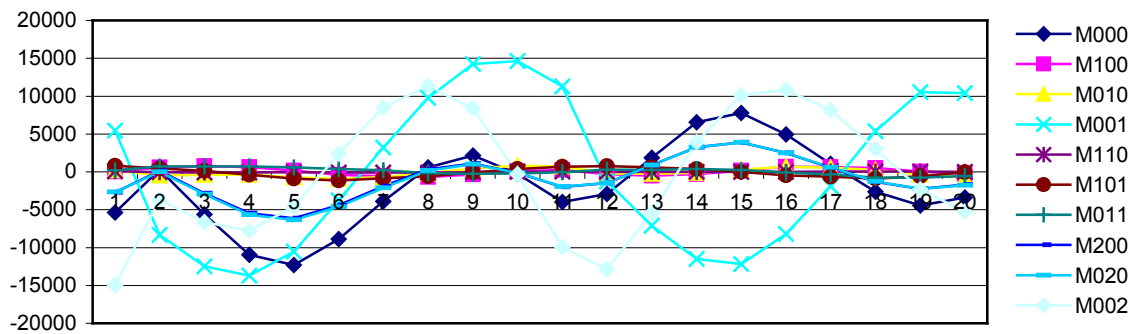
Figure 5.21 3D horizon tracking tasks.



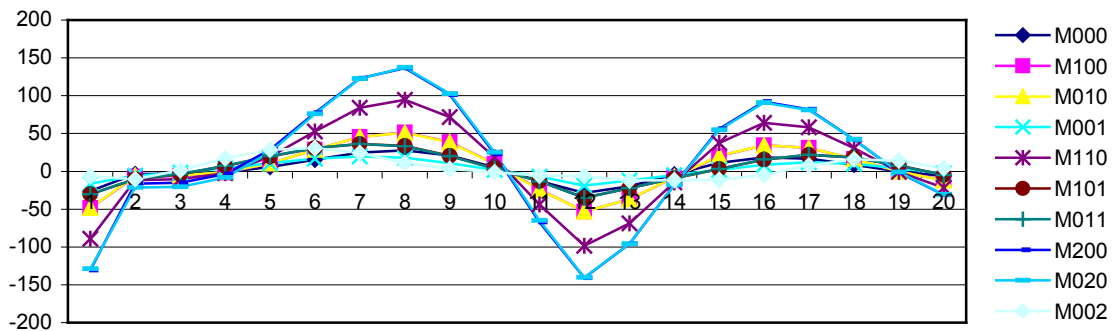
(a) 1D Geometric moments



(b) 1D Gaussian-Hermite moments

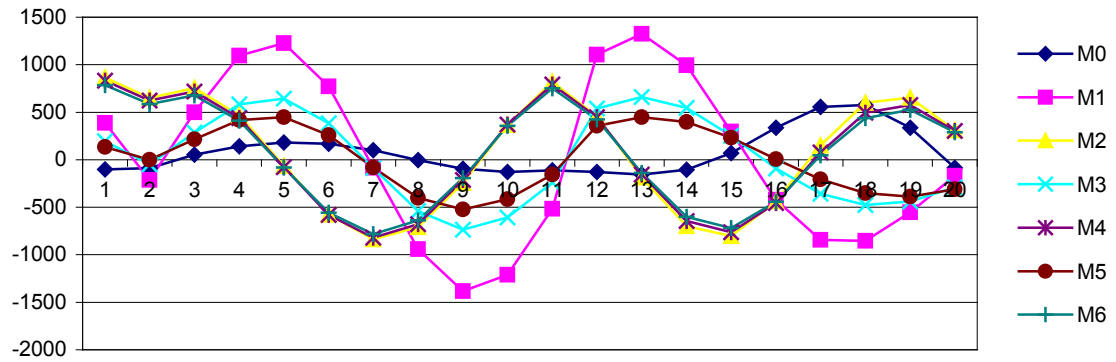


(c) 3D Geometric moments

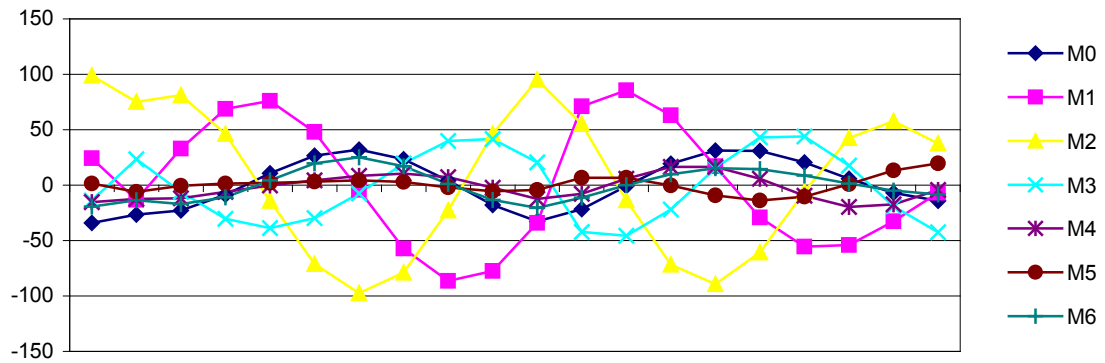


(d) 3D Gaussian-Hermite moments

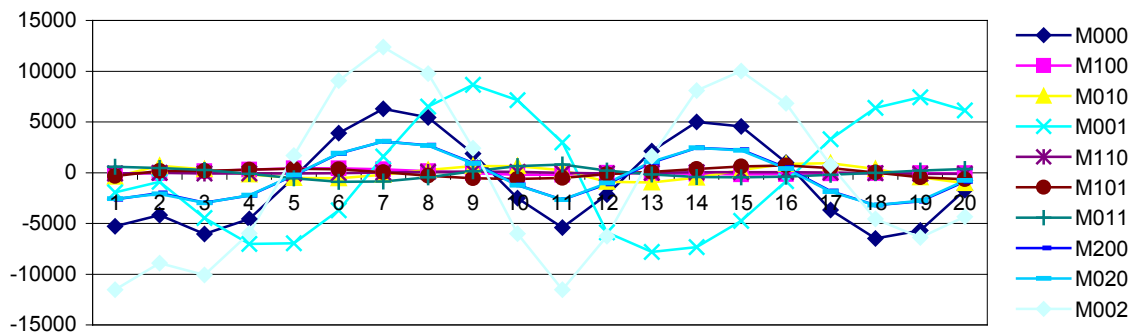
Figure 5.22 Moment feature vector around of First horizon seed.



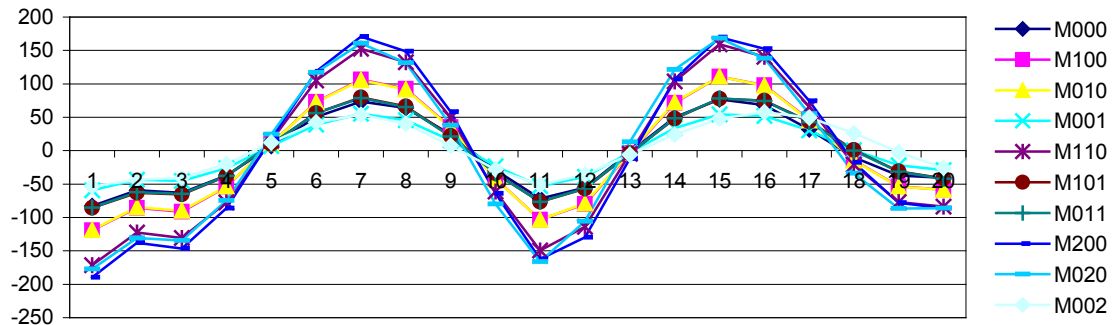
(a) 1D Geometric moments



(b) 1D Gaussian-Hermite moments



(c) 3D Geometric moments



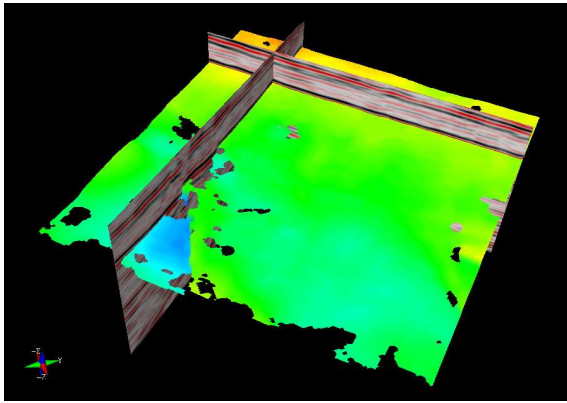
(d) 3D Gaussian-Hermite moments

Figure 5.23 Moment feature vectors around of 1st seed for second horizon.

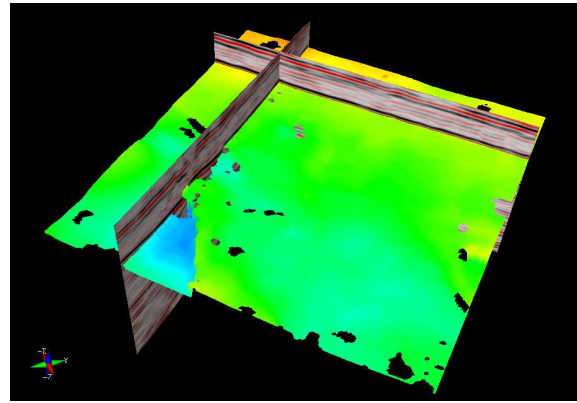
Table 5.3 Normalization coefficients of moments for Euclidean distance.

Sample	First horizon				1 st seed for second horizon			
	3D Geometric moments		3D Gaussian-Hermite moments		3D Geometric moments		3D Gaussian-Hermite moments	
	$\mu_2(1)$	$\mu_2(2)$	$\mu_2(1)$	$\mu_2(2)$	$\mu_2(1)$	$\mu_2(2)$	$\mu_2(1)$	$\mu_2(2)$
s1	656.0484	11933.79	82.78578	157.1305	505.548	2752.087	58.15642	70.31799
s2	873.9117	8346.73	87.40634	158.5337	595.6392	1561.919	49.64861	61.78954
s3	1328.942	8268.353	101.7338	176.6714	925.4215	5581.73	115.3388	149.6921
s4	1769.343	11576.48	129.6953	224.1641	1354.413	13625.88	229.4904	296.5337
s5	1978.8	17589.36	166.0376	294.1668	1617.457	21568.39	341.3592	436.778
s6	1665.842	23509.7	197.1896	358.141	1511.127	25229.54	398.7338	505.4634
s7	1466.003	26621.42	204.8446	377.4947	1058.353	22572.97	371.3921	467.4836
s8	1021.029	23952.48	176.2552	327.778	533.7764	14836.57	267.8384	333.582
s9	608.5076	15120.51	118.1316	217.65	340.4485	5860.587	131.7096	160.72
s10	285.1359	5152.872	51.36725	90.10923	287.0669	114.3869	25.06592	29.29059
s11	138.5426	2715.864	11.22943	15.30023	420.8425	5715.62	70.16843	94.5703
s12	230.8524	10762.06	23.52634	48.35215	856.5953	14138.07	202.6078	264.5249
s13	482.392	20671.69	80.26422	158.3518	1209.121	20896.07	333.8664	427.7165
s14	820.8292	26786.18	135.1579	261.9816	1416.361	22609.95	403.189	508.6147
s15	1311.034	26807.61	166.5868	312.7529	1410.845	18857.68	385.1117	478.4419
s16	1550.185	23602.19	165.0176	299.0088	1127.455	12343.96	298.6395	366.4859
s17	1940.713	18145.37	138.4664	243.8963	674.6505	7033.07	193.2338	237.6673
s18	1702.462	12653.36	103.7029	182.6132	400.8251	5175.655	121.0874	152.3962
s19	1118.925	9836.074	76.25389	140.1605	386.3826	7649.424	106.9565	140.4654
Average	1244.827	17687.34	128.5241	234.8007	978.9866	14355.89	250.8843	316.6506

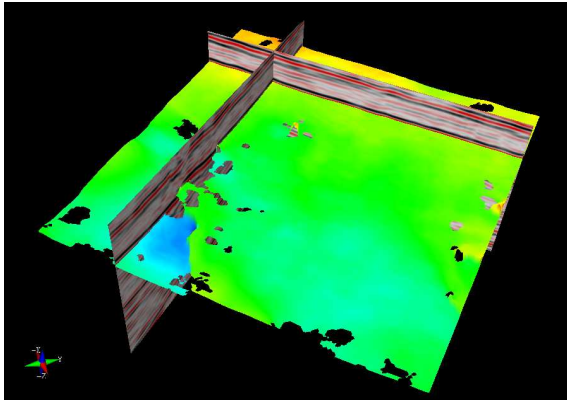
For 3D geometric moments and 3D Gaussian-Hermite moments, σ is also set to 0.26 and the feature is represented by the vector [M000, M100, M010, M001, M110, M101, M011, M200, M020, M002]. We take local region which size is 7*7*7 for computing 3D moments of the seed sample. We calculate Geometric moments and Gaussian-Hermite moments values of 19 samples around seed under in 1D case and in 3D case.



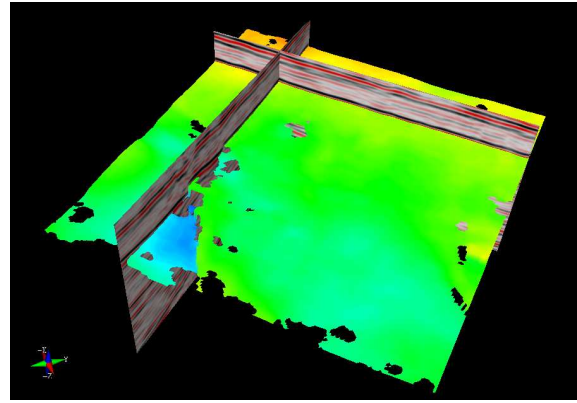
(a)



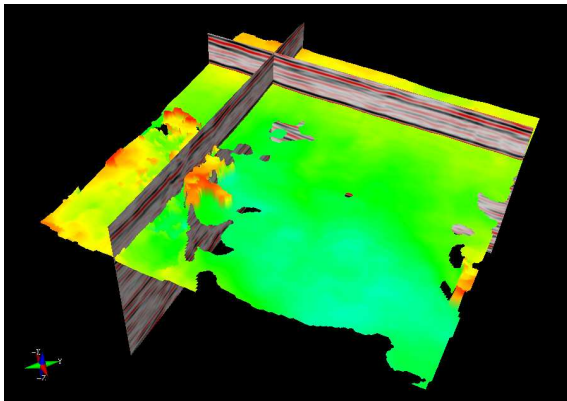
(b)



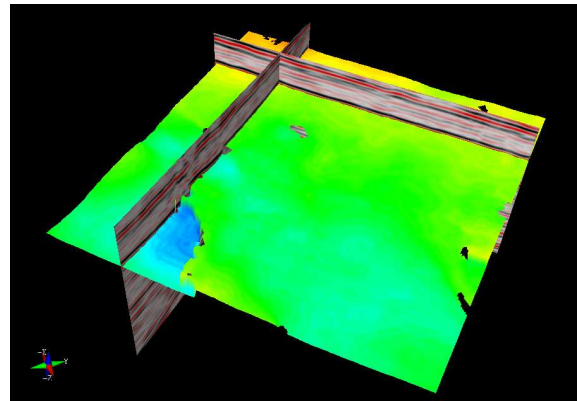
(c)



(d)



(e)



(f)

Figure 5.24 3D horizon tracking with first seed.

- | | |
|----------------------------------|--|
| (a) Correlation method; | (b) Higher order statistics method |
| (c) 1D Geometric moments method; | (d) 1D Gaussian-Hermite moments method |
| (e) 3D Geometric moments method; | (f) 3D Gaussian-Hermite moments method |

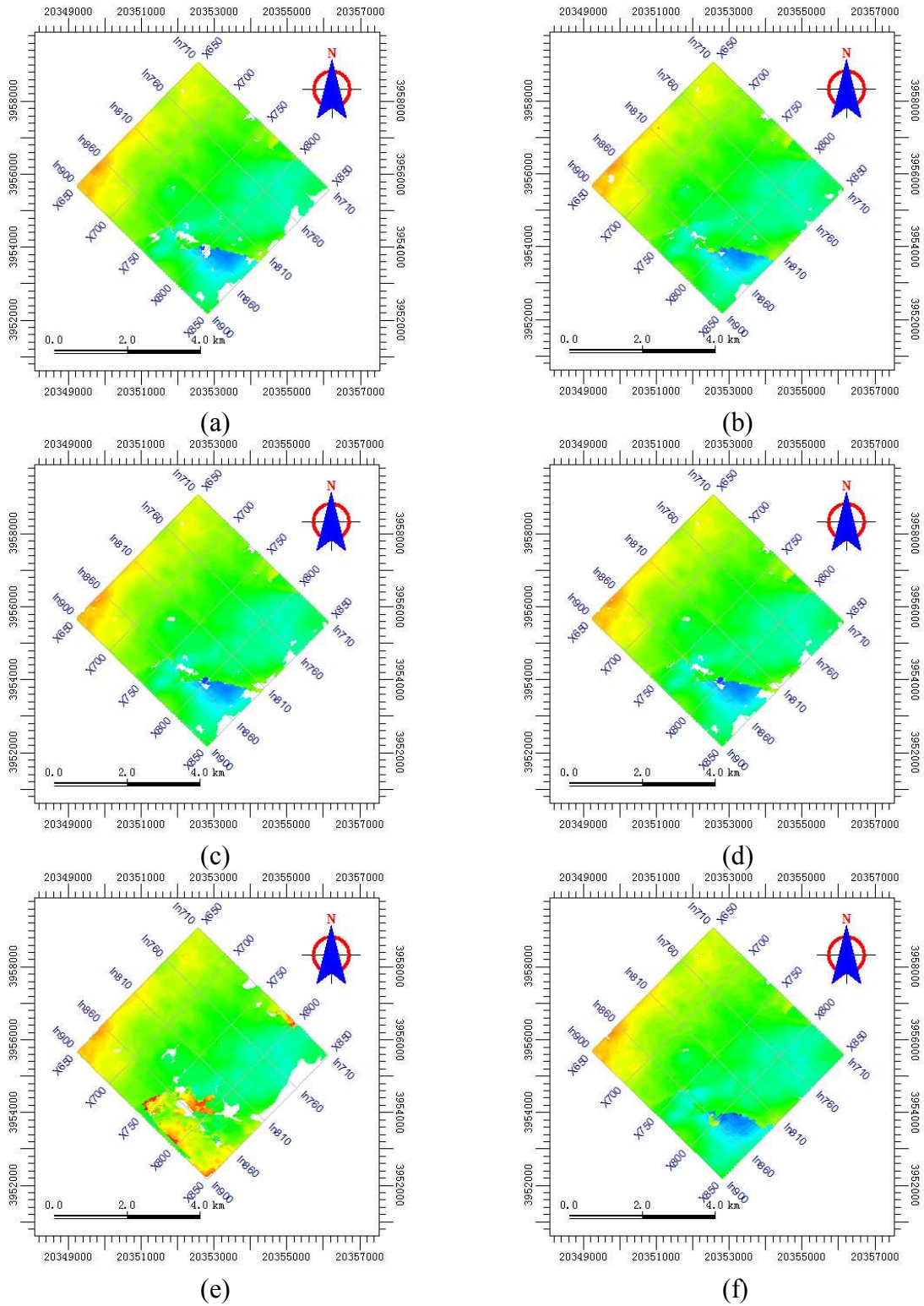
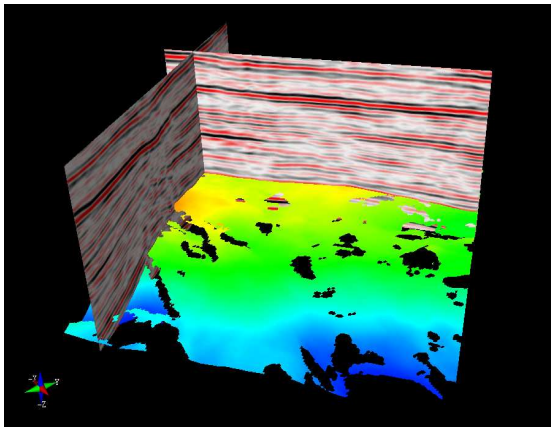
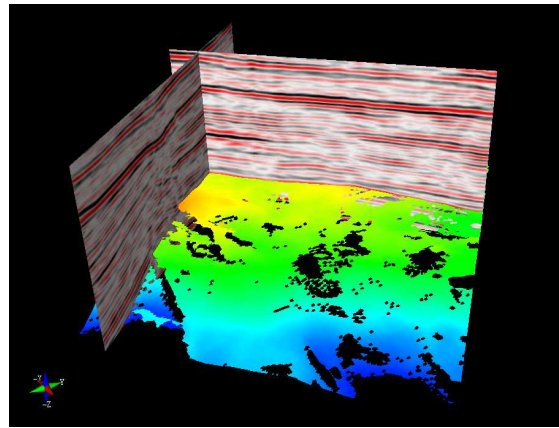


Figure 5.25 Map views of 3D horizon tracking with second seed.

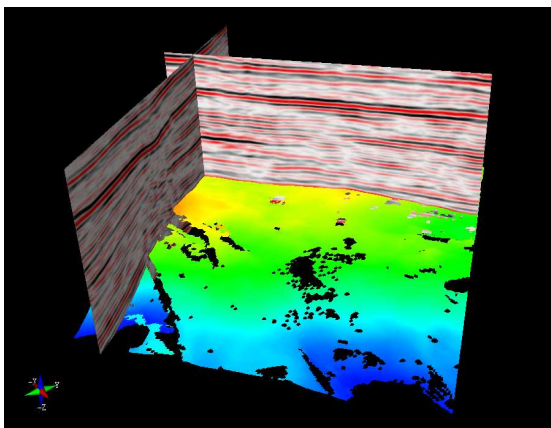
- (a) Correlation method;
- (b) Higher order statistics method;
- (c) 1D Geometric moments method;
- (d) 1D Gaussian-Hermite moments method;
- (e) 3D Geometric moments method;
- (f) 3D Gaussian-Hermite moments method.



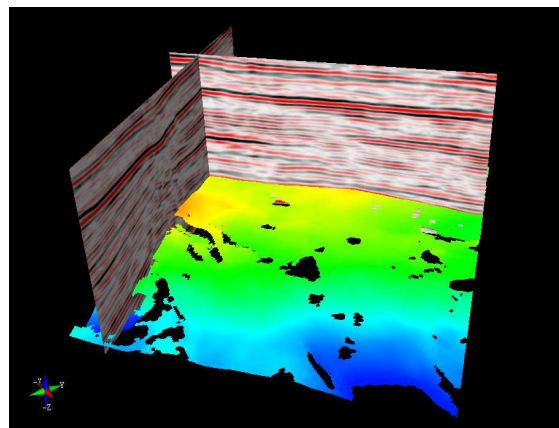
(a)



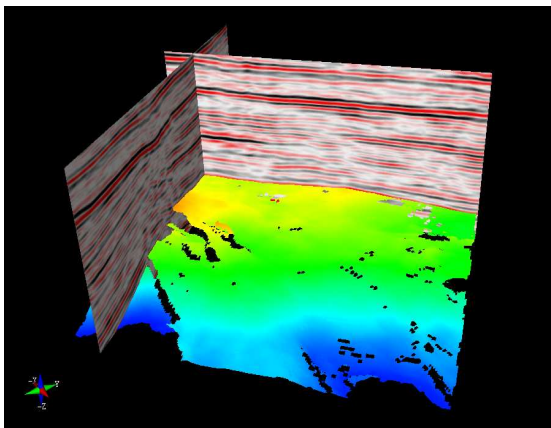
(b)



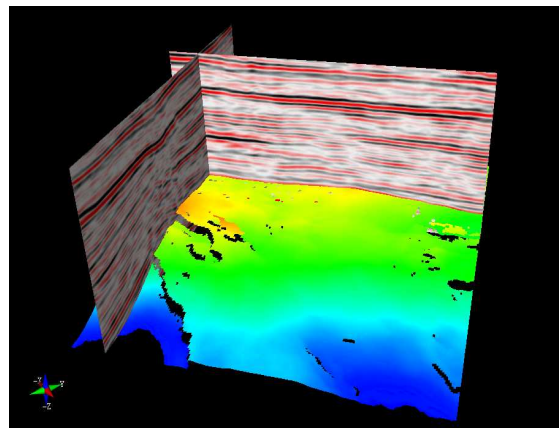
(c)



(d)



(e)



(f)

Figure 5.26 3D horizon tracking with second seed.

- (a) Correlation method; (b) Higher order statistics method;
(c) Geometric moments method; (d) Gaussian-Hermite moments method;
(e) 3D Geometric moments method; (f) 3D Gaussian-Hermite moments method.

Figure 5.22 and Figure 5.23 show the values. In 3D case auto-tracking by geometric moments and Gaussian-Hermite moments, we need to estimate the two normalization coefficients parameters α_1 and α_2 in the equation(5.30). With data from the Figure 5.22 and Figure 5.23, those two parameters can be get. Table 5.3 shows the computation result. The parameter α_1 is $\mu_2(1)$ and α_2 is $\mu_2(2)$ which lies line ‘Average’. Two examples of auto-tracking have been shows From Figure 5.24 to Figure 5.27.

As can be seen from Figure 5.24 and Figure 5.25, first horizon tracks more efficient. Some regions couldn’t be tracked over by correlation method, HOS method 1D geometric moments method, and 1D Gaussian-Hermite moments method. We can find that correlation method has similarity result with HOS method. Many of those regions are different among first two methods and other four methods. It can be seen from Figure 5.24(f), 3D Gassian-Hermite moments method has a perfect tracking.

Figure 5.26 and Figure 5.27 show the tracking result of second horizon. Because there are much faults in this horizon. Tracking result is poor efficient at all of six methods. Result shows that correlation method maybe unsuitable to track horizon through much faults. It also can be seen from Figure 5.27 (f), 3D Gassian-Hermite moments method has an acceptable tracking.

Two experiments show that 3D Gassian-Hermit moments method is a powerful tools for horizon tracking. It can be done well in both smooth horizon and discontinue horizon. The performance results of six methods are shown in Table 5.4 and Table 5.5. The time value of the methods in the tables is an average of five times. Because of much discontinuity in second horizon, there are increasing values of tracking in methods 3D geometric moments and 1D / 3D Gaussian-Hermite moments. But the number of samples matched is less than first horizon.

Table 5.4 Computation result of 3D horizon tracking with first seed.

Method	Samples matched	Time(s)
Cross-correlation	36240	6.475
Higher order statistics	36412	6.803
1D Geometric moments	34877	12.796
1D Gaussian-Hermite moments	35861	61.719
3D Geometric moments	35990	89.219
3D Gaussian-Hermite moments	37962	121.171

Table 5.5 Performance result of 3D horizon tracking with second seed

Method	Samples matched	Time(s)
Cross-correlation	31780	5.328
Higher order statistics	33903	5.938
1D Geometric moments	32130	10.796
1D Gaussian-Hermite moments	34265	63.906
3D Geometric moments	34896	91.578
3D Gaussian-Hermite moments	34992	119.422

5.4 3D Gaussian-Hermite moment invariants-based approach for horizon interpretation

The problem of tracking horizon is highly relevant, and there are no established ‘gold standards’ yet to which new methods can be compared to. As described in the previous Section 5.2 and 5.3, for each sample from seismic data volume we compute its feature vector based on geometric moments and Gaussian-Hermite moments when searching within 3D volume.

Because seismic data can be considered volume with texture and seismic images are also characterised by specific textures which can provide valuable information for locating potential oil reservoirs, we track the seismic horizon follow the texture. In Figure 5.28, it can be seen that two regions ‘a’ and ‘b’ have different texture orientations. However, we desire calculate feature vectors of region b using 3D moments as in Figure 5.29. Thus the feature vector of region ‘b’ is similar to feature vector of region ‘a’.

Moment invariants are rational functions of the moments that remain constant in value when the density is subjected to transformation. Moment invariants are well established for character recognition in 2D image analysis ([Hu, 1962](#)), and have been extended for 3D pattern only much later ([Flusser et al., 2003](#); [Mamistvalov, 1998](#); [Sadjadi and Hall, 1980](#)) and have not been applied to problems in structural seismic yet. In comparison with a huge number of papers on 2D moment invariants, only few papers on 3D and n-D invariants have been published. Sadjadi and Hall ([1980](#)) pioneered the development of 3D Geometric moment invariants from 2D moment. They built a family of three invariant moments with a degree up to the second-order. Using the notion of complex moments Lo and Don ([1989](#)) constructed a

family of twelve invariant moments with orders up to the third degree. Rothe et al (1996) presented the normalization method to determine invariants . Xu and Li (2006a) generalized curve moments from 2D to 3D Euclidean space, and use geometrical method to derive 3D curve moments invariants of different orders under similarity transformation. Xu and Li (2007) also generalized projective moment invariants from 2D to 3D space, and select permutation invariant cores for generation of 3-D projective moment invariants. Ong et al (2007) present a theoretical framework to derive translation and scale invariants for 3D Legendre moments, by using generates 3D Legendre invariants from the existing 3D geometric moment invariants and eliminates the displacement and scale factors from Legendre polynomials to generate translation and scale invariants.

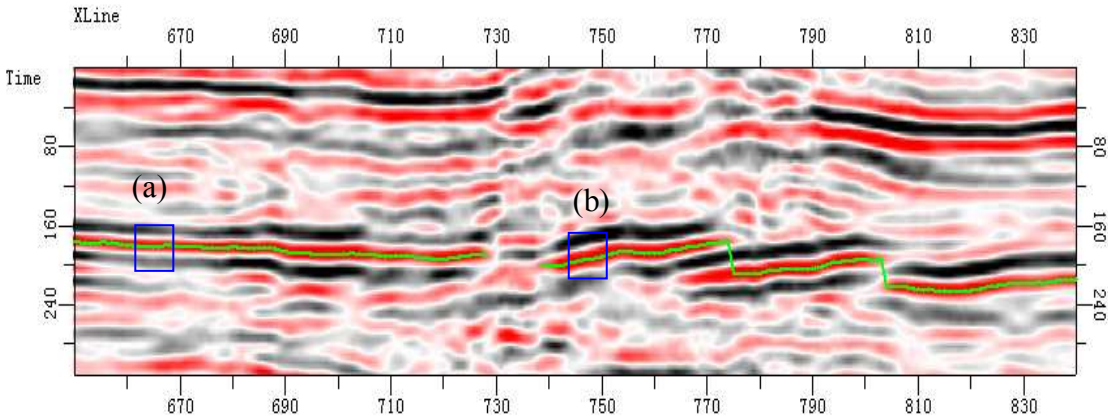


Figure 5.28 Calculation feature vector two region using moments in a case.

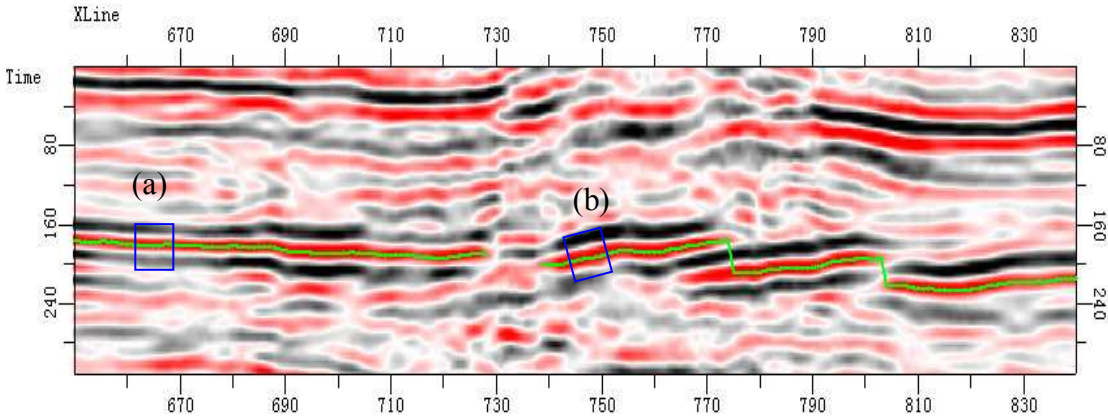


Figure 5.29 Calculation feature vector two region using moments in rotational case.

In this section, we will present the 3D Gaussian-Hermite moment invariants from 3D geometric moment invariants and apply these properties into horizon auto-tracking. This approach is motivated by the excellent performance of the moment invariants. If we replace

moments by central or normalized moments in these relations, we obtain invariants not only to rotation but also to translation and/or scaling, which also ensures invariance to rotation around an arbitrary point. However, once we have the formulas, the proof of rotation invariance is easy.

5.4.1 3D Gaussian-Hermite moment invariants

5.4.1.1 3D Gaussian-Hermite moment invariants to translation

The central moments do not change under the translation of coordinates, if

$$\begin{aligned}x' &= x + \alpha \\y' &= y + \beta \\z' &= z + \gamma\end{aligned}\tag{4.32}$$

Then

$$\eta_{pqr}'(x', y', z') = \eta_{pqr}(x, y, z)\tag{4.33}$$

where α, β, γ are constants.

5.4.1.2 3D Gaussian-Hermite moment invariants to rotation

3D rotation moment invariants were first introduced in 1980 by Sadjadi and Hall ([1980](#)), who employed the results of the theory of algebraic invariants and derived invariants to a rotation around the origin. They presented two invariants of the second order. Xu and Li ([Xu and Li, 2008](#)) presented six typical moment invariants consist of 1 second and fourth-order, 2 third-order and 3 fourth-order moment invariants. Some of these invariants have already existed in former literature. There are 6 third-order and 3 second- and third-order moment invariants in Lo and Don's paper ([1989](#)).

From those invariants, we can derive following Gaussian-Hermite moment invariants of the second order.

$$I_1^{3D} = \mu_{200} + \mu_{020} + \mu_{002}\tag{4.34}$$

$$I_3^{3D} = \mu_{200}\mu_{020}\mu_{002} + 2\mu_{110}\mu_{101}\mu_{011} - (\mu_{002}\mu_{110}^2 + \mu_{020}\mu_{101}^2 + \mu_{200}\mu_{011}^2)\tag{4.35}$$

$$I_2^{3D} = \mu_{200}\mu_{002} + \mu_{020}\mu_{002} + \mu_{200}\mu_{020} - (\mu_{110}^2 + \mu_{101}^2 + \mu_{011}^2)\tag{4.36}$$

$$I_4^{3D} = m_{200}^2 + m_{020}^2 + m_{002}^2 + 2(m_{110}^2 + m_{101}^2 + m_{011}^2) \quad (4.37)$$

$$I_5^{3D} = m_{200}^3 + m_{020}^3 + m_{002}^3 + 6m_{110}m_{101}m_{011} + 3(m_{200}m_{110}^2 + m_{200}m_{101}^2 + m_{020}m_{110}^2 + m_{020}m_{011}^2 + m_{002}m_{101}^2 + m_{002}m_{011}^2) \quad (4.38)$$

These moment invariants characterize the density of an object independently from the object's position or orientation. The particular functions are not invariant to scale. Since moments are continuous, the employed invariant functions of the moments are continuous as well. Slight changes in the density correspond to slight changes in the moment invariants. Similar density functions can be identified by identifying similar moment invariants. Thus, a feature vector of moment invariants can serve to describe densities independently from their position and orientation in 3D space.

5.4.1.3 3D Gaussian-Hermite moment invariants to contrast changes

So far, we have considered invariants to spatial transformations only. However, in practice the features used in a recognition system should also be invariant to gray level or colour changes. In this section we consider contrast stretching only, which is a very simple gray level transform given by

$$f'(x, y, z) = a \cdot f(x, y, z) \quad (4.39)$$

where a is a positive stretching factor. Therefore, we can get moment invariants as:

$$I_1^{3D} = \frac{1}{\mu_{000}} (\mu_{200} + \mu_{020} + \mu_{002}) \quad (4.40)$$

$$I_3^{3D} = \frac{1}{\mu_{000}^3} \left((\mu_{200}\mu_{020}\mu_{002} + 2\mu_{110}\mu_{101}\mu_{011}) - (\mu_{002}\mu_{110}^2 + \mu_{020}\mu_{101}^2 + \mu_{200}\mu_{011}^2) \right) \quad (4.41)$$

$$I_2^{3D} = \frac{1}{\mu_{000}^2} \left(\mu_{200}\mu_{002} + \mu_{020}\mu_{002} + \mu_{200}\mu_{020} - (\mu_{110}^2 + \mu_{101}^2 + \mu_{011}^2) \right) \quad (4.42)$$

$$I_4^{3D} = \frac{1}{\mu_{000}^2} \left(m_{200}^2 + m_{020}^2 + m_{002}^2 + 2(m_{110}^2 + m_{101}^2 + m_{011}^2) \right) \quad (4.43)$$

$$I_5^{3D} = \frac{1}{\mu_{000}^3} \left(m_{200}^3 + m_{020}^3 + m_{002}^3 + 6m_{110}m_{101}m_{011} + 3(m_{200}m_{110}^2 + m_{200}m_{101}^2 + m_{020}m_{110}^2 + m_{020}m_{011}^2 + m_{002}m_{101}^2 + m_{002}m_{011}^2) \right) \quad (4.44)$$

5.4.2 3D Gaussian-Hermite moment invariants-based method for horizon auto-tracking

We have described a workflow based on moments for 3D horizon tracking in previous Section 5.2.7. Here, we replaced the modular "Compute the K feature of candidate by moments" with "Compute the K feature of candidate by Gaussian-Hermite moment invariants". Then we test our method with real seismic data set used in section 5.3.2. We process horizon track in real seismic data volume under local sub-volume with size $7*7*7$. The result is shown in Figure 5.30 and Figure 5.31. It can be found that moment invariants method is more robust for horizon tracking across fault.

5.4.3 Multi-scale approach based on 3D Gaussian-Hermite moment invariants

In preview section 5.4.2, we use local sub-volume with size $7*7*11$. In this section, we will track the horizon under different scale. The experiment task is divided two parts: single scale and combining scale.

In the single scale mode, we perform horizon tracking in real seismic data volume under local sub-volume with size $5*5*5$. Next, we perform horizon auto-tracking in real seismic data volume under local sub-volume with another size $9*9*9$.

Figure 5.32 and Figure 5.33 show the result of scale sub-volume size $5*5*5$. Figure 5.34 and Figure 5.35 show the result of scale sub-volume size $9*9*9$. From Figure 5.30 to Figure 5.35, we notice that an appropriate scale can be efficiently performed over discontinuous areas.

Finally, we construct a combination of feature vector from the feature vectors under the three scales. The result is shown in Figure 5.36 and Figure 5.37. Combination scale mode has a few advantages than single scale mode.

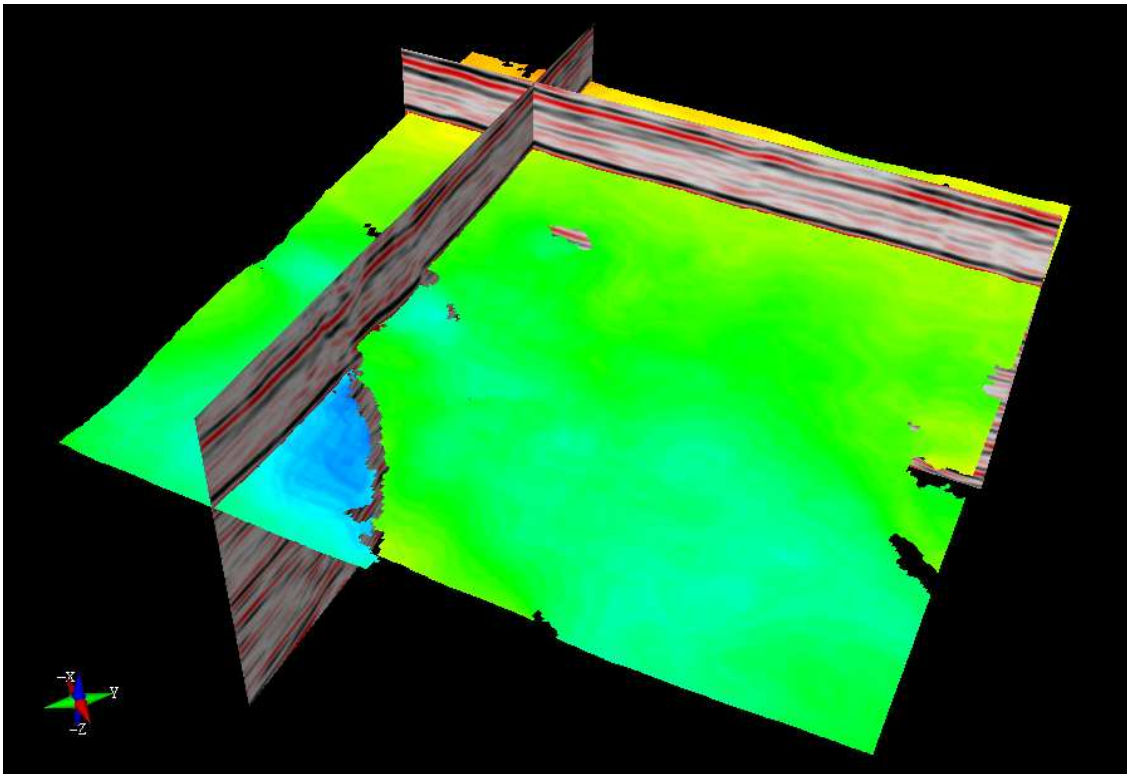


Figure 5.30 3D horizon tracking based on Gaussian-Hermite moment invariants under scale $7*7*7$.

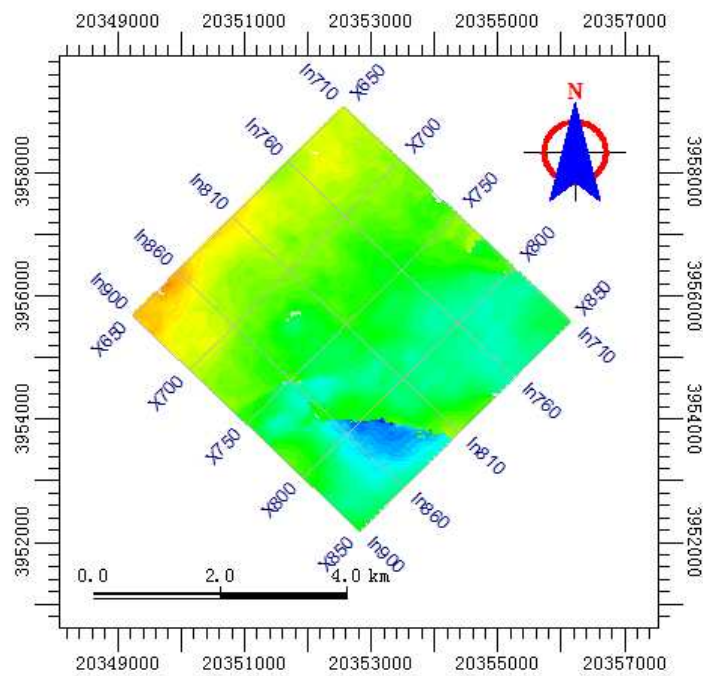


Figure 5.31 Maps for 3D horizon tracking based on Gaussian-Hermite moment invariants under scale $7*7*7$.

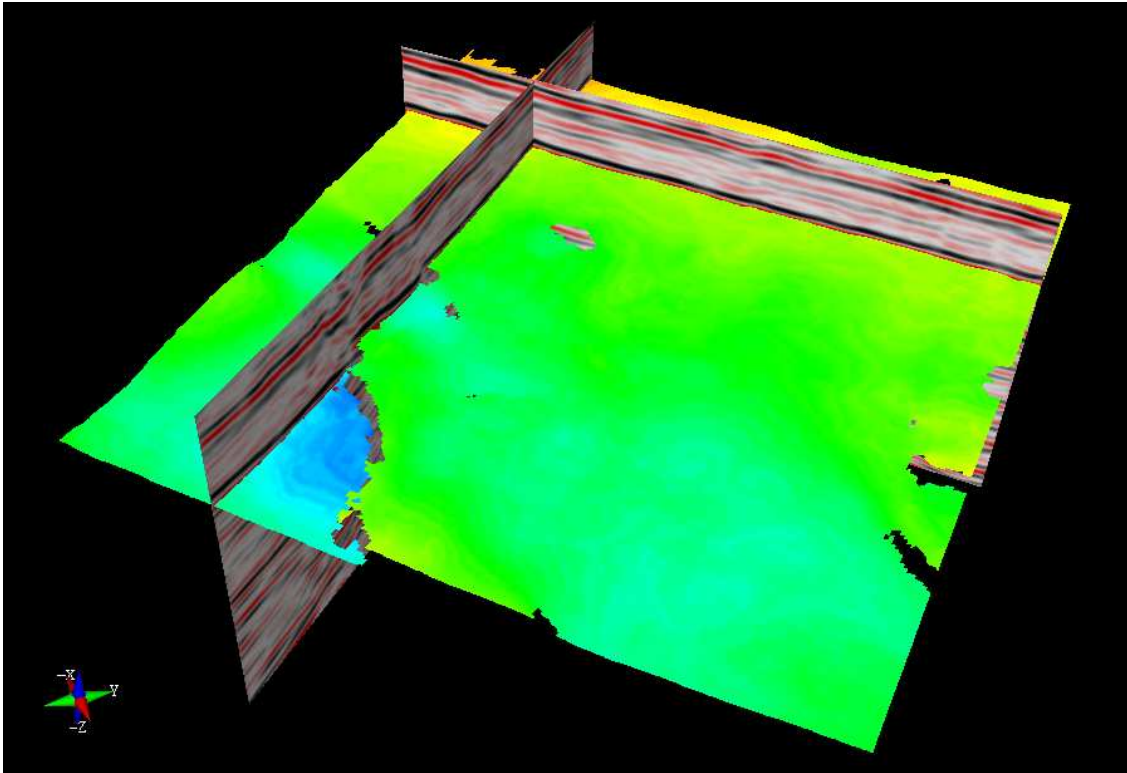


Figure 5.32 3D horizon tracking based on Gaussian-Hermite moment invariants under scale $5*5*5$.

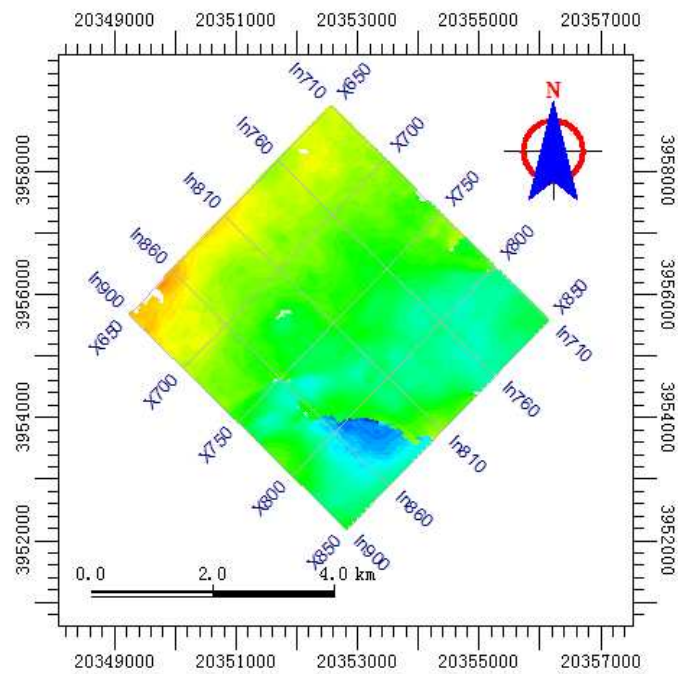


Figure 5.33 Maps for 3D horizon tracking based on Gaussian-Hermite moment invariants under scale $5*5*5$.

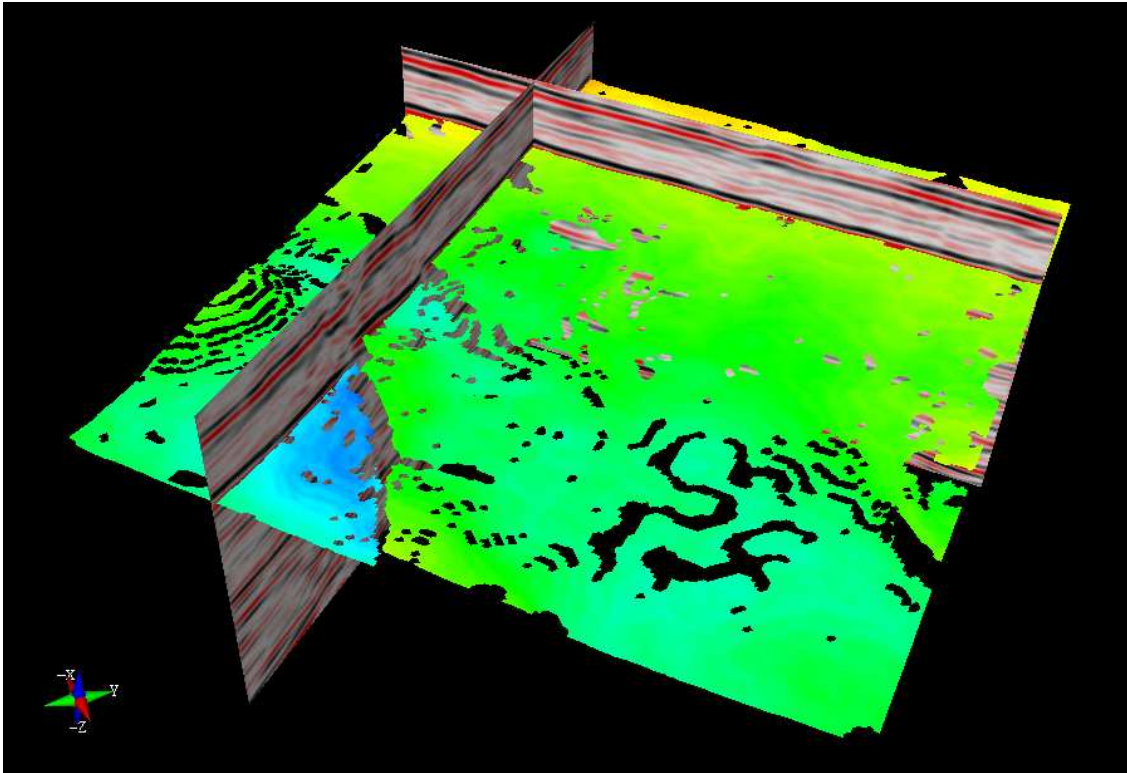


Figure 5.34 3D horizon tracking based on Gaussian-Hermite moment invariants under scale $9*9*9$.

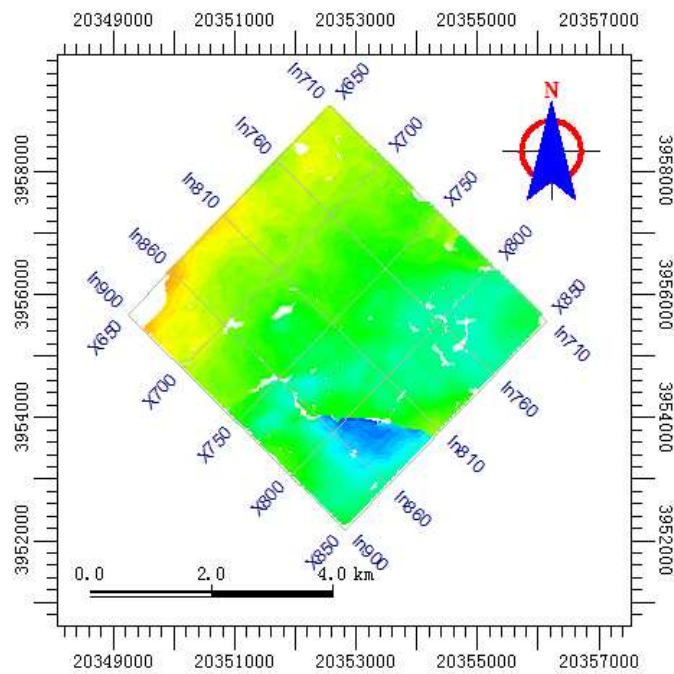


Figure 5.35 Maps for 3D horizon tracking based on Gaussian-Hermite moment invariants under scale $9*9*9$.

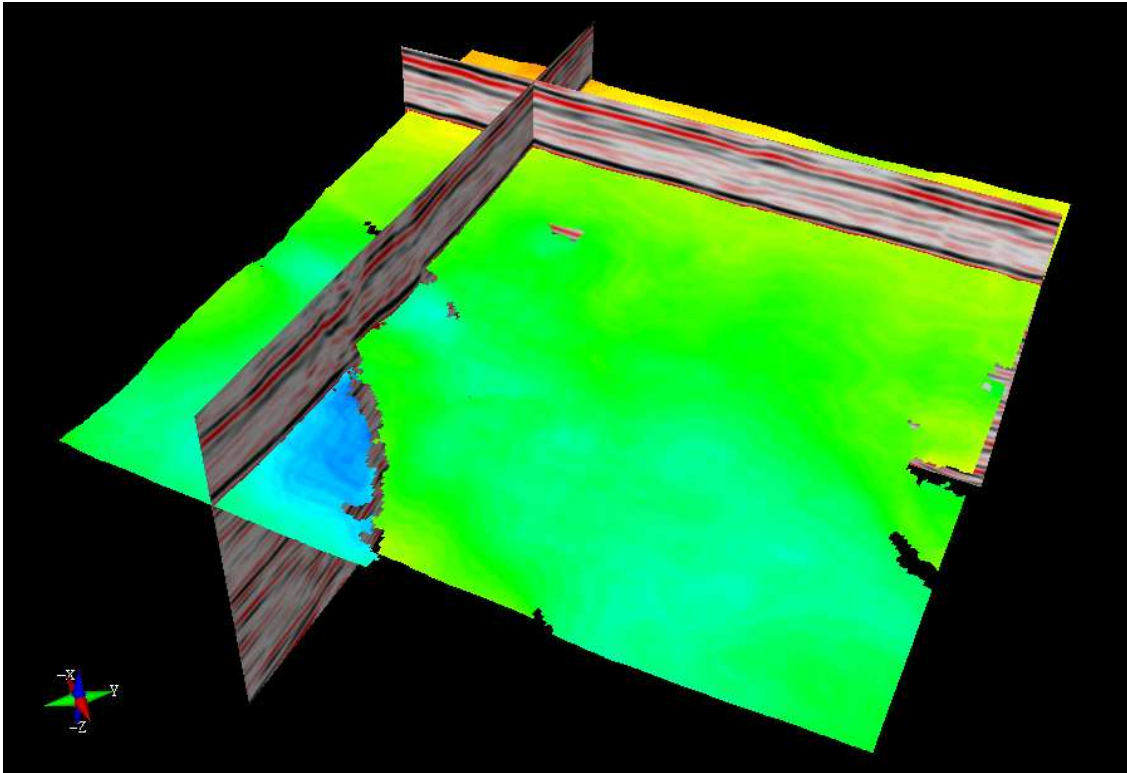


Figure 5.36 3D horizon tracking based on Gaussian-Hermite moment invariants under combining scale.

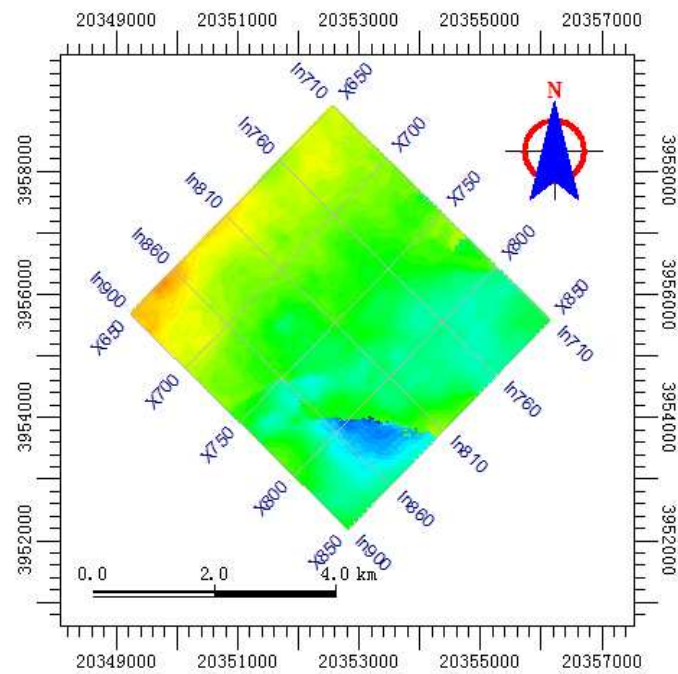


Figure 5.37 Maps for 3D horizon tracking based on Gaussian-Hermite moment invariants under combining scale.

5.5 Horizon self overlaps

It is advantageous in seismic data processing and interpretation to reduce a seismic data volume to its internal reflection-based surfaces or horizons. Collectively, these surfaces form the skeleton of the seismic volume. Many methods have been described to extract or track one horizon or surface at a time through a volume of seismic data. Most of these methods create surfaces that eventually overlap themselves. Thus, the same surface may have multiple depths (or reflection times) associated with the same spatial position. Figure 5.38 illustrates three surfaces across a fault. In region A, surface H₁ has two different reflection times. There is same phenomenon to surface H₂ in region B and surface H₃ in region C.

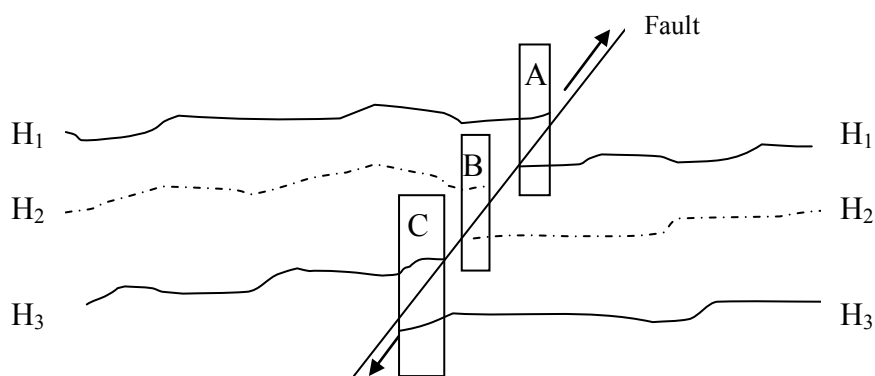


Figure 5.38 Some surfaces with multiple reflection times.

Some methods prevent multi-valued surfaces by discarding all but one value per location. Typically, as shown in Figure 5.39, they store only the first one encountered during the execution of the process and simply do not record later ones. Moreover, if multiple surfaces are tracked, one surface may overlay another surface at one same location, while the opposite relationship occurs at another location. Collectively, these situations may be termed topologically inconsistent. The published approaches to date, some of which are summarized below, largely ignore topological consistency.

Cheng and Lu described a method to extract the seismic skeleton from two dimensional data. Problems introduced by the third dimensions are neither discussed nor resolved in ([Cheng and Lu, 1989](#)). The procedure uses an iterative approach where strong horizons are tracked initially, while weaker ones are tracked in later iterations. At any iteration, the tracking is confined to areas delineated by horizons already tracked in earlier iterations. Tracking is performed by correlating multiple neighbouring traces simultaneously. Combining the two approaches allows incorporation of the geologic fabric into the results. This method is also described by Lu and Cheng in ([Lu and Cheng, 1990](#)).

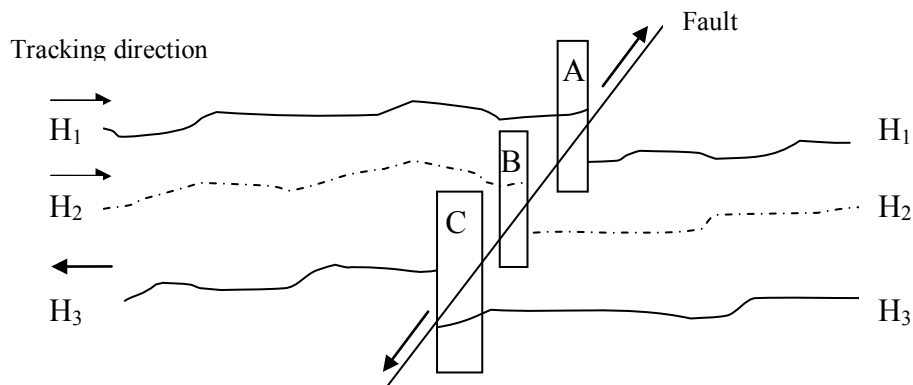


Figure 5.39 Tracking result of single reflection time.

In (Li et al., 1997), Li et al disclosed the utility of using the seismic skeleton for the interpretation of seismic data. The seismic skeleton is two dimensional, and when a horizon splits, the decision regarding which branch to follow is not geologically motivated. Instead, the method attempts to correlate events across three neighboring traces in such a way that dip changes are minimized. The method includes only iterative growing of horizons. Further, Vasudevan et al continued of their earlier work, realizing that skeletonization has geoscience applications beyond seismic processing and interpretation in (Vasudevan et al., 2005).

Huang(1990) described a two dimensional method of horizon growth allowing horizons to cross and penetrate each other, which violates the stratigraphic paradigm that geologic strata do not cross. The method reveals only the generation of horizons by picking events, peaks for example, building a tree of all potential linkages between these events, and then selecting the ones which yield the most linear horizons. Branches of the lineage tree are chosen to minimize a cost function of horizon nonlinearity.

Dunn and Czernuszenko (2006) described a three-dimensional geobody picker and analyzer. In this patent, a few select geobodies are picked, which may include geobodies having attribute values within a specified range or geobodies adjacent to certain attribute values. During picking, the geobodies are analyzed using a map view criteria to detect and eliminate self-overlapping geobodies, and yielding composite geobodies instead. The composite geobodies satisfy at least the topological condition of no self overlaps, but the boundaries between geobodies are determined by the order in which the voxels are detected.

James (2008) described a seismic autopicker that generates single valued horizons and often takes the correct branch when horizons split. The interpreter initializes the method by

manually selecting one or multiple seed points in a 3D seismic data volume. The algorithm uses first seed point for picking a set of secondary points from neighboring traces which are then treated as new seed points and repeats the algorithm procedure. The algorithm assigns an iteration number corresponding to the number of times the algorithm repeated to each of the seed points. Secondary picks that led to self overlap are rejected, but topological consistency with other horizons is not revealed. The algorithm is basically based on controlled marching.

Imhof et al ([2011](#)) described a method for merging surfaces identified in a seismic volume or seismic attribute data volume to form larger surfaces representing subterranean geologic structure or geophysical state of matter, comprising merging neighbouring surfaces in a topologically consistent way. In this patent, reflection-based surfaces may be automatically created in a topologically consistent manner where individual surfaces do not overlap themselves and sets of multiple surfaces are consistent with stratigraphic superposition principles. Initial surfaces are picked from the seismic data, and then broken into smaller parts that are predominantly topologically consistent, whereupon neighbouring patches are merged in a topologically consistent way to form a set of surfaces that are extensive and consistent. Surfaces or geobodies thus extracted may be automatically analyzed and rated based on a selected measure such as one or more direct hydrocarbon indications. Topological consistency for one or more surfaces may be defined as no self overlap plus local and global consistency among multiple surfaces.

To resolver the self overlaps, we define a structure to store point information of horizon map in our moments based method. The structure includes information:

- Location information: x, y ;
- Tracking list of result information: time, Euclidean distance value.

We modify the “Record candidate” process in the workflow chart of 3D horizon tracking by moments at the Figure 5.10 in section 5.2.7 to “Record candidate information, update tracking list of the candidate” and “Update the candidate queue”. This modified workflow chart is shown in Figure 5.40. In contrast, new structure for the tracking method can employ a diverse set of techniques to achieve good performance, including taking different searching order. For each of eight neighbour traces of the current trace in which candidate seed is, we can evaluate a serial of features upon determination of the candidate “seed” in the range of searching window.

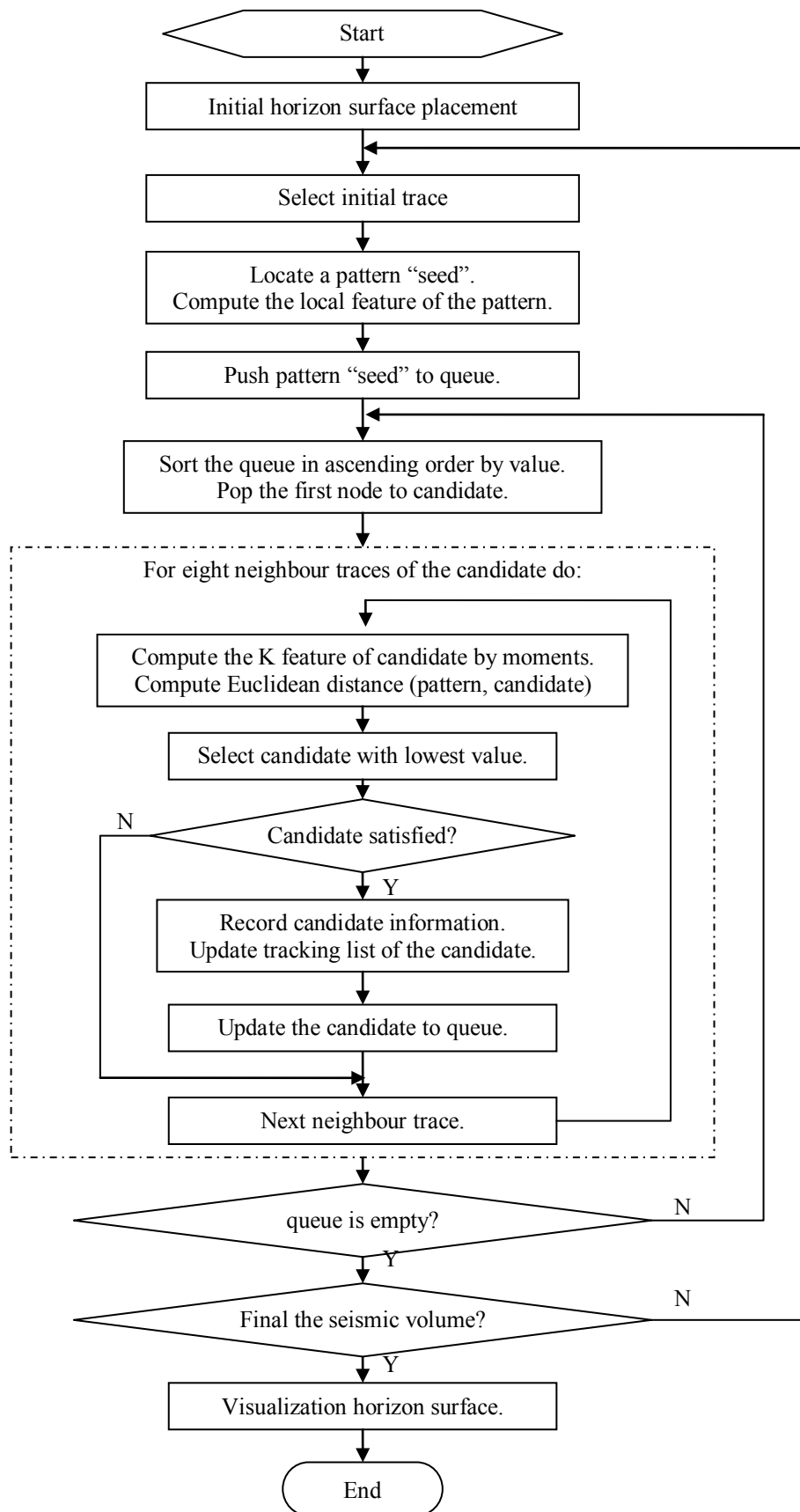


Figure 5.40 The modified workflow chart of 3D horizon tracking by moments

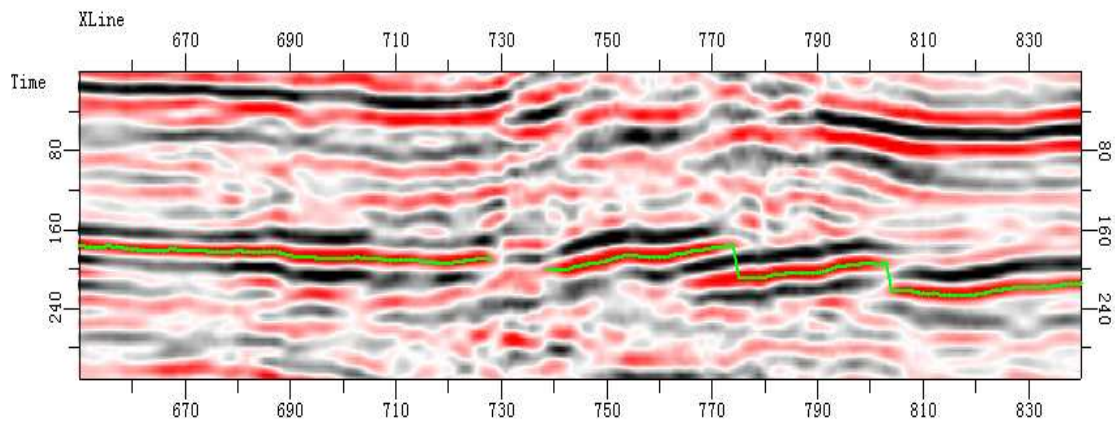


Figure 5.41 A real horizon auto-tracking has some self overlaps.

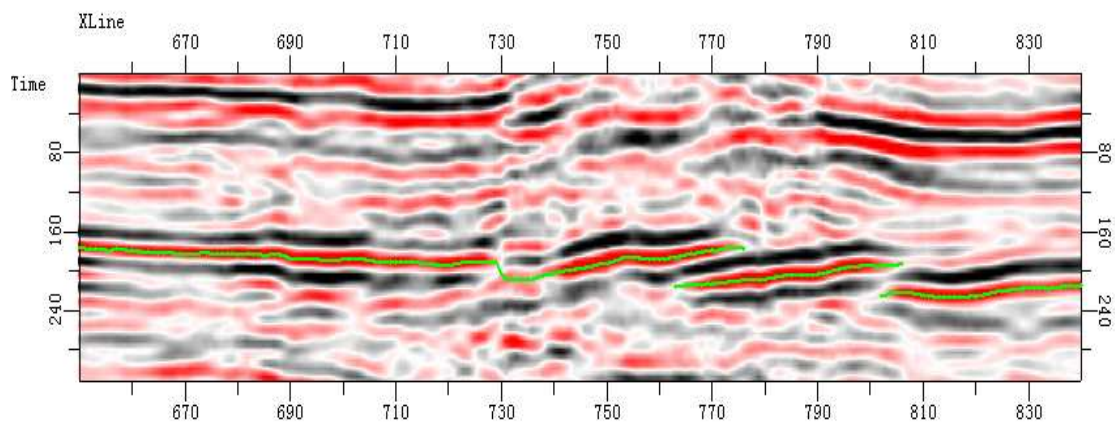


Figure 5.42 The horizon auto-tracking by modified workflow.

After evaluating feature, we can get the Euclidean distance between the feature of the pattern “seed” and each feature by Equation(5.30). The candidate with lowest value is selected as potential candidate “seed”. If this candidate “seed” is verified and satisfied, it is recorded in horizon surface map. At the same time this matching information is compared to the tracking list. If an existing node with same information has been searched, the matching information is ignoring; otherwise the matching information is inserted to tracking list. Then we update the seed queue. We repeat “pop-evaluate-push” process until the queue of candidate seeds is empty. When the seed queue is empty, another decision is performed to determine if the horizon tracking is final in the seismic volume. If tracking is not over the volume, another initial trace is selected to continue until the process is completed. For result in Figure 5.41, we can get the tracking result as be shown in Figure 5.42.

Finally, we process visualization of the tracking result. Before changing the structure of point information of horizon map, the display is very simple. We construct a cell polygon using

four neighbour points. In this case, the same surface has only one depth (or reflection time) associated with the same spatial position. We inquire four neighbour point positions for a point position. If the value difference between points is beyond a threshold, the cell polygon is ignored. With new structure, however, situation is changed. Now the same surface may have multiple depths (or reflection times) associated with the same spatial position. To construct a cell polygon using four neighbour points, we have to choose a suitable value from the tracking list of the point. It is also depend on value difference whether the cell polygon is ignored. According to neighbour cell polygons the current cell polygon is merged to a larger surface. Finishing surface tracking, the tracking result with multiple surfaces is visualized to interpreter.

5.6 Conclusion

In this chapter, we try to concern the researches of interpreting seismic horizon based on moments, which are the important study on the exploration, identification and production of hydrocarbons. Auto-pickers, as Dorn (1998) pointed out, are all sensitive to noise, and the path which the auto-picker follows should be considered carefully. Moments of images provide efficient local descriptors and have been used extensively in image analysis applications. We approach method based on geometrical moments and Gaussian-Hermite moments to the task of 2D/3D horizon auto-tracking. With moments, the feature vector is then constructed by several order of moment. After obtaining feature vector, a matching algorithm based on Euclidean distance, between the referent feature vector of seed and feature vector of each candidate seeds, is performed to choose a candidate with the lowest value distance. The comparisons are made under both 2D and 3D conditions of correlation method, higher order statistics method, and moments-based method. Some visualization examples are also illustrated. The experiments show that the moments-based method is an efficient tool for horizon auto-tracking.

3D Gaussian-Hermite moment invariants are presented here as horizon tracking technique. Compared to other horizon tracking techniques, moment invariants have some drawbacks and some advantages. Like some other horizon tracking techniques, e.g. correlation-based method, the computation heavily depends on a seed point. The moment invariant feature vector continuously varies when rotational transforming the density with respect to the seed point. Moment invariant methods successfully detect similarities of features conserved in detail. Finally we propose a modified tracking method to solve the horizon self overlaps, which are very common in horizon auto-tracking.

6 Seismic facies analysis using 3D moments

Most of the hydrocarbons (gas and oil) occur in sedimentary rocks that were generated in different depositional environments (for example: river channels, delta systems, submarine fans, carbonate mounds and reefs). Seismic waves penetrating into and reflected within sedimentary rock bodies yield a seismic image of their external shape and of their internal texture. Therefore, the analysis of the external shape of seismic bodies and its internal textures, which is called seismic facies analysis ([Mitchum et al., 1977](#)), helps to specify the depositional environment of the investigated sedimentary rocks. An analysis of the seismic facies is a must in seismic interpretation to determine the depositional environment and to locate potential reservoirs, especially in complex oilfields. Generally, different sedimentary rocks yield different seismic facies. The seismic facies of a buried carbonate mound or reef, for example, differs significantly from a submarine fan or a delta system. Hence, each depositional system has its particular seismic facies ([Schlaf et al., 2005](#)).

To recognize and analyze seismic facies with regard to the geologic environment is one of the goals of seismic stratigraphy ([Dumay and Fournier, 1988](#)). There are two major problems in seismic facies analysis: the first is to determine which seismic parameters are discriminants for characterizing the seismic facies; the second is to be sure that there is a link between the seismic parameters and the geological facies which is investigated by interpreter. To define the seismic facies, it is important to take into account all the information contained in the seismic traces. Thus, interpreter need to study simultaneously a large number of seismic parameters computed from the traces. Then interpreter have to determine which variables, among all those interpreter could compute, discriminate facies in each case being studied. The most efficient way to deal with these two requirements is to carry out multivariate analyses of the seismic parameters extracted from traces.

Nowadays, automatic seismic facies analysis techniques have been growing as an important interpretation tool for the oil exploration industry. Depending on the reservoir knowledge, the seismic facies analysis could be supervised by a priori geological information, or could be unsupervised, when there are not enough data to guide the analysis. For a seismic interpreter, seismic facies analysis still is a monotonous and time consuming task. Hence, a process is highly required which makes this interpretation step automatic.

6.1 Seismic Facies Analysis

Seismic facies originally were defined based on qualitative but objective descriptions of the seismic trace shape ([Mitchum et al., 1977](#)). The seismic facies correspond to amplitude, phase, and frequency variations along and between traces in a specific interval of a seismic data. In every seismic facies analysis system it is a must to find out in what kind of depositional environment the investigated rocks were generated. If the depositional environment of a sedimentary rock is known then further exploration and production strategies can be refined and optimized ([Stoker et al., 1997](#)).

Seismic facies analysis is a tool to describe depositional environments out of seismic data. It applies certain techniques that can help to specify depositional environments. Seismic facies analysis technique is mostly based on ([Schlaf et al., 2005](#)):

- the external shapes of seismic bodies;
- boundary relationships between those bodies;
- the internal texture of those bodies.

The external form and areal association of seismic facies units provides information on gross depositional environments, sediment source and geological setting. In seismic facies analysis, some basic types of external shapes can be differentiated. Those individual units or sequences includes sheet, sheet drape, wedge, bank, lens, mound, fan, and fill (channel fill, slope-front fill and basin fill) ([Mitchum et al., 1977](#)).

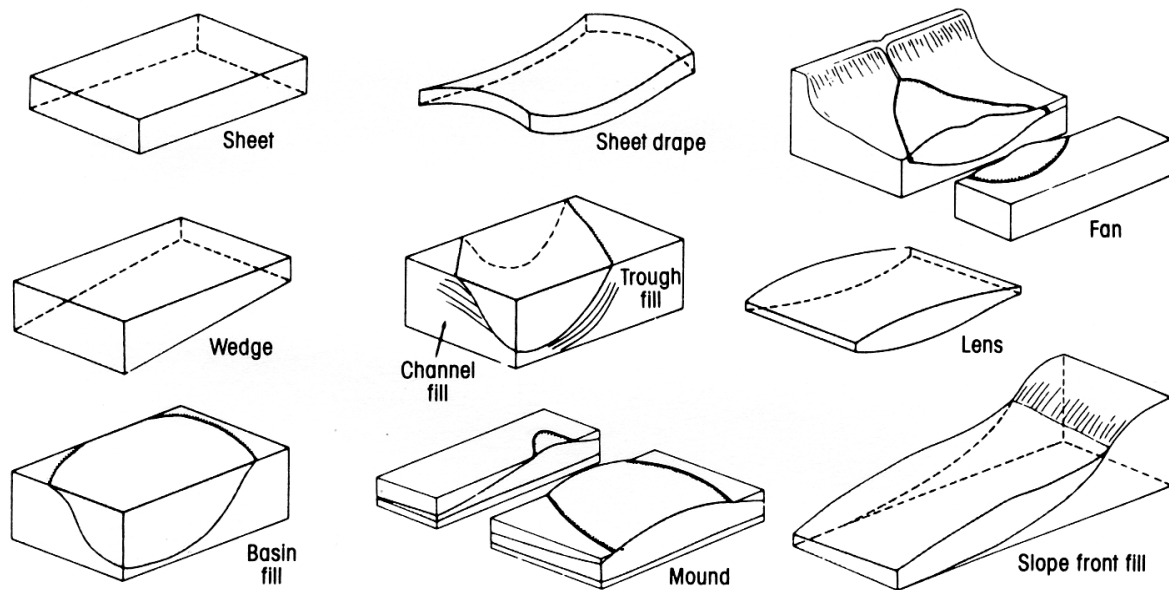


Figure 6.1 3D shapes of seismic facies units.

The boundaries between different shapes are reflection terminations. The identification of any of these shapes can only be established from a 2D grid of seismic profiles which allows the geometry of the sequence to be build up in a quasi-three-dimensional manner. The mapping of reflection terminations is the key to seismic facies analysis. Problems in mapping reflection terminations can arise when terminations laterally pass into concordant relationships.

The recognition of these features on a seismic profile is based on a number of seismic reflection parameters of which character of the single reflection, configuration of reflections within sequences, and external form of facies units or sequences are the most obvious and directly analysed parameters. The main features of these parameters are summarized below. Most general terms used to describe these parameters, is shown in the Figure 6.1, were originally defined by Mitchum et al ([1977](#)).

In seismic interpretation, clustering seismic data can be used to extract more information about structures and geology of underground units. Waveform classification is a popular method. It has been successfully applied to oil and gas reservoir prediction. In waveform classification, seismic waveforms are classified using clustering analysis technology. In this method, the number of classes is a key parameter. Choosing this parameter is difficult as the geological characters vary from field to field. In fact, a good understanding of geology and seismic data is required to correctly determine the number of seismic facies. In field application, the number of classes usually varies 5 to 15 depending on the complexity of the seismic signal and the time thickness of the reservoir. The result of classification would be too

smooth if the number of classes is very small. On the contrary, the result would be too detailed to be interpreted if the number of classes is too great. Regardless of pattern recognition or neural network, the result is better if the distances between clusters are larger and the distances between samples in each cluster are smaller. This criterion is used to determine the number of classes in our method.

In the classification process, it is assumed that two samples are in the same facies class if they are characterized by similar values in all input seismic attribute volumes, and therefore probably correspond to similar geologic environments. To automatically subdivide a seismic cube into shapes and textures, a certain strategy should be applied. It is recommended to follow the proposal of Mitchum and Vail (1977). They propose two steps: (1) subdivide a seismic data set into bodies (sequences) that have a certain external shape and that are separated by surfaces of discontinuity, called sequence boundaries, and, (2) to analyze the texture of those bodies.

There are two primary categories of classification methods applied in seismic facies analysis: Unsupervised and Supervised. An unsupervised classification gives the interpreter insight by showing how a waveform is changing within the survey. Aside from defining an analysis interval, unsupervised classification does not use any a priori information to determine how a seismic trace is classified, and the results are entirely data driven. A neural network quantifies the changes in waveform into discrete segments and the different character types can be displayed as colour variations on a map or profile. The unsupervised seismic facies classification is usually applied in the preliminary phase, when the reservoir properties should be estimated almost exclusively with the seismic data. Another classification is supervised facies classification. Within this type of classification method, the a priori information is usually obtained through well logs data and its associated petrophysics analysis, which is always punctual compared to the large seismic volume density. Seismic modelling can provide interpreters a way to improve their understanding of the possible seismic responses observed in the classification process. Experience and geologic knowledge of the reservoirs make it easier to encompass all possible variations in terms of structural and petrophysical changes and to relate the lateral variations of seismic facies to possible reservoir parameter changes. This is sometimes an ambiguous and interpretative process.

Independent of whether seismic facies analysis is supervised or not, it can be implemented using the workflow shown in Figure 6.2 (Johann et al., 2001).

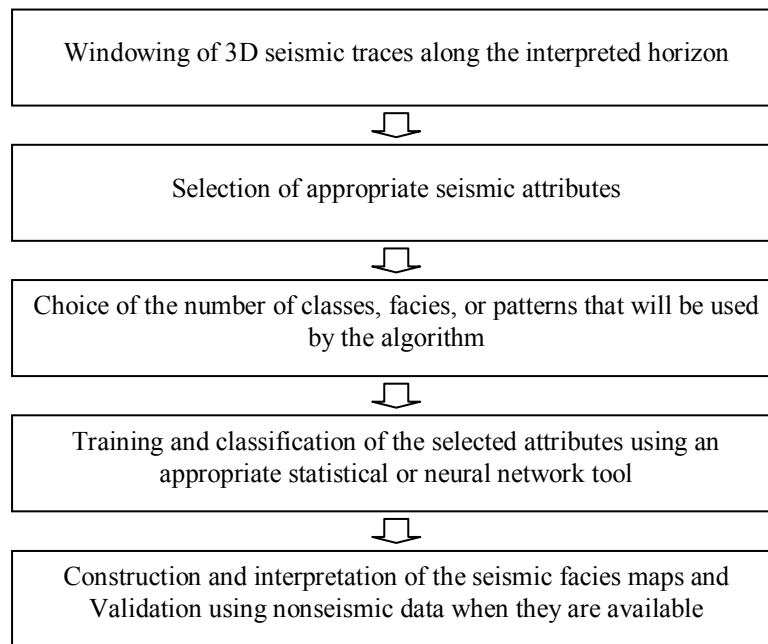


Figure 6.2 Workflow for general seismic facies analysis.

For a better understanding of the method employed in seismic facies analysis it is necessary to introduce some important concepts applied in this approach.

6.1.1 Principal component analysis

Principal component analysis (PCA) is probably the oldest and best known of the techniques of multivariate analysis. The origins of statistical techniques are often difficult to trace. However, it is generally accepted that the earliest descriptions of the technique now known as PCA were given by Pearson ([1901](#)), and developed independently by Hotelling ([1933](#)). PCA is a statistical technique for performing dimension reduction ([Gurney and Gurney, 1997](#); [Mardia et al., 2000](#)). The central idea of PCA is to reduce the dimensionality of a data set consisting of a large number of interrelated variables, while retaining as much as possible of the variation present in the data set ([Jolliffe, 2002](#)). This is achieved by transforming to a new set of variables, the principal components, which are uncorrelated, and which are ordered so that the first few retain most of the variation present in all of the original variables. PCA is a mathematical procedure that finds principal directions in a multidimensional data and determines the optimal shift and rotation of the data, so that it is expressed in those principal directions. PCA is a way of identifying patterns in data, and expressing the data in such a way as to highlight their similarities and differences ([Smith, 2002](#)). Since patterns in data can be hard to find in data of high dimension, where the luxury of graphical representation is not available, PCA is a powerful data-driven tool for that describes the relationships between

multiple variables and their classification as homogenous sets. The other main advantage of PCA is that once these patterns have been found in the data, and the data is compressed, for instance by reducing the number of dimensions, without much loss of information.

To increase the information available for seismic facies classification, multiple post-stack seismic attribute volumes derived from original seismic data are used in seismic facies classification study. Seismic samples from input volumes are projected into a multidimensional plot in which the number of dimensions corresponds to the number of input volumes. Then, the main data trends (principal axes) are found in the data cloud. The data samples are projected on the principal axes. The output of this procedure is a set of new 3D volumes named PCA components.

Hagen ([1982](#)) employed principal component analysis to study the lateral differences in porosity, Dumay and Fournier ([1988](#)) employed both the principal component analysis and the discriminant factor analysis to identify the seismic facies. Analysis of the PCA results was based on eigenvalues, contribution, and cumulated inertia. Only the first several components were selected as input for the hierarchical classification. These components contributed more than 85% to the data and contained important information about the main data trends. The noise and redundant data were adsorbed by the fourth component. The PCA analysis also helped understand the relationship between the PCA components and the input attributes. For example, the first PCA component happened to be mostly affected by the amplitude envelope with a minor contribution from fluid factor. However, all four input volumes have contributed to the definition of this PCA component. Therefore, it is difficult to relate the results back to the input attributes using cross-plots. The interpretation of the results of the classification with PCA still can be achieved using the calibration to well data and detailed analysis of morphologic patterns on vertical seismic sections, horizon and proportional slices, and 3D views.

6.1.2 The K-means clustering

K-means clustering algorithm uses an iterative algorithm that minimizes the sum of distances from each sample to its cluster centroid over all clusters ([Seber, 1984](#)). This algorithm moves samples between clusters until the sum cannot be decreased further. The result is a set of clusters that are as compact and well-separated as possible.

An optimal clustering algorithm should minimize the distance between the elements of each group and, at the same time, maximize the distance between the different clusters.

K -means clustering algorithm can be done by the following steps ([Sabeti and Javaherian, 2009](#)):

- Start with K random cluster centroids.
- Assign each new samples to the cluster with the closest centroid. After all samples have been assigned the new centroid for each cluster is calculated.
- Repeat second step until new centroids are not changed.

There are several ways of measuring distance ([Theodoridis and Koutroumbas, 1999](#)); Sabeti and Javaherian use Equation (6.1) to compute the distance between the elements of each group.

$$E = \sum_{i=1}^k \sum_{j=1}^{n_i} d^2(x_{ij}, m_i) \quad (5.1)$$

where E represents the sum of square-errors for all samples in the dataset, x_{ij} is the j^{th} sample in the i^{th} cluster, m_i is the center or mean of the i^{th} cluster, n_i is the number of samples in the cluster, k is the number of clusters and d is the Euclidian distance which is defined by the following equation ([Shen et al., 2005](#)):

$$d(x_{ij}, m_i) = (x_{ij} \quad m_i)(x_{ij} \quad m_i)^T \quad (5.2)$$

For simplicity, Matos ([2007](#)) use the Euclidian norm. To compute the distance between the elements of each group, they use the average distance S_k between each element x_i and its group centroid c_k :

$$S_k = \frac{\sum_i \|x_i - c_k\|}{N_k} \quad (5.3)$$

where N_k is the number of elements in the group. The distance between the k and l groups is computed as the distance between their centroids:

$$d_{kl} = \|c_k - c_l\| \quad (5.4)$$

The partitive clustering algorithm divides the data set into a predefined number of clusters, trying to minimize some error function, with the number of groups chosen and verified through SOM visualization. To automate the classification process, Matos use the index DBI

([Davies and Bouldin, 1979](#)) as a means of evaluating the results of the K-means partitioning.

The best clustering corresponds to the minimum DBI given by:

$$DBI = \frac{1}{K} \sum_{k=1}^K \max_{l \neq k} \left\{ \frac{S_k + S_l}{d_{kl}} \right\} \quad (5.5)$$

where K is the number of groups, S_k and S_l are defined by equation (6.3), and d_{kl} is defined by equation (6.4). DBI values smaller than unity represent separate groups, whereas values larger than unity represent groups that may overlap.

6.1.3 Statistical analyses

A useful automatic seismic facies mapping tool has to combine information about shapes and textures within these shapes. Only a combination of shapes and textures enables a meaningful seismic facies analysis fulfilling the requirements of seismic stratigraphy. Mapping of seismic bodies has to be done on the basis of reflection terminations. As soon as a seismic data set is subdivided into different shapes, texture analysis within each of the shapes can be achieved.

Statistical analyses have been applied to seismic data in order to characterize a seismic facies related to a geologic environment. The techniques which have been used are conventional or multidimensional statistics. Most of the previous works use multidimensional data analyses because the techniques take a large number of seismic parameters into account simultaneously.

Conticini ([1984](#)) carried out conventional statistical analyses (cross-plots, star diagrams) on attributes of the traces such as continuity, instantaneous frequency, and analytical signal modulus. His aim was to identify the different facies encountered in fluvial deposits. Mathieu and Rice ([1969](#)) studied lateral variations in sand-shale ratio for a reservoir formation. They analyzed trace amplitudes by means of discriminant factor analyses and pointed out the possibility of grouping the traces (either synthetic seismograms computed from well data or real traces) with respect to the prevailing lithology. Hagen ([1982](#)) studied real seismic traces at a reservoir level in order to emphasize lateral variations of the formation porosity. He took into account frequencies estimated at the reservoir level. A principal components analysis reduced the number of parameters used to describe each trace. Then the new parameters, the principal components, were used in a clustering algorithm to group traces that correspond to porosity areas.

Khattri and Gir ([1976](#)), Khattri et al ([1979](#)) Sinvhal and Khattri ([1983](#)) Sinvhal et al ([1984](#)) studied real and synthetic traces simultaneously. They generated synthetic sedimentary

sequences by means of first-order Markov chains or by Monte Carlo simulations. Only a few lithologies were used in the studies, i.e., binary sequences with sand and shale or shale and coal. The impulse response was computed and analyzed with variables estimated from the autocorrelation function and from the power spectrum. Conventional and multidimensional analysts (histograms, Kolmogorov-Smirnov tests, discriminant factor analyses) on the variables permitted trace classification with regard to the sedimentary sequence type. The study of real seismic data, in formations with lateral sand-shale ratio variation, corroborated the value of applying discriminant analyses to the computed variables.

Bois ([1980](#), [1981](#), [1982](#)) developed two techniques based on pattern recognition: one with and one without prior learning. Bois' techniques were tested on a reservoir formation in order to define facies limits. Bois computed, on the portion of each seismic trace at the level of the reservoir, the first three coefficients of an autoregressive adjustment of the traces. After defining a pseudo-distance based on these coefficients Bois applied clustering techniques. The process with prior learning calibrated seismic facies (traces) to a nearby well. If the studied traces were near the learning traces (as defined by the pseudo-distance), the seismic facies were classified with the corresponding calibrated facies.

Matlock and Asimakopoulos ([1986](#)) characterized the rapid facies variations in a 150 ms thick reservoir formation. Parameters were related to the frequency characteristics of the traces and seismic traces classified by comparison to reference traces located near wells where reservoir facies were found. Multidimensional statistical techniques clearly defined the limits between the different erent facies on the two seismic lines studied.

Dumay and Fournier ([1988](#)) described a methodology for automatic facies recognition. The methodology for automatic facies recognition used two types of multidimensional analyses: clustering techniques and factor analyses. The methodology based upon two steps. First is a learning step beginning with computation of seismic parameters for the learning traces. Learning is followed by multidimensional analyses and a predictive step which allows an automatic facies classification. The automatic recognition is reliable and fast; the facies map obtained combines several discriminant parameters simultaneously. The most important problem remaining is to make the connection between the seismic facies interpreter has characterized and the geologic facies interpreter is trying to characterize. The physical meaning of some of the chosen discriminant variables is not entirely clear. A modelling step sometimes helps relate the geologic variations to the measured seismic parameters, but this step is not always sufficient. There are problems with the way we evaluate some of the seismic parameters; for example, the parameters computed from the spectrum. Indeed, it is

very difficult to estimate the frequency characteristics of a signal for a very short time interval. Second is a predictive step which allows automatic facies recognition. In this step, authors compute the previously chosen discriminant parameters on unknown seismic traces and classify the unknown traces with regard to the learning traces.

Pennington et al ([2001](#)) developed a algorithm based on modified cross-correlation model for seismic facies analysis. The algorithm can:

- realign a mistracked horizon;
- discern subtle changes in seismic trace patterns;
- easily perform pattern recognition for user-specified traces over a survey;
- provide continuous output values;
- combine and visualize the results for multiple trace pattern analysis (posterior-classification).

The algorithm is a modified cross-correlation model, which is a standard method for estimating the degree to which two series are correlated. Consider two series of signals $X(i)$ and $Y(i)$ where $i = 1, 2, \dots, N$. The cross-correlation, R , at delay d is defined as

$$R = \frac{\sum_i^N (X(i) - X_m)(Y(i-d) - Y_m)}{\left(\sum_i^N (X(i) - X_m)^2 \right)^{1/2} \left(\sum_i^N (Y(i-d) - Y_m)^2 \right)^{1/2}} \quad (5.6)$$

where X_m and Y_m are the means of the corresponding series and d is the time window for possible horizon mistracking. The denominator in the expressions above serves to normalize the correlation coefficients such that it ranges from -1 to 1 . A value of one indicates maximum correlation while zero indicates no correlation. A high negative correlation exhibits a high correlation but of the inverse of one of the series. However, this cross-correlation is focused on the relative similarity of patterns between two time series rather than absolute similarity. Hence, this expression was modified such that it can judge the difference in absolute values within the shape. The modified expression is written below, showing an additional factor that computes for similarity of amplitude on an absolute value:

$$R = \frac{\left(\frac{\sum_i^N [(X(i) - X_m)](Y(i-d) - Y_m)}{\left(\sum_i^N (X(i) - X_m)^2 \right)^{1/2} \left(\sum_i^N (Y(i-d) - Y_m)^2 \right)^{1/2}} \right) \left(\frac{\sum_i^N |Y(i)|}{\sum_i^N |X(i)|} \right)}{\quad} \quad (5.7)$$

This algorithm, as implemented, can also correct for possible horizon mistracking by searching an amount of time (d samples specified by the user) in order to find the highest value for R. The output values for R are continuous from -1 to 1 and provide a value at every trace.

6.1.4 Structure of Artificial Neural Networks

The perceptron ([Rosenblatt, 1958](#)) is the most used artificial neuron in neural network configurations and is based on the nonlinear model proposed by McCulloch and Pitts ([1943](#)). Artificial Neural Networks (ANNs) are a mathematical model that tries to simulate the structure and functionalities of biological neural networks. ANNs derive their computing power from their distributed massively parallel structure and their ability to learn and generalize, making possible the resolution of complex problems in different knowledge areas. The number of types of ANNs and their uses is very high. Since the first neural model by McCulloch and Pitts ([1943](#)) there have been developed hundreds of different models considered as ANNs. The differences in them might be the functions, the accepted values, the topology, the learning algorithms, etc.

The artificial neuron is the information processing unit—the fundamental element for the operation of the ANN—but still primitive if compared to those found in the brain. The artificial neurons, as well as the biological neurons, have input connections, output connections and an internal process that generates an output signal in response to the input signal. The artificial neurons, shown in Figure 6.3, are formed by ([Veronez et al., 2011](#)):

- Input signals (x_1 , x_2 and x_m) or input information, which might come from the environment or from the activation of other neurons.
- A set of weights (w_{k1} , w_{k2} , w_{km}), which describe the connection forces; that can be positive, representing excitatory junctions; or negative, inhibiting the activation of the neuron. When there is no connection between two neurons the synaptic weight is null.
- Sum function (Σ), which represents the summation of the input signals multiplied by their respective weights, constituting a linear combiner.

- Activation function $[\varphi(\cdot)]$, which restricts the output amplitude of the neuron, in an interval normalized between $[0;1]$ or $[-1,1]$.
- Output signal (y_k), which is the result generated by the neuron.

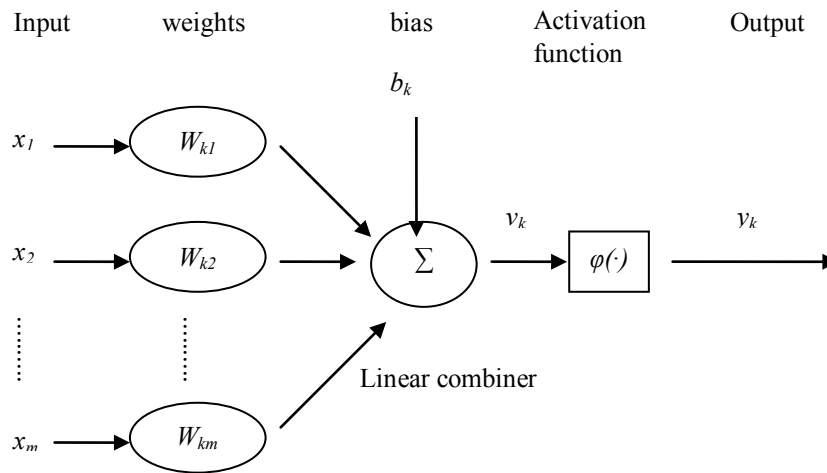


Figure 6.3 Structure of artificial neurons

Every piece of input information has an associated weight, also known as the synaptic weight, which mathematically represents its degree of importance for that neuron. The input signals of the neurons are multiplied by their synaptic weight, and the summation of this result added to the bias forms the input information of the neuron. The three most common activation functions are hardlimit function, linear function, and sigmoid function.

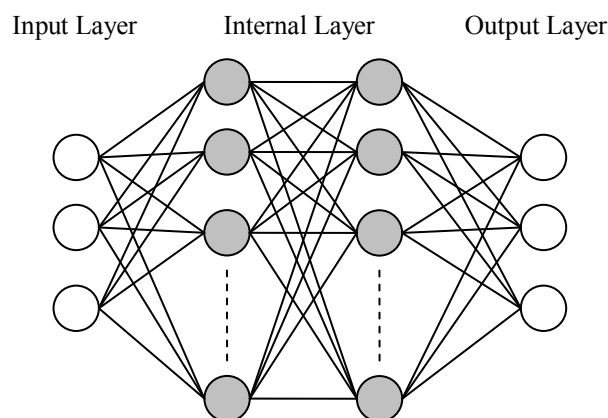


Figure 6.4 Structure of multilayer artificial neurons.

Among the different ANN models, the Multilayer Perceptron Model (MLP), shown in Figure 6.4, is particularly popular. In the MLP there is an input layer, one or more intermediary layers, and the output layer which provides the network result.

The great potential for parallelism is one interesting aspect of some neural networks. Parallelism allows processing huge amounts of data without excessive memory requirements. Generally, the design of a neural network is composed by three main steps ([Haykin, 1999](#)):

- **Configuration** - how layers are organized and connected;
- **Learning** - how information is stored;
- **Generalization** -- how neural network produces reasonable outputs for inputs not found in the training.

For several decades, artificial ANNs have been used successfully in a variety of different application areas. In most cases an ANN is an adaptive system that changes its structure based on external or internal information that flows through the network during the learning phase. The operation of ANNs is inspired by the human brain. Modern neural networks are non-linear statistical data modelling tools. Due to their non-linear structure, ANNs can represent more complex features from data, which are not always possible using statistical techniques or traditional deterministic methods. The major advantage of ANNs over conventional methods is that there is no need to know the intrinsic theory of the problem, nor the necessity to analyze the relationships that are not fully known among the variables involved in modelling.

ANNs have assisted in data reduction processes through classifications applied to a wide spectrum of aspects (from traffic solutions and medicinal purposes to geophysical interpretations). In the geosciences area, ANNs have been used to model complex phenomena involving variables difficult to obtain. However some ANN applications involve easily obtainable variables for the solution of problems, but which are usually difficult to solve using conventional mathematical methods. In evapotranspiration and surface temperature modeling; geophysics in lithological classification([Bhatt, 2002](#); [Yang et al., 2004](#)); soil science ([Zacharias and Wessolek, 2007](#)). In the case of seismic data mining, Strecker and Uden ([2002](#)) used an unsupervised approach where the neural network is free to search, to recognize, and to classify structural patterns in an n-dimensional vector field spanning the entire 3D input seismic attribute data set. Within the data set, each data sample is defined by a unique combination of physical, geometric, and hybrid attributes and is treated as an n-dimensional vector.

6.1.5 Self-Organizing Maps

Kohonen defined the self-organizing process in its most fundamental in his early researches ([Kohonen, 1981](#), [1982](#), [1984](#)). The Self-Organizing Map (SOM) is an unsupervised-learning (adaptive) algorithm in the neural-network category. It means that the representations of information are determined automatically from the metric relationships between the data items; no 'teacher' is needed, i.e. no input -output relations are defined a priori. The SOM forms a nonlinear projection from a high-dimensional data manifold onto a regular, usually two-dimensional, grid. Thereby it carries out clustering, visualization and abstraction of the multidimensional input data.

The SOM algorithm computes the collection of the models so that it optimally describes the domain of (discrete or continuously distributed) observations. The models are automatically organized in a meaningful two-dimensional order so that similar models become closer to each other in the grid than the more dissimilar ones. In this sense the SOM is a similarity graph and a clustering diagram. Its computation is a non-parametric, recursive regression process. These three subprocesses, broadcasting of the input, selection of the winner and adaptation of the models in the spatial neighbourhood of the winner, seem to be sufficient, in the general case, to define a self-organization process that then results in the emergence of the topographically organized 'maps'. It has to be emphasized, however, that the mathematical theory is extremely difficult and its development is still in progress. Proofs exist only for the simplest cases by Cottrell ([1998](#)).

The Self-Organizing Map is intended as a viable alternative to more traditional neural network architectures. Its analytical description has already been developed further in the technical than in the biological direction. A large number of scientific publications on the SOM have been written, The main application areas are:

- statistical analysis at large, in particular data mining and knowledge discovery in databases;
- analysis and control of industrial processes and machines;
- new methods in telecommunications, especially optimization of telephone traffic and demodulation of digital signals;
- medical and biological applications.

The SOM is closely related to vector quantization methods. It is currently one of the most

important tools for the non-supervised seismic facies analysis ([Coleou et al., 2003](#)).

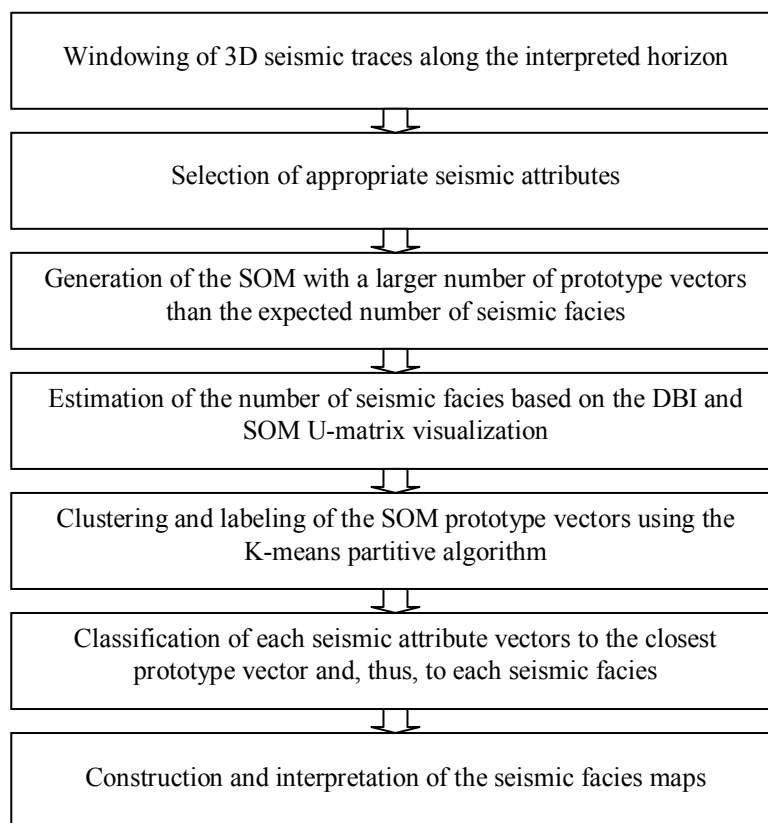


Figure 6.5 Workflow for non-supervised seismic facies analysis based on SOM clustering using waveform attributes.

Poupon et al ([1999](#)) demonstrated SOM usefulness in seismic facies analysis. Basically, in this scheme, each of the model classes corresponds to a discrete class of patterns and the problem then becomes a decision process. All model classes are “self-organized” and updated at each iteration. The final classes are assigned to each trace, each of them is labeled with the corresponding model classes or colours. Notice that changing the time of first sample in the series, due to horizon mistracking, can significantly alter the vector value.

To obtain a more quantitative clustering of data properties, SOM groups could be visualized using the U-matrix and chosen manually. However, the manual selection of the clusters could be tedious and imprecise. Agglomerative, or partitive, SOM clustering or U-matrix segmentation using image processing algorithms ([Costa and de, 1999](#)) provides an automated means of clustering. Matos et al ([2007](#)) use a K-means partitive clustering algorithm. In contrast to conventional K-means, they cluster the prototype vectors instead of the original data ([Vesanto and Alhoniemi, 2000](#)). In this manner, large data sets formed by the SOM prototype vectors can be indirectly grouped. The proposed method not only provides a better understanding about the group formations, but it is also computationally efficient ([Vesanto et](#)

al., 1999). Another benefit of this methodology is noise reduction because the prototype vectors represent local averages of the original data without any loss of resolution. The flowchart in Figure 6.5 shows the proposed methodology for non-supervised seismic facies analysis based on the SOM clustering by Matos.

6.2 3D moments-based approach for seismic facies analysis

In section 5.2.3, we have introduced the definition of 3D geometric moments and have proposed the definition of 3D Gaussian-Hermite moments. We have also discussed the 3D moments-based estimation features of local volume in section 5.2.4.

6.2.1 3D Feature extraction of seismic traces

The local characteristics of the structure are expressed in terms of geometry and intensity information. They are computed from the 3D moments up to the order 2 inside a cube window centred on the point of interest seismic trace. Then we define a metric to describe the feature of each cube windows with a 1D vector by several order of moment:

$$\mathbf{V} = [\eta_0, \eta_1, \eta_2, \dots, \eta_n] \quad (5.8)$$

Of course, it is not necessary to construct the feature vector with all order of moments. We can arbitrarily select the moment with certain orders however, different order of moment constructing the feature vector, the different representation ability will exhibit. Here, we construct the feature from the 12 moments up to order 3 ($M_{000}, M_{100}, M_{010}, M_{001}, M_{110}, M_{101}, M_{011}, M_{200}, M_{020}, M_{002}, M_{003}, M_{005}$).

6.2.2 The workflow for seismic facies using 3D moments attribute

The flowchart in Figure 6.6 shows the proposed methodology for non-supervised seismic facies analysis based on the SOM clustering using 3D moments attribute. The flowchart starts with getting data of the seismic traces data within a subvolume along the interpreted horizon. Then we extract the feature vector using 3D moments algorithm. In non-supervised seismic facies analysis, the estimation of the number of existing seismic facies in the feature vector data is typically determined in an empirical way. We estimate the number of seismic facies through SOM visualization. We begin by choosing a number for the SOM prototype vectors that is larger than the number of expected groups in the data. Even though only qualitative

information is generated, by using concepts of geomorphology, this procedure can be a quite powerful interpretation tool.

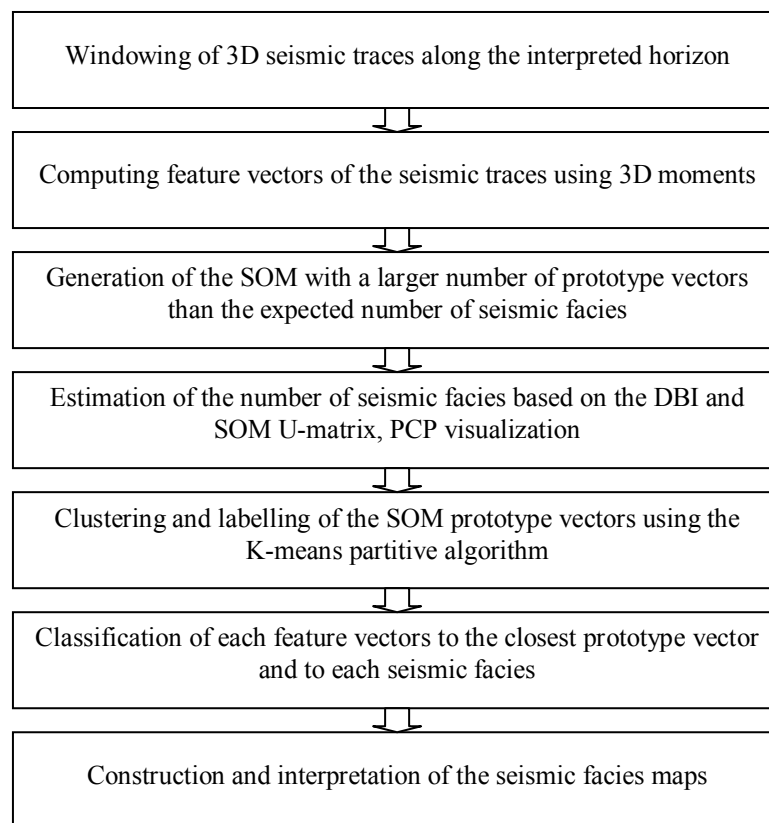


Figure 6.6 Workflow for seismic facies analysis based on SOM clustering using 3D moments attribute

To obtain a more quantitative clustering of data properties, SOM groups could be chosen manually or be visualized using visual tools. However, the manual selection of the clusters could be tedious and imprecise. The clustering output of SOM can be represented using three visual techniques:

- The first is the unified distance matrix, or U-matrix ([Ultsch, 1993](#); [Ultsch and Siemon, 1990](#)). In this display, the distances between the patterns are represented in a 2D hexagonal grid with gray shading. A cluster is an area of the SOM map represented by light shading, whereas borders between clusters appear as dark edges. Another visual component on the U-matrix display is the size of the dot in each node, representing the number of hits in that node. In the U-matrix image, the intensity of each pixel corresponds to the respective estimated distance. Therefore, the U-matrix not only shows the average distance between each element, it also shows the gradient between them.
- The second visual display is the multi-dimensional visualization of the patterns discovered with a parallel coordinate plot, PCP ([Inselberg, 1985](#)), using a nested-means scaling

procedure. This visualization tool can be used to investigate the presence of multidimensional clusters ([Wegman and Luo, 1997](#)). The PCP adaptation in the visual strategy displays the weight vector of each SOM node as polygonal segments, the colour and thickness of which come from the U-matrix display.

- The third display is a geographic map view of the patterns discovered, where the seismic traces are displayed according to their x- and y coordinates with a colour coding from the U-matrix display. More detailed descriptions of each of the graphic components are presented in ([Marroquín et al., 2009](#)).

After SOM learning, the partitive clustering algorithm will divide the data set into a predefined number of clusters, trying to minimize some error function, with the number of groups chosen and verified through SOM visualization. To automate the classification process, we also use the index DBI ([Davies and Bouldin, 1979](#)) as a means of evaluating the results of the K-means partitioning. The best clustering corresponds to the minimum DBI given by equation(6.5).

Then, we classify each feature vectors to the closest prototype vector and to each seismic facies. Finally we construct the seismic facies maps.

6.3 Example of seismic facies analysis

We selected a sub-volume from a 3D seismic survey located in the middle of China. The sub-volume covers an area of 190*200(interval 30m) and a 4-ms sampling rate. We now apply the proposed methodology to this sub-volume. Before seismic facies analysis, We use auto-tracking method based on 3D Gaussian-Hermite moments to interpret a seismic horizon. Figure 6.7 shows the result in case inline section and in case crossline section. The map is shown in Figure 6.8.

Then, we compute feature vectors of the seismic traces using 3D moments, and cluster facies using SOM with a larger number of prototype vectors than the expected number of seismic facies. The analysis results with the proposed algorithm along the interpreted horizon are shown from Figure 6.9 to Figure 6.13. Figure 6.9 shows the U-matrix. In this example, six groups or facies are easily identified from the U-matrix, and the classification result was excellent. In contrast to the U-matrix display, the PCP graphic display shown in Figure 6.10 suggests the presence of six distinctive associations of seismic facies. Figure 6.11 shows the automatic classification of six groups. Finally, the classification with six groups is shown in

Figure 6.12 and Figure 6.13.

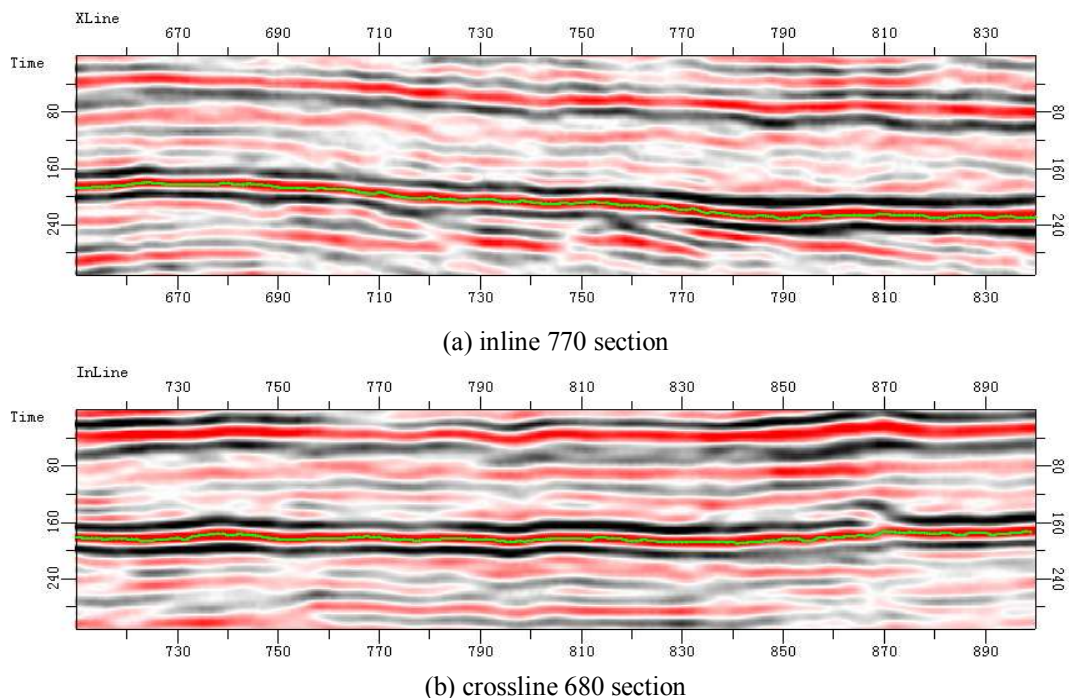


Figure 6.7 The interpretation of horizon for facies analysis.

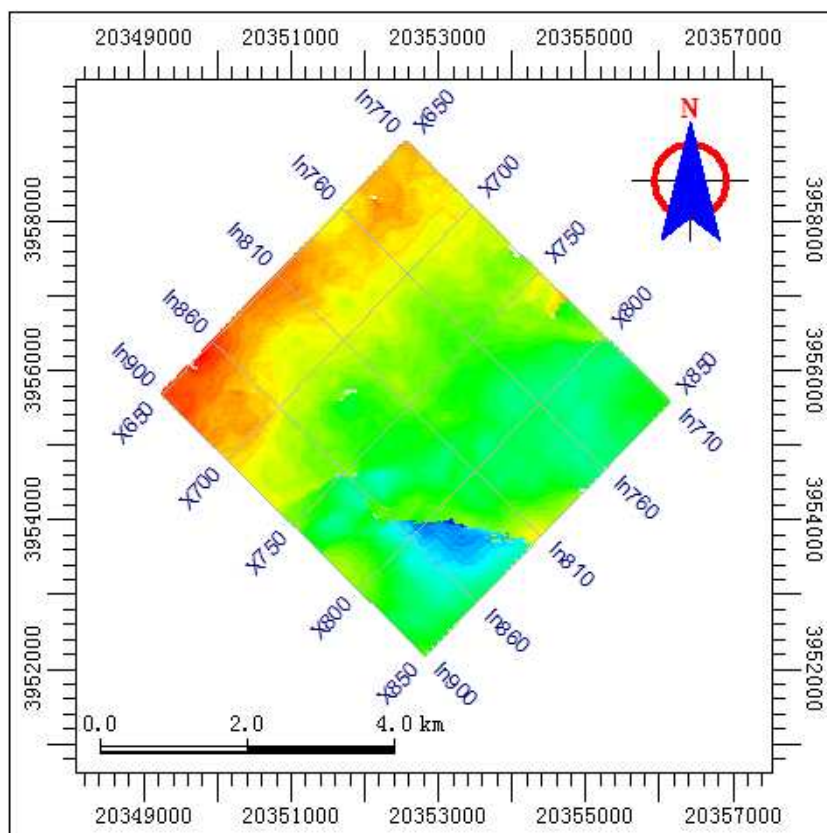


Figure 6.8 The map of horizon for facies analysis

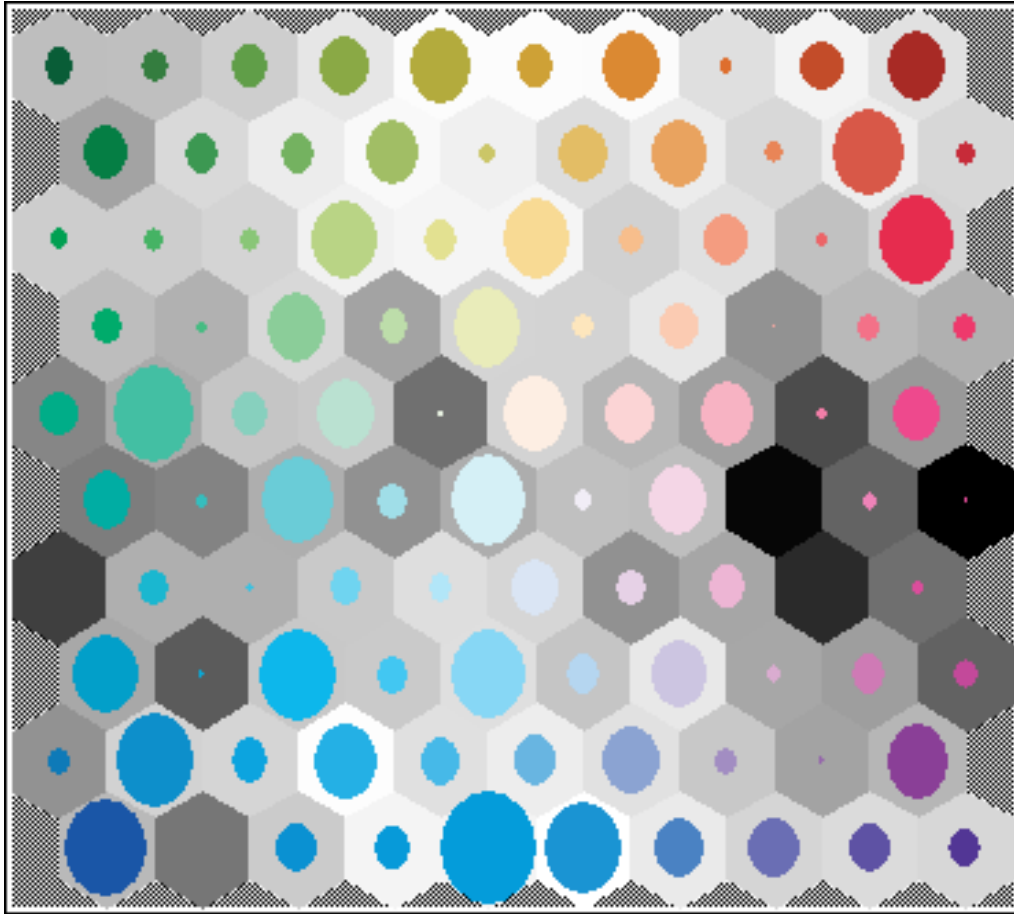


Figure 6.9 The U-matrix display.

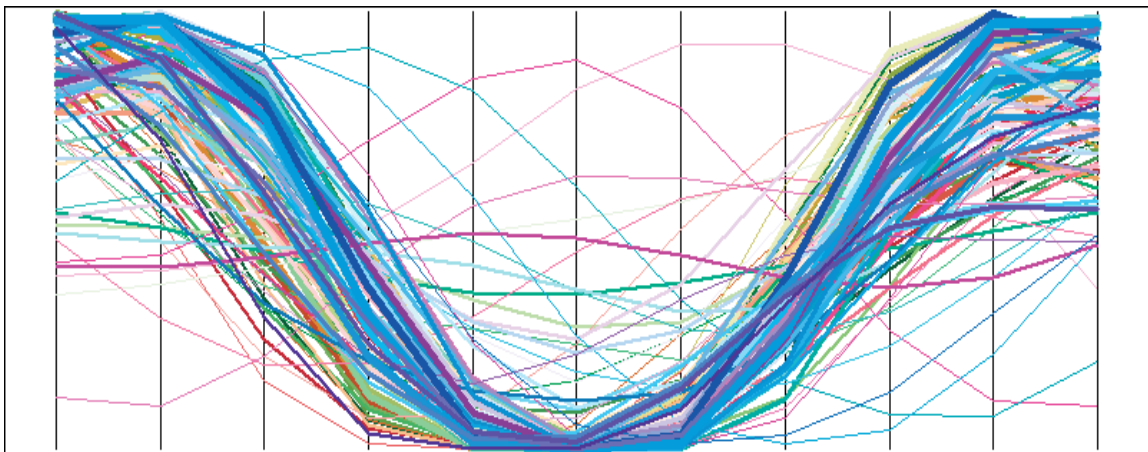
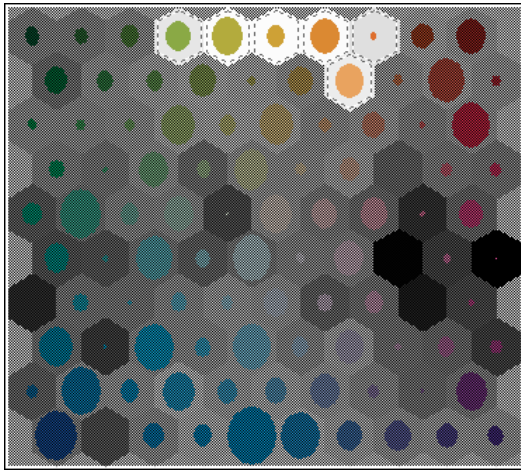
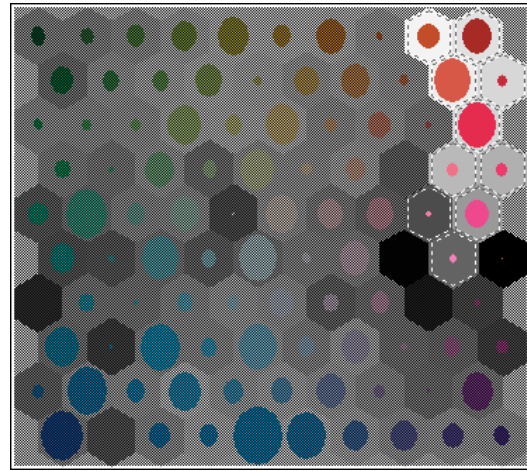


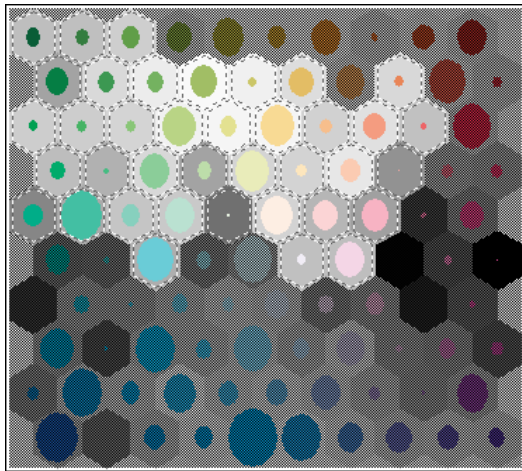
Figure 6.10 The PCP graphic display.



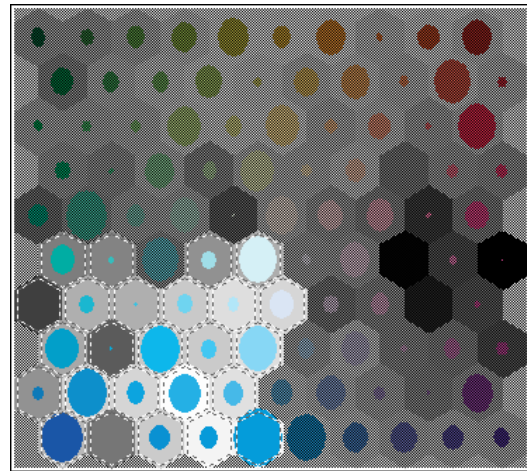
(a)



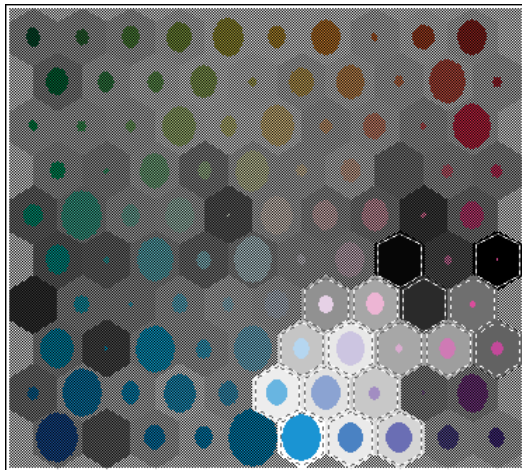
(b)



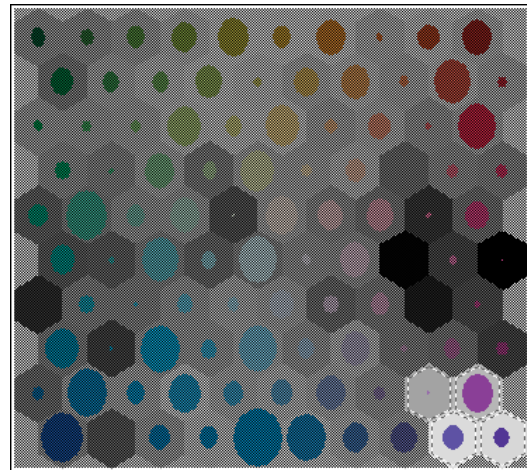
(c)



(d)



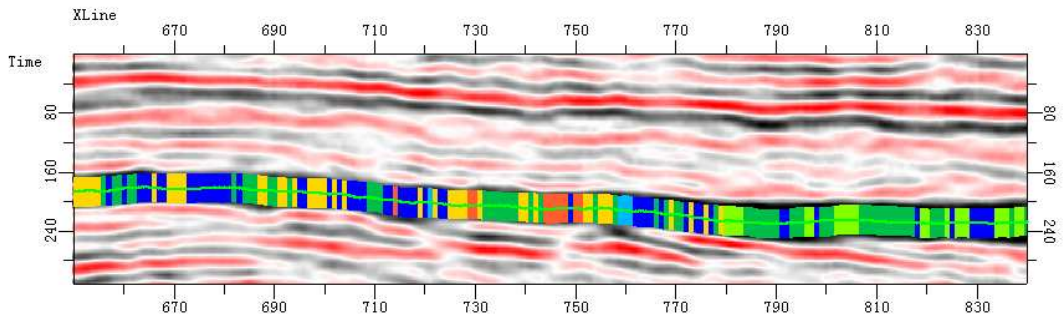
(e)



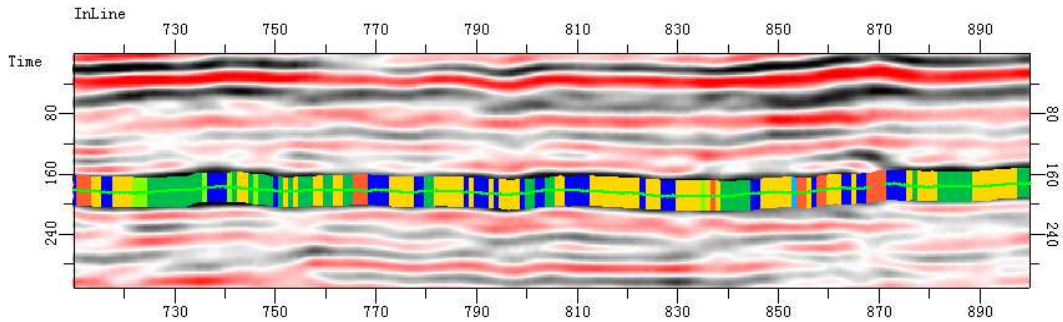
(f)

Figure 6.11 Automatic classification of U-matrix.

- | | |
|------------------|-------------------|
| (a) First class; | (b) Second class; |
| (c) Third class; | (d) fourth class; |
| (e) Fifth class; | (f) Sixth class. |



(a) inline 770 section



(b) crossline 680 section

Figure 6.12 The result of seismic facies analysis.

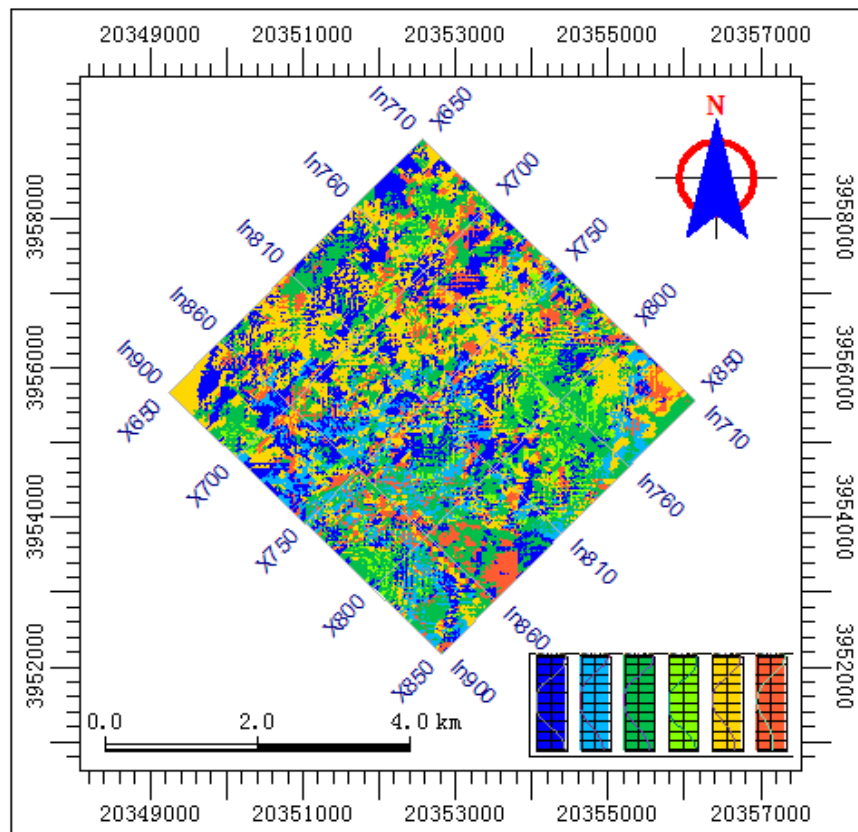


Figure 6.13 The map result of seismic facies analysis

6.4 Conclusion

Seismic facies analysis is one important task of the seismic interpretations. Automatic seismic facies analysis techniques can be applied in seismic exploration to improve our efficiency and to reduce costs. Clustering is the organization of patterns in such way that all patterns in a single cluster have a natural relation, and patterns not in the same clusters are in some way different. However, clustering is a subjective process because the same data set can be partitioned differently depending on the specific criterion used for clustering. Therefore, it is important to investigate the characteristics of the problem of interest with the objective to select an appropriate clustering strategy. SOM is a technology that visual-based data mining approach combines a clustering process. With data visualization techniques (e.g., U-Matrix, PCP graphic and geographic mapping displays), it can provide an environment for exploring patterns in the data sets.

In this chapter, we have reviewed some different clustering algorithms applied to automated seismic facies analysis. We present an approach based on 3D Gaussian-Hermite moments to extract the feature vectors of the seismic data traces. Then we use unsupervised clustering algorithms (SOM) and visualization tools (U-Matrix, PCP) to cluster those feature vectors. The integrated environment for visual-based data mining approach using SOM gives the best performance in interpreting the correct cluster structure in seismic data sets. Offering information for interactive visual exploration of data sets, this visual-based strategy enhances user interpretation. The excellent result of the seismic facies analysis suggests that the method proposed in this work is an important tool for seismic exploration because it is more robust to interpretation errors.

7 Parallel processing and Volume visualization

Today Seismic volumes are typically tens of gigabytes, and hundreds of gigabytes are not uncommon. 64-bit operating systems have enabled much larger system memory, but both system memory and texture memory on the graphics processing unit (GPU) remain scarce resources compared to the size of the data sets.

In the past decades, applications enjoyed an automatic increase in performance as CPU vendors competed to increase the clock speed in each new generation of chips ([Heck, 2006](#)). With these advances seismic data interpretation can be migrated from big machine to PC. However physical limitations such as power consumption and heat dissipation have largely ended this era. The CPU vendors are now competing to increase the number of "cores" in each new generation of chips. Dual-core and quad-core chips are already common, with higher - core chips coming soon. Multi-core processors offer software developers the ability to apply more resources at a particular problem. These additional resources can be employed to offer two types of advantages, improved turnaround time or solving larger problem domains. To take advantage of this new performance in seismic interpretation, software developers will need to embrace multithreading technology.

In the area of the exploration and production, visualization technology plays a critical role in gaining insight from data. The process of interpreting a seismic survey data begins with a broad view of the seismic data. Seismic section or slice movies and volume rendering are particularly useful in developing an initial understanding of the structural and stratigraphic context of the reservoir. In volume rendering, an entire volume is displayed on the screen, and the interpreter has control of the viewpoint and the opacity of the volume. In the extreme case, where the opacity is set to one, the rendered volume looks like a solid cube. By changing the opacity of the data, the interpreter can view into the seismic volume. It is possible to see the

3D structure of reflections and to begin to understand the relationships between horizons and faults prior to any interpretation. With advances in multi-core threading programming, seismic data management, efficient computing and GPU based rendering, great progresses can be achieved in volume visualization and volume interpretation.

7.1 Parallel processing

In many cases, taking advantage of the performance benefits requires developers to thread their applications. Effectively threading an application is a nontrivial task that requires domain knowledge in multi-core architecture, parallelism fundamentals, and a threading development process. In order to operate on large 3D data sets in a cost-effective manner, applications for seismological analysis and visualization use some new computer techniques, such as multithreads, or computer clusters, to do analysis computations.

7.1.1 General introduction of computer architecture

Flynn ([1972](#)) presented four classifications of computer architectures defined are based upon the number of concurrent instruction (or control) and data streams available in the architecture: Single Instruction, Single Data stream (SISD); Single Instruction, Multiple Data streams (SIMD); Multiple Instruction, Single Data stream (MISD); Multiple Instruction, Multiple Data streams (MIMD). Visually, these four architectures are shown below where each "PU" is a processing unit. For many years, the microprocessor community has translated Moore's Law of transistor density into a direct doubling of single-threaded performance every 18 months ([Moore, 1965](#)). Applications ran faster on each new processor version, and new versions were released frequently. Today, the era of single processor systems is over. The multi- and many-core systems world is here. Developers are entering a phase where taking full advantage of the power of multi-core processors is critical for customers to continue to accelerate innovation and to improve their business success.

A multi-core processor is a single computing component with two or more independent actual processors (called "cores"), which are the units that read and execute program instructions ([TechTarget, 2004](#)). The data in the instruction tells the processor what to do. The instructions are very basic things like reading data from memory or sending data to the user display, but they are processed so rapidly that human perception experiences the results as the smooth operation of a program. An example of such a processor is the Intel Core Duo processor which is comprised of two similar processor cores in the same die (Figure 7.2).

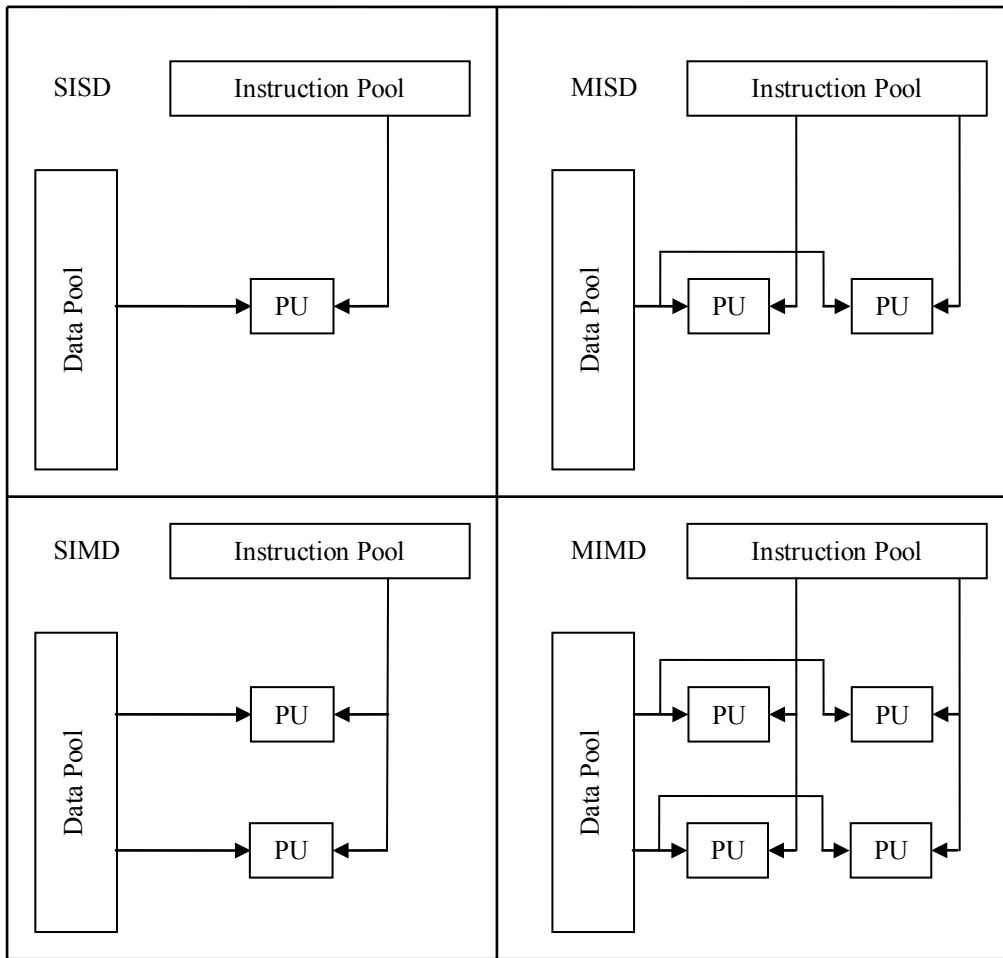


Figure 7.1 Four classifications of computer architectures by Flynn.

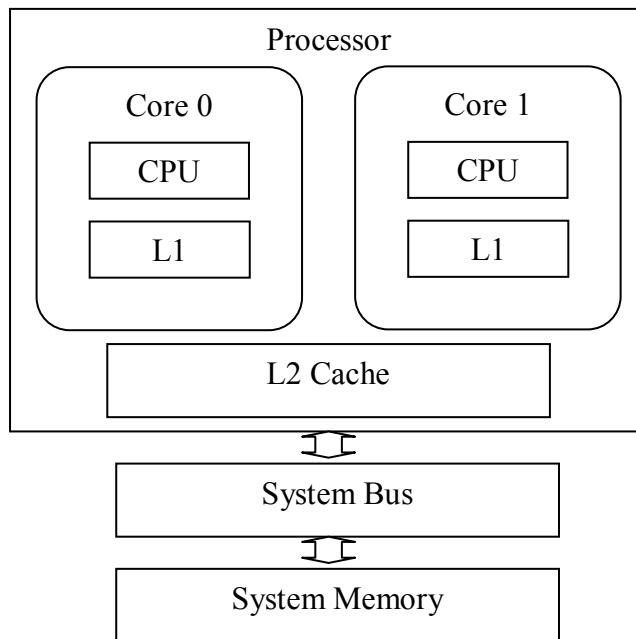


Figure 7.2 Dual-core processor architecture.

Multi-core processors are widely used across many application domains including general-purpose, embedded, network, digital signal processing (DSP), and graphics. The improvement

in performance gained by the use of a multi-core processor depends very much on the software algorithms used and their implementation. In particular, possible gains are limited by the fraction of the software that can be parallelized to run on multiple cores simultaneously. In the best case, so-called embarrassingly parallel problems may realize speedup factors near the number of cores, or even more if the problem is split up enough to fit within each core's cache, avoiding use of much slower main system memory. Most applications, however, are not accelerated so much unless programmers invest a prohibitive amount of effort in re-factoring the whole problem.

A computer cluster consists of a set of loosely connected computers that work together so that in many respects they can be viewed as a single system ([wikipedia, 2011](#)). Clusters are usually deployed to improve performance and availability over that of a single computer, while typically being much more cost-effective than single computers of comparable speed or availability ([Bader and Pennington, 2001](#)).

7.1.2 Typical threaded model

In computer science, a thread is the entity within a process that can be scheduled for execution. All threads of a process share its virtual address space and system resources ([MSDN, 2011](#)). It generally results from a fork of a computer program into two or more concurrently running tasks. On a single processor, multithreading generally occurs by time-division multiplexing (as in multitasking): the processor switches between different threads. This context switching generally happens frequently enough that the user perceives the threads or tasks as running at the same time. On a multiprocessor or multi-core system, the threads or tasks will actually run at the same time, with each processor or core running a particular thread or task. Threads differ from traditional multitasking operating system processes in that ([Kumar, 2010](#)):

- Processes are typically independent, while threads exist as subsets of a process.
- Processes carry considerable state information, whereas multiple threads within a process share state as well as memory and other resources.
- Processes have separate address spaces, whereas threads share their address space.
- Processes interact only through system-provided inter-process communication mechanisms.
- Context switching between threads in the same process is typically faster than context

switching between processes.

There are two typical threaded models: single threading model and multiple threaded model. A typically single threaded model is showed in Figure 7.3.

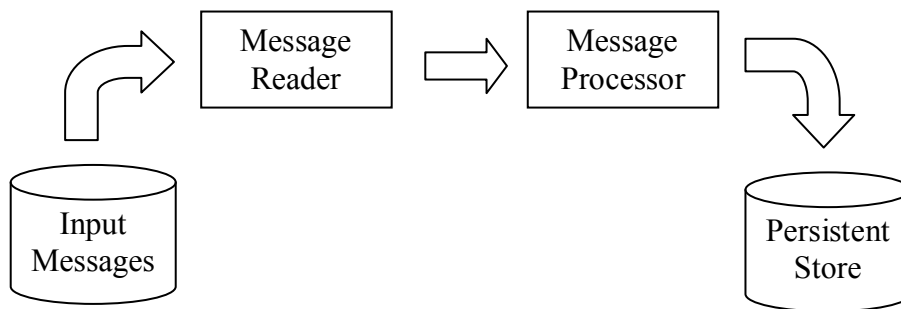


Figure 7.3 Single threaded model

Multithreading as a widespread programming and execution model allows multiple threads to exist within the context of a single process. These threads share the process' resources but are able to execute independently. The threaded programming model provides developers with a useful abstraction of concurrent execution. However, perhaps the most interesting application of the technology is when it is applied to a single process to enable parallel execution on a multiprocessor system. A typically multiple threaded model is showed in Figure 7.4.

In a multi-threaded operation, all threads in a single process exist in the same address space and share all the resources belonging to the process. The .NET Framework supports a multi-threaded operation in developing .NET applications. Multiple threads within a single process can manage the multi-tasks of an application. As compared to multiple processes, multiple threads can increase the throughput of an application and simplify program structure. In a multi-threaded operation, the application does not require any special mechanism to communicate between its tasks, and less system resources are needed for context switching between the tasks.

Multiple threads can accomplish various tasks while working in a single application domain. They can communicate to a Web server and a database over a network. They can perform operations that are time taking and can distinguish various tasks of varying priority. Multiple threads also enable the user interface to be more responsive during the time allocation of background tasks. However, one should avoid using multiple threads in a single application domain, as the consumption of operating-system resources can be minimized and the application performance enhanced. The frequent use of threads can cause the computer to consume more memory.

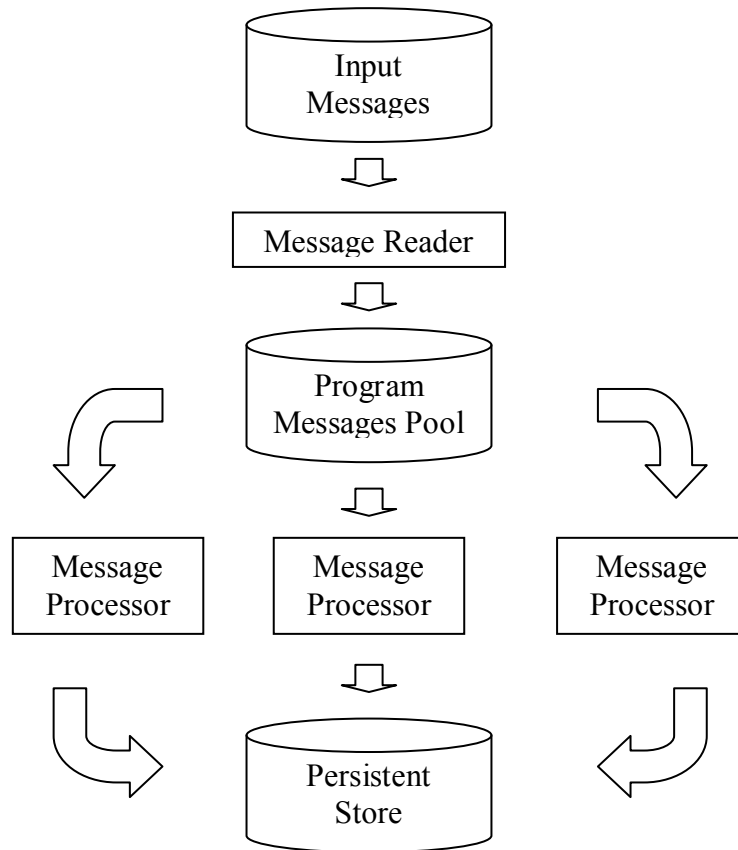


Figure 7.4 Multiple threaded model

7.1.3 Parallel programming in seismic interpretation

The basic unit of scheduling is generally the thread ([Goetz, 2002](#)); if a program has only one active thread, it can only run on one processor at a time. If a program has multiple active threads, then multiple threads may be scheduled at once. In a well-designed program, using multiple threads can improve program throughput and performance.

Development of parallel software has traditionally been thought of as time and effort intensive ([Grama, 2003](#)). This can be largely attributed to the inherent complexity of specifying and coordinating concurrent tasks, a lack of portable algorithms, standardized environments, and software development toolkits.

Parallel processing is also called parallel computing ([Almasi and Gottlieb, 1989](#)). Parallel processing is the method of breaking large problems down into smaller constituent components, tasks or calculations that are solvable in parallel. In computers, parallel processing is the processing of program instructions by dividing them among multiple processors with the objective of running a program in less time. In the earliest computers,

only one program ran at a time. An early form of parallel processing allowed the interleaved execution of two programs together. In a multiprogramming system, multiple programs submitted by users were each allowed to use the processor for a short time. To users it appeared that all of the programs were executing at the same time.

Traditionally, software has been written for serial computation. During the past 20 years, the trends indicated by ever faster networks, distributed systems, and multi-processor computer architectures (even at the desktop level) clearly show that parallelism is the future of computing. Main reasons of using parallel processing are following:

- Save time;
- Solve larger problems;
- Provide concurrency;
- Cost savings;
- Use of non-local resources;
- Overcoming memory constraints;
- Limits to serial computing.

There are several parallel programming models in common use: shared memory, threads, message passing, data parallel, and hybrid. Parallel programming models exist as an abstraction above hardware and memory architectures. Parallel programming techniques can benefit from multiple cores directly. Some existing parallel programming models such as Cilk++, OpenMP, OpenHMPP, FastFlow, Skandium, and MPI can be used on multi-core platforms. Intel introduced a new abstraction for C++ parallelism called TBB. Other research efforts include the Codeplay Sieve System, Cray's Chapel, Sun's Fortress, and IBM's X10.

In developing applications, Large-scale scientific problem solving involves three interactive disciplines as shown in following figure ([Morrison, 2003](#)). As shown in figure, theoretical scientists develop mathematical models that computer engineers solve numerically; the numerical results may then suggest new theories. Experimental science provides data for computational science, and the latter can model processes that are hard to approach in the laboratory.

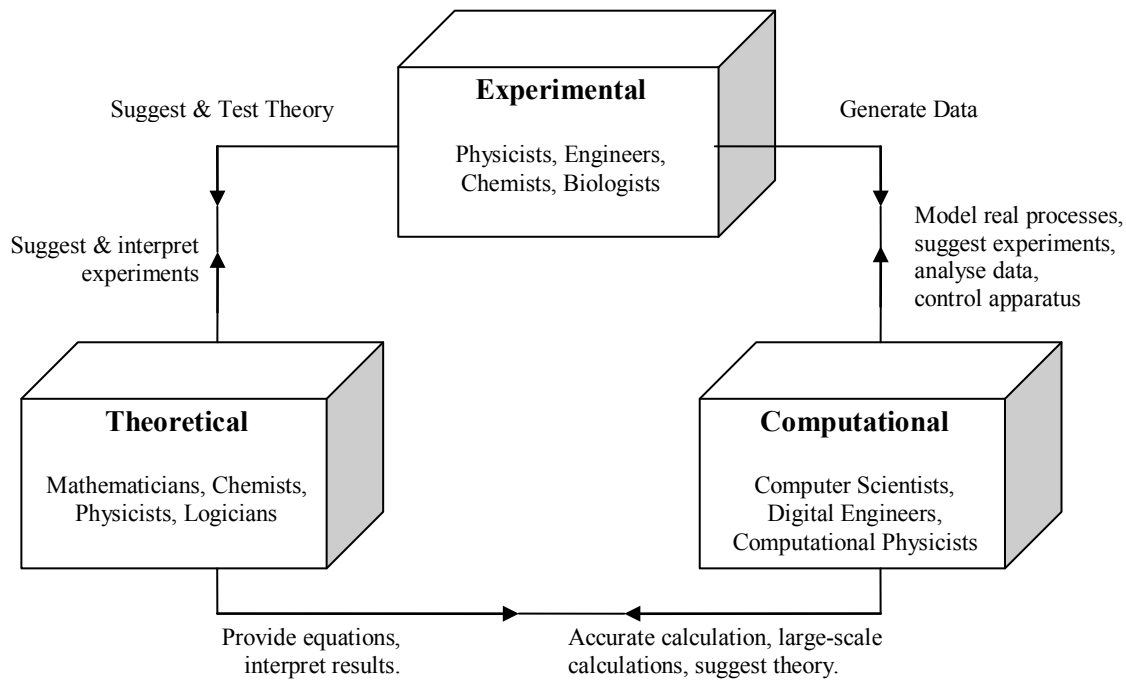


Figure 7.5 Interaction among Experiment, Theory and Computation

For designing parallel programs, we should pay attention to following steps ([Barney, 2009](#)):

- Undoubtedly, the first step in developing parallel software is to first understand the problem that we wish to solve in parallel. If we are starting with a serial program, this necessitates understanding the existing code also.
- Before spending time in an attempt to develop a parallel solution for a problem, determine whether or not the problem is one that can actually be parallelized.
- Identify the program's hotspots.
- Identify bottlenecks in the program
- Identify inhibitors to parallelism;
- Investigate other algorithms if possible.
- Break the problem into discrete "chunks" of work that can be distributed to multiple tasks. This is known as decomposition or partitioning (domain decomposition and functional decomposition).
- Process communications between multiple tasks.

Scientific applications often demand more performance than a single processor can deliver. Therefore applications have to conduct computations in parallel. A considerable problem in the seismic processing field is the fact that seismic data are large and require a correspondingly large memory size and processing time. In seismic field, parallel processing algorithms deliver high performance calculations in multiple aspects such as seismic horizon tracking, seismic facies analysis, attribute computations, and interactive volume visualization.

Matthas et al ([1998](#)) achieved Fortran performance within a factor of at most four with a parallel Java implementation of a basic geophysical algorithm on to major system platforms, both on a shared memory and a distributed memory parallel computer. They implemented the high resolution velocity analysis operator using the JavaParty.

Thomson et al ([2006](#)) proposed using overlapping, tapered windows to process seismic data in parallel. Thomson's method consists of numerically tight linear operators and adjoints that are suitable for use in iterative algorithms and is also highly scalable and makes parallel processing of large seismic data sets feasible. With definition of the Parallel Windowed Fast Discrete Curvelet Transform (PWFDCCT), the authors apply it to a seismic data interpolation algorithm. Alhashim ([2009](#)) proposed a parallel approach based windowing operator that divides large seismic data into smaller more manageable data sets that can fit in memory so that it is possible to apply the Bayesian separation process in parallel with minimal harm to the image quality and data integrity.

Leif ([Leif, 2007](#)) discusses how algorithms involving discretized polygon surfaces can efficiently utilize the parallelism provided by clusters. In his work, Leif provides a general framework for representing polygonal structures used for computations over seismic volume data on clusters and, supporting dynamic operations. The framework consists of three main parts: 1) efficient caching and transfer of voxels between cluster nodes, 2) efficient discretization or voxelization of polygon surfaces, and 3) efficient load-balancing.

7.1.3.1 Computing seismic attributes in parallel programming

A task could be processed parallel if it has features:

- The serial program calculates one element at a time in sequential order;
- The calculation of elements is independent of one another - leads to an embarrassing parallel situation;
- The problem should be computationally intensive;

- Independent calculation of array elements insures there is no need for communication between tasks.
- Each task executes the portion of the loop corresponding to the data it owns.
- Notice that only the outer loop variables are different from the serial solution.

Seismic data volume could be represented by Figure 7.6. As we have introduced in section 2.1, seismic attribute is a quantitative measure of a seismic characteristic of interest. There are a lot of complex calculations in extracting many attributes. Interpreters have to spend much time on waiting result of calculation. Calculation of most attributes is corresponding to local regional data. Therefore, calculation performance can be improved in parallel programming.

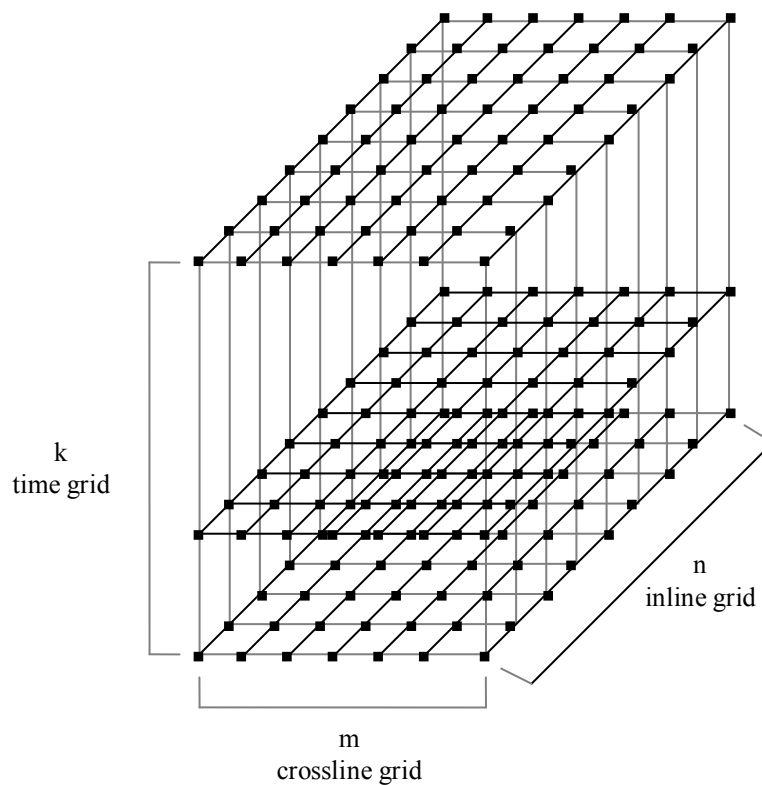


Figure 7.6 Representing 3D seismic data by grid.

For parallelization calculation, we modify the representation of seismic data volume. Figure 7.7 illustrates the modification. This modification is corresponding to the power of parallel computing, where N is numbers of threads according to CPU cores.

We will take multi-threading technique to implement our method. The threads are designed two classes: master thread and worker thread. The master thread initializes environment parameters, creates and destroys worker thread, blocks edge of seismic data for worker

threads, schedulers communication and synchronization, and collects results from worker thread. The worker thread receives information, performs its share of computation and send results to master.

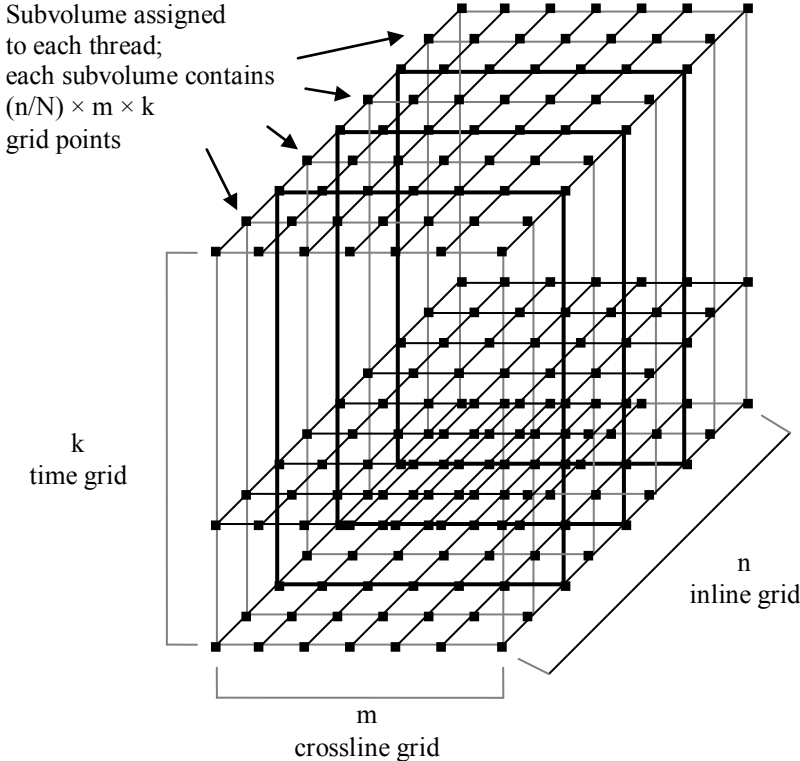


Figure 7.7 Representing 3D seismic data by multiple subvolume.

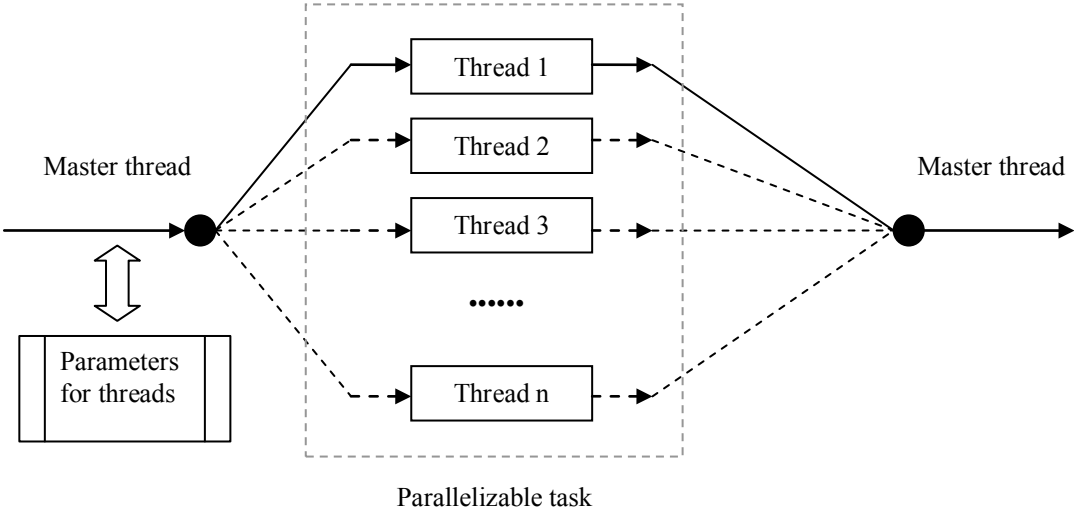


Figure 7.8 Parallelization using multi-threading.

We construct the structure of parallelization using multi- threading as shown in Figure 7.8. The solid line indicates master thread execution flow, and the dotted line indicates worker

thread execution flow. The pseudo codes of master thread and worker thread illustrate in Table 7.1 and Table 7.2.

Table 7.1 Pseudo code of master thread for attribute computation.

Get the numbers of threads according to CPU cores
Initialize the environment parameters
Calculate information for worker threads
Block information of the seismic data for each worker thread
Create worker thread
Send each worker thread information
Send each worker thread block information
Receive from each worker thread results
Send destroy command to worker thread
Compose results from each worker thread
Destroy itself

Table 7.2 Pseudo code of worker thread for attribute computation.

Receive information from master thread
Receive block information from master thread
Calculate block attribute
Send results to master thread
Wait command to destroy self from master thread
Destroy itself

The previous solution adopts static load balancing scheme. But this scheme has some disadvantages:

- Each task has a fixed amount of work to do;
- May be significant idle time for faster or more lightly loaded processors - slowest tasks determines overall performance;
- Static load balancing is not usually a major concern if all tasks are performing the same

amount of work on identical machines.

In case having a load balance problem (some tasks work faster than others), we may benefit by using a "thread pool pattern" scheme to solve it. This scheme has the structure as shows in. In computer programming, the thread pool pattern is where a number of threads are created to perform a number of tasks, which are usually organized in a queue. Typically, there are many more tasks than threads. As soon as a thread completes its task, it will request the next task from the queue until all tasks have been completed. The thread can then terminate, or sleep until there are new tasks available. The number of threads used is a parameter that can be tuned to provide the best performance. Additionally, the number of threads can be dynamic based on the number of waiting tasks.

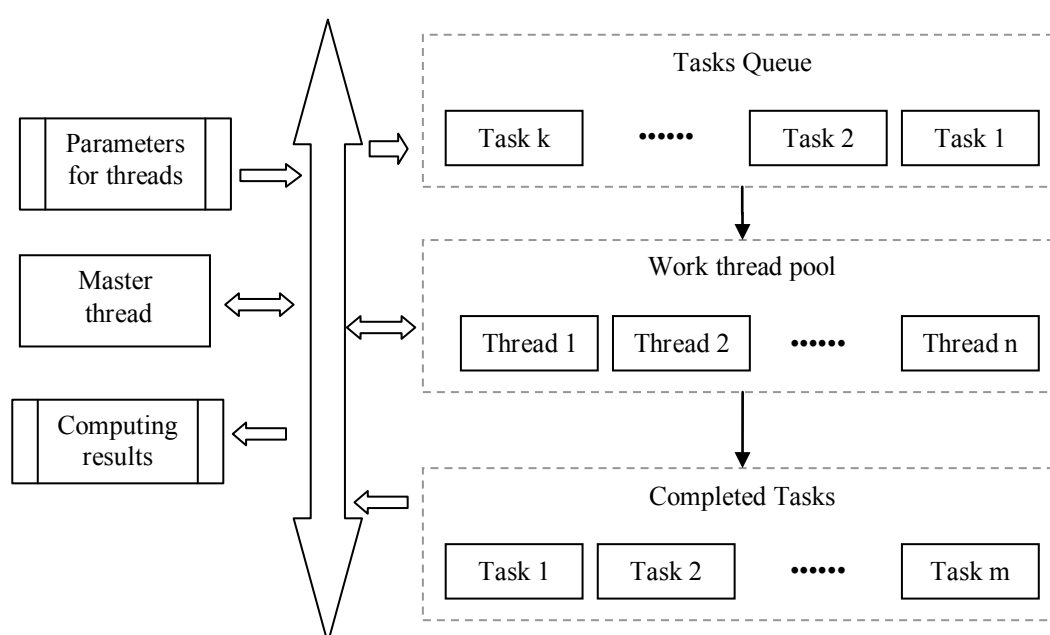


Figure 7.9 Parallelization using multi-threading with thread pool pattern.

We also design two classes thread. First is employed Master thread:

- Holds pool of tasks for worker processes to do
- Sends worker a task when requested
- Collects results from workers

Second class is worker threads which are constructed a thread pool. Each repeatedly does the following:

- Gets task from master process
- Performs computation
- Sends results to master

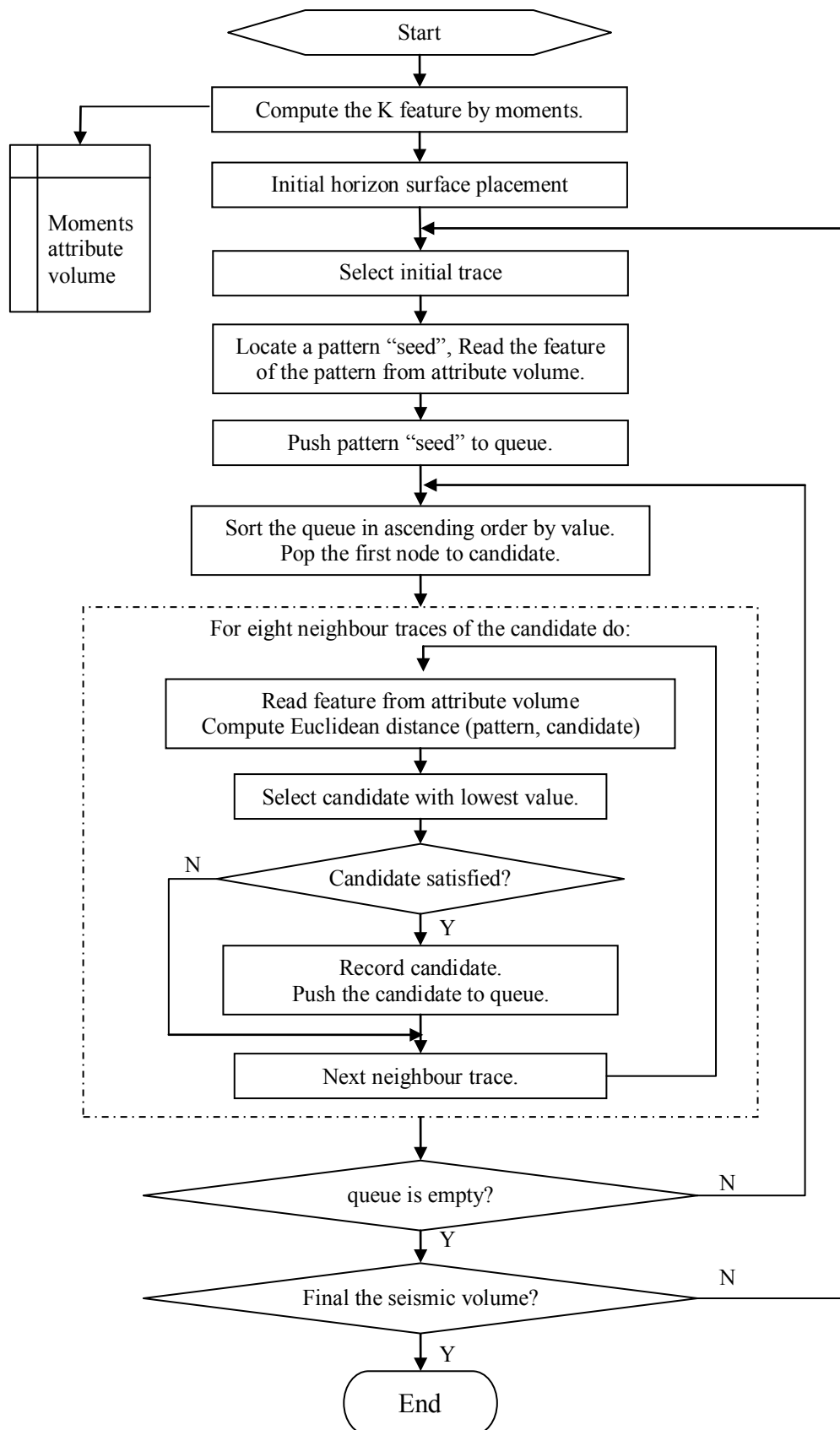


Figure 7.10 The workflow chart of 3D horizon tracking using moments attribute volume.

7.1.3.2 Auto-tracking seismic horizon in parallel programming

We have presented our methods of 3D moments-based horizon auto-tracking in section 5.2. In

this methodology, we need compute 3D moments feature vectors of local regions. If we frequent track different horizons, pre-computing moments features is a nice idea. Therefore, we can take parallel processing to create an attribute volume. Then we will directly match the feature using the attribute. The modification method is shown in Figure 7.10.

7.2 Volume visualization and volume interpretation

The seismic data volume ultimately has to be interpreted by geologists and geophysicists ([Neff et al., 2000a](#)). The quality of their interpretation depends on their experience and knowledge, but it is also dependent on how the data volume is presented to them. The conventional approach for interpreting 3D seismic data is usually confined to a 2D or 2.5D environment. Recent advancements in computing and visualization technologies allow interpreters to visualize, interpret and integrate full 3D seismic attributes into their geophysical interpretation.

For geovolume visualization interpretation (GVI) , recognition, colour, motion, and isolation are the four main techniques ([Sheffield et al., 2000](#)).

- Recognition refers to determining the distinguishing characteristics of an event to be mapped, then processing the data to enhance those characteristics for the purpose of visualization and geobody mapping. In this step, the choice of attributes is made. The ability to calculate and examine many attributes with no penalty for wrong choices is critical for fast recognition of anomalies. By examining many attributes, the best set of attributes for characterizing the event can be selected.
- Colour refers to the selection of an optimum colour scheme for visualizing the property of interest.
- Motion is one of the most critical aspects of GVI; it is motion that taps the human sub-conscious and allows interpreters to see relationships between data in space and time.
- Isolation is the ability to separate the events of interest from other data, and is another key feature of GVI.

3D volume visualization is a method of seismic interpretation in which the geo-physicist directly evaluates the seismic reflectivity of the subsurface in 3D space by applying various levels of transparency to the data. The technology and philosophy of 3D-volume visualization differ dramatically from conventional line-based interpretation and includes new

interpretation strategies and methodologies.

There are two basic types of visualization:

- Map-based (surface visualization)
- Volume-based (volume visualization).

Surface visualization results from mapping individual horizons and faults, and then reinterpreting them collectively therefore its position in the workflow follows surface mapping. Volume visualization is based on an entirely different attribute of the data transparency. It represents a major paradigm shift in 3D seismic data interpretation.

Volume interpretation assumes that the seismic reflectivity of the subsurface is an "in situ" 3D model of the subsurface which, by its nature, consists of integrated structural, stratigraphic, and amplitude features in 3D space. The purpose of volume interpretation is to see the details of that "untouched" in situ model, and to formulate an accurate concept.

Therefore, its position in the work flow should proceed illustrating or mapping that concept. In summary, the general interpretation workflow is as follows:

- Formulate the concept via volume interpretation
- Illustrate that concept via maps and surfaces
- Perform surface visualization to evaluate the surfaces in 3D space.

Volume visualization work flows must include interpretation strategies for a wide variety of problems. The volume interpretation workflow is designed to address flat intervals of strata, dipping units, and individual targets such as bright amplitudes.

The work flow begins by performing quality control measures specifically for visualization sensitivities, then obtaining overviews of the data where regional and specific objectives are identified. Depending on the nature of the objective, a "focusing strategy" either time windowed, detection, or horizon-keyed (sculpting) is chosen to isolate the objective in preparation for the application.

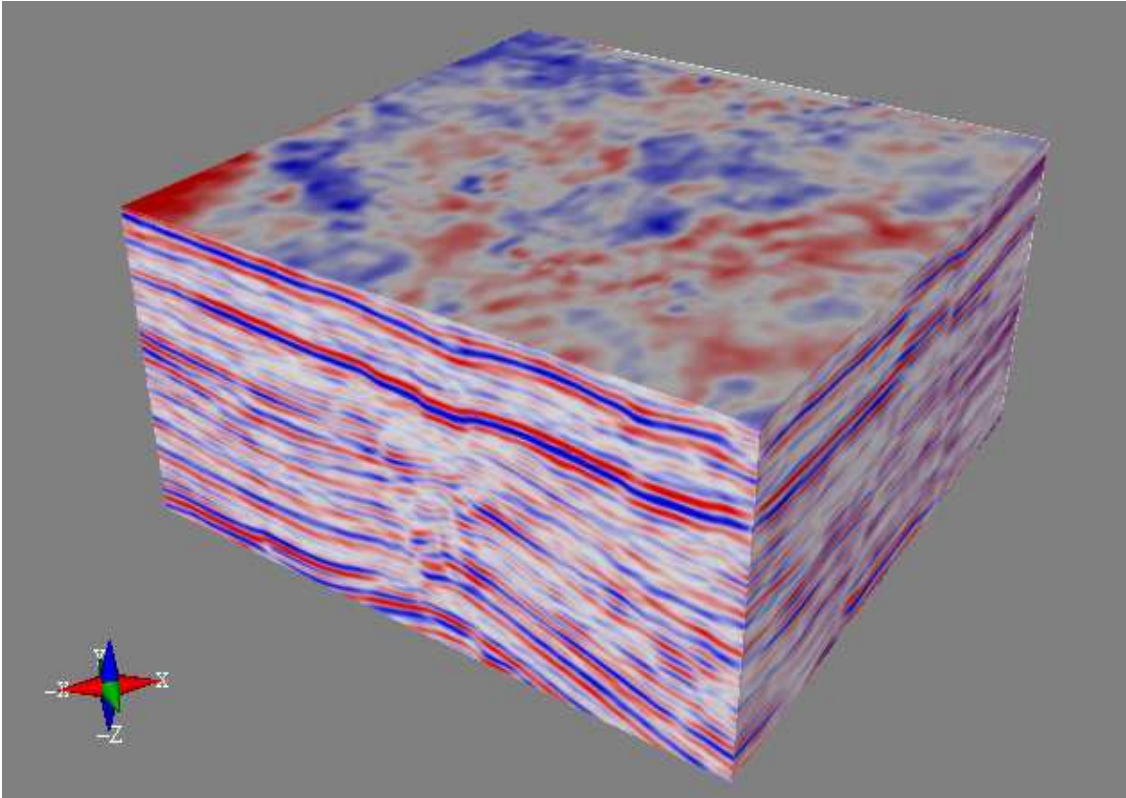


Figure 7.11 Surface visualization

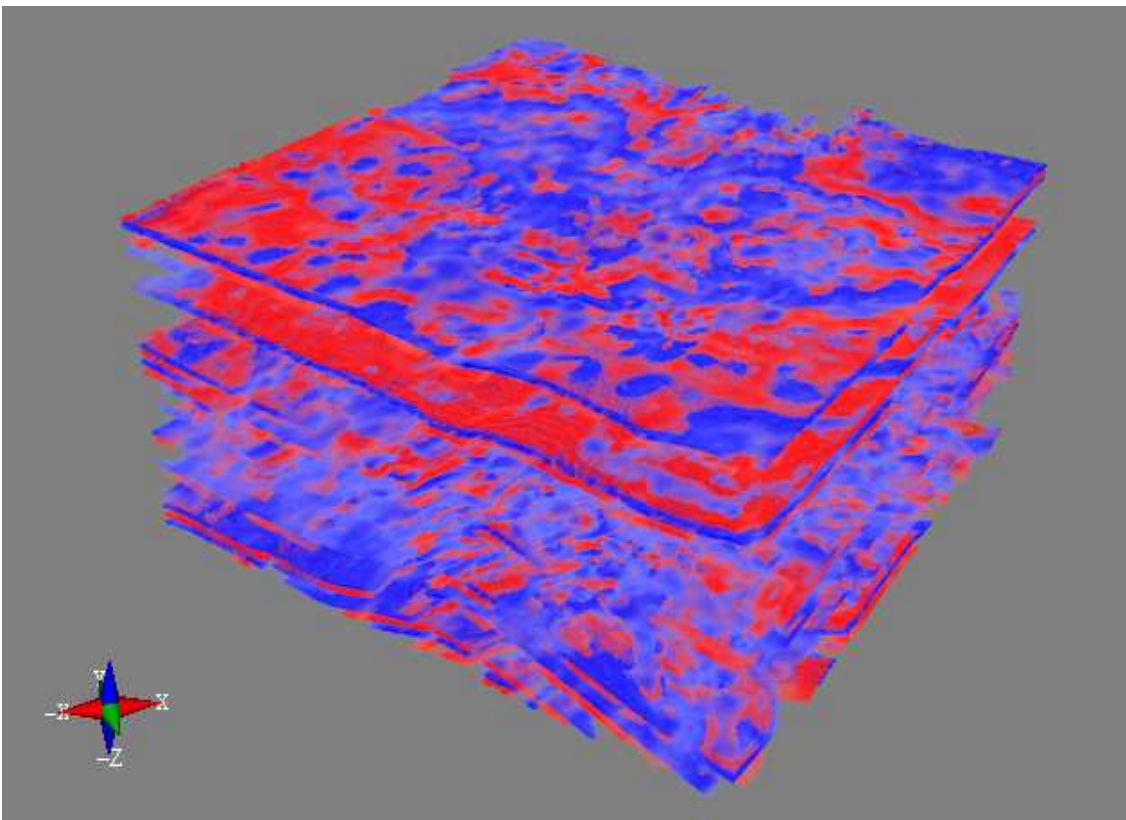


Figure 7.12 Volume visualization

Volume interpretation provides a method for geoscientists to quickly evaluate complex structural and stratigraphic and amplitudes in 3D space. The demand for fast detailed interpretation can be accomplished utilizing visualization strategies. The challenge of interpreting the growing number of large 3D volumes is now more manageable. As volume-interpretation skills increase, so will the efficiency of obtaining more answers without mapping, thus reducing the time for the 3D interpretation phase of the project.

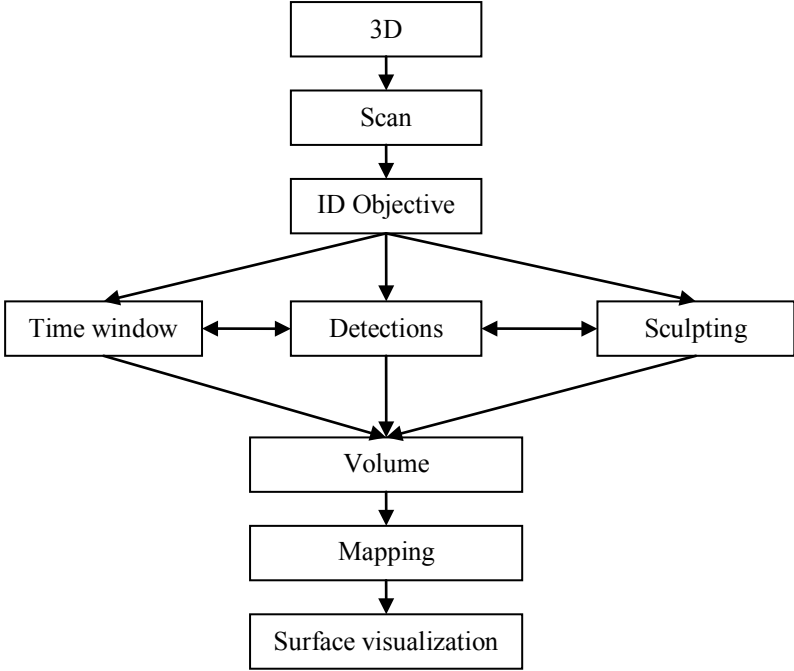


Figure 7.13 Volume visualization and interpretation workflow.

In this section, we adapt high quality volume rendering algorithms from the computer graphics industry based on Open-Scene-Graph (OSG) engine to improve the imaging. The OSG is an open source high performance 3D graphics toolkit, used by application developers in fields such as visual simulation, games, virtual reality, and scientific visualization and modelling. Written entirely in Standard C++ and OpenGL it runs on all Windows platforms, OSX, GNU/Linux, IRIX, Solaris, HP-Ux, AIX and FreeBSD operating systems. The OSG is now well established as the world leading scene graph technology, used widely in the vis-sim, space, scientific, oil-gas, games and virtual reality industries. OSG improves the applications efficiency using the capabilities of the recent programmable graphics hardware.

We present a formal framework for the design of modular software systems. The framework is shown in Figure 7.14. The data manager modular provides data to interpretation for attributes computation, horizon tracking, fault extracting, and facies analysis.

All results of interpretation are stored back to data manager modular. All data can be displayed by visualization modular. Also, the visualization modular could provide advices for interpretation algorithms. In many methods of interpretation, some visualization techniques is employed to offer information for interactive visual exploration. In addition, we will present a versatile multimodal volume rendering system that enables the efficient co-visualization of several volumes.

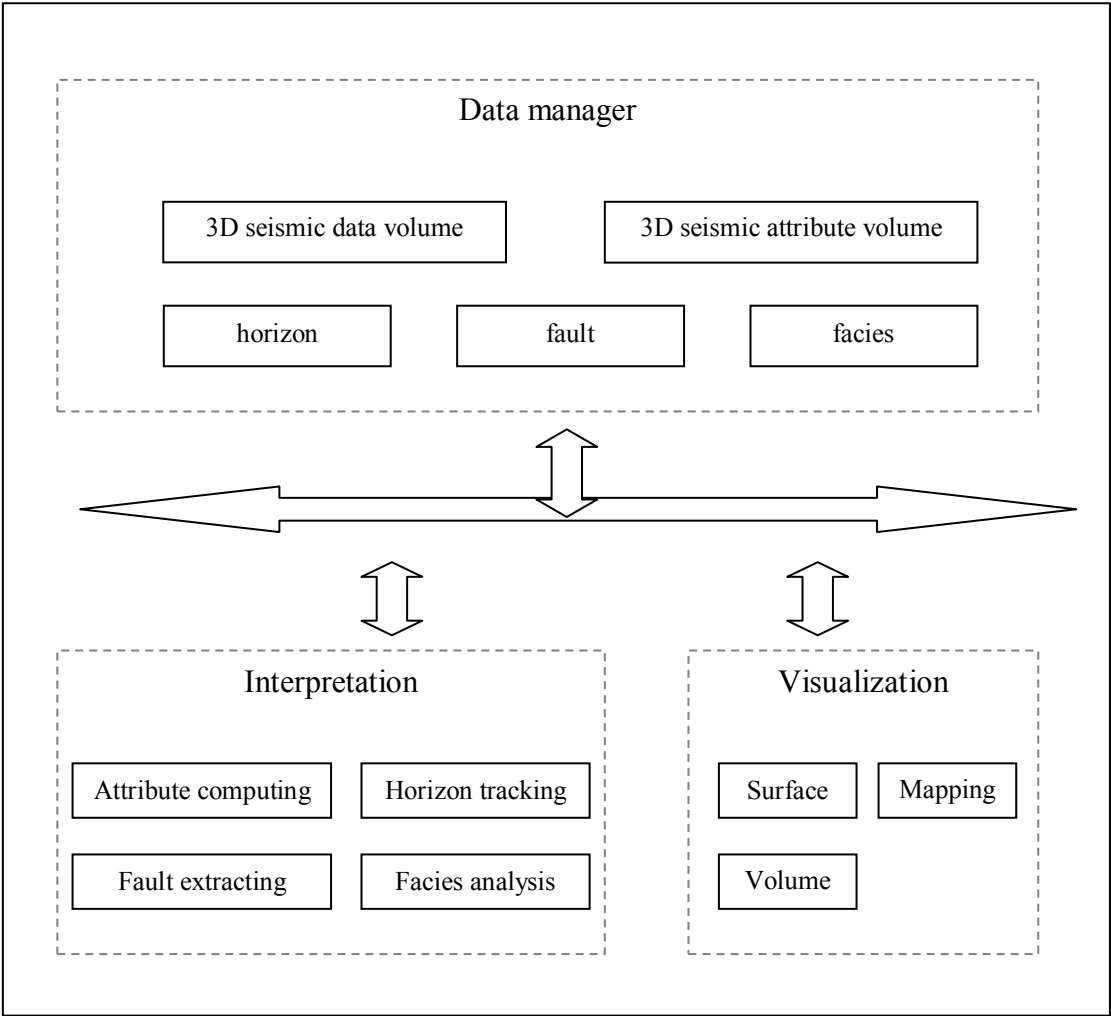


Figure 7.14 Framework for the design of modular software system.

Various display methods are shown in Figure 7.15 and Figure 7.16. Trough adjusting the parameters in Figure 7.17, the objects which interpreters are interesting in will be more clearly represented. Figure 7.18 shows this adjusting.

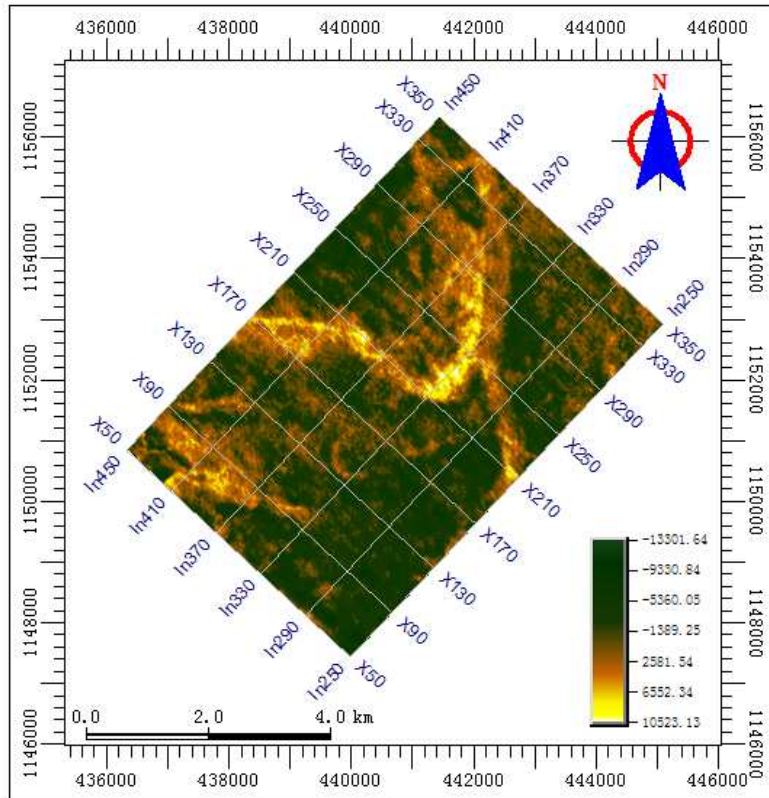


Figure 7.15 An example of mapping display.

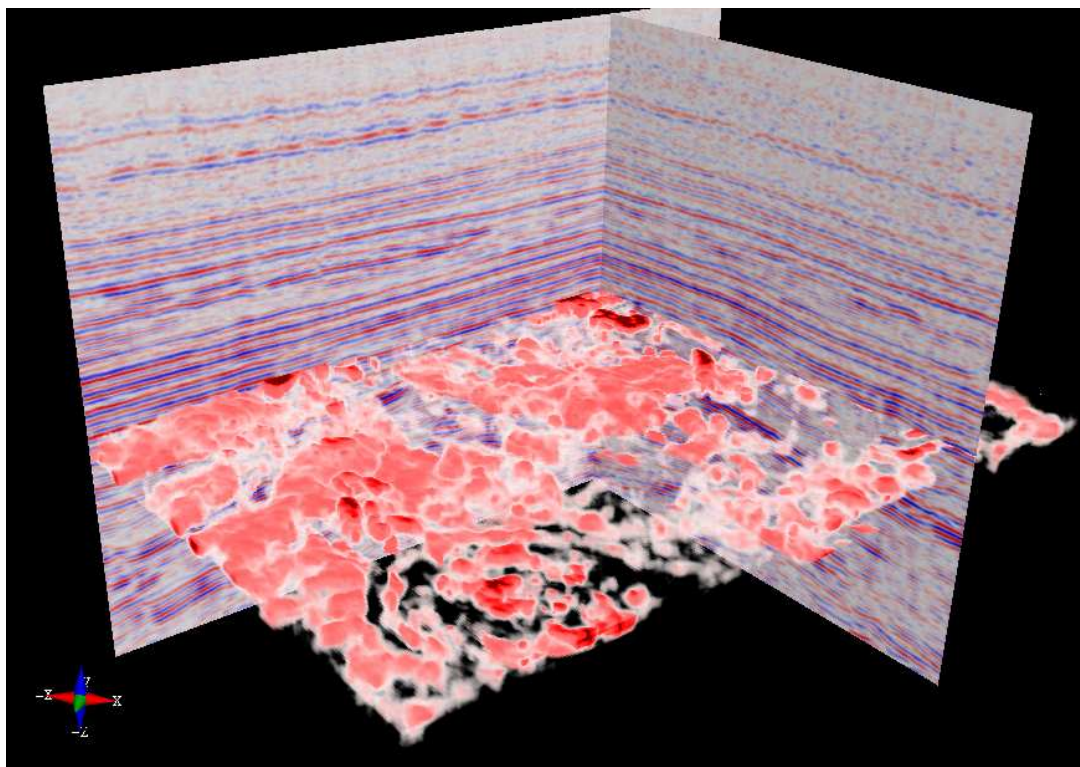


Figure 7.16 A result of control alpha for volume visualization.

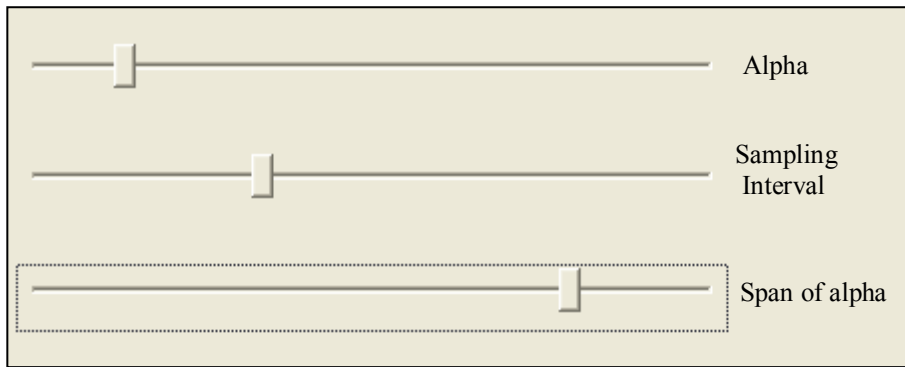


Figure 7.17 Parameters adjustment of volume visualization.

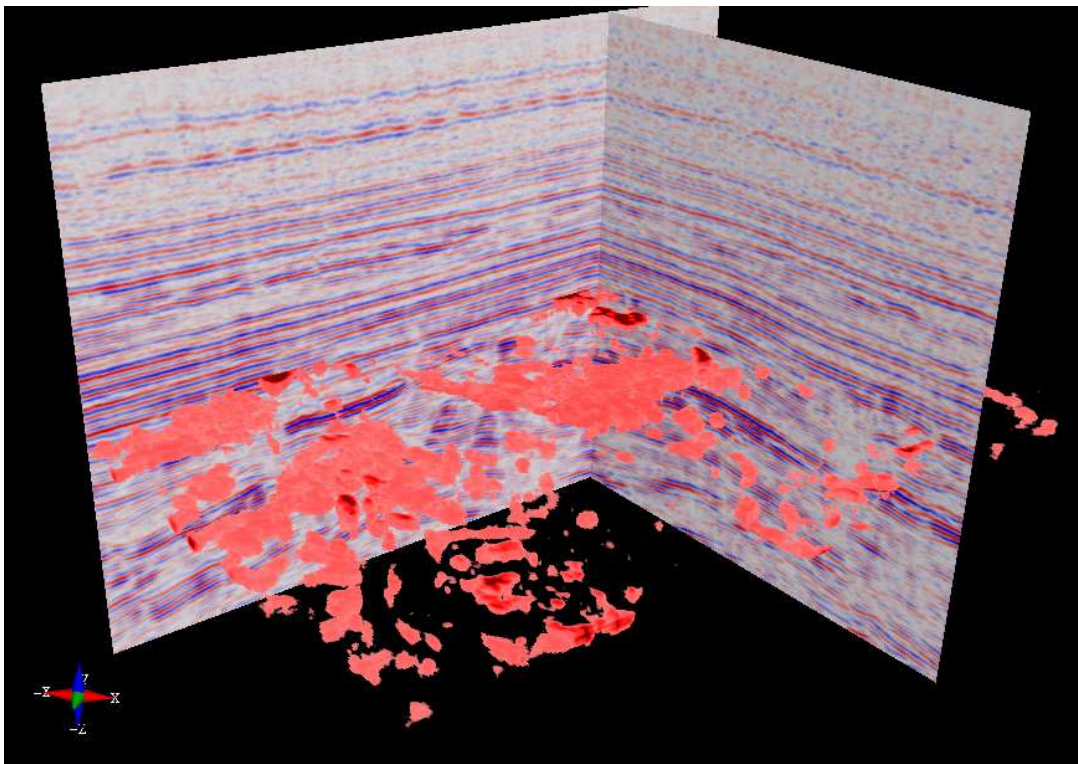


Figure 7.18 Another result of control alpha for volume visualization.

As the use of 3D seismic interpretation continues to become part of the main stream work process with the industry, visualization techniques also continue to evolve as software and hardware improves. In the past ten years, volume rendering tools have been progressively adopted by the geophysical community as the emergence of high-end graphics workstations with 3D texture capabilities made real-time volume rendering possible. Many interactive volume rendering packages are now available for seismic interpretation. However, interpretation is still mostly done in 2D. Using classical volume rendering with high spatial frequencies of seismic data make it very difficult to produce meaningful volume images and often results in cluttered useless images.

7.3 Conclusion

Multi-core processors can offer software developers the ability to apply more resources at a particular problem. The software threads are executed on a single processor or on many processors simultaneously. Taking advantage of those new performances into seismic data field, we compute the seismic attributes and track the horizon with parallel programming. It can be seen that both computation and interpretation have been efficient. Interpreters can save their time and resources into others interesting tasks. Volume visualization technology and volume interpretation may help interpreter to insight into 3D seismic data and accelerate the interpretation process. In the our research, we adapt high quality volume rendering algorithms based on Open-Scene-Graph (OSG) 3D engine to improve application efficiency in the imaging and visualization.

8 Conclusion

Seismic attributes are a descriptive and quantifiable characteristic of seismic data sets, and so they represent subsets of the total information contained in the original seismic data sets. The advance in seismic attribute technology has led to the use of seismic attributes as feature vectors of seismic interpretation and predictors of reservoir properties. Especial coherence attribute, it has great advantages in recognizing faults and fractures, interpreting ancient channels, edge detection of oil-gas reservoir, or other discontinuous features, etc. In the thesis, we proposed a method of stepwise dip scanning coherence algorithm based on eigenstructure. The algorithm proved to be highly efficient.

In this thesis, we have introduced Gaussian-Hermite moments. We made a profound study on invariant moments and 3D case about this kind of moments.

Because of their capabilities to extract invariant global features, moments and functions of moments have been extensively applied in the field of image processing: image analysis and pattern recognition, with applications ranging from edge detection, image classification and segmentation, texture analysis, coherency estimation, invariant identification, target identification, object classification, image coding and reconstruction, scene analysis, image reconstruction, and 3D object analysis. In the thesis, we presented the definition of 3D orthogonal Gaussian-Hermite moments derived from orthogonal 2D Gaussian-Hermite moments and the general definition of 3D geometric moments. We have also derived 2D rotation and translation invariants from Gaussian-Hermite moments.

From the present study we have concluded that the moments approach, special Gaussian-Hermite moments approach, for seismic image analysis and seismic interpretation has many advantages over the conventional methods. Moments of images provide efficient local descriptors and have been used extensively in image analysis applications. Some diverse

usages of Gaussian-Hermite moments and moment invariants in some applications are exhibited as: coherency estimation, pattern recognition. We also discuss seismic image analysis by moments. Applications are shown that Gaussian-Hermite moments are effective tools for image analysis. The 3D moments provide an efficient power to extract features of local sub-volume within 3D seismic data volume. With these feature extracted, the property vector is constructed to estimate difference between two patterns.

After studying many auto-tracking methods of seismic horizon, we have found that they are mostly depended on the information of single seismic trace. Our method, based on 3D geometric moments and 3D Gaussian-Hermite moments, is depended on the information of local sub-volume. After obtaining feature vector, a matching algorithm based on Euclidean distance, between the referent feature vector of seed and feature vector of each candidate seeds, is performed to choice a candidate with the lowest value distance. The experiments show that the moments-based method is an efficient tool for horizon auto-tracking. 3D Gaussian-Hermite moment invariants are also presented in the thesis as horizon tracking technique. Compared to other horizon tracking techniques, moment invariants have some drawbacks and some advantages. Like some other horizon tracking techniques, e.g. correlation-based method, the computation heavily depends on a seed point. The moment invariant feature vector continuously varies when rotational transforming the density with respect to the seed point. Moment invariant methods successfully detect similarities of features conserved in detail. Because the same surface may have multiple depths (or reflection times) associated with the same spatial position, we propose a modified tracking method to solve the horizon self overlaps.

The problem of identification of seismic facies is solved by reducing the multiclass classification problem to a two-class classification problem using the modular neural network system. It is important to investigate the characteristics of the problem of interest with the objective to select an appropriate clustering strategy. Popular networks that use unsupervised learning are Kohonen feature maps ([Kohonen, 1984](#)). SOM is a technology that visual-based data mining approach combines a clustering process. We have approached method of seismic facies analysis. Our approach starts with extracting feature vectors by 3D Gaussian-Hermite moments. Then we cluster the feature vectors through SOM algorithm with data visualization techniques U-Matrix and PCP graphic. It can be learnt that method provides an environment for exploring patterns in the data sets.

Today, there is tremendous progress in computer technology. Chip multi-threading (CMT) brings to hardware the concept of multi-threading, similar to software multi-threading. Multi-

core processors can offer software developers the ability to apply more resources at a particular problem. The software threads are executed on a single processor or on many processors simultaneously. Taking advantage of those new performances into seismic data field, we compute the seismic attributes and track the horizon with parallel programming. It can be seen that both computation and interpretation have been efficient. Interpreters can save their time and resources into others interesting tasks. Volume visualization technology and volume interpretation may help interpreter to insight into 3D seismic data and accelerate the interpretation process. In the our research, we adapt high quality volume rendering algorithms based on Open-Scene-Graph (OSG) 3D engine to improve the imaging and visualization.

The study on Gaussian-Hermite moments is not complete. Its 3D invariant moments is still needed to study. In future we plan to automatically track seismic fault surface. Seismic data sets typically contain a large number of faults at many different spatial scales. Faults are important subsurface features that are often of interest to the geologist. Knowledge of the location of the faults is critical to understanding a geological system. The analogy of the moments to mechanical moments allows a deeper understanding of the central moments of second order $\mu_{2,0}$, $\mu_{0,2}$ and $\mu_{1,1}$. They contain terms, in which the gray value function $f(x, y)$, i.e. the density $\rho(x, y)$ of the object is multiplied with the square of the distance from the center of gravity (x_c, y_c) . Exactly the same terms are available in the inertial tensor, known from physical mechanics. The three central moments of second order build the components of the inertial tensor of the rotation of the object about its centre of gravity:

$$J = \begin{bmatrix} \mu_{2,0} & \mu_{1,1} \\ \mu_{1,1} & \mu_{0,2} \end{bmatrix}$$

Using the inertial tensor analogy several further parameters could be derived from the central moments of second order.

- The main inertial axis could be derived by calculating the eigenvalues of the inertial tensor:

$$\lambda_{1,2} = \sqrt{\frac{1}{2} * (\mu_{2,0} + \mu_{0,2}) \pm \sqrt{4 * \mu_{1,1}^2 - (\mu_{2,0} - \mu_{0,2})^2}}$$

- The orientation of the object is defined as the tilt angle between the x-axes and the axis, around which the object can be rotated with minimal inertia. This corresponds to the eigenvector with minimal eigenvalue. In this direction the object has its biggest extension. It is calculated as follows:

$$\theta = \frac{1}{2} \arctan \frac{2\mu_{1,1}}{\mu_{2,0} - \mu_{0,2}}$$

With those parameters, we can calculate the coherency attribute from the seismic data. Then we shall develop auto-tracking methodology for extracting seismic fault surface.

In our approach of horizon auto-tracking, we only involve one seismic attribute. Multiple attributes also can be used in this approach. Therefore, next step we will study horizon auto-tracking on multi-attribute. This research work maybe takes new advantages. For multi-scale approach based on 3D Gaussian-Hermite moment invariants, we will discuss the effects of selecting different σ .

In our approach of parallel processing, we only involve the multiple threading based on single computer. However, today's seismic volumes are achieving terabytes. It is impossible to treat such volume based on a single PC. Computer clusters can be usually deployed to improve performance and availability over that of a single computer. We plan to use of computer clusters for processing huge seismic data volume and auto-tracking horizon.

References

- Abu-Mostafa, Y.S., Psaltis, D., 1984. Recognitive aspects of moment invariants. *IEEE Transactions on Pattern Analysis and Machine Intelligence* 6, 6, pp. 698-706.
- Abu-Mostafa, Y.S., Psaltis, D., 1985. Image normalization by complex moments. *IEEE Transactions on Pattern Analysis and Machine Intelligence* 7, 1, pp. 46-55.
- Acosta, M., Cheung, Y., Lees, J., Sembroski, C., Zeitlin, M., 2006a. System and method for analyzing and imaging three-dimensional volume data sets, U.S. Pat. 7006085.
- Acosta, M., Cheung, Y., Lees, J., Sembroski, C., Zeitlin, M., 2006b. System and method for analyzing and imaging three-dimensional volume data sets, U.S. Pat. 7098908.
- Alberts, P., Warner, M., Lister, D., 2000. Artificial neural networks for simultaneous multi Horizon tracking across discontinuities, Annual International Meeting SEG, Calgary, Ca.
- AlBinHassan, N.M., Luo, Y., Al-Faraj, M.N., 2006. 3D edge-preserving smoothing and applications. *Geophysics* 71, 4, pp. P5-P11.
- Alhashim, F., 2009. Seismic Data Processing with the Parallel Windowed Curvelet Transform Seismic Data Processing with the Parallel Windowed Curvelet Transform, Master of Science. University of British Columbia.
- Almasi, G.S., Gottlieb, A., 1989. Highly parallel computing. Benjamin/Cummings Pub. Co.
- Anstey, N.A., 1964. Correlation techniques - A review. *Geophysical Prospecting* 12, 4, pp. 355-382.
- Ashcroft, W.A., Ashcroft, W., 2011. A Petroleum Geologist'S Guide To Seismic Reflection: PART I Basic topics and 2D interpretation. Wiley-Blackwell Pub.
- Aurnhammer, M., Tonnies, K.D., 2002. Image processing algorithm for matching horizons across faults in seismic data, Int. Conf. of Association for Mathematical Geology, Terra Nostra, pp. 63-69.
- Bader, D.A., Pennington, R., 2001. Cluster Computing: Applications. *The International Journal of High Performance Computing* 15(2), pp. 181-185.

- Bahorich, M., Farmer, S., 1995. 3-D seismic discontinuity for faults and stratigraphic features: the coherence cube. *The Leading Edge* 14, 10, pp. 1053-1058.
- Bakker, P., 2002. Image structure analysis for seismic interpretation. Technische universiteit Delft.
- Bakker, P., Van Vliet, L.J., Verbeek, P.W., 1999. Edge preserving orientation adaptive filtering, *IEEE Conf. on Computer Vision and Pattern Recognition*, Fort Collins, CO , USA.
- Barnes, A.E., 2001. Seismic attributes in your facies, *Canadian Society of Exploration Geophysicists Recorder*, 26, September, pp. 41-47.
- Barney, B., 2009. Introduction to Parallel Computing: Part 2 Designing and implementing parallel programs. *Dr. Dobb's Journal*.
- Berkhout, A.J., 2004. The data-driven seismic value chain, providing a business context for the velocity issue. 52, pp. 481-487.
- Bhatia, A.B., Wolf, E., 1954. On the circle polynomials of Zernike and related orthogonal sets, *Mathematical Proceedings of the Cambridge Philosophical Society*. Cambridge University Press, pp. 40-48.
- Bhatt, A., 2002. Reservoir Properties from Well Logs Using Neural Networks, PhD thesis, Department of Petroleum Engineering and Applied Geophysics. Norwegian University of Science and Technology, Trondheim, Norway.
- Bienati, N., Spagnolini, U., 1998. Traveltime picking in 3D data volumes, 60th EAGE Conference & Exhibition Extended, Abstracts, Session 1-12, pp. 98-112.
- Bigun, J., Granlund, G.H., Wiklund, J., 1991. Multidimensional orientation estimation with applications to texture analysis and optical flow. *IEEE Transactions on Pattern Analysis and Machine Intelligence* 13, 8, pp. 775-790.
- Blinov, A., Petrou, M., 2005. Reconstruction of 3-D Horizons From 3-D Seismic Datasets, *IEEE Transactions on Geoscience and Remote Sensing*, pp. 1421-1431.
- Bodine, J.H., 1984. Waveform analysis with seismic attributes, 54th Annual International Meeting, SEG, session S9.1.
- Bois, P., 1980. Autoregressive Pattern Recognition Applied To The Delimitation Of Oil And Gas Reservoirs. *Geophysical Prospecting* 28, 4, pp. 572-591.
- Bois, P., 1981. Determination Of The Nature Of Reservoirs By Use Of Pattern Recognition Algorithm With Prior Learning. *Geophysical Prospecting* 29, 5, pp. 687-701.
- Bois, P., 1982. Some comments on the application of pattern recognition to oil and gas exploration. *Geoexploration* 20, 1-2, pp. 147-159.
- BondÁR, I., 1992. Seismic horizon detection using image processing algorithms. *Geophysical Prospecting* 40, 7, pp. 785-800.
- Bronstein, A.M., Bronstein, M.M., Kimmel, R., 2005. Three-Dimensional Face Recognition. *International Journal of Computer Vision*. vol 64(1), 1, pp. 5-30.
- Brown, A.R., 1996. Seismic attributes and their classification. *The Leading Edge* 15, 10, pp. 1090-1090.

- Brown, A.R., 2001. Understanding seismic attributes. *Geophysics* 66, 1, pp. 47-48.
- Brown, A.R., 2004. Interpretation of three-dimensional seismic data, 5th ed. American association of Petroleum Geologists Memoir.
- Canterakis, N., 1997. Fast 3D Zernike Moments and Invariants. Tech. Report, Inst. of Informatic, Univ. Friburg, Germany.
- Carter, N., Lines, L.R., 1999. Fault imaging of Hibernia 3-D seismic data using edge-detection and coherency measures. CREWES Research Report, vol 11.
- Chang, T., Kuo, C.J., 1993. Texture analysis and classification with tree-structured wavelet transform, *IEEE Transactions on Image Processing* 2(4), pp. 429-441.
- Chen, Y., Dougherty, E., 1994. Grey-Scale Morphological Granulometric Texture Classification. *Optical Engineering* 88, 8, pp. 2713-2722.
- Cheng, Y.-C., Lu, S.-Y., 1989. The Binary Consistency Checking Scheme and Its Applications to Seismic Horizon Detection, *IEEE Transactions on Pattern Analysis and Machine Intelligence*, 11, pp. 439-447
- Chong, C.W., Raveendran, P., Mukundan, R., 2003. Translation invariants of Zernike moments. *Pattern Recognition* 36, 8, pp. 1765-1773.
- Chong, C.W., Raveendran, P., Mukundan, R., 2004. Translation and scale invariants of Legendre moments. *Pattern Recognition* 37, 1, pp. 119-129.
- Chopra, S., 2002. Coherence cube and beyond. *First Break* 20.1, pp. 27-33.
- Chopra, S., Marfurt, K.J., 2005. Seismic attributes --- A historical perspective. *Geophysics* 70, 5, pp. 3SO-28SO.
- Chopra, S., Marfurt, K.J., 2007. Seismic attributes for prospect identification and reservoir characterization. *Society of Exploration Geophysicists*.
- Chopra, S., Marfurt, K.J., 2008. Emerging and future trends in seismic attributes. *The Leading Edge* 27, pp. 298-819.
- Chopra, S., Marfurt, K.J., 2010. Integration of coherence and volumetric curvature images. *The Leading Edge* 29, 9, pp. 1092-1107.
- Claerbout, J., 1985. *Imaging the Earth's Interior*. England: Blackwell Scientific Publications, Oxford.
- Cohen, I., Coifman, R.R., 2002. Local discontinuity measures for 3-D seismic data. *Geophysics* 67, 6, pp. 1933-1945.
- Coleou, T., Poupon, M., Azbel, K., 2003. Interpreter's Corner---Unsupervised seismic facies classification: A review and comparison of techniques and implementation. *The Leading Edge* 22, 10, pp. 942-953.
- Conticini, F., 1984. Seismic facies quantitative analysis: New tool in stratigraphic interpretation. *SEG Technical Program Expanded Abstracts* 3, 1, pp. 680-682.

- Cooke, D., Sena, A., O'Donnell, G., Muryanto, T., Ball, V., 1999. What is the best seismic attribute for quantitative seismic reservoir characterization? SEG Technical Program Expanded Abstracts 18, 1, pp. 1588-1591.
- Cordsen, A., Galbraith, M., Peirce, J., 2000. Planning Land 3-D Seismic Surveys. Society of Exploration Geophysicists.
- Costa, J.A.F., de, A., 1999. Cluster analysis using self-organizing maps and image processing techniques, IEEE International Conference on Systems, Man, and Cybernetics, pp. 367-372.
- Cottrell, M., Fort, J.C., Pagès, G., 1998. Theoretical aspects of the SOM Algorithm. Neuro computing 21, pp. 119-138.
- Crawford, M.F., Medwedeff, D.A., 1999. Automated extraction of fault surfaces from 3-D seismic prospecting data. Atlantic Richfield Company (Los Angeles, CA), U. S. Pat.5987388.
- Cross, G., Jain, A., 1983. Markov Random Field Texture Models. IEEE Transactions on Pattern Analysis and Machine Intelligence 5(1), 1, pp. 25-39.
- David, C.P., 2008. Détection d'hétérogénéités linéaires dans les textures directionnelles : application à la détection de failles en sismique de réflexion PhD thesis. Université de Bordeaux 1.
- Davies, D., Bouldin, D., 1979. A Cluster Separation Measure. Pattern Analysis and Machine Intelligence, IEEE Transactions on PAMI-1, 2, pp. 224-227.
- Donias, M., David, C.P., Berthoumieu, Y., Laviaille, O., Guillon, S., Keskes, N., 2007. New fault attribute based on robust directional scheme. Geophysics 72, 4, pp. P39-P46.
- Dorn, G.A., 1998. Modern 3-D seismic interpretation. The Leading Edge 17, 9, pp. 1262-1272.
- Dorn, G.A., 1999. Method and system for horizon interpretation of seismic surveys using surface draping U.S. Pat. 5894417.
- Dorn, G.A., Hammon III, W.S., Carlson, J.A., 2010. EXTRACTION OF DEPOSITIONAL SYSTEMS, U.S. Pat. 20100250210.
- du Buf, J.M.H., Kardan, M., Spann, M., 1990. Texture feature performance for image segmentation. Pattern Recognition 23, 3-4, pp. 291-309.
- Dudani, S.A., Breeding, K.J., McGhee, R.B., 1977. Aircraft identification by moment invariants. IEEE Trans. on Computers 26, 1, pp. 39-46.
- Dumay, J., Fournier, F., 1988. Multivariate statistical analyses applied to seismic facies recognition. Geophysics 53, 9, pp. 1151-1159.
- Dunn, P.A., Czernuszenko, M.K., 2006. Method for performing stratigraphically-based seed detection in a 3-D seismic data volume. ExxonMobil Upstream Research Company (Houston, TX, US), U. S. Pat. 7024021.
- Estepar, R.S.J., 2005. Local Structure Tensor for Multidimensional Signal Processing. Applications to Medical Image Analysis, PhD thesis. University of Valladolid, Spain.
- Fehmers, G.C., Hocker, C.F.W., 2003. Fast structural interpretation with structure-oriented filtering. Geophysics 68, 4, pp. 1286-1293.

- Florack, L., 1997. Image structure. Computational Imaging and Vision, volume 10, Kluwer Academic Publishers.
- Flusser, J., Boldys, J., Zitová, B., 2003. Moment Forms Invariant to Rotation and Blur in Arbitrary Number of Dimensions. IEEE Transactions on Pattern Analysis and Machine Intelligence 25, 2, pp. 234-246.
- Flusser, J., Suk, T., 1993. Pattern recognition by affine moment invariants. Pattern Recognition 26, 1, pp. 167-174.
- Flusser, J., Suk, T., Zitova, B., 2009. Moments and moment invariants in pattern recognition. Wiley & Sons Ltd.
- Flynn, M.J., 1972. Some Computer Organizations and Their Effectiveness. IEEE Trans. Comput. C-21, p. 948.
- Gersztenkorn, A., Marfurt, K.J., 1999. Eigenstructure-based coherence computations as an aid to 3-D structural and stratigraphic mapping. Geophysics 64, 5, pp. 1468-1479.
- Gibson, D., Spann, M., Turner, J., 2003. Automatic Fault Detection for 3D Seismic Data, Digital Image Computing: Techniques and Applications, pp. 821-830.
- Goetz, B., 2002. Introduction to Java threads. ibm.com/developerWorks.
- Goff, D.F., Vincent, L., Deal, K.L., Kowalik, W.S., Bombarde, S., Lee, S., Volz, W.R., Jones, R.C., 2003. Process for interpreting faults from a fault-enhanced 3-dimensional seismic attribute volume, U.S. Pat. 20030112704.
- Graham, R., 1962. Snow removal--A noise-stripping process for picture signals. IEEE Transactions on Information Theory 8, 2, pp. 129-144.
- Gram, A., 2003. Introduction to parallel computing. Addison-Wesley.
- Gurney, K., Gurney, K.N., 1997. An introduction to neural networks. UCL Press.
- Hagen, D.C., 1982. The application of principal components analysis to seismic data sets. Geoprospection 20, 1-2, pp. 93-111.
- Hall, M., 2007. Smooth operator: Smoothing seismic interpretations and attributes. The Leading Edge 26, 1, pp. 16-20.
- Haralick, R.M., 1979. Statistical and structural approaches to texture. Proceedings of the IEEE 67, 5, pp. 786-804.
- Hausdorff, F., 1921a. Summationsmethoden und Momentfolgen. I. Mathematische Zeitschrift 9, pp. 74-109.
- Hausdorff, F., 1921b. Summationsmethoden und Momentfolgen. II. Mathematische Zeitschrift 9, pp. 280-299.
- Haykin, S.S., 1999. Neural networks: a comprehensive foundation, 2 ed. Prentice Hall.
- Heck, M.M., 2006. 3D Visualization for Oil and Gas Evolves, HPCWire October 2006.

- Hildebrandt, T.H., Schoenberg, I.J., 1933. On Linear Functional Operations and the Moment Problem for a Finite Interval in One or Several Dimensions. *The Annals of Mathematics*, Second Series, Vol. 34, No. 2, pp. 317-328
- Hocker, C., Fehmers, G., 2002. Acquisition/Processing---Fast structural interpretation with structure-oriented filtering. *The Leading Edge* 21, 3, pp. 238-243.
- Hosny, K.M., 2007a. Exact and fast computation of geometric moments for gray level images. *Applied Mathematics and Computation* 189, 2, pp. 1214-1222.
- Hosny, K.M., 2007b. Exact Legendre moment computation for gray level images. *Pattern Recognition* 40, 12, pp. 3597-3605.
- Hotelling, H., 1933. Analysis of a complex of statistical variables into principal components. *J. Educ. Psych.* 24, pp. 417-441,498-520.
- Hu, M.K., 1962. Visual pattern recognition by moment invariants. *IEEE Trans. on Information Theory* 8, 2, pp. 179-187.
- Huang, K.-Y., 1990. Branch and bound search for automatic linking process of seismic horizons. *Pattern Recognition* 23, 6, pp. 657-667.
- Imhof, M.G., Gillard, D.G., Hussenoeder, S., Pavel, D., Terrell, M., Kumaran, K., Schroeder, F., 2011. Seismic Horizon Skeletonization, U.S. Pat.20110048731.
- Inselberg, A., 1985. The plane with parallel coordinates. *The Visual Computer* 1, 2, pp. 69-91.
- Jacquemin, P., Mallet, J.-L., 2005. Automatic faults extraction using double hough transform. *SEG Technical Program Expanded Abstracts* 24, 1, pp. 755-758.
- James, H., 2008. System and Method for Displaying Seismic Horizons with Attributes, U.S. Pat.20080285384.
- Jeong, W.K., Whitaker, R., Dobin, M., 2006. Interactive 3d seismic fault detection on the graphics hardware, In *Eurographics / IEEE VGTC Workshop on Volume Graphics*, pp. 111-118.
- Jerome, R., 2009. Improving Zernike Moments Comparison for Optimal Similarity and Rotation Angle Retrieval. *IEEE Transactions on Pattern Analysis and Machine Intelligence* 31, pp. 627-636.
- Johann, P.R.S., de Castro, D.D., Barroso, A.S., Petrobras S.A, 2001. Reservoir Geophysics: Seismic Pattern Recognition Applied to Ultra-Deepwater Oilfield in Campos Basin, Offshore Brazil, *SPE Latin American and Caribbean Petroleum Engineering Conference*, Buenos Aires, Argentina, March 2001, pp. 25-28.
- Jolliffe, I.T., 2002. *Principal component analysis*, Series: Springer Series in Statistics, 2nd ed. Springer, New York.
- Julesz, B., 1975. Experiments in the visual perception of texture. *Scientific American*, 232, 4, 34-43.
- Keskes, N., Zaccagnino, P., Rether, D., Mermey, P., 1983. Automatic extraction of 3-D seismic horizons. *SEG Technical Program Expanded Abstracts* 2, 1, pp. 557-559.

- Khatti, K., Gir, R., 1976. A Study Of The Seismic Signatures Of Sedimentation Models Using Synthetic Seismograms. *Geophysical Prospecting* 24, 3, pp. 454-477.
- Khatti, K., Sinval, A., Awasthi, A.K., 1979. Seismic Discriminants Of Stratigraphy Derived From Monte Carlo Simulation Of Sedimentary Formations. *Geophysical Prospecting* 27, 1, pp. 168-195.
- Kobbelt, L., Vorsatz, J., Labsik, U., Seidel, H.P., 1999. A Shrink Wrapping Approach to Remeshing Polygonal Surfaces. *Computer Graphics Forum (Proc. of Eurographics '99)* 18, 3, pp. 119-130.
- Koenderink, J., 1984. The structure of images. *Biological Cybernetics* 50, 5, pp. 363-370.
- Kohonen, T., 1981. Automatic Formation of Topological Maps of Patterns in a Self-Organizing System, *Proceedings of the 2nd Scandinavian Conference on Image Analysis*. Pattern Recognition Society of Finland, pp. 214-220.
- Kohonen, T., 1982. Self-organized formation of topologically correct feature maps. *Biological Cybernetics* 43, 1, pp. 59-69.
- Kohonen, T., 1984. *Self-organisation and associative memory*. Springer-Verlag.
- Kumar, D., 2010. Concept of threads used in different operation system. Deptt. of computer Sc. & IT.
- Kuwahara, M., Hachimura, K., Eiho, S., Kinoshita, M., 1976. Processing of RI-angiocardigraphic images., in: Preston, K., Onoe, M. (Eds.), *Digital Processing of Biomedical Images*. Plenum Press edition, New York, pp. 187-202.
- Kyprianidis, J.E., Kang, H., Döllner, J., 2009. Image and Video Abstraction by Anisotropic Kuwahara Filtering. *Computer Graphics Forum* 28, 7, pp. 1955-1963.
- Kyprianidis, J.E., Semmo, A., Kang, H., Döllner, J., 2010. Anisotropic Kuwahara Filtering with Polynomial Weighting Functions, *Theory and Practice of Computer Graphics*, pp. 25-30.
- Lavest, P., Chipot, Y., 1993. Building complex horizons for 3-D seismic. *SEG Technical Program Expanded Abstracts* 12, 1, pp. 159-161.
- Lavialle, O., Pop, S., Germain, C., Donias, M., Guillon, S., Keskes, N., Berthoumieu, Y., 2007. Seismic fault preserving diffusion. *Journal of Applied Geophysics* 61, 2, pp. 132-141.
- Leif, C., 2007. *Framework for Polygonal Structures Computations on Clusters*, Master. Norwegian University of Science and Technology, Department of Computer and Information Science:Insti.
- Levine, M.D., 1985. *Vision in man and machine*. McGraw-Hill.
- Li, G.-X., Yang, B., Dai, M., 2011. Multi-scale image description with rotation invariants of Gaussian-Hermite moments 2011 International Conference on Wavelet Analysis and Pattern Recognition (ICWAPR 2011) Guilin, China, 10 - 13 July 2011, pp. 12-17
- Li, G.X., Yang, B., Dai, M., 2010a. Coherency estimation based on spectrum Gaussian-Hermite moments, in: Du, Z., Liu, B. (Eds.), *International Conference on Image Processing and Pattern Recognition in Industrial Engineering SPIE*, Xi'an, China, 7-10 August 2010, pp. 78202S-78207.

- Li, G.X., Yang, B., Dai, M., 2010b. Stepwise dip scanning coherence algorithm based on eigenstructure, RST 23eme reunion des sciences de la terre, Vol. 1, Bordeaux, France., 25 - 29 Octobre 2010.
- Li, Q., Vasudevan, K., Cook, F.A., 1997. Seismic skeletonization: A new approach to interpretation of seismic reflection data. *J. Geophys. Res.* 102, B4, pp. 8427-8445.
- Li, Y.J., 1992. Reforming the theory of invariant moments for pattern recognition. *Pattern recognition* 25, 7, pp. 723-730.
- Liao, S.X., Pawlak, M., 1996. On image analysis by moments. *IEEE Transactions on Pattern Analysis and Machine Intelligence* 18, 3, pp. 254-266.
- Linari, V., Santiago, M., Pastore, C., Azbel, K., Poupon, M., 2003. Seismic facies analysis based on 3D multiattribute volume classification, La Palma Field, Maracaibo, Venezuela. *The Leading Edge* 22, 1, pp. 32-36.
- Lo, C.-h., Don, H.-s., 1989. 3-D Moment Forms: Their Construction and Application to Object Identification and Positioning. *IEEE Transactions on Pattern Analysis and Machine Intelligence* 11, 10, pp. 1053-1064.
- Lomask, J., Guitton, A., Fomel, S., Claerbout, J., Valenciano, A.A., 2006. Flattening without picking. *Geophysics* 71, 4, pp. P13-P20.
- Lu, S.-y., Cheng, Y.-c., 1990. An iterative approach to seismic skeletonization. *Geophysics* 55, 10, pp. 1312-1320.
- Lu, W., Li, Y., Zhang, S., Xiao, H., Li, Y., 2005. Higher-order-statistics and supertrace-based coherence-estimation algorithm. *Geophysics* 70, 3, pp. 13-18.
- Luo, L.M., Hamitouche, C., Dillenseger, J.L., Coatrieux, J.L., 1993. A moment-based three-dimensional edge operator. *IEEE Trans. on Biomedical Engineering* 40, 7, pp. 693-703.
- Luo, Y., Higgs, W.G., Kowalik, W.S., 1996. Edge detection and stratigraphic analysis using 3D seismic data. *SEG Technical Program Expanded Abstracts* 15, 1, pp. 324-327.
- Luo, Y., Marhoon, M., Dossary, S.A., Alfaraj, M., 2002. Acquisition Processing---Edge-preserving smoothing and applications. *The Leading Edge* 21, 2, pp. 136-158.
- Ma, L., Tan, T.N., Wang, Y.H., Zhang, D.X., 2004. Local intensity variation analysis for iris recognition. *Pattern Recognition* 37, 6, pp. 1287-1298.
- Mademlis, A., Axenopoulos, A., Daras, P., Tzovaras, D., Strintzis, M.G., 2006. 3D content-based search based on 3D Krawtchouk moments, *Int. Symp. on 3D Data Processing Visualization and Transmission*, Chapel Hill, NC, pp. 743-749.
- Mamistvalov, A.G., 1998. n-Dimensional Moment Invariants and Conceptual Mathematical Theory of Recognition n-Dimensional Solids. *IEEE Transactions on Pattern Analysis and Machine Intelligence* 20, 8, pp. 819-831.
- Mardia, K.V., Kent, J.T., Bibby, J.M., 2000. *Multivariate analysis*, 7 ed. Academic Press.
- Marfurt, K.J., Kirilin, R.L., Farmer, S.L., Bahorich, M.S., 1998. 3-D seismic attributes using a semblance-based coherency algorithm. *Geophysics* 63, 4, pp. 1150-1165.

- Marfurt, K.J., Sudhaker, V., Gersztenkorn, A., Crawford, K.D., Nissen, S.E., 1999. Coherency calculations in the presence of structural dip. *GEOPHYSICS* 64, 1, pp. 104-111.
- Maroni, C.-S., Quinquis, A., Vinson, S., 2001. Horizon Picking on Subbottom Profiles Using Multiresolution Analysis. *Digital Signal Processing* 11, 4, pp. 269-287.
- Marroquín, I.D., Brault, J.-J., Hart, B.S., 2009. A visual data-mining methodology for seismic facies analysis: Part 1 --- Testing and comparison with other unsupervised clustering methods. *Geophysics* 74, 1, pp. P1-P11.
- Marsh, T., Tyrrell, J., Evins, L., 2005. Role of Automated Techniques in Improving Volume-based Structural Interpretation. *First Break* 23, pp. 89-93.
- Mathieu, P.G., Rice, G.W., 1969. Multivariate analysis used in the detection of stratigraphic anomalies from seismic data. *Geophysics* 34, 4, pp. 507-515.
- Matlock, R.J., Asimakopoulos, G.T., 1986. Can seismic stratigraphy problems be solved using automated pattern analysis and recognition? *The Leading Edge* 5, 9, pp. 51-55.
- Matos, M.C.d., Osorio, P.L.M., Johann, P.R.S., 2007. Unsupervised seismic facies analysis using wavelet transform and self-organizing maps. *Geophysics* 72, 1, pp. P9-P21.
- Matthas, J., Michael, P., Martin, K., 1998. Large-scale parallel geophysical algorithms in Java: a feasibility study. *The Leading Edge* 17, 12, pp. 1662-1666.
- McCulloch, W., Pitts, W., 1943. A logical calculus of the ideas immanent in nervous activity. *Bulletin of Mathematical Biology* 5, 4, pp. 115-133.
- Medioni, G., Tang, C.-K., Lee, M.-S., 2000. *Tensor Voting: Theory and Applications*, Proceedings of RFIA 2000, Paris, France, February
- Miguel, R.D., 1995. Segmentation d'images à partir d'opérateurs de cohérence. Application aux images sismiques. ENSERB, Pessac.
- Mitchum, R.M., Vail, P.R., 1977. Seismic stratigraphic interpretation procedure, AAPG Memoir; *Seismic Stratigraphy - Applications to Hydrocarbon Exploration* 26, pp. 135-143.
- Mitchum, R.M., Vail, P.R., Sangree, J.B., 1977. Seismic stratigraphy and global changes of sea level - Part 6: Stratigraphic interpretation of seismic reflection patterns in depositional sequence. *Seismic Stratigraphy - Applications to Hydrocarbon Exploration: AAPG Memoir* 26, pp. 117-133.
- Miyamoto, Y., Shirazi, M.N., Uehara, K., 2000. Texture analysis and classification using bottom-up tree-structured wavelet transform, Proceedings of the 6th Pacific Rim international conference on Artificial intelligence. Springer-Verlag, Melbourne, Australia, pp. 802-802.
- Moore, G.E., 1965. Cramming more components onto integrated circuits. *Electronics* 38(8), p. 114.
- Morrison, R.S., 2003. *Cluster Computing - Architectures, Operating Systems, Parallel Processing & Programming Languages*.
- MSDN, 2011. About Processes and Threads. <http://msdn.microsoft.com/en-us/library/windows/desktop/ms681917%28v=vs.85%29.aspx>.

- Mukundan, R., 2004. Some computational aspects of discrete orthonormal moments. *IEEE Trans. on Image Processing* 13, 8, pp. 1055-1059.
- Mukundan, R., Ong, S.H., Lee, P.A., 2001. Image analysis by Tchebichef moments. *IEEE Trans. on Image Processing* 10, 9, pp. 1357-1364.
- Mukundan, R., Ramakrishnan, K.R., 1998. *Moment functions in image analysis Theory and applications*. World scientific publishing Co. Pte. Ltd., Singapore.
- Neff, D., Singleton, J., Grismore, J., Layton, J., Keskula, E., 2000a. Seismic interpretation using true 3-D visualization. *The Leading Edge* 19, 5, pp. 523-525.
- Neff, D.B., Grismore, J.R., Lucas, W.A., 2000b. Automated seismic fault detection and picking. Phillips Petroleum Company (Bartlesville, OK), U. S. Pat.6018498.
- Oliver, H., 2011. Digital Signal Processing Resources Available. <http://www.staff.ncl.ac.uk/oliver.hinton/eee305/Chapter6.pdf>
- Ong, L.-Y., Chong, C.-W., Besar, R., 2007. An approach to 3-D object recognition using Legendre moment invariants, *International Conference on Intelligent and Advanced Systems*, Kuala Lumpur 25-28 Nov. 2007 pp. 671- 674
- Papari, G., Petkov, N., Campisi, P., 2007. Artistic Edge and Corner Enhancing Smoothing. *IEEE Transactions on Image Processing* 16, 10, pp. 2449-2462.
- Patel, D., Giertsen, C., Thurmond, J., Gjelberg, J., Gröller, M.E., 2008. The Seismic Analyzer: Interpreting and Illustrating 2D Seismic Data. *IEEE Transactions on Visualization and Computer Graphics* 14, 6, pp. 1571-1578.
- Pearson, K., 1901. On lines and planes of closest fit to systems of points in space. *Philosophical Magazine* 2, 6, pp. 559-572.
- Pedersen, S.I., Randen, T., Sonneland, L., Steen, O., 2002. Automatic fault extraction using artificial ants. *SEG Technical Program Expanded Abstracts*. 21, pp. 512-525.
- Pennington, W.D., Acevedo, H., Len, S., Minaeva, A., Wood, J., Xie, D., 2001. Calibration of Seismic Attributes for Reservoir Characterization. *Annual Technical Progress Report*, Michigan Technological University.
- Pouliquen, F.L., 2003. *Operateurs discrets pour l'estimation adaptative et optimale de l'orientation application à l'imagerie sismique*, Ecole doctorale des sciences physiques et de l'ingénieur. Bordeaux 1, Bordeaux.
- Poupon, M., Azbel, K., Ingram, J.E., 1999. Integrating seismic facies and petro-acoustic moldering. *World Oil magazine*, pp. 75-80.
- Randen, T., Monsen, E., Signer, C., Abrahamsen, A., Hansen, J.O., Saeter, T., Schlaf, J., 2000. Three-dimensional texture attributes for seismic data analysis. *SEG Technical Program Expanded Abstracts* 19, 1, pp. 668-671.
- Randen, T., Pedersen, S.I., Signer, C., Sonneland, L., 1999. Image processing tools for geologic unconformity extraction, In *Proceedings of IEEE Nordic Signal Processing Symposium*, pp. 9-11.

- Randen, T., Sønneland, L., 2005. Atlas of 3D Seismic Attributes, Mathematical Methods and Modelling in Hydrocarbon Exploration and Production, in: Iske, A., Randen, T. (Eds.). Springer Berlin Heidelberg, pp. 23-46.
- Reddi, S.S., 1981. Radial and angular moment invariants for image identification. IEEE Transactions on Pattern Analysis and Machine Intelligence 3, 2, pp. 240-242.
- Reiss, T.H., 1991. The revised fundamental theorem of moment invariants. IEEE Transactions on Pattern Analysis and Machine Intelligence 13, 8, pp. 830-834.
- Reuze, P., Coatrieux, J.L., Luo, L.M., Dillenseger, J.L., 1993. A 3D Moment Based Approach for Blood Vessel Detection and Quantification in MRA. Journal of Technology and Health Care, 93(1), pp. 181-188.
- Robertson, J.D., 1989. Reservoir management using 3-D seismic data. The Leading Edge 8, 2, pp. 25-31.
- Rojey, A., Jaffret, C., Cornot-Gandolph, S., Durand, B., Jullin, S., Valais, M., 1997. Natural gas: production, processing, transport. Editions Technip, Paris, France.
- Rosenblatt, F., 1958. The Perceptron: A probabilistic model for information storage and organization in the brain. Psychological Review Vol 65 (6), 6, pp. 386-408.
- Rosenfeld, A., Kak, A.C., 1982. Digital Picture Processing, 2nd. Academic Press, Inc.
- Rothe, I., Süsse, H., Voss, K., 1996. The Method of Normalization to Determine Invariants. IEEE Transactions on Pattern Analysis and Machine Intelligence 18, 4, pp. 366-376.
- Sabeti, H., Javaherian, A., 2009. Seismic Facies Analysis Based on K-means Clustering Algorithm Using 3D Seismic Attributes, 1st International Petroleum Conference & Exhibition, EAGE Shiraz, Iran.
- Sadjadi, F.A., Hall, E.L., 1978. Numerical computation of moment invariants for scene analysis, Proc. IEEE Conf. on Pattern Recognition and Image Processing, Chicago, pp. 181-187.
- Sadjadi, F.A., Hall, E.L., 1980. Three-Dimensional Moment Invariants. IEEE Transactions on Pattern Analysis and Machine Intelligence PAMI-2(2), 2, pp. 127-136.
- Scales, J., 1997. Theory of Seismic Imaging. Samizdat Press.
- Schlaf, J., Randen, T., Sønneland, L., 2005. Introduction to Seismic Texture, in: Iske, A., Randen, T. (Eds.). Springer Berlin Heidelberg, pp. 3-21.
- Seber, G.A.F., 1984. Multivariate observations, 1 ed. Wiley-Interscience, New York.
- Serra, J.P., 1982. Image analysis and mathematical morphology. Academic Press.
- Sheffield, T.M., Meyer, D., Lees, J., Payne, B., Harvey, E.L., Zeitlin, M.J., Kahle, G., 2000. Geovolume visualization interpretation: A lexicon of basic techniques. The Leading Edge 19, 5, pp. 518-522.
- Shen, J., 1997. Orthogonal Gaussian-Hermite moments for image characterization, SPIE Intelligent Robots Computer Vision XVI, Pittsburgh, 15 Oct., pp. 224-233.

- Shen, J., Chang, S.I., Lee, E.S., Deng, Y., Brown, S.J., 2005. Determination of cluster number in clustering microarray data. *Applied Mathematics and Computation* 169, 2, pp. 1172-1185.
- Shen, J., Shen, W., Shen, D., 2000. On geometric and orthogonal moments. *International Journal of Pattern Recognition and Artificial Intelligence*. vol 14(7), 7, pp. 875-894.
- Shen, J., Shen, W., Shen, D.F., Wu, Y.F., 2004. Orthogonal moments and their application to motion detection in image sequences. *Int. Jour. Information Acquisition* 1, 1, pp. 77-87.
- Sheriff, R., Geldart, L., 1995. *Exploration Seismology* (2nd). Cambridge University Press.
- Sheriff, R.E., 1978. *A first course in geophysical exploration and interpretation*. International Human Resources Development Corporation, Boston.
- Siguaw, S.G., Estes-Jackson, J.E., Ingraham, S.E., Shewmake, D.W., 2001. An integrated 3-D reservoir characterization at Riverton Dome Field, Wyoming. *The Leading Edge* 20, 11, pp. 1226-1238.
- Sim, D.-G., Kim, H.-K., Park, R.-H., 2004. Invariant texture retrieval using modified Zernike moments. *Image and Vision Computing* 22, 4, pp. 331-342.
- Simpson, A.L., Howard, R.E., 1996. Method and apparatus for identifying fault curves in seismic data. Landmark Graphics Corporation (Houston, TX), U. S. Pat.5537320.
- Sinvhal, A., Khattri, K., 1983. Application of seismic reflection data to discriminate subsurface lithostratigraphy. *Geophysics* 48, 11, pp. 1498-1513.
- Sinvhal, A., Khattri, K.N., Sinvhal, H., Awasthi, A.K., 1984. Seismic indicators of stratigraphy. *Geophysics* 49, 8, pp. 1196-1212.
- Smith, L.I., 2002. A tutorial on Principal Components Analysis. http://www.cs.otago.ac.nz/cosc453/student_tutorials/principal_components.pdf.
- Sommer, I., Muller, O., Domingues, F.S., Sander, O., Weickert, J., Lengauer, T., 2007. Moment invariants as shape recognition technique for comparing protein binding sites. *Bioinformatics* 23, 23, pp. 3139-3146.
- Stark, T.J., 1991. "Surface slices:" Interpretation using surface segments instead of line segments. *SEG Technical Program Expanded Abstracts* 10, 1, pp. 259-262.
- Stark, T.J., 1996. Surface slice generation and interpretation: A review. *The Leading Edge* 15, 7, pp. 818-819.
- Stoker, M.S., Pheasant, J.B., Josenhans, H., 1997. Seismic methods and interpretation. In Davies, TA, et al., eds., *Glaciated continental margins: An atlas of acoustic images*: New York, Chapman Hall, pp. 9-26.
- Strecker, U., Uden, R., 2002. Data mining of 3D poststack seismic attribute volumes using Kohonen self-organizing maps. *The Leading Edge* 21, 10, pp. 1032-1037.
- Strzelecki, M., Materka, A., 1997. Markov Random Fields as Models of Textured Biomedical Images, Proc. 20th National Conf. Circuit Theory and Electronic Networks KTOiUE '97, Kołobrzeg, Poland, pp. 493-498.
- Suk, T., Flusser, J., 2003. Combined blur and affine moment invariants and their use in pattern recognition. *Pattern Recognition* 36, 12, pp. 2895-2907.

- Taner, M.T., 2001. Seismic attributes, Canadian Society of Exploration Geophysicists Recorder, pp. 48-56.
- Taner, M.T., F. Koehler, R. E. Sheriff, 1979. Complex seismic trace analysis. Geophysics 44, pp. 1041-1063.
- Tang, C.-K., Medioni, G., 2002. Curvature-Augmented Tensor Voting for Shape Inference from Noisy 3D Data. IEEE Transactions on Pattern Analysis and Machine Intelligence 24, 6, pp. 858-864.
- Tang, C.-K., Medioni, G., Lee, M.-S., 2001. N-Dimensional Tensor Voting and Application to Epipolar Geometry Estimation. IEEE Transactions on Pattern Analysis and Machine Intelligence 23, 8, pp. 829-844.
- Teague, M.R., 1980. Image analysis via the general theory of moments. Jour. of Optical Society America 70, pp. 920-930.
- TechTarget, 2004. multi-core processor.
<http://searchdatacenter.techtarget.com/definition/multi-core-processor>.
- Teh, C.H., Chin, R.T., 1988. On Image Analysis by the Methods of Moments. IEEE Transactions on Pattern Analysis and Machine Intelligence 10, 4, pp. 496-513.
- Theodoridis, S., Koutroumbas, K., 1999. Pattern Recognition. Academic Press, Inc.
- Thomson, D., Hennenfent, G., Modzelewski, H., Herrmann, F.J., 2006. A parallel windowed fast discrete curvelet transform applied to seismic processing. SEG Technical Program Expanded Abstracts 25, 1, pp. 2767-2771.
- Tong, W.-S., Tang, C.-K., Medioni, G., 2001. First order tensor voting and application to 3-D scale analysis, CVPR 2001, pp. 175-182.
- Tong, W.-S., Tang, C.-K., Mordohai, P., Medioni, G., 2004. First Order Augmentation to Tensor Voting for Boundary Inference and Multiscale Analysis in 3D. IEEE Transactions on Pattern Analysis and Machine Intelligence 26, 5, pp. 594-611.
- Treitel, S., Robinson, E., 1966. Seismic wave propagation in layered media in terms of communication theory. Geophysics vol. 31(1), pp. 17-32.
- Tuceryan, M., 1994. Moment based texture segmentation. pattern Recognition Letters 15, 7, pp. 659-668.
- Tuceryan, M., Jain, A.K., 1998. Texture Analysis, in: Chen, C.H., Pau, L.F. (Eds.), The Handbook of Pattern Recognition and Computer Vision (2nd Edition). World Scientific Publishing, pp. 207-248.
- Tugnait, J.K., 1993. Time delay estimation with unknown spatially correlated Gaussian noise. IEEE Trans. On Signal Processing 41, 2, pp. 549-558.
- Ulsch, A., 1993. Knowledge Extraction from Self-Organizing Neural Networks, in: Opitz, O., Lausen, B., Klar, R. (Eds.), Information and Classification. Springer, pp. 301-306.
- Ulsch, A., Siemon, H.P., 1990. Kohonen's Self Organizing Feature Maps for Exploratory Data Analysis, Proceedings of International Neural Networks Conference (INNC). Kluwer Academic Press, pp. 305-308.

- Vasudevan, K., Eaton, D., Cook, F.A., 2005. Adaptation of seismic skeletonization for other geoscience applications. *Geophysical Journal International* 162, 3, pp. 975-993.
- Veronez, M.R., Florêncio de Souza, S., Matsuoka, M.T., Reinhardt, A., Macedônio da Silva, R., 2011. Regional Mapping of the Geoid Using GNSS (GPS) Measurements and an Artificial Neural Network. *Remote Sensing* 3, 4, pp. 668-683.
- Vesanto, J., Alhoniemi, E., 2000. Clustering of the self-organizing map. *Neural Networks, IEEE Transactions on* 11, 3, pp. 586-600.
- Vesanto, J., Himberg, J., Alhoniemi, E., Parhankangas, J., 1999. Self-organizing map in Matlab: the SOM toolbox, In *Proceedings of the Matlab DSP Conference*, pp. 35--40.
- Wang, L., Dai, M., 2007. Application of a new type of singular points in fingerprint classification. *Pattern Recognition Letters* 28, 13, pp. 1640-1650.
- Wegman, E., Luo, Q., 1997. High Dimensional Clustering Using Parallel Coordinates and the Grand Tour. *Computing Science and Statistics* 28, pp. 361-368.
- Weickert, J., 1996. Anisotropic diffusion in image processing, PhD thesis. University of Kaiserslautern.
- Weickert, J., 1997. A review of nonlinear diffusion filtering, in: ter Haar Romeny, B., Florack, L., Koenderink, J., Viergever, M. (Eds.), *Scale-Space Theory in Computer Vision*. Springer Berlin / Heidelberg, pp. 1-28.
- Weickert, J., 1998. Anisotropic diffusion in image processing. *ECMI Series*, Teubner-Verlag, Stuttgart.
- Weickert, J., 1999. Coherence-Enhancing Diffusion Filtering. *International Journal of Computer Vision* 31, 2, pp. 111-127.
- Werghe, N., Xiao, Y., 2002. Wavelet Moments for Recognizing Human Body Posture from 3D Scans, *Proceedings of the 16 th International Conference on Pattern Recognition (ICPR'02) Volume 1 - Volume 1*. IEEE Computer Society, p. 10319.
- wikipedia, 2011. Computer cluster. http://en.wikipedia.org/wiki/Computer_cluster.
- Wong, R.Y., Hall, E.L., 1978. Scene matching with invariant moments. *Computer Vision Graphics and Image Processing* 8, 1, pp. 16-24.
- Wong, W.H., Siu, W.C., Lam, K.M., 1995. Generation of moment invariants and their uses for character recognition. *Pattern Recognition Letters* 16, 2, pp. 115-123.
- Wu, Y.F., Shen, J., 2005. Properties of orthogonal Gaussian-Hermite moments and their application. *EURASIP Jour. Applied Signal Processing* 2005, 4, pp. 588-599.
- Wu, Y.F., Shen, J., Dai, M., 2005. Traffic object detections and its action analysis. *Pattern Recognition Letters* 26, 13, pp. 1963-1984.
- Xu, D., Li, H., 2006a. 3-D Curve Moment Invariants for Curve Recognition, *Intelligent Computing in Signal Processing and Pattern Recognition*, pp. 572-577.
- Xu, D., Li, H., 2006b. 3-D Surface Moment Invariants, *International Conference on Pattern Recognition*, pp. 173-176.

- Xu, D., Li, H., 2007. 3-D projective moment invariants. *The Journal of Information and Computational Science* 4, 1.
- Xu, D., Li, H., 2008. Geometric moment invariants. *Pattern Recognition* 41, 1, pp. 240-249.
- Yang, B., Dai, M., 2011. Image analysis by Gaussian–Hermite moments. *Signal Processing* 91, 10, pp. 2290-2303.
- Yang, B., Dai, M., 2012. Image reconstruction from continuous Gaussian–Hermite moments implemented by discrete algorithm. *Pattern Recognition* 45, 4, pp. 1602-1616.
- Yang, B., Li, G., Zhang, H., Dai, M., 2011. Rotation and translation invariants of Gaussian–Hermite moments. *Pattern Recognition Letters* 32, 9, pp. 1283-1298.
- Yang, Y., Aplin, A.C., Larter, S.R., 2004. Quantitative assessment of mudstone lithology using geophysical wireline logs and artificial neural networks. *Petroleum Geoscience* 10, 2, pp. 141-151.
- Yap, P.T., Paramesran, R., Ong, S.H., 2003. Image analysis by Krawtchouk moments. *IEEE Trans. on Image Processing* 12, 11, pp. 1367-1377.
- Yilmaz, Ö., Doherty, S.M., 1987. *Seismic data processing*. Society of Exploration Geophysicists.
- Yokoya, N., Levine, M.D., 1989. Range image segmentation based on differential geometry: a hybrid approach. *IEEE Transactions on Pattern Analysis and Machine Intelligence* 11, 6, pp. 643-649.
- Zacharias, S., Wessolek, G., 2007. Excluding organic matter content from pedotransfer predictors of soil water retention. *Soil Sci. Soc. Am. J.* 71, pp. 43-50.
- Zhang, X.D., 1996. *Time series analysis- High order statistics method*. Tsinghua University Press, Beijing.
- Zhu, H.Q., Shu, H.Z., Liang, J., Luo, L.M., Coatrieux, J.L., 2007a. Image analysis by discrete orthogonal Racah moments. *Signal Processing* 87, 4, pp. 687-708.
- Zhu, H.Q., Shu, H.Z., Xia, T., Luo, L.M., Coatrieux, J.L., 2007b. Translation and scale invariants of Tchebichef moments. *Pattern Recognition* 40, 9, pp. 2530-2542.
- Zhu, H.Q., Shu, H.Z., Zhou, J., Luo, L.M., Coatrieux, J.L., 2007c. Image analysis by discrete orthogonal dual Hahn moments. *Pattern Recognition Letters* 28, 13, pp. 1688-1704.

Notations

$\psi_{pq}(x,y)$	Basis function of general moment
m_{pq}	Geometric moment of order $(p+q)$
μ_{pq}	Central moment of order $(p+q)$
m_{pqr}	3D Geometric moment of order $(p+q+r)$
μ_{pqr}	3D Central moment of order $(p+q+r)$
$P_p(x)$	Legendre polynomial of degree p
L_{pq}	Legendre moment of order $(p+q)$
V_{pq}	Zernike polynomial of degree p
Z_{pq}	Zernike moment of order p
R_{pq}	Radial polynomial corresponding to Zernike polynomial
$\tilde{t}_p(x)$	Scaled discrete Tchebichef polynomial of degree p
T_{pq}	Discrete Tchebichef moment of order (p, q)
$\hat{K}_n(x; p, K)$	Weighted Krawtchouk polynomial of degree n
Q_{nm}	Krawtchouk moment of order (n, m)
$\hat{H}_p(x; \sigma)$	Gaussian-Hermite polynomial of degree p
$\tilde{H}_p(i, K; \sigma)$	Discrete version of the p^{th} degree Gaussian-Hermite polynomial
η_{pq}	Gaussian-Hermite moment of order (p, q)
$\tilde{\eta}_{pq}$	Gaussian-Hermite central moment of order (p, q)
I_p	Rotation invariants of Gaussian-Hermite moment
η_{pqr}	3D Gaussian-Hermite moment of order (p, q, r)
$\tilde{\eta}_{pqr}$	3D Gaussian-Hermite central moment of order (p, q, r)
I_p^{3D}	3D Rotation invariants of Gaussian-Hermite moment
C_{an}	Confidence of anisotropy or isotropy;
C_1	Cross-correlation based coherence algorithm;

C_2	Multi-trace semblance based coherence algorithm;
C_3	Eigenstructure based coherence algorithm;
$d_{i,j}$	Average of absolute difference in the differencing coherence algorithm;
$C(t)$	Cross-correlation coefficient
$J_{HOS}(d)$	Higher order statistics coefficient
$D_{t,t+1}^i$	Euclidean distance between pattern samples
$\hat{P}_{t,t+1}^i$	Sample selected among potential candidates
DBI	Davies and Bouldin index of clustering
V_f	Feature vector of moments

Publications of author

Publications on Journals:

Bo Yang, Gengxiang Li, Huilong Zhang, Mo Dai, 2011. "Rotation and translation invariants of Gaussian–Hermite moments". *Pattern Recognition Letters*, Volume 32, Issue 9, 1283-1298.

Publications on Conferences:

Gengxiang Li, Bo Yang, Mo Dai, 2010. "Coherency estimation based on spectrum Gaussian-Hermite moments", in: Du, Z., Liu, B. (Eds.), *International Conference on Image Processing and Pattern Recognition in Industrial Engineering 1ed.* SPIE, Xi'an, China, 7 August 2010, Volume 7820, pp. 78202S-78202S-7.

Gengxiang Li, Bo Yang, Mo Dai, 2011. "Multi-scale image description with rotation invariants of Gaussian-Hermite moments", 2011 *International Conference on Wavelet Analysis and Pattern Recognition (ICWAPR 2011)*, Guilin, China, 10 - 13 July 2011, pp. 12-17.

Workshops on Conferences:

Gengxiang Li, Bo Yang, Mo Dai, 2010. "Stepwise dip scanning coherence algorithm based on eigenstructure", *RST 23eme reunion des sciences de la terre*, 25 - 29 Octobre 2010, Volume 1, Bordeaux, France.